University of Wollongong

Research Online

University of Wollongong Thesis Collection 1954-2016

University of Wollongong Thesis Collections

2015

Particle inertial focusing and separation in serpentine microchannels: mechanisms and applications

Jun Zhang
University of Wollongong

Follow this and additional works at: https://ro.uow.edu.au/theses

University of Wollongong

Copyright Warning

You may print or download ONE copy of this document for the purpose of your own research or study. The University does not authorise you to copy, communicate or otherwise make available electronically to any other person any copyright material contained on this site.

You are reminded of the following: This work is copyright. Apart from any use permitted under the Copyright Act 1968, no part of this work may be reproduced by any process, nor may any other exclusive right be exercised, without the permission of the author. Copyright owners are entitled to take legal action against persons who infringe their copyright. A reproduction of material that is protected by copyright may be a copyright infringement. A court may impose penalties and award damages in relation to offences and infringements relating to copyright material. Higher penalties may apply, and higher damages may be awarded, for offences and infringements involving the conversion of material into digital or electronic form.

Unless otherwise indicated, the views expressed in this thesis are those of the author and do not necessarily represent the views of the University of Wollongong.

Recommended Citation

Zhang, Jun, Particle inertial focusing and separation in serpentine microchannels: mechanisms and applications, Doctor of Philosophy thesis, School of Mechanical, Materials and Mechatronic Engineering, University of Wollongong, 2015. https://ro.uow.edu.au/theses/4492

Research Online is the open access institutional repository for the University of Wollongong. For further information contact the UOW Library: research-pubs@uow.edu.au

UNIVERSITY OF WOLLONGONG

School of Mechanical, Materials and Mechatronic Engineering

Faculty of Engineering and Information Sciences

Particle inertial focusing and separation in serpentine microchannels: mechanisms and applications

Jun Zhang

"This thesis is presented as part of the requirements for the award of the Degree of

Doctor of Philosophy in Mechanical Engineering

University of Wollongong"

Oct 2015

ABSTRACT

Inertial microfluidic technology, which manipulates (e.g. focusing, separation, trapping etc.) micro-particles by the intrinsic fluid dynamics and inertial effects, has attracted significant interests over the past decade. Compared with other microfluidic manipulation technologies (e.g. dielectrophoresis, magnetophoresis, acoustophoresis etc.), inertial microfluidics possesses superior advantages including simple structure and extremely high throughput. High throughput is especially useful for the isolation of rare target cells, where large volume of biological sample needs to be processed in a short time. The functionality of inertial microfluidics relies on the inertial migration phenomenon and/or curvature-induced secondary flow.

To date, two major classes of curving channels in inertial microfluidics have been presented, including 1) spiral channels, with consistent direction of curvature, and 2) serpentine channels, with alternating curvature. In spiral channels, curvature is along one direction, where secondary flow reaches steady state after long enough distance, and becomes almost uniform within each cross-section. So analysis of inertial focusing in spiral channels can be simplified by static superposition of inertial lift force and secondary flow drag force within a typical channel cross-section. Therefore, its mechanism has been extensively investigated and uncovered. However, in serpentine channels with alternating curvatures, the mechanism becomes more complex and has been rarely reported. For example, with alternating curvatures, secondary flow may not approach steady state at each curvature, and accumulation of this unsteady induces non-intuitive and unpredictable phenomenon. Furthermore, the varying secondary flow in the cross sections of alternating curvatures makes the inertial focusing process more complicated.

The main objective of this research is to conduct a comprehensive investigation on the inertial focusing and separation in symmetric serpentine channels, including mechanism and applications. In our work, three basic focusing patterns were observed: (i) single focusing streak at the channel centre; (ii) two focusing streaks at two sidewalls; and (iii) transition patterns. The mechanism of these three focusing patterns were studied and discussed. Disagreed with previous argument that single focusing streak cannot be obtained in symmetric serpentine channels due to the complete counteraction of symmetric secondary flow during opposite curvatures, we

verified that sufficient single focusing streak could be achieved in symmetric serpentine channels. Through numerical simulation, analytical analysis and experimental validation, the positive effects of Dean flow on particle focusing were uncovered, besides its well-known mixing effects by the counter-rotating streamlines. This finding extends our understanding on the effects of Dean flow on the particle focusing in the curved channels, revealing the new possible explanation to uncover other non-intuitive inertial focusing phenomenon.

Besides the mechanism, the potential application of serpentine channels in particle filtration and separation was also explored. The two-sided focusing pattern was exploited to extract blood plasma in a high-throughput manner. As an effective filtration device, more than 99.95% blood cells could be removed in a single process, with a very high recovery yield of 46% plasma collected. The parallelization design rules for the serpentine channel were also proposed, and their feasibility was verified by the fabrication and experiment of microfluidic device with eight parallel serpentine channels.

In addition, complete separation of particles by differential lateral equilibrium positions in serpentine channels was demonstrated. The complete separation was based on the overlap of two distinct focusing patterns in the serpentine channel: single central focusing pattern of large particles and two-sided focusing pattern of small particles. And this separation scheme is a great advance compared with the previous reported asymmetric serpentine channels, in which particle separation was based on the filtration concept and could not provide high purity as well as high recovery for both particles. The excellent separation performance of the proposed serpentine channels was demonstrated through the effective classification of a series of particle mixtures, including mixtures of polystyrene particles, mixture of erythroleukemia cells and blood cells, as well as blood cells mixture.

Finally, based on the above investigation about the inertial focusing in the serpentine channels, we, for the first time, proposed an innovative hybrid device which coupled dielectrophoresis (DEP) force and inertial lift forces in the serpentine channels. The vertical DEP force was employed to modify the inertial focusing positions in three dimensional, and the interaction between inertial lift force and DEP force was analysed in detail. The effects of DEP force on the three different focusing

patterns in the serpentine channels were investigated. The results indicate that this hybrid device has great potential for multi-criteria particle manipulation and classification.

In summary, we hope that our study can not only extend the fundamental understanding of inertial focusing in serpentine channels, but also provide versatile and effective particle separation and manipulation platforms, for the practical application of biological sample treatment and clinical diagnosis.

ACKNOWLEDGEMENTS

First of all, I would like to express my greatest gratitude to my three supervisors: Professor Weihua Li and Professor Gursel Alici from University of Wollongong, as well as Professor Nam-Trung Nguyen from Griffith University, for their supervision and advice during the course of my study as a PhD candidate. They continuously supervised my research progress and directed me in the right track of my study. Without their patient encouragement and valuable suggestions, this work would not have been possible.

I would like also express my deep gratitude to Professor Dino Di Carlo and his group members Ms Anne-Marie Dieters, Mr Soroush Kahkeshani and Mr Jonathan Lin etc. from University of California, Los Angeles (UCLA), for their helpful discussion on inertial microfluidics, and thoughtful arrangement for my visiting in UCLA. I also appreciate very much Professor Nam-Trung Nguyen for the precious opportunity to work in his lab in Griffith University, and Ms Lacey Shaw for the proper arrangement during my visit. I am also thankful to Mr Majid Hejazian and Dr John Holleran for the valuable discussion and meaningful collaboration in Griffith University.

Then I would like to show great appreciation to Professor Ronald Sluyter and Dr Aleta Pupovac from Illawarra Health and Medical Research Institute (IHMRI), University of Wollongong. They kindly provided the technical training and support on the cell culture, staining and flow cytometer testing etc. which are crucial in the testing of my microfluidic devices. In addition, I am very thankful for their volunteer donation of blood sample to my research.

Special thanks go to Dr Ming Li and Dr Tongfei Tian for their rich practical experience and patient instruction, which really helped me through lots of problems in the early stage. My great gratitude is expressed to Mr Sheng Yan, who is not only a talent research fellow, but also a close friend to me. I am also grateful to other colleagues who helped me in this or that way: Dr Rahim Mutlu, Dr Miao Guo, Dr Xianzhou Zhang, Miss Dan Yuan and Mr Chao Pan etc. Thanks go to the administration staffs of Faculty and technicians of Engineering, ITS and SMART building for their great supports and services.

I appreciate financial support from the China Scholarship Council (CSC) and IPTA scholarship from University of Wollongong. Without these financial supports, I can’t come to this beautiful place to continue my higher degree study.

Last but not least, my deep gratitude is given to my family, especially to my wife Mrs Tingting Liu and my mother Mrs Lanxia Zhu, for their support, encouragement, love and sacrifice. They make this work more meaningful than it is.

PUBLICATIONS

1. **J. Zhang**, S. Yan, R. Sluyter, W. Li, G. Alici, and N.-T. Nguyen, "Inertial particle separation by differential equilibrium positions in a symmetrical serpentine micro-channel," *Scientific reports*, vol. 4, art. no. 4527, 2014. (**Nature Publishing Group**)
2. **J. Zhang**, S. Yan, G. Alici, N.-T. Nguyen, D. Di Carlo, and W. Li, "Real-time control of inertial focusing in microfluidics using dielectrophoresis (DEP)," *RSC Advances*, vol. 4, pp. 62076-62085, 2014.
3. **J. Zhang**, W. Li, M. Li, G. Alici, and N.-T. Nguyen, "Particle inertial focusing and its mechanism in a serpentine microchannel," *Microfluidics and Nanofluidics*, vol. 17, pp. 305-316, 2014.
4. **J. Zhang**, S. Yan, W. Li, G. Alici, and N.-T. Nguyen, "High throughput extraction of plasma using a secondary flow-aided inertial microfluidic device," *RSC Advances*, vol. 4, pp. 33149-33159, 2014.
5. S. Yan, **J. Zhang**, M. Li, G. Alici, H. Du, R. Sluyter, *et al.*, "On-chip high-throughput manipulation of particles in a dielectrophoresis-active hydrophoretic focuser," *Scientific reports*, vol. 4, art. no. 5060, 2014. (**Nature Publishing Group**)
6. S. Yan, **J. Zhang**, G. Alici, H. Du, Y. Zhu, and W. Li, "Isolating plasma from blood using a dielectrophoresis-active hydrophoretic device," *Lab on a Chip*, vol. 14, pp. 2993-3003, 2014.
7. M. Li, W. Li, **J. Zhang**, G. Alici, and W. Wen, "A review of microfabrication techniques and dielectrophoretic microdevices for particle manipulation and separation," *Journal of Physics D: Applied Physics*, vol. 47, art. no. 063001, 2014.
8. S. Yan, **J. Zhang**, Y. Yuan, G. Lovrecz, G. Alici, H. Du, *et al.*, "A hybrid dielectrophoretic and hydrophoretic microchip for particle sorting using integrated pre-focusing and sorting steps," *Electrophoresis*, 2014, DOI: 10.1002/elps.201400397.
9. S. Yan, **J. Zhang**, H. Chen, G. Alici, H. Du, Y. Zhu, *et al.*, "Making a hydrophoretic focuser tunable using a diaphragm," *Biomicrofluidics*, vol. 8, art. no. 064115, 2014.

10. **J. Zhang**, M. Li, W. Li, and G. Alici, "Inertial focusing in a straight channel with asymmetrical expansion–contraction cavity arrays using two secondary flows," *Journal of Micromechanics and Microengineering*, vol. 23, art. no. 085023, 2013.
11. Z. Zhang, N. Jan, T. Ren, and **J. Zhang**, "Influence of void space on microscopic behavior of fluid flow in rock joints," *International Journal of Mining Science and Technology*, vol. 24, pp. 335-340, 2014.
12. **J. Zhang**, M. Li, W. Li, and G. Alici, "Investigation of trapping process in "Centrifuge-on-a-chip"," in *Advanced Intelligent Mechatronics (AIM), 2013 IEEE/ASME International Conference on*, 2013, pp. 1266-1271.

TABLE OF CONTENTS

ABSTRACT i
ACKNOWLEDGEMENTS iv
PUBLICATIONS vi
LIST OF FIGURES xii
LIST OF TABLES xxvi
LIST OF ABBREVIATION xxvii
LIST OF NOTATION xxviii
1 Introduction 1
1.1 Background and motivation 1
1.2 Objectives 3
1.3 Outline of the thesis 4
2 Literature review 7
2.1 Particle manipulation in microfluidic platform 7
2.2 Active techniques and passive techniques 8
2.2.1 Active techniques 8
2.2.2 Passive techniques 10
2.3 Fundamental fluid dynamics and particle dynamics in inertial microfluidics 14
2.3.1 Basic fluid dynamics in inertial microfluidics 14
2.3.2 Fundamental dynamics of particle movement in a microfluidic channel 19
2.4 The recent progress of inertial microfluidics 36
2.4.1 Straight channels 36
2.4.2 Spiral channels 42
2.4.3 Straight channels with pillar arrays or expansion-contraction arrays 49
2.4.4 Serpentine channels 58
2.5 Conclusion 61
3 Inertial focusing in symmetric serpentine channels: single central focusing pattern 63
3.1 Introduction 63
3.2 Materials and methods 63

3.2.1 Design and fabrication of the micro-channel 63
3.2.2 Particle suspension 65
3.2.3 Experimental setup and method 65
3.2.4 Numerical simulation 66
3.3 Results and discussion 67
3.3.1 Particles inertial focusing in symmetric serpentine channels 67
3.3.2 Focusing mechanism and design considerations 68
3.3.3 Validation of focusing concept and determination of correction coefficient ε 76
3.3.4 Effects of the Reynolds number 78
3.3.5 Effects of particle size and particle inertia 80
3.3.6 Position and velocity of particles at the outlet 82
3.4 Conclusion 84
4 Inertial focusing in symmetric serpentine channels: two-sided focusing pattern and its application on plasma extraction 85
4.1 Introduction 85
4.2 Materials and methods 86
4.2.1 Design and fabrication 86
4.2.2 Particle and cell preparation 86
4.3 Results and discussion 87
4.3.1 Inertial focusing in straight channels 87
4.3.2 Secondary flow aided inertial focusing in serpentine channels 89
4.3.3 Effects of particle size 91
4.3.4 Extraction of blood plasma 95
4.3.5 Effects of haematocrit (Hct) 97
4.3.6 Parallelization technique 98
4.4 Conclusion 102
5 Inertial particle separation by differential equilibrium positions: employing overlap between single central focusing pattern and two-sided fcousing pattern 103
5.1 Introduction 103
5.2 Materials and methods 105
5.2.1 Device fabrication 105
5.2.2 Cell culture 105

5.2.3 Particle and cell mixture preparation 106
5.2.4 Experimental setup and method 106
5.3 Results and discussion 107
5.3.1 Differential equilibrium positions of different-sized particles 107
5.3.2 Separation of polystyrene particles 110
5.3.3 Separation of biological particles 114
5.4 Conclusion 120
6 Real-time control of inertial focusing in microfluidics using dielectrophoresis (DEP) 123
6.1 Introduction 123
6.2 Materials and Methods 124
6.2.1 Design and fabrication of the DEP-inertial hybrid device 124
6.2.2 Particle preparation 125
6.2.3 Experimental setup and methods 125
6.3 Mechanism 125
6.3.1 Inertial migration 125
6.3.2 The n-DEP force in interdigitated electrodes (IDEs) 126
6.3.3 Coupling of n-DEP force and inertial lift force along vertical direction 128
6.4 Results and Discussions 133
6.4.1 Inertial focusing patterns in serpentine channels under varying Re 133
6.4.2 Influence of n-DEP on two-sided inertial focusing pattern: modification of focusing pattern by levitation of particles 134
6.4.3 Influence of n-DEP on inertial single-stream focusing pattern: sheath-less three-dimensional focusing 136
6.4.4 Influence of n-DEP on inertial transitional focusing patterns: pinching of widely distributed particles into a tight focusing streak 137
6.4.5 V_{pp}-Re operation map 139
6.5 Conclusions 141
7 Conclusions and future work 143
7.1 Conclusions 143
7.1.1 The mechanism of single central focusing pattern 143

7.1.2 The mechanism of two-sided focusing pattern and its application on plasma extraction 143
7.1.3 High throughput separation of particles by differential equilibrium positions in serpentine channels 144
7.1.4 Manipulation of particles by a hybrid DEP-inertial microfluidic device 144
7.2 Future work 145
7.2.1 Separation of multiple particles by cascaded connected serpentine channels 145
7.2.2 Separation and enrichment of circulating tumor cells (CTCs) by the serpentine channels 145
7.2.3 Exploring the application of the hybrid DEP-inertial microfluidic device 146
References 148

LIST OF FIGURES

Figure 1–1 The outline of the overall work. 4

Figure 2–1 Three typical DEP microfluidic devices, (a) electrode-based DEP (eDEP) [72], (b) electrode-less/insulator-based DEP (iDEP) [73], and (c) contactless DEP (cDEP) [71, 74]..... 9

Figure 2–2 (a) Schematic image about cell-MP (magnetic particle) binding [76]. (b) Magnetic particles in the magnetic field deflect from their original moving direction depending on the size and magnetic susceptibility of each particle [33, 52]. (c) A schematic representation of the ferromicrofluidic device with permanent magnets [78]. 9

Figure 2–3 (a) 1D and 2D Microfluidic Acoustic tweezers using standing surface acoustic waves (SSAW) [55]. (b) Schematics of the particle separation by the axial acoustic forces when they enter the working region of the SSAW [54]. .. 10

Figure 2–4 Four types of micro-scale filter: (a) Membrane-type; (b) Weir-type; (c) Pillar-type; (d) Cross-flow type [79]. 11

Figure 2–5 High resolution separation of particles by size in a matrix of obstacles: Deterministic lateral displacement [12]. 12

Figure 2–6 A schematic principle of hydrophoretic separation [85]. Shaded- and lined-areas denote lower and upper slanted obstacles, respectively. The flow direction is along the y-axis. 13

Figure 2–7 (A) Inertial migration in a straight channel with circular cross-section. (B) Second flow in a curve channel [6]. 14

Figure 2–8 Fluidic resistor for the hydraulic resistance and Hagen-Poiseuille's law is analogous to a resistor for the electric resistance and Ohm's law. Reproduced from reference [103]. 19

Figure 2–9 Rotation induced lift force for a rigid cylinder and sphere in a uniform flow. 23

Figure 2–10 Lateral force on a sphere in a simple shear flow. V is the relative velocity of particle to fluid. (a) $V > 0$ indicates that particle moves faster than the fluid, leading the flow. (b) $V < 0$ means that particle moves slower than the fluid, lagging the flow. The direction of lateral lift force always directs toward the side where magnitude of relative velocity V is maximum. 26

Figure 2–11 Shear-gradient lift force exerted on a neutrally buoyant rigid sphere in a Poiseuille flow. In the moving frame with the particle, the relative velocity of fluid to particle is larger on the wall side due to the parabolic fluid velocity profile. Reproduced from reference [110]. 27
Figure 2–12 (a) Particle size is far less than the characteristic dimension of channel, and the motion of immersed particle is primarily influenced by a single wall. (b) Particle size is of the of the order of the dimension of channel, and boundaries retard significantly the motion of the object. (c) Main flow direction is perpendicular to the boundary. (d) Main flow direction is parallel to the boundary..... 30
Figure 2–13 (a) Balance of shear gradient lift force and wall lift force results in the inertial equilibrium positions in a Poiseuille flow. (b) The net lift coefficient is the function of particle lateral position x and Reynolds number Re. Reproduced from reference [117]. 32
Figure 2–14 Deformability-induced lift force directs to the channel centre, and shifts inertial equilibrium positions closer to the channel center, compared with the rigid spherical particles. 35
Figure 2–15 (a) Inertial equilibrium positions in a circular channel. (b) Inertial equilibrium positions in a rectangular channel with square cross-section. (c) Inertial equilibrium positions in a rectangular channel with low aspect ratio. And illustration of two-stage migration model proposed by Zhou and Papautsky [116]. (d) The lateral migration speed U_L and minimum channel length for particle focusing $L_{\min}$..... 38
Figure 2–16 (a) Label free isolation of adrenal cortical progenitor cells by size-based differential inertial focusing in a straight channel [133]. (b) Classifying and separating cells and particles by deformability in inertial microfluidics. Besides inertial lift forces, deformable cells experiencing an extra deformability-induced lift force than rigid particles, shifting deformable cells towards channel centreline [121]. (c) Pathogen removal from blood using margination phenomenon in a straight channel. Deformable RBCs migrate axially to the channel centre, resulting in margination of other relative rigid cell types (bacteria, platelets and leukocytes) towards the channel walls, and subsequently removed from the side outlets [135]. (d) Separation of pathogenic bacteria from

diluted blood in a series-connected straight channel which utilizes a unique differential transit time by size-dependent inertial lift forces to obtain cell separation [136]. (e) Complete separation of particles in a cascaded channel with two straight segments with different aspect ratios (*AR*s). Randomly-distributed particles first flow through a high *AR* channel where particles are focused at two sidewalls facing the centre of channel heights. After all the particles are fully focused, the channel expands into a low *AR* channel, which modifies equilibrium positions to the centre of channel width. Since larger particles experiencing much stronger migration velocity, reach refocusing much faster than the smaller ones, thus enabling a separation of particles [137]. (f) Rapid inertial solution exchange in a straight channel for controlled interaction of reagents with cells and particles [138]. (g) Extremely high throughput microfluidic flow cytometry employing inertial ordering in 256 high *AR* parallel channels and high-speed optical interrogation method [139]. 41

Figure 2–17 (a) Schematic illustration of inertial separation by particle size in a curved microchannel and its important design parameters [140]. (b) A typical distribution of velocity in a curved channel with Aspect ratio of 1, and θ=90º [140]. (c) Superposition of inertial lift force and Dean flow in curved channel modifies the number and position of the inertial focusing positions [6]. (d) Size-based separation along the direction of stokes drag exerted by the Dean flow. A large bead mainly experiences a net outward force due to main outward velocity around channel centre, while a small bead is dominated by the inward velocity distribution near top and bottom walls [140]. 44

Figure 2–18 (a) Schematic of a microfluidic flow cytometry, in which spiral channel is applied as a particle focuser to provide high-throughput sheath-less 3-D focusing, followed by the downstream laser induced fluorescence setup for particle detection and counting [125]. (b) Microfluidic device consists of a spiral channel followed by an encapsulation part. The spiral channel promotes single cell stream ordering with a precise longitudinal spacing, and it is critical for downstream encapsulation of cells into the droplet [126]. (c) Continuous triplet-particle separation in a spiral channel by the Dean-coupled inertial migration [142]. (d) Schematic illustration of cell cycle synchronization in a spiral channel. Under the influence of inertial lift force and Dean drag force,

asynchronous cell populations with different sizes will be differential ordering at the end of spiral channel for purification [147]. (e) Double spiral microchannel for tumour cell separation and enrichment [143]. (f) A multiplexed microfluidic device stacked by three spiral channels for ultra-high throughput CTCs capturing and enrichment [150, 151]. (g) Enhanced inertial separation of Leukocytes from red blood cells using spiral channel with trapezoid cross-section. At the outlet, the larger white blood cells focus near the inner walls, while smaller red blood cells are trapped at the core of dean vortex near the outer wall [146]. (h) Ultra-fast, label-free enrichment of CTCs from blood samples by a spiral microfluidic device with trapezoid cross-section [145]. 48

Figure 2–19 (a) Schematic of three dimensional hydrodynamic focusing in a contraction-expansion array (CEA) channel which is consisted of a straight channel with contraction-expansion arrays patterned on single side [153]. (b) Inertial separation of particles by size in a CEA channel under the assistance of a sheath flow [129]. (c) Label-free high throughput separation of cancer cells from whole blood in a CEA microchannel. Large cancer cells are influenced dominantly by the inertial lift forces, migrating towards s1, while small cells (red blood cells and white blood cells) are dominated by Dean drag, shifting towards s2 [155]. (d) Inertial focusing in a straight channel patterned with symmetrical expansion-contraction array on both sides (multi-orifice microchannel). The ordered particle distribution is achieved at central or side regions according to a particle Reynolds number [156]. (e) Continuous inertial separation in a multi-orifice microchannel according to the size-dependent lateral migration termed as Multiorifice Flow Fractionation [157]. (f) Continuous high-throughput separation of human breast cancer cells (MCF-7) from blood cells by a combination of multi-orifice flow fractionation (MOFF) and dielectrophoresis (DEP). The inertial separation in MOFF takes advantage of the high-throughput filtration of blood cells, and the serially connected DEP separator further enhances the separation efficiency and purity [159]. (g) Schematic of Multi-stage Multiorifice Flow Fractionation (MS-MOFF) design [158]. (h) Modified detection of malaria by the integration of inertial microfluidic processing and PCR detection. Inertial enrichment and purification

of malaria parasites from blood in a symmetrical expansion-contraction channel provides more reliable and specific PCR-based detection [160]. 52
Figure 2–20 (a) “Centrifuge-on-a-chip” for the functions of selective trapping, enrichment, labelling and solution exchange [164]. Basically, there are three steps for the functionality of the “Centrifuge-on-a-chip”: (i) inertial focusing in the straight channel, (ii) lateral migration in the expanding area; and (iii) circulation within horizontal micro-vortex. (b) Isolation and concentration of cancer cells and mesothelial cells from malignant pleural effusions by automated Centrifuge chip for improved molecular and cytomorphological diagnostics [166]. (c) Vortex-aided inertial microfluidic device for continuous sorting of particles by size. By utilizing the similar trapping mechanism of Centrifuge chip, larger particles are trapped in the horizontal vortices in the contraction-expansion chambers. A modified side outlet in each trapping chamber siphons them out continuously, meanwhile smaller particles exist through the main channel [165]. (d) Schematics of size-based Multi-modal microfluidic sorter. This microfluidic system can achieve continuous multimodal sorting (with multi cutoff sizes) of microparticles with high resolution and high tunability [168]. (e) Rotational control of single cells by microvortices in a diamond-shaped chamber [162]. 55
Figure 2–21 (a) Engineering desired inertial flow deformation by programing a sequence of cylindrical pillars within a straight microchannel [169]. (b) Schematic illustration of synthesis of shaped polymeric microfibers using a programmable inertial microfluidic system [100]. (c) Single stream inertial focusing of microparticles in a straight channel with programmable micropillars. The sequential pillars induce local helical vortices to bring particles to a single focusing equilibrium positions [171]. (d) Exchange of solution around cells or particles by controllable cross-stream translation of fluid in micropillar sequenced microchannel [172]. 57
Figure 2–22 (a) Inertial focusing of particles in serpentine microchannel. In a straight channel with square cross-section, focusing of particles into four single streamlines is observed, with each of them facing the centre of each wall. For a symmetric serpentine channel, the symmetry of system reduces focusing to two streams. Above a critical Dean number, focusing is disturbed. In an asymmetric

serpentine channel, focusing down to a single stream is observed, and more complex with Dean number increased [96]; (b) Equilibrium filtration by differential inertial focusing in a serpentine channel with 62 asymmetric turns, and 5 outlets. Above a critical size cut-off, particles are well focused as a single stream, while particles below this cut-off size remain unfocused [173]. (c) Schematic of microfluidic flow cytometry system. Combination of asymmetrically serpentine microchannel section with a high aspect ratio straight section provides three dimensional single stream focusing [174]. (d) A hybrid microfluidic device which integrates deterministic lateral displacement (DLD), inertial focusing in asymmetrical serpentine channel and magnetophoresis (MP) to isolate rare circulating tumour cells (CTCs) in an antigen–dependent and independent way [175]. (e) Deformability cytometry to characterise mechanical morphology of single cells in large population. Inertial focusing of cells in a serpentine channel orders cells along a single stream is followed by the downstream hydrodynamic pinching [40]. 60

Figure 3–1 The fabricated microfluidic device and illustration of dimension of serpentine channel. 64

Figure 3–2 Experimental setup for inertial microfluidic device. 66

Figure 3–3 Three different particle focusing patterns in a serpentine channel with varying flow conditions, (I) Inertial lift force dominated region with two-sided focusing streaks, (II) transition region with a wide single central focusing band, and (III) Secondary flow dominated region with a single focusing streak at the channel centre. The error bars indicate the width of the focusing streak. Particle diameter is 10 μm. 68

Figure 3–4 Focusing mechanism of particles in a serpentine channel. (a) Schematic view of particles focusing in a serpentine channel. (b) The trajectory and speed of particles in a serpentine channel. The coloured curves are the dynamic trajectory of micro-particles, and the colour legend is the speed of particles. Particle trajectory is obtained and speed by the numerical simulation. (c) The viscous drag F_D in the cross section of the channel. (d) Schematic illustration of centrifugal movement of single particle within one turn. 69

Figure 3–5 (a) The counter-rotating vortex in the cross section of serpentine channel with different aspect ratios (*AR*s), (i) *AR*=1/5 and (ii) *AR*=3/5. (b) The fluid

velocity along z (vertical) direction is responsible for the mixing effect. Its average magnitude is plotted under (i) zigzag channel with different aspect ratios when input velocity is constant (1 m/s), and (ii) different input velocities when AR is set as 1/5. The average velocity along z axis is calculated as: $vzdSS$, where S is the area of channel cross section, and v_z is fluid velocity along z direction..... 75

Figure 3–6 Particle equilibrium positions by inertial migration in a straight channel with different aspect ratios (ARs). (a) Four equilibrium positions when AR=1 [6]. (b) Two equilibrium positions when AR=1/3~1/2 [10]. (c) No distinct equilibrium positions along the long face when AR=1/5. 76

Figure 3–7 (a) The overview of particles focusing in a serpentine channel. (b) The numerical results of particles' trajectory at the inlet, typical zigzag periods and outlet of a serpentine channel. (c) The experimental streak images of fluorescent particles in the corresponding positions of the serpentine channel. (d) Particle streak width and position. (i) Determination of particle streak width and streak position from fluorescence intensity profile. (ii) Particle streak width under different numbers of zigzag turns. The input fluid average velocity is 1.1 m/s, corresponding to the Reynolds number of 110. Particle diameter is 9.9 μm. 77

Figure 3–8 The particle streak width under different flow conditions (Reynolds number). 79

Figure 3–9 Particle streak images observed from fluorescence microscope (left) and particles snapshot image obtained from micro-PIV system (right) under different flow conditions. 80

Figure 3–10 The effects of particle size and solution density on the critical Reynolds number for particle focusing. 81

Figure 3–11 (a) Particle longitudinal space under different flow conditions. Particles are highlighted with red circle. (b) The particle velocity at the outlet. (i) Particle velocity is calculated as particle displacement divided by residence time Δt (100 μs). Particle positions at two moments are superposed with two different colours. Green symbol is particles at the initial moment, and red symbol is particle position after Δt. (ii) Particle average velocity with respect to input fluid velocity. Particle average velocity is calculated as: $\left(\sum_{i=1}^{n} \Delta x_i / \Delta t\right) / n$. Two blue

dots are schematic position of particles within channel cross-section at the outlet. Fluid maximum velocity is calculated as U_m=1.5U_f [96]. 83
Figure 4–1 Inertial focusing phenomenon in a straight channel with cross sections of (width × height) of (a) 50 μm×42 μm, *AR*=0.84; (b) 100 μm×42 μm, *AR*=0.42. 87
Figure 4–2 Inertial focusing phenomenon in a straight channel with cross sections of (width × height) of 200 μm×42 μm, *AR*=0.21. 88
Figure 4–3 (a) Fluid velocity profiles along the channel width for straight channels with different cross-sections. Velocity distribution is evaluated along the central plane y = 0. (b) Velocity profiles along the channel depth for straight channels with different cross-sections. Velocity distribution is evaluated along the central plane x = 0. Velocity is normalized by input average velocity V_{avg}..... 89
Figure 4–4 (a) Schematic illustration of particle inertial focusing process in a serpentine channel. (b) Dynamic analysis of particles within eight typical cross-sections under the influence of secondary flow. (c) The theoretical inertial equilibrium positions and the experimental particle trajectory. (d) The fluorescent images of particle trajectory in different zigzag periods of a serpentine channel. 91
Figure 4–5 Two-sided inertial focusing pattern in a serpentine channel for polystyrene beads with 10 μm in diameter. (Left) Fluorescent intensity profile and (Right) their corresponding fluorescent images at different zigzag periods. 92
Figure 4–6 Two-sided inertial focusing pattern in a serpentine channel for polystyrene beads with 5 μm in diameter. (Left) Fluorescent intensity profile and (Right) their corresponding fluorescent images at different zigzag periods. 93
Figure 4–7 Two-sided inertial focusing pattern in a serpentine channel for polystyrene beads with 3 μm in diameter. (Left) Fluorescent intensity profile and (Right) their corresponding fluorescent images at different zigzag periods. 94
Figure 4–8 (a) Three particle-free regions at the channel outlet, and their corresponding volumetric flow rates. (b) The normalized fluid flow rate within particle free regions for different-sized particles. (c) The concentrations of 3

μm, 5 μm and 10 μm polystyrene beads suspension before and after a single filtration process, and (d) their corresponding fluorescent images in the hemocytometer. 95
Figure 4–9 (a) Schematic illustration of the extraction of plasma in the symmetric serpentine channel; (b) Bright field image of filtration of blood cells at the outlet; (c) Concentration of blood cells after each process, inserted with bright field images of blood sample before and after each filtration. In the second process, the input blood sample is the blood plasma obtained from the first process. Error bars represent the standard deviation of three measurements in hemocytometer. (d) (Left) Working image of the microfluidic device, one can clearly observe that the tubes of outlet #1 is clear, indicating barely red blood cells passing through, while tubes of inlet and outlet #2 are in red colour, filled with massive red blood cells; (Right) Optical images of input blood sample and two collections from each outlets. 96
Figure 4–10 Effects of blood haematocrit (Hct) on two sided inertial focusing. (a) The bright field images of blood cells focusing at the end of serpentine channel (left) and bifurcation outlet (right). (b) The bright field intensity profile at the end of serpentine channel along the channel width. It should be noted that in bright field images, the higher the intensity, the less cells occupy, allowing more illuminating light to be captured by camera. 98
Figure 4–11 (a) Schematic structure of the parallelized microfluidic device with eight serpentine channels; (b) The picture of fabricated parallelized inertial microfluidic device. The blue food dye was injected into the device for better visualization of micro-channel structure; (c) Fluidic circuit of the parallelized microfluidic device; (d) Simulated flow field within one trifurcation outlet unit. 100
Figure 4–12 Bright field images at each outlet bifurcation in the parallel device. The uniform streamline splitting and blood cells filtration at each outlet validate our parallelization design considerations. 101
Figure 5–1 (a) Experimental observation of outlet fluorescent streak images for different-sized particles under various flow conditions; (b) Translation of particle focusing pattern into three standard regions in the Reynolds number – particles diameter space. 108

Figure 5–2 Quantitative illustration of focusing positions and widths for different-sized particles under various flow conditions. Error bars indicate the streak width, which was determined by standard FWHM (full width at half maximum). The streak position was taken as the middle of the half maximum intensity. . 109
Figure 5–3 The optimization of fluid streamline bifurcation at the outlet. 110
Figure 5–4 (a) Schematic illustration of the micro-channel structure used for particle separation in this work. A filter upstream of the serpentine channel prevents the channel from being blocked by large debris. A trifurcation outlet system with two symmetrical side branches merged together as a single outlet #2 was used. (b) Superimposed fluorescent images illustrating the distribution and position of the 10 μm (pseudo-coloured green) and 3 μm (pseudo-coloured red) particles in different periods of serpentine channel. (c) (i) Fluorescent images of the particle mixture at the outlet of the serpentine channel, and (ii) its cross sectional fluorescence intensity profile presents differential equilibrium positions for binary particles. (iii) Pictures of particles suspension before and after processing indicate an effective particle separation in the serpentine channel. 111
Figure 5–5 Separation of 3 μm and 10 μm particles in the serpentine channel. (a) Fluorescent images of collections from control and two outlets. The control is particle mixture collected before passing through the serpentine channel. Pseudo-coloured green and red dots represent 10 μm and 3 μm particles respectively. (b) Particle concentrations from control and two outlets under different processing flow conditions (flow rate or Reynolds number). (c) The purity of particles from two collectors at various flow conditions. (d) The separation efficiency for 3 μm and 10 μm particles under different flow conditions. Error bars represent the standard deviation of three measurements by hemocytometry..... 113
Figure 5–6 Separation of 5 μm and 13 μm particles in the serpentine channel. (a) Fluorescent images of collections from control and two outlets. Pseudo-colored green and red dots represent 13 μm and 5 μm particles respectively. (b) Particle concentrations from control and two outlets under three different processing flow conditions. (c) The purity of particles from two collectors at various flow conditions. (d) The separation efficiency for 5 μm and 13 μm particles under

different flow conditions. Error bars represent the standard deviation of three measurements by hemocytometry. 114
Figure 5–7 (a) Concentrations of 5 μm polystyrene beads and MEL cells from control and two outlets under the flow condition of Re=120. (b) Purity of 5 μm polystyrene beads and MEL cells before and after a single process by the proposed microfluidic device. (c) FSA-SSC data of flow cytometric data indicate relative percent of (i) input mixture of 5 μm polystyrene beads and MEL cells, (ii) collection from outlet #1, and (iii) collection from outlet #2. The number near the gated group represents the percentage of group number on the total particle events. (d) FSA-cell counts data reveals the cell/particle size distribution from each collection. The FSA data is proportional to the particle size 116
Figure 5–8 The bright field and fluorescence images from control and two collections. In bright field image, both of MEL cells and 5 μm polystyrene beads can be observed. While in fluorescent images, only 5 μm fluorescent polystyrene beads can be observed. The number of MEL cells can be easily obtained by subtracting number of 5 μm polystyrene beads from the total number of MEL cells and 5 μm polystyrene beads. 117
Figure 5–9 Separation of MEL cells from the whole blood cells. (i) FSC-SSC results of cells mixture; (ii) FSC-SSC results of collection #1 indicate purified MEL cells; (iii) FSC-SSC results of collection #2. 118
Figure 5–10 Separation of white blood cells from the whole blood. (i) FSC-SSC results of input whole blood cells, it is very hard to observe the existence of white blood cells from massive red blood cells; (ii) FSC-SSC results of collection #1, the percentage of white blood cells is increased to about 40.4%; (iii) FSC-SSC results of collection #2. 118
Figure 6–1 (a) Schematic of DEP-inertial microfluidic device; and (b) the photo of DEP-inertial microfluidic device. The serpentine micro-channel is embedded in the PDMS slab, and the slab is bonded with a clean glass slide where interdigitated electrodes (IDEs) are patterned. The particle suspension is delivered into the micro-channel by a syringe pump. An alternating current (AC) signal is imported into the IDEs, activating DEP force to levitate particles along the vertical *z* direction. 124

Figure 6–2 (a) The electrical field and n-DEP force distribution within a longitudinal section. The arrow vectors represent the magnitude and direction of n-DEP force. The magnitude of n-DEP force along *z* direction is implied by the vectors' colour, and corresponds to the left colour bar. Colour map surface shows the electric field distribution, and corresponds to the right colour bar. (b) Longitudinal distribution of n-DEP force along *z* direction (F_{DEPz}). (c) Vertical distribution of n-DEP force along *z* direction (F_{DEPz}). COMSOL Multi-physics 4.3 was used to calculate the electric field, and the DEP force was calculated using equation (6-1). Particle diameter is 10 μm, and Re[$K(\omega)$] for polystyrene beads in DI water at electric frequency of 1MHz is approximated as -0.5..... 128

Figure 6–3 (a) The distribution of dielectrophoresis (DEP) force F_{DEP} and inertial lift force F_L along the height of the channel *z*. The inertial lift force is obtained from the analytical solution from Matas et al. [117, 203] and n-DEP force is obtained from the simulation results by COMSOL Multi-physics. Particle diameter is 10 μm. (b) At relative low applied voltages, two stable equilibrium positions (A and D) along *z* exist, which are modifications of the original inertial equilibrium positions. The direction of the net force (red arrows) on both sides of stable positions will always point to themselves because they can overcome any small disturbance. However, point B is in an unstable position because the net force along both sides is directed outwards, and a little disturbance will induce the particles to move away from point B. The blue dashed curve is the mirror image of the F_L negative part on a positive coordinate. (c) At a critical voltage (V_{cpp}), the F_{DEP} curve is tangential with the F_L negative mirroring curve at point C, which is in a half stable (saddle) position. If particles were shifted downward ($z < z_C$), the net force will attract particles back to position C, but when the particles were shifted upward ($z > z_C$), the net force is directed upwards and particles will never return. (d) When the applied voltage is higher than the critical voltage V_{cpp}, there is only one vertical equilibrium position D on the upper half of the channel..... 129

Figure 6–4 A schematic illustration of particle migration progress in the channel cross-section under increasing voltage within a cross section of DEP-inertial microfluidic device. DEP force competes with inertial lift force along *z*

direction, thus alters the final vertical position of particles. As a result, the inertial focusing process and pattern can be tuned in three dimensions. 131
Figure 6–5 (a) Simulated particles' trajectories released from different heights. (b) Normalized particle streak widths after traveling through different channel lengths. The particles released near the channel vertical centre focus into the channel lateral centre much faster than that released near channel walls, because fluid velocity is at maximum at the channel centre, and its corresponding secondary flow drag and centrifugal force is much stronger than that near channel walls. 132
Figure 6–6 (a) Schematic 3D structure of one period in the serpentine channel and (b) its side view optical image; (c) The fabricated PDMS device was used to observe the serpentine channel from both top-down and side-side view in the experiments. (d-h) Inertial particle focusing patterns under varying flow conditions: (d) Re=41.7; (e) Re=62.5; (f) Re=83.3; (g) Re=104.2; (h) Re=125. (Left) Top views of fluorescent particles trajectory at the last zigzag period of serpentine; (Middle) Sided views of fluorescent particles at the last zigzag period; and (Right) The dynamic equilibrium positions of particles at cross-section A-a. 133
Figure 6–7 Migration of particle focusing patterns under different AC voltages of (a) $V_{p\text{-}p}$=0 v, (b) $V_{p\text{-}p}$=18 v, (c) $V_{p\text{-}p}$=27 v, (d) $V_{p\text{-}p}$=36 v and (e) $V_{p\text{-}p}$=54 v. (Left) trajectory of fluorescent particles from Top view, and (Right) their corresponding postulated dynamic equilibrium positions within two typical cross-sections "A-a" and "B-b". Flow condition is Re=62.5. 135
Figure 6–8 Migration of particle single central focusing patterns under different AC voltages of (a) $V_{p\text{-}p}$=0 v, (b) $V_{p\text{-}p}$=36 v, (c) $V_{p\text{-}p}$=72 v and (d) $V_{p\text{-}p}$=90 v. (Left) trajectory of fluorescent particles from top view, and (Right) their corresponding postulated dynamic equilibrium positions within two typical cross-sections "A-a" and "B-b". Flow condition is Re=114.6. 137
Figure 6–9 Migration of particle transitional focusing patterns under different AC voltages of (a) $V_{p\text{-}p}$=0 v, (b) $V_{p\text{-}p}$=18 v, (c) $V_{p\text{-}p}$=54 v, (d) $V_{p\text{-}p}$=81 v and (e) $V_{p\text{-}p}$=99 v. (Left) trajectory of fluorescent particles from top view, and (Right) their corresponding postulated dynamic equilibrium positions within two typical cross-sections "A-a" and "B-b". Flow condition is Re=99. 139

Figure 6–10 Distribution of lateral fluorescence intensity with various applied voltages. 140
Figure 6–11 V_{pp}-Re map illustrates the working range of DEP-inertial microfluidic device. The red triangles are experimental data where particles are pushed onto the top half of the channel. The applied voltages are larger than the critical voltage. The empty rectangles are experimental data where particles under bottom half part of channel are focused into a single central focusing streak under the effects of DEP force. The solid rectangles are the experimental data where DEP force is not sufficient to alter particle inertial focusing pattern in bottom half part of channel. 141

LIST OF TABLES

Table 1 Comparison of existing inertial microfluidic techniques for binary-particle separation 121

LIST OF ABBREVIATION

AC: Alternating current

AP: Acoustophoresis

CTCs: Circulating tumour cells

cDEP: Contactless DEP

DEP: Dielectrophoresis

DLD: Deterministic lateral displacement

eDEP: Electrode-based DEP

*h*RBCs: Healthy red blood cells

HCT: Haematocrit

iDEP: Electrode-less/insulator-based DEP

*i*RBCS: Malaria-infected RBCs

IDEs: Interdigitated electrodes

MP: Magnetophoresis

MOFF: Multiorifice Flow Fractionation

MEL: Murine erythroleukemia

MACS: Magnetic activated micro-cell sorter

PFF: Pinched flow fractionation

RBCs: Red blood cells

SSAW: Standing surface acoustic waves

WBCs: White blood cells

LIST OF NOTATION

a: Particle diameter

A: Cross-sectional area of the channel

AR: Aspect ratio of the channel

C: Wetted perimeter

Ca: Capillary number, defined as: $Ca = \frac{\mu U a}{\sigma h}$

d: Distance between drop and centre of channel

d^*: Dimensionless distance, defined as: $d^* = \rho_f \, l_w v_s / \mu$

D: Diffusion coefficient

D_C: Diameter for a cylindrical channel

f_L: Dimensionless coefficient of inertial lift force

f_d: Viscous drag coefficient

F_L: Net inertial lift force

F_{LS}: Shear gradient lift force

F_{LW}: Wall lift force

F_{DEP}: Dielectrophoretic (DEP) force

F_{drag}: Viscous drag force

F_{LR}: Magnus force (or rotation-induced lift force)

F_S: Saffman force (or slip-shear induced lift force)

F_{Cent}: Centrifuge force of particles

$F_{L,deformation}$: Deformability-induced lift force

$F_{L,inertial}^{center}$: Inertial lift force near channel centre

h: Height of microchannel

H: Hydraulic diameter of channel

I: Electric current

k: Boltzmann's constant

K: Dean number

Kn: Knudsen number

K_{wall}: Wall drag multiplier of rigid sphere moving in a cylindrical tube

$K(\omega)$: Clausius–Mossotti (CM) factor

L: Channel length

l_w: Distance between sphere centre and boundary walls

P: Fluid pressure

ΔP: Pressure difference

Pe: Péclet number

Q: Flow rate

r: Radius of particle orbit

r_H: Hydraulic radius of the channel, $r_H = 2A/C$

r_p: Particle radius

R: Radius of curvature in curved channel

R_α: Radius of cylindrical channel

Re: Reynolds number, defined as: $\mathrm{Re}=\rho_f U_f H/\mu$

R_E: Electric resistance

R_H : Hydraulic resistance

Re': Particle Reynolds number, defined as $Re' = v_t \rho_f a/\mu$

Re_s: Reynolds number defined by the sedimentation velocity and particle diameter a, defined as $Re_s = \rho_f a v_s/\mu$

R_p: Particle Reynolds number in inertial microfluidics, defined as: $R_p = R_e \frac{a^2}{H^2}$

S: Cross-sectional area of particles

T: Temperature

$\vec{u}_f$: Fluid velocity vector

U_f: Average velocity of fluid

U_m: Maximum velocity of fluid

U_L: lateral migration velocity of particle

U_D: Magnitude of secondary flow velocity

v_t: Relative velocity of fluid to particle

v_{fr}: Radial velocity of fluid

v_{pr}: Radial velocity of particles

v_{prr}: Relative velocity of particle and fluid elements along the radial direction

v_{pt}: Tangential velocity of particles

v_s: Sedimentation velocity of the sphere in a quiescent fluid

V: Relative velocity between particle and fluid at the streamline through the centre of the particle

V_E : Electrical voltage

V_{pp}: Peak-to-peak voltage

w: Width of microchannel

We: Weber number, defined as $We = \frac{\rho_f U^2 a}{\sigma}$

ρ_f: Fluid density

μ: Dynamic viscosity of fluid

λ: Molecular mean free path

Ω : Angular velocity

υ: Kinetic viscosity

γ: Shear rate

δ: Blockage ratio, defined as $\delta = a/D_C$

σ: Surface tension

ε_m: Permittivity of the medium

1 INTRODUCTION

1.1 Background and motivation

Microfluidics is referred to the science that deals with the behaviour, precise control and manipulation of fluids and particles, using channels with dimensions of tens to hundreds of micrometres [1]. It is also considered as a technology that provides a miniaturisation platform for the biomedical and chemical application, called Lab-on-a-chip, or micrometre-scale total analysis systems (μTAS) [2]. Benefit from the precise control and manipulation of biological particles and its surrounding microenvironment, this fascinating technology holds superior advantages compared with conventional macro-scale platforms (e.g. centrifuge, petri dish and flow cytometry etc.), including but not limited to (i) reduced sample and reagent volumes, (ii) fast sample processing, (iii) high sensitivity, (iv) low cost, (v) improved portability, and (vi) the potential to be highly integrated and automated to reduce human intervention and error [3, 4]. One ambitious goal of micro-fluidics community is to develop highly integrated, portable and cost-effective diagnostic devices for research laboratory or clinics, to diagnose and analyse target pathogens or cells directly, eliminating the time-consuming and toilsome laboratory analysis procedures.

In microfluidics, precise manipulation (i.e. focusing, separation and ordering etc.) of bio-particles (i.e. cells and bacteria) is an essential capability, with a variety of applications. For example, focusing and ordering micro-particles along a single chain in three dimensional enables single-cell level detection and analysis. It is an important component in on-chip flow cytometry to prevent any cells from missing within detection zone. Separation of micro-particles according to their unique biophysical natures (size, density, shape, deformability and antigen expression etc.) allows for routine biological sample preparation (e.g., blood, lymphatic tissue and tissue digestates), target cell isolation and enrichment, and wastewater purification etc [5, 6].

Various techniques have already been proposed and developed to manipulate particles in microfluidics. According to the source of the manipulating force, they can be categorised as active and passive techniques. Active techniques such as dielectrophoresis (DEP) [7], magnetophoresis (MP) [8] and acoustophoresis (AP) [9]

etc. rely on an external force field, whereas passive techniques depend entirely on the channel geometry or intrinsic hydrodynamic forces, such as pinched flow fractionation (PFF) [10], deterministic lateral displacement (DLD) [11] and inertial microfluidics [5] etc. An active technique generally allows for a more precise control of target particles, as well as being very flexible for a wide range of biological particles and tuneable in real-time. However, the flow speed is always limited because particles must be exposed to the outer force field for sufficient duration to achieve effective functionality. In contrast, a passive microfluidic device is often very simple, robust and has a higher flow rate, without auxiliary expensive equipment to supply extra force field.

Among passive microfluidic technology, inertial microfluidics has attracted great attention recently due to its extremely high throughput/rate (~ml/min), which is especially necessary for applications of rare target particles, such as the isolation of circulating tumour cells (CTCs) [12]. In contrast to the common sense that, in microfluidics, fluid inertia is negligible (stokes flow region, $Re \rightarrow 0$, $Re=\rho_f U_f H/\mu$, where ρ_f, U_f and μ are fluid density, average velocity and dynamic viscosity respectively, and H is characteristic channel dimension), inertial microfluidic devices work in an intermediate range (~1 < Re < ~100) between stokes flow and turbulent flow (Re ~ 2000). The finite inertia of fluid brings about several intriguing inertial effects that are basic elements of inertial microfluidics including: (i) inertial migration and (ii) secondary flow.

Inertial migration/focusing is a phenomenon where randomly dispersed particles in the entrance of a straight channel migrate laterally to several cross-sectional equilibrium positions after a long enough distance, which was first observed more than 50 years ago [13, 14]. This phenomenon has been widely recognised by the counteraction of two inertial effects: 1) the shear gradient lift force F_{LS}, due to the curvature of the fluid velocity profile and its interaction with a finite-size particle, which directs particles away from channel centre, and 2) the wall lift force F_{LW}, a result of the flow field interaction between the suspending particle and the adjacent walls, which pushes the particle away from the wall. The equilibrium positions are resulted from the balance between these two inertial lift forces.

The secondary flow usually appears in a curved channel (or a disturbance obstacle). It is induced by a pressure gradient in the radial direction, because of fluid momentum mismatch in the centre and near-wall region within the curvature [5]. The introduction of this secondary flow in inertial focusing brings some benefits. For example, it can modify the inertial equilibrium positions by imposing an additional viscous drag force on particles perpendicular to the main stream. Size-dependent differential focusing of particles according to the balance between inertial lift force and secondary flow drag (F_L/F_D) promises the complete particle separation. In addition, it can reduce the channel length/footprint, due to the mixing effects of secondary flow, assisting particles to reach equilibrium position faster. However, the introduction of secondary flow inevitably complicates inertial focusing process and demands deeper insights on the mechanism for better instruction on design of practical inertial microfluidic devices.

1.2 Objectives

There are two major classes of curving channel in inertial microfluidics, including 1) spiral channels, with consistent direction of curvature, and 2) serpentine channels, with alternating curvature. In spiral channels, curvature is along one direction, and secondary flow is consistent when it reaches steady status. Analysis of inertial focusing in spiral channels is always simplified as static superposition of inertial lift force and secondary flow drag within a cross-section [15-18]. However, in serpentine channels with alternating curvatures, the situation becomes more sophisticated. With alternating curvatures, secondary flow may not approach steady state after each curvature, and accumulation of this unsteady induces unpredictable and non-intuitive phenomenon. The varying secondary flow in the cross sections of alternating curvatures makes the inertial focusing and its mechanism more complex, hindering their wide applications. It is argued that the effects of curvature-induced secondary flow will be counteracted by its corresponding opposite segment in symmetrical serpentine channels, thus secondary flow modified single focusing stream can only be achieved in asymmetric serpentine channels, but it may be not always true due to the unsteady state of fluid and particle movement in each curvature. Therefore, the objective of our research is to explore the unexploited inertial focusing phenomenon in the curved channels, specifically, serpentine channels with the symmetrical

curvature, and improve our fundamental understanding on the observed focusing phenomena through numerical simulation and analytical analysis. In addition, the potential applications of these intriguing inertial focusing phenomena will be explored.

1.3 Outline of the thesis

The outline of this thesis is shown in Figure 1-1.

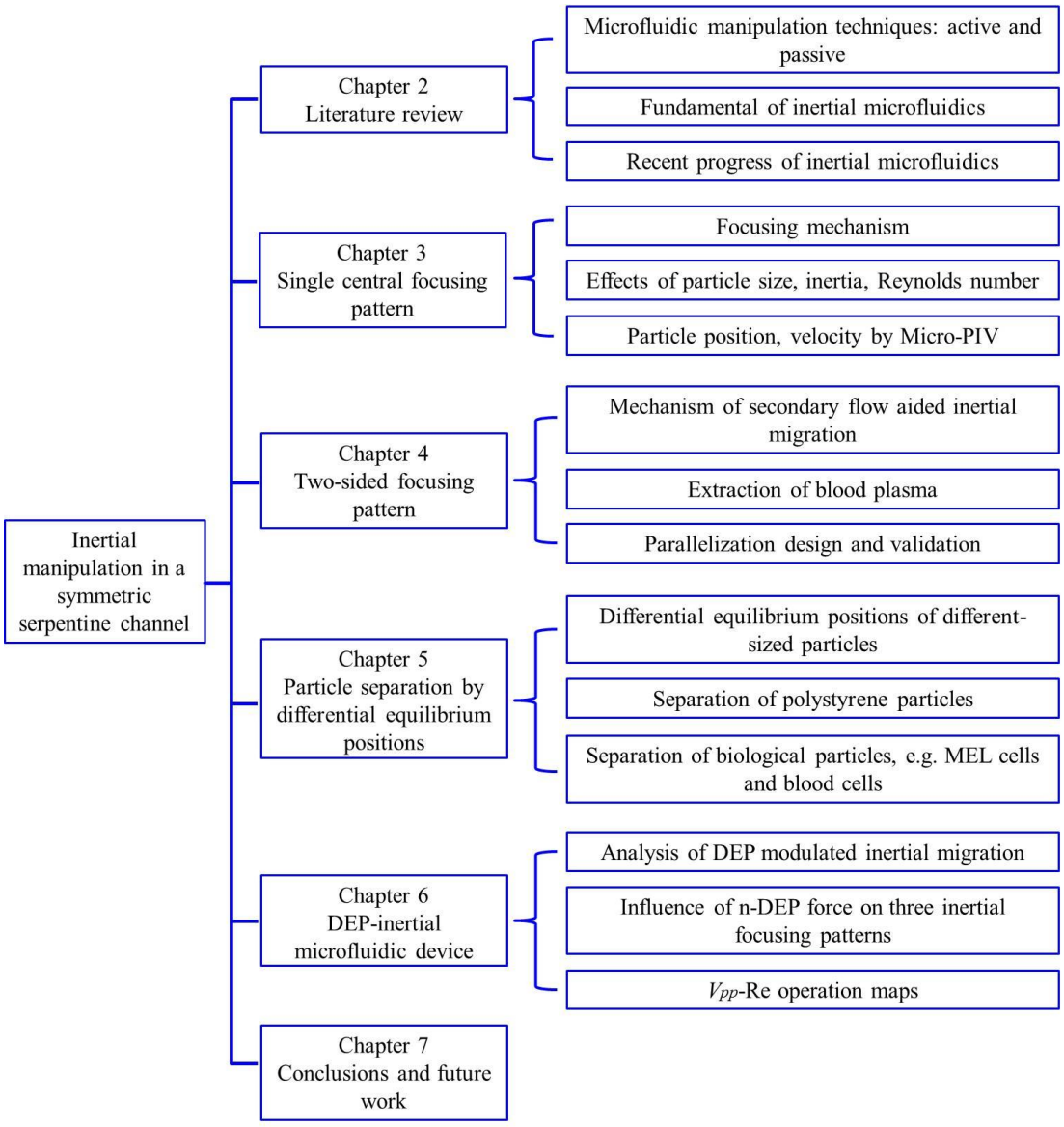

Figure 1–1 The outline of the overall work.

In Chapter 2, we first summarise the existing techniques of particle manipulation in microfluidic platform, including active and passive techniques. Then, the

fundamental of inertial microfluidics, including basic fluid dynamics of inertial microfluidics, and fundamental dynamics of particle movement in inertial microfluidics are discussed. Finally, a comprehensive review on the current progress of inertial microfluidic technology is presented.

In Chapter 3, a serpentine channel with symmetric alternating curvatures is proposed, and three different focusing patterns are observed in the experiments: (i) single central focusing pattern, where a single focusing particle streak is located at the channel centre, (ii) two-sided focusing pattern, where particles are focused as two streaks near the two sidewalls; and (iii) transition pattern, a transitional status that the two sided focusing pattern transforms into the single central focusing pattern. This chapter will mainly investigate the mechanism of the single central focusing pattern through analytical analysis, numerical simulation and experimental validation. The effects of particle size, Reynolds number and particle inertia on the focusing performance will also be studied.

In Chapter 4, the mechanism of the two-sided focusing pattern is investigated, and its application on the extraction of blood plasma is demonstrated. The effects of particle size and blood cell concentration on the filtration performance are also studied. In addition, the parallelization design for this symmetric serpentine channel is proposed and discussed, and experimental validation is provided to demonstrate the feasibility of the proposed design scheme.

In Chapter 5, particle separation by size-dependent differential equilibrium positions in serpentine channels is introduced. The size-dependent equilibrium positions of different particles are first illustrated in a Reynolds number-particle focusing pattern map. The overlap of single central focusing and two-sided focusing pattern for binary particles enables the complete separation in the serpentine channels. The separation of polystyrene beads, biological cells (i.e. MEL cells and blood cells) is conducted, with excellent separation purity and efficiency demonstrated.

Chapter 6 proposes an innovative hybrid DEP-inertial microfluidic device. An interdigitated electrode is patterned on the bottom of serpentine channel, generating negative repulsive DEP force to levitate particles along the vertical direction. Then,

the inertial focusing pattern along the horizontal plane is modified. The mechanism of DEP-inertial microfluidic device is analysed, and the effects of DEP force on three different focusing patterns are investigated by experiments.

Chapter 7 finishes with conclusions on this thesis, and summaries the major finding and contribution of current work, as well as pointing out the future direction of this area.

2 LITERATURE REVIEW

2.1 Particle manipulation in microfluidic platform

There are several components that need to be developed to achieve different functions in the microfluidic platform, such as micro-valve [19, 20], micro-pump [21, 22], mixing [23-25], separation/sorting [11, 26-34], focusing [15, 35-37], stretching [38, 39], trapping [40, 41] and detection [42-45], etc. As basic manipulation abilities, focusing and separation is essential in various microfluidic systems, because these two manipulation abilities have a variety of applications. For example, in the flow cytometry, particles/cells are aligned and ordered along a specific interrogation path so that only one cell/particle moves through the laser beam at a given moment. Meanwhile, in order to get more purified bio-particles sample from the heterogeneous original sample, separation/sorting unit is needed in the upstream process for purification, so that the influence of background particles can be eliminated in the downstream analysis steps. The existing techniques for particle manipulation in microfluidics include dielectrophoresis [46-49], magnetophoresis [30, 32, 50, 51], acoustophoresis [52-54], mechanical filter [26, 55-57], cell-affinity micro-chromatography [29, 58-60], hydrophoresis [61-63], deterministic lateral displacement [11, 64-66], and inertial microfluidics [5, 18, 67] etc. Among these methods, Cell-affinity micro-chromatography relies on the molecular interactions of antibody with specific types of cells, while other methods are label-free, depending on the intrinsic property of cells, such as size, shape, density, deformability and dielectric property. According to the origin of dominant forces for the particle manipulation, it can be further sorted as passive techniques (mechanical filter, deterministic lateral displacement, hydrophoresis and inertial microfluidics) and active techniques (dielectrophoresis, magnetophoresis and acoustophoresis). For active techniques, the dominant forces can be adjusted simultaneously in the process of experiments, but requiring more complex system and supplementary equipment. For passive techniques, the dominant forces can’t be controlled simultaneously, but they can be operated standalone in a much simpler manner. In the following sections, we will first give a brief review on each technique. Following that, a comprehensive review on the inertial migration and recent progress of inertial microfluidics will be presented.

2.2 Active techniques and passive techniques

2.2.1 Active techniques

2.2.1.1 Dielectrophoresis (DEP)

Dielectrophoresis (DEP) is a phenomenon that neutral particles in a non-uniform electrical field will be polarized, and an induced electrical force will exert on the particles, directing them toward or against the electric field maxima. According to the format of electrode and the applied electric field, the DEP can be sorted as (1) electrode-based DEP (eDEP), (2) electrode-less/insulator-based DEP (iDEP) and (3) contactless DEP (cDEP). In traditional electrode-based DEP, the non-uniform electric field is generated by the underlying micro-electrodes. Their shape and configuration determine the electric field distribution and then the trapping and separating area of micro-particles [68], Figure 2-1(a). In insulator-based/electrode-less DEP, non-uniform field is created by the disturbance of insulator embedded in the electric field [69], Figure 2-1(b). In contactless DEP, electrodes are not in direct contact with the biological sample, but isolated by thin insulating barriers [70], Figure 2-1(c). The absence of contact between electrodes and sample solution in microfluidic device can prevent fouling, bubble formulation and contamination of biological sample.

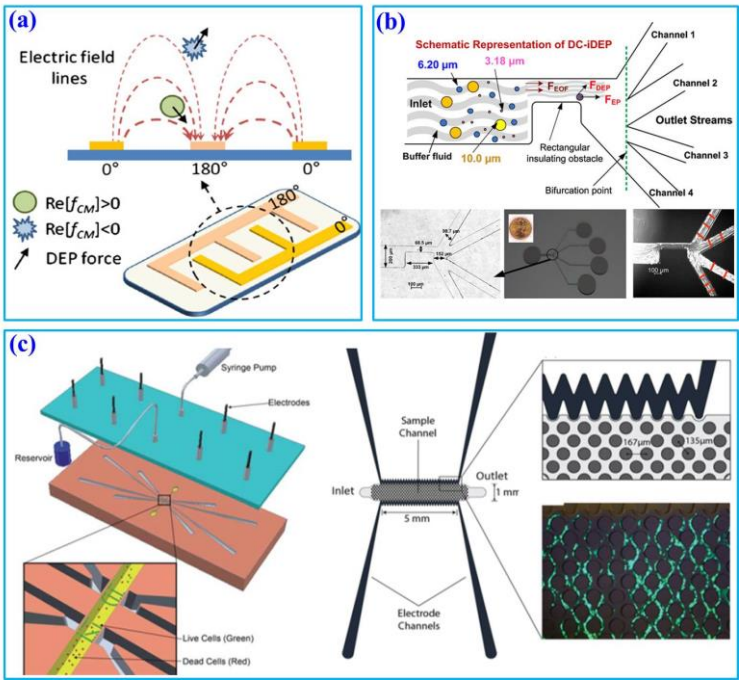

Figure 2–1 Three typical DEP microfluidic devices, (a) electrode-based DEP (eDEP) [71], (b) electrode-less/insulator-based DEP (iDEP) [72], and (c) contactless DEP (cDEP) [70, 73].

2.2.1.2 Magnetophoresis (MP)

Magnetophoresis is referred to a migration phenomenon of particles under the influence of magnetic field. It is a simple sorting and manipulation approach that is not affected by changes in solution pH, ionic concentration, surface charge, and temperature [74]. Magnetophoresis can be divided into two aspects according to whether magnetic label is needed: one is Magnetic activated micro-cell sorter (MACS) where cells need to be bonded with magnetic beads [75], Figure 2-2(a), and then be sorted by attractive magnetic force under external magnetic field, Figure 2-2(b); another is label-free, the non-magnetic cells suspended in the ferrofluids or paramagnetic ions can be sorted due to suffering different magnetic buoyancy forces under external non-uniform magnetic field according to their sizes and magnetic susceptibilities [33, 35, 50, 76], Figure 2-2(c).

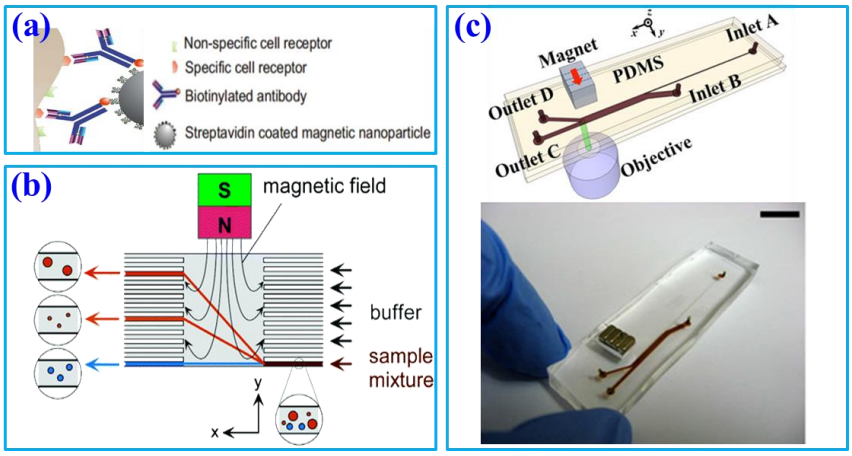

Figure 2–2 (a) Schematic image about cell-MP (magnetic particle) binding [75]. (b) Magnetic particles in the magnetic field deflect from their original moving direction depending on the size and magnetic susceptibility of each particle [32, 51]. (c) A schematic representation of the ferromicrofluidic device with permanent magnets [77].

2.2.1.3 Acoustophoresis (AP)

Ultrasonic acoustic field within a microchannel, induced by piezoelectric material, can produce radiation acoustic force to manipulate particles or cells. It recently finds its application in the Attune flow cytometer. This approach is gentle on cells and is label-free. The technique has been tailed as an invisible tweezer to actively pattern particles and cells, Figure 2-3(a). Also, acoustic force can be utilized to separate particles or cells according to size, density and compressibility [52]. One typical design for particle separation using standing surface acoustic waves (SSAW) was shown in Figure 2-3(b). In addition, there are other active techniques in microfluidics, such as optical tweezer [40], which will not be detailed here.

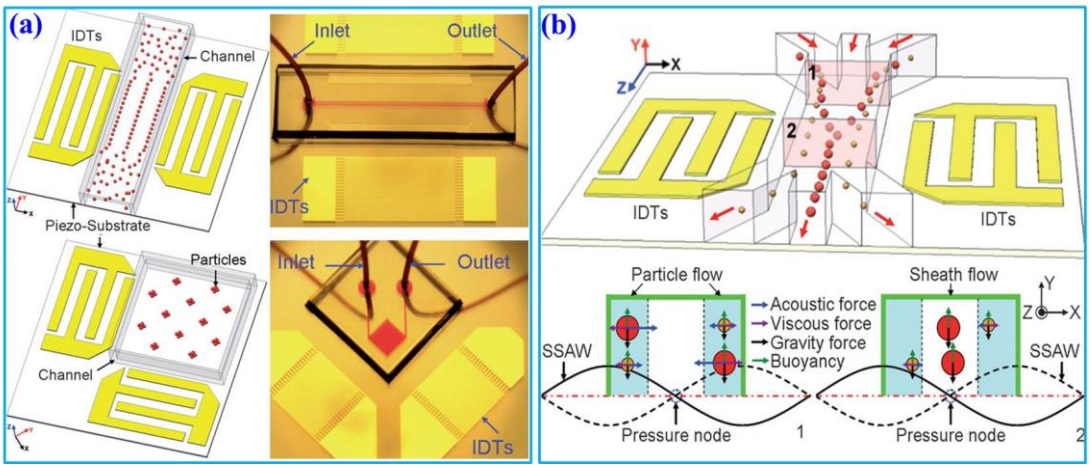

Figure 2–3 (a) 1D and 2D Microfluidic Acoustic tweezers using standing surface acoustic waves (SSAW) [54]. (b) Schematics of the particle separation by the axial acoustic forces when they enter the working region of the SSAW [53].

2.2.2 Passive techniques

2.2.2.1 Mechanical filter

As a very common label-free separation method, the separation criterion of micro-scale filter is particles/cells' size and deformability. Its basic principle is that particles larger than a critical size will be trapped in fabricated micro-structure, and particles smaller than this size or they can deform enough to get through the microstructure will follow the streamline, and then separation of different particles is achieved. This microstructure can be the pores on the membrane or the arrays of

micro-pillars embedded in the micro-channel. There are typical four types of mechanical filters for particle separation or filtration: membrane, weir, pillar and cross-flow, as shown in Fig 2-4.

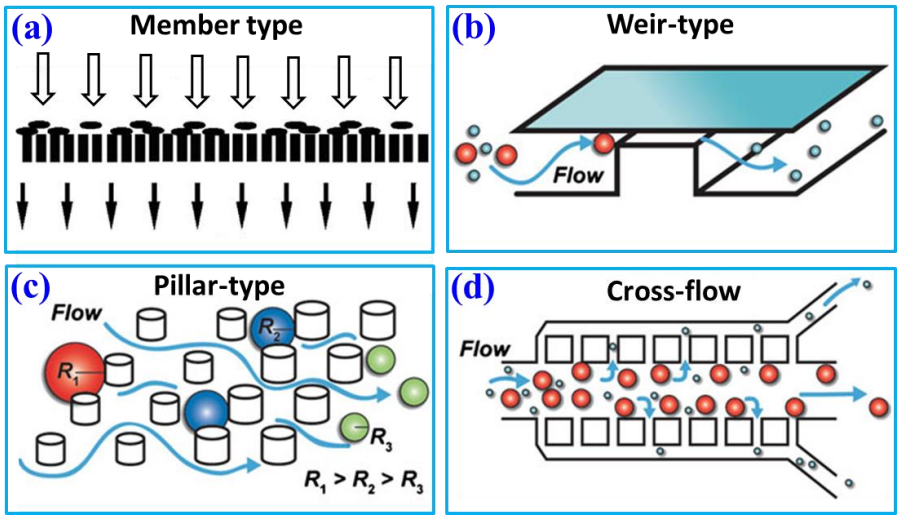

Figure 2–4 Four types of micro-scale filter: (a) Membrane-type; (b) Weir-type; (c) Pillar-type; (d) Cross-flow type [78].

2.2.2.2 Deterministic lateral displacement (DLD)

The first Deterministic Lateral Displacement (DLD) microfluidic device was reported by Huang et al. [11]. It has shown an incredible separation of around 10 nanometers in the classification of microspheres with diameters of 0.8, 0.9 and 1.0 micrometers. In DLD, the periodic arrays of micrometer-scale obstacles are patterned within a microchannel, and asymmetric bifurcation of laminar streamlines around these pillars leads to size-based deterministic paths of particles [11, 66, 79], Figure 2-5. This brilliant separation device has been demonstrated by extraction of blood plasma from blood [80], classification of large epithelial cells from smaller fibroblast cells [81], separation of parasites from human blood [65], isolation of cancer cells from blood [64, 82], and purification of fungal spores [83].

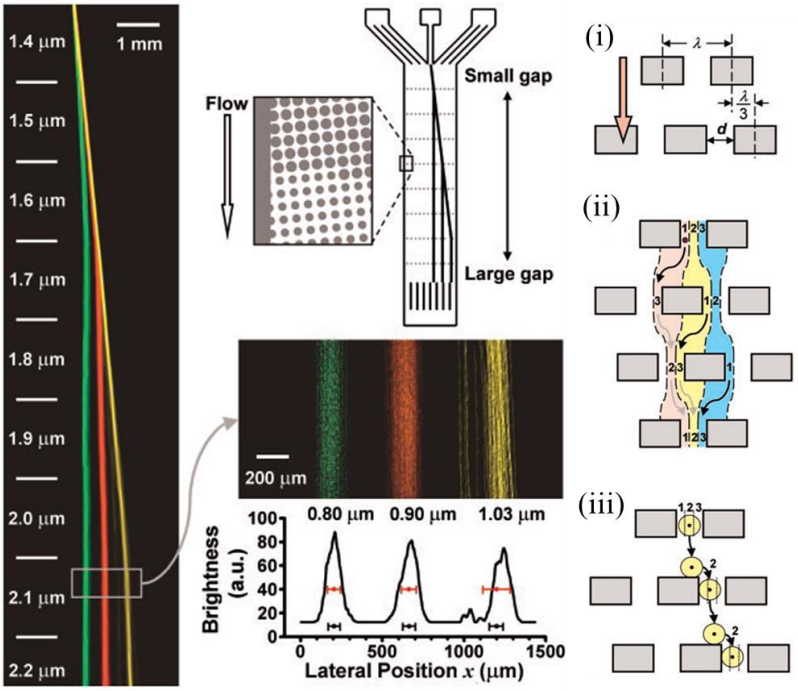

Figure 2–5 High resolution separation of particles by size in a matrix of obstacles: Deterministic lateral displacement [11].

2.2.2.3 Hydrophoresis (HP)

The slanted ridges in the micro-channel were first introduced by Stroock et al. [23] for the enhancement of mixing in micro-channel as a chaotic mixer. Later, they have been also proven useful in the focusing and separation of cells. The concept of "hydrophoresis" indicates that the movement of suspended particles is due to the influence of a microstructure-induced pressure field, which was first introduced by Choi and his co-workers [62, 63, 84, 85]. In their devices, the slanted obstacles are placed on the top and bottom of the channel, then a lateral pressure gradient is created so that micro-particles can be deflected and arranged along the lateral flows. A typical hydrophoresis microchannel was shown in Figure 2-6. The slanted obstacles drive lateral flows across the x-axis by which particles are pushed to a sidewall. Then, the focused particles flow clockwise following the rotating flows generated by the bottom-side obstacles and move to the bottom of a channel. The large particle is located in the area where there is no lateral pressure gradients and stays in the focused position. On the other hand, the small particle is exposed to lateral pressure gradients along the x-axis and deviates from its focused position [84].

Therefore, it enables size-based separation of particles according to the differential lateral positions.

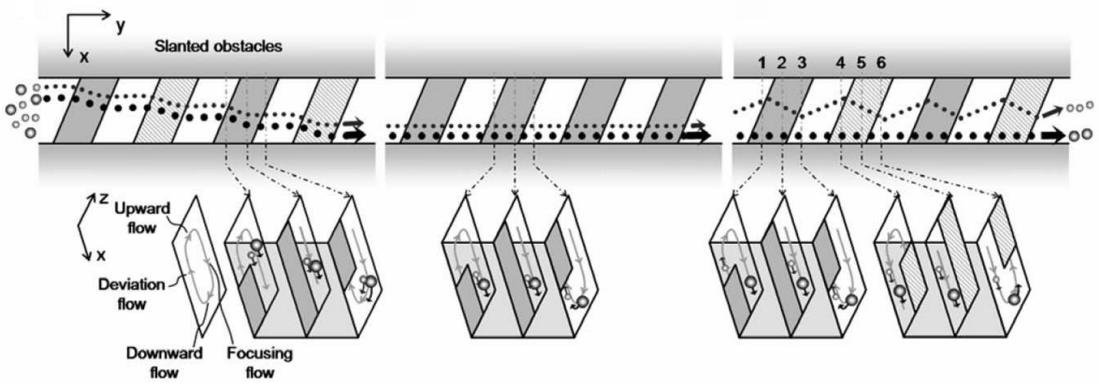

Figure 2–6 A schematic principle of hydrophoretic separation [84]. Shaded- and lined-areas denote lower and upper slanted obstacles, respectively. The flow direction is along the y-axis.

2.2.2.4 Inertial microfluidics

The inertial migration is a phenomenon that randomly dispersed particles in the entrance of a straight channel migrate laterally to several cross-sectional equilibrium positions after a long enough distance, as shown in Figure 2-7(a), which was observed more than 50 years ago [13, 86-88]. After its observation, although a number of experimental studies and theoretical analyses were conducted to explore the mechanism of this migration phenomenon [86, 89-93], it had not been taken into account in the practical application until the emergence of microfluidic technology recently, where particles' size is comparable with the characteristic dimension of microchannel. Inertial microfluidics is then termed as the technique which utilizes particles' inertial migration and other inertial effects (such as Dean flow in curved channel, Figure 2-7b), to manipulate fluids or particles [5]. The group of Di Carlo has conducted a series of fundamental study on the mechanism of inertial migration [94-96] and intense exploitation of this technique on the cellular sample preparation [97], cancer diagnosis [98] and material synthesis [99] etc.

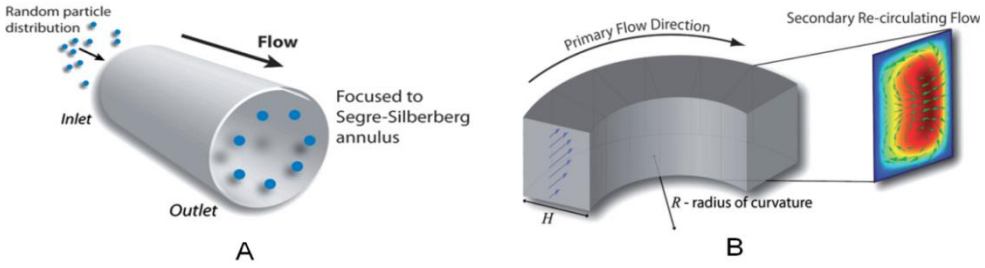

Figure 2–7 (A) Inertial migration in a straight channel with circular cross-section. (B) Second flow in a curve channel [5].

The inertial microfluidics itself is a huge area with different aspects. Rather than covering all the aspects of it, two of its main aspects, i.e. mechanism and application, are selected to be discussed in detail. In the following, the basic mechanism of inertial migration will first be discussed, including basic fluid dynamics in inertial microfluidics and dynamics of particle movement in microchannel with finite inertia. Then, a review with the current state of the art inertial microfluidics design and its applications will be presented.

2.3 Fundamental fluid dynamics and particle dynamics in inertial microfluidics

2.3.1 Basic fluid dynamics in inertial microfluidics

Fluid dynamics itself is a huge area with numerous sub-fields, and here we only discuss three basic sections, including continuum approximation that is the necessary precondition for the suitable governing equations of fluid dynamics, formula of Navier-Stokes equations and Hagen–Poiseuille's law that is very useful for the design of complex fluidic circuit.

2.3.1.1 Continuum

In macroscopic scale, the governing equations of fluid dynamics are derived based on continuum approximation from the statistic aspect. All the molecular effects are summed to space-averaged macroscopic or continuum-based quantities, such as the fluid density, temperature and velocity. However, when the characteristic dimension is too small, even to the scale of molecular mean free path λ (the distance travelled by a molecule between two successive collisions), the continuum approximation may be no longer applicable, and the utilization of the governing equations based on the

continuum approximation may cause a major error, which needs to be clarified. A non-dimensional parameter for gas micro-flow is the Knudsen number, which is defined as the ratio of the mean free path over a characteristic dimension *H* [100].

$$Kn \equiv \frac{\lambda}{H} \tag{2-1}$$

(i) For $Kn \leq 10^{-2}$, the fluid can be considered as a continuum;

(ii) For $Kn \geq O(10)$, it is considered as a free-molecular flow;

(iii) For $10^{-2} < Kn < 0.1$, slip flow;

(iv) For $0.1 < Kn < 10$, transition flow.

At standard conditions for air, the value of the Knudsen number $Kn = 1$ corresponds to the characteristic dimension of $H = 65nm$. So air flow in a microchannel with diameter larger than 6.5 μm is still applicable as a continuum.

In liquid, the molecules are too close to each other, so that strong intermolecular interaction dominates the motion of the molecules. Moreover, the mean free path of the liquid molecules is in the order of the mean molecular spacing. Therefore it makes little sense to talk about the mean free path of liquid molecular. Liquid water is held together primarily with hydrogen bonds. The maximum length of a hydrogen bond in water is about 3 angstroms (=10^{-10} m), and the average length is about 1.9 angstroms. In principle, water flow in a microchannel with a diameter larger than tens of nano-meter can still be considered as a continuum. Thus, taking water flow as a continuum in inertial microfluidic system, with a common characteristic channel dimension from tens to hundreds of micro-meters, is reasonable. Therefore, governing equations of fluid dynamics based on continuum approximation are applicable to analyse the flow characteristics in inertial microfluidics.

2.3.1.2 Governing equations

For the flows in microfluidic device, the fluids are mainly water or aqueous solution. So they are normally incompressible and mostly Newtonian fluid (viscosity remains constant regardless of shear stress and loading history). The Navier-Stokes (N-S)

equations for the laminar, incompressible, Newtonian fluid without body force can be expressed as [100]:

$$\rho \frac{\partial \vec{u}_f}{\partial t} = -\rho \vec{u}_f \bullet \nabla \vec{u}_f - \nabla P + \mu \nabla^2 \vec{u}_f \tag{2-2}$$

(Rate of change of momentum) = (convective force) + (pressure force) + (viscus force)

where $\vec{u}_f$ is the fluid velocity vector, expressed as $(u\vec{\imath}, v\vec{\jmath}, w\vec{k})$ in a Cartesian coordinate system. $\vec{\imath}, \vec{\jmath}, \vec{k}$ are unit vectors of a 3-D Cartesian coordinate system. P, ρ and μ are pressure, density and viscosity of fluid. ∇ is the Nabla operator, $= \vec{\imath}\frac{\partial}{\partial x} + \vec{\jmath}\frac{\partial}{\partial y} + \vec{k}\frac{\partial}{\partial z}$. ∇^2 is the Laplace operator, $= \frac{\partial^2}{\partial x^2} + \frac{\partial^2}{\partial y^2} + \frac{\partial^2}{\partial z^2}$.

When a flow reaches its steady state, the components with variables time t in N-S equations can be eliminated:

$$\rho \vec{u}_f \bullet \nabla \vec{u}_f = -\nabla P + \mu \nabla^2 \vec{u}_f \tag{2-3}$$

In conventional microfluidic system, the flow inertia is negligible with very slow flow speed and very tiny channel, because the dimensionless Reynolds number ($Re = \rho_f U_f H/\mu$) describing the ratio between inertial and viscous forces in a flow is far less than 1. Then it can be further simplified as stokes flow (or creeping flow) by neglecting inertial component, i.e. eliminating left hand side of N-S equations in equation (2-3):

$$\nabla P = \mu \nabla^2 \vec{u}_f \tag{2-4}$$

Here, we can see that stokes flow is laminar flow, but the inverse statement is not necessarily true [5].

In addition, the continuity equation is:

$$\nabla \bullet \vec{u}_f = 0 \tag{2-5}$$

In practice, the additional boundary conditions (i.e. inflow, outflow and wall) need to be specified to solve the detailed problem.

By the theorem of mirror-symmetry time-reversal, Bretherton [101] and Saffman [87] pointed out that there is no lateral force on a single rigid sphere suspended in a fluid on the basis of stokes flow in a unidirectional flow, independent of the velocity profile and relative size of particle to channel. Therefore in inertial microfluidics with finite Reynolds number (10s < Re < 100s), neglecting inertia term by using stokes equation approximation will lead to incorrect results. A full expression of N-S equation is preferred.

2.3.1.3 Hagen–Poiseuille's law

For the flow in a long cylindrical channel with radius R_α, after long enough distance the flow reaches the steady and fully-developed state. The velocity field is unidirectional, and steady as well as convection terms in equation (2-2) are all zero. The governing equation can then be expressed in the cylindrical coordinates (r, θ, z) as [102]:

$$0 = -\frac{\partial P}{\partial z} + \frac{\mu}{r}\frac{\partial}{\partial r}\left(r\frac{\partial u_z}{\partial r}\right) \tag{2-6}$$

Given $\frac{\partial P}{\partial z}$ is constant along coordinate r, as well as the wall boundary condition $u_z = 0$ at $r = R_\alpha$, the solution is:

$$u_z = \frac{R_\alpha^2 - r^2}{4\mu}\left(-\frac{\partial P}{\partial z}\right) \tag{2-7}$$

This pressure-driven motion is termed as Poiseuille flow. We can see that the velocity profile is parabolic across the channel diameter. The maximum velocity is $U_m = \frac{R_\alpha^2}{4\mu}\left(-\frac{\partial P}{\partial z}\right)$ at the channel center $r = 0$.

In pressure-driven flow, one may concern more about how to control the volumetric flow rate by outer pressure, rather than the detailed flow filed distribution. So it is important to know the relationship between pressure drop and volumetric flow rate, that's the origin of Hagen-Poiseuille's law. By integrating the

velocity distribution along cross-section of a circular channel in equation (2-7), one can get:

$$Q = \frac{\pi R_\alpha^2}{8\mu}\left(-\frac{\partial P}{\partial z}\right) \tag{2-8}$$

Assuming the pressure gradient along channel length is uniform, then $-\frac{\partial P}{\partial z}$ can be expressed as $\Delta P/L$, here ΔP is the pressure difference along a finite channel length L. The equation (2-8) is simplified as:

$$Q = \frac{\pi R_\alpha^2}{8\mu L}\Delta P \tag{2-9}$$

Similar to Ohm's law that describing linear relationship between voltage V_E, current I and electric resistance R_E: $V_E = IR_E$. The relationship between ΔP and Q can also been linked linearly by defining a hydraulic resistance R_H [102], Figure 2-8.

$$R_H = \frac{8\mu L}{\pi R_\alpha^2} \tag{2-10}$$

$$\Delta P = QR_H \tag{2-11}$$

It should be noted that above equations are derived based on a straight channel with circular cross section. For non-circular channel, a good approximation can be achieved by replacing channel radius R in equation (2-10) with equivalent hydraulic radius r_H. Hydraulic radius of the channel is defined as $r_H = 2A/C$, where A is cross-sectional area of the channel and C is the wetted perimeter [102].

$$R_H = \frac{8\mu L}{\pi r_H^2} \tag{2-12}$$

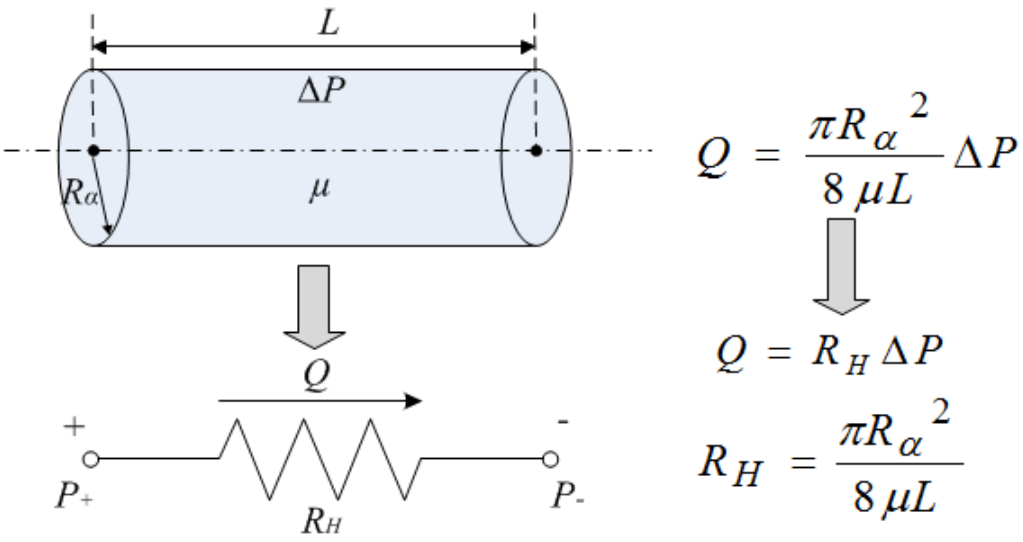

Figure 2–8 Fluidic resistor for the hydraulic resistance and Hagen-Poiseuille's law is analogous to a resistor for the electric resistance and Ohm's law. Reproduced from reference [102].

For more complicated fluidic network design in microfluidic device, it may be divided into several branches or sub-branches either in serial or in parallel configuration, so the net hydraulic resistance can be obtained through analysis of analogous electric circuit. This analogous electric circuit method is actually very useful in the parallelization design of inertial microfluidic system, since focusing and separation performance is very sensitive to the flow rate in each functional microchannel, and proper streamline bifurcation at the outlet is crucial for high purity separation and collection.

2.3.2 Fundamental dynamics of particle movement in a microfluidic channel

2.3.2.1 Viscous drag force

Drag force arises when an object moves through a fluid or, alternatively, when fluid flows past an object. The origin of the drag force lies in the need to displace the elements of the fluid out of the way of the moving object. The drag force on a moving spherical particle can be expressed as:

$$F_{drag} = S * f_d = \pi a^2 f_d / 4 \quad (2\text{-}13)$$

where S is the cross-sectional area of moving particles, and a is the diameter of spherical particle. f_d is viscous drag coefficient which is always determined by the defined particle Reynolds number $Re' = v_t \rho_f a/\mu$, here v_t is relative velocity of fluid to particle [103].

The viscus drag coefficient f_d can be divided into four sections according to the range of particle Reynolds number [103].

(a) When $10^{-4} < Re' < 0.2$

$$f_d = 12\frac{\mu v_t}{a} \tag{2-14a}$$

Then

$$F_{drag} = 3\pi\mu a v_t \tag{2-14b}$$

This is actually the well-known formula of stokes drag. It has been widely used for analytical analysis for simplicity, especially when relative velocity of fluid to particle v_t is very small.

(b) When $0.2 < Re' < 500\sim100$

$$f_d = 12\frac{\mu v_t}{a}(1 + 0.15Re'^{0.687}) \tag{2-15a}$$

Then

$$F_{drag} = 3\pi\mu a v_t(1 + 0.15Re'^{0.687}) \tag{2-15b}$$

(c) When $500\sim1000 < Re' < 2 \times 10^5$

$$f_d = 0.22\rho_f v_t^2 \tag{2-16a}$$

Then

$$F_{drag} = 0.055\pi a^2 \rho_f v_t^2 \tag{2-16b}$$

(d) When $Re' > 2 \times 10^5$

$$f_d = 0.05\rho_f v_t^2 \tag{2-17a}$$

Then

$$F_{drag} = 0.0125\pi a^2 \rho_f v_t^2 \quad (2\text{-}17b)$$

Subsequently, Khan and Richardson examined the experimental data and suggested a very good equation can agrees well for values of Re' up to 10^5 [103]:

$$f_d = (1.84Re'^{-0.31} + 0.293Re'^{0.06})^{3.45} \rho_f v_t^2 \quad (2\text{-}18a)$$

$$F_{drag} = \frac{\pi}{4} a^2 \rho_f v_t^2 (1.84Re'^{-0.31} + 0.293Re'^{0.06})^{3.45} \quad (2\text{-}18b)$$

2.3.2.2 Diffusion

Brownian motion is the random motion of suspending particles immersed in a fluid (liquid or gas), which is resulted from their frequent collision with the atoms or molecules in the gas or liquid. Diffusion is ubiquitous in particle-fluid system. According to EINSTEIN-SMOLUCHOWSKI theory, the mean square distance that a particle diffuses in time *t* is expressed as *r* [104]:

$$< r^2 >= 6Dt \quad (2\text{-}19)$$

where *D* is the diffusion coefficient, according to the Stokes-Einstein relationship, it can be given by:

$$D = \frac{kT}{3\pi\mu a} \quad (2\text{-}20)$$

where k is Boltzmann's constant, which is about 1.3806488×10^{-23} J/K. T is the temperature, μ is viscosity of medium and a is the particle diameter [104]. From the above equation, we can see that the higher the temperature T, the greater the diffusion coefficient D. In contrast, the larger the particle size a or the higher the medium viscosity μ, the lesser the diffusion coefficient. In a typical microfluidic system, it is normally operated under the room temperature, say 25 ºC. The diffusion coefficient for a 1 μm particle in water is about 4×10^{-13} m/s. Furthermore, when the particle-fluid system is not static, but moving along the micro-channel, the Péclet number *Pe* can be employed to evaluate the relative importance of convection to diffusion:

$$Pe = \frac{HU}{D} \tag{2-21}$$

where H is the characteristic dimension of channel and U is the characteristic velocity of fluid. The large Péclet number indicates that the convection dominates the transport of particles in the flow, while the small Péclet number represents that diffusion plays a primary role in transport.

In inertial microfluidics, the characteristic linear velocity of fluid is in the scale of ~m/s, and the characteristic dimension of micro-channel is normally in the order of ~100 μm. The Péclet number for 1-μm particles in inertial microfluidics is ~2.5×10^8, indicating that convection dominates the transport of particles rather than diffusion. Therefore, diffusion is normally neglected in the analysis of particle trajectory in inertial microfluidics for micro-sized particles.

2.3.2.3 Inertial lift forces

Inertial migration is an interesting phenomenon that the randomly dispersed particles in the entrance of a straight channel migrate laterally to a narrow annulus at about 0.6 times of tube radii from the axis after a long enough distance in a circular tube, which was first quantitatively measured by Segre and Silberberg in 1960s [13, 14]. After that, a series of analytical analysis and numerical simulation have been conducted to explain this counter-intuitive phenomenon [86, 89-93]. However, the full problem is one of great complexity and difficulty, as not only the effect of inertia needs to be calculated for a particle in a parabolic velocity profile, but also the presence of the tube walls must be taken into account. The walls are clearly very important to the existence of the phenomenon. Without a wall, the flow will be uniform and there is even no velocity gradient, generating no rotation motion on a force-free rigid sphere, and consequently no lateral lift force appears. The existence of walls creates a fluid velocity gradient (shear rate), and corresponding shear-induced particle rotation, as well as shear rate gradient in a fully-bounded flow (e.g. Poiseuille flow). The extra drag due to the walls makes the particle lagging behind the main stream, which depends only on the relative size of particle to tube as well as the distance from the wall. There are at least four different lateral lift forces due to the existence of walls: (i) slip-rotation lift force or Magnus force F_{LR}, due to the slip-rotation motion; (ii) slip-shear lift force or Saffman force F_S, caused by slip shear

motion; (iii) shear gradient lift force F_{LS}, due to the gradient of fluid shear rate; and (iv) wall lift force F_{LW}, which is a direct consequence of the flow field interaction between the suspending particles and the adjacent walls [87]. Among these lift forces, only the last one is the direct results of wall existence, so it is named directly as wall lift force. While for other three types of lift forces, because they are originated by the indirect effects of walls, i.e. the effects of shear rate, shear gradient or rotational motion on the local flow field surrounding the suspended particles, therefore they are named by their respective direct causes.

2.3.2.3.1 Magnus force—slip-rotation induced lift force F_{LR}

In an inviscid flow with uniform velocity U, a stationary cylinder is rotating with constant angular velocity Ω, see figure 2-9. Assuming no slip velocity at the surface of the cylinder, the fluid velocity at the bottom part is lower than the velocity at the upper part. According to the Bernoulli principle, the pressure is higher at the lower part than that in the upper part of the cylinder. As a result, a lift force F_{LR} is developed to lift the cylinder. The magnitude of this lift force, per unit length of the cylinder is [105]:

$$\vec{F}_{LR} = \pi\rho_f^2 a\vec{U} \times \vec{\Omega} \tag{2-22}$$

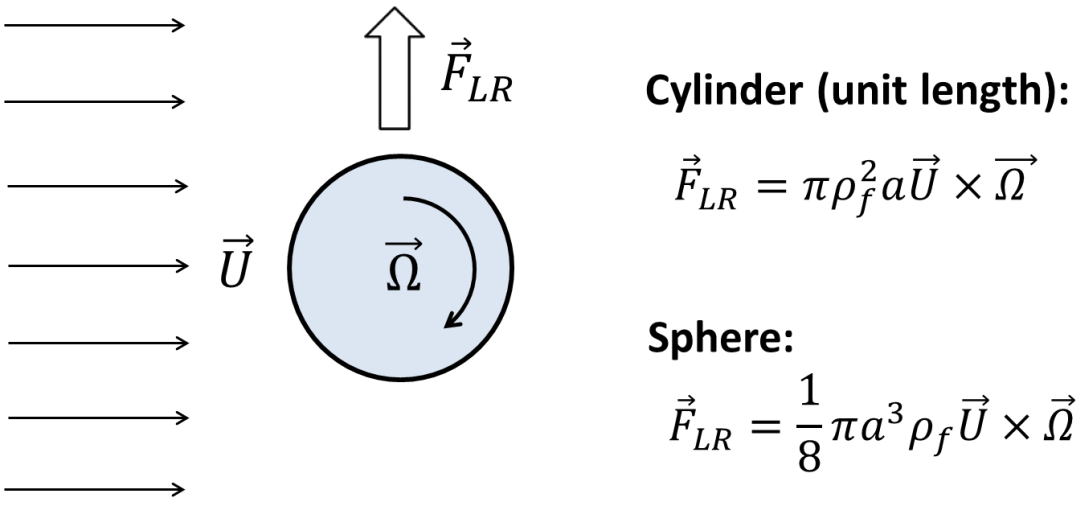

Figure 2–9 Rotation induced lift force for a rigid cylinder and sphere in a uniform flow.

For a rigid sphere rotating in a fluid, similar to the cylinder, a lateral lift force appears due to the transverse pressure difference, and this force is called "Magnus lift force" [106]:

$$\vec{F}_{LR} = \frac{1}{8}\pi a^3 \rho_f \vec{U} \times \vec{\Omega} \tag{2-23}$$

When the sphere is not stationary, but simultaneously translating through the fluid with a velocity $\vec{u}_p$, just need to replace fluid velocity vector $\vec{U}$ with relative velocity $(\vec{u}_f - \vec{u}_p)$, then we get:

$$\vec{F}_{LR} = \frac{1}{8}\pi d^3 \rho_f (\vec{u}_f - \vec{u}_p) \times \vec{\Omega} \tag{2-24}$$

The direction of Magnus force is perpendicular to the plane defined by the vectors of the relative velocity and the axis of rotation. In the case of a sphere rotating with angular velocity $\vec{\Omega}_s$ in a rotational flow field, then the vector $\vec{\Omega}$ represents the relative rotation between the fluid and the sphere:

$$\vec{\Omega} = \vec{\Omega}_s - 0.5\nabla \times \vec{u}_f \tag{2-25}$$

Magnus force can be considered as a result of the pressure difference induced by the streamline asymmetry, due to the rotation of the sphere. Although above particular expressions are only valid for low Reynolds numbers, this kind of lift force due to the rotation of a body in a uniform flow is also present in more strongly inertial flows [107]. In fact, as a result of the outer velocity filed disturbance by the rotation, where fluid inertia is essential, the Magnus force would not appear in creeping flow, but present in all rotating flows with finite relative velocity no matter it is viscous or inviscid [105].

2.3.2.3.2 Saffman force—slip-shear induced lift force F_S

In an unbounded simple shear flow, with constant shear rate and zero shear gradient, Saffman [87] calculated the lateral lift force on a sphere by the matched asymptotic expansion method. The force was recognised arising from the interaction of the Stokeslet velocity field around the particle with the velocity gradient (shear rate). The magnitude of this force is:

$$F_S = \frac{K}{4} V a^2 (\gamma v^{-1})^{1/2} \tag{2-26}$$

where K is a numerical constant (K~81.2), γ is velocity gradient (or shear rate), υ is the kinetic viscosity and V is the relative velocity between particle and fluid at the streamline through the centre of the particle. It should be pointed out that this force is the only effect of shear rate, independent of rotation of particle. In the real situation, the spheres are free to move, and a relative rotation will be induced by the shear. Consequently, a Magnus-type force may appear on the sphere. In most practical flows, the effects of rotation and shear cannot be considered as independent, and a simple superposition of the two lift forces would inevitably bring errors [105]. It has showed that unless the rotation speed is much greater than the rate of shear, for a freely rotating particle $\Omega = \frac{1}{2}\gamma$, Saffman force F_S, due to the interaction of slip velocity (Stokeslet flow field) and shear, will generally by at least one order of magnitude larger than Magnus force F_{LR} due to the interaction of slip (Stokeslet flow field) and particle rotation when the Reynolds number is small [107].

The direction of Saffman force is always towards the side where the magnitude of relative velocity V is maximum, Figure 2-10. In the case of a neutrally buoyant particles in a Poiseuille flow, the particle is force-free and the Stokeslet generated by the lag of the particle relative to the shear flow (slip-shear) is balanced by an opposite Stokeslet originating from the curvature of the base flow, so there is basically no net Stokeslet in the base flow, consequently no Saffman force acts on the sphere [107]. Saffman force is more relevant in the case of non-neutrally buoyant particles in a vertical flow, or additional outer force (electrical or magnetic) [67, 108] acting on the particle to lag or lead fluid flow significantly, creating obvious net Stokeslet flow field. At this situation, the Saffman force will direct to the channel centreline when particles lag the flow, or direct toward the channel walls when particles lead the flow.

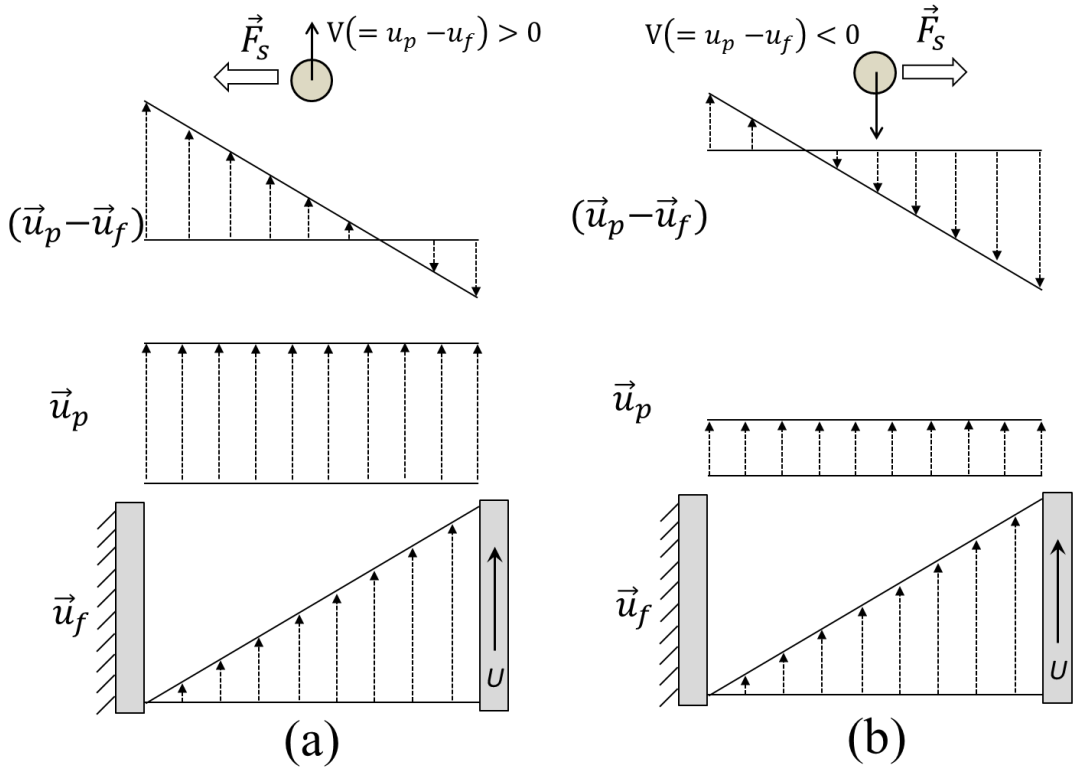

Figure 2–10 Lateral force on a sphere in a simple shear flow. *V* is the relative velocity of particle to fluid. (a) $V > 0$ indicates that particle moves faster than the fluid, leading the flow. (b) $V < 0$ means that particle moves slower than the fluid, lagging the flow. The direction of lateral lift force always directs toward the side where magnitude of relative velocity *V* is maximum.

2.3.2.3.3 Shear-gradient lift force F_{LS}

As mentioned above, in the Poiseuille flow, the Stokeslet generated by the lag of the particle relative to the shear flow (slip-shear) may be balanced by an opposite Stokeslet originating from the curvature of the base flow. Furthermore, the curvature of fluid velocity profile can even reverse this trend as shown in Figure 2-11. It can be clearly seen that, due to the parabolic nature of velocity profile, the magnitude of relative velocity of fluid to particle is much higher on the left side of particle than that on the right side. And it overwhelms the asymmetry caused by lag velocity. Similar to Saffman force, the dissymmetry of relative velocity causes a low pressure on left/wall side, generating a shear-gradient lift force F_{LS} that's opposite to the Saffman force. The Shear-gradient lift force leads particles migrating away toward walls until the wall lift force F_{LW} repel and balance it [107, 109].

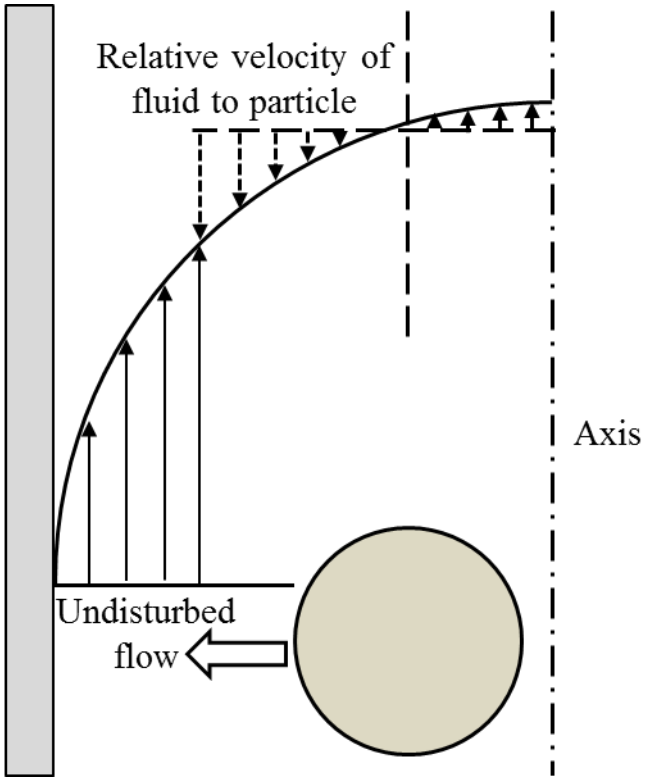

Figure 2–11 Shear-gradient lift force exerted on a neutrally buoyant rigid sphere in a Poiseuille flow. In the moving frame with the particle, the relative velocity of fluid to particle is larger on the wall side due to the parabolic fluid velocity profile. Reproduced from reference [109].

2.3.2.3.4 Wall-induced lift force F_{LW}

In the previous sections, we mainly talk about the indirect effects of walls on the suspending particles. That is, the existence of wall creates fluid shear rate, shear gradient and rotational motion of spherical particles. And the flow field disturbance around particles due to these effects i.e. shear rate, shear gradient and particle rotation induces several lateral lift forces on the particles. In this section, we will concentrate on the direct flow field interactions between particles and their adjacent walls: wall lift force F_{LW}. In order eliminate influences of other effects e.g. shear rate to the lateral lift force, one possible scheme is to investigate the motion of particles near a wall in a stagnant fluid.

In general, the effect of a wall on the motion of immersed objects is to retard the motion of the object in both parallel and perpendicular directions, as well as exerting a transverse migration motion. Two kinds of distinct interactions between immersed

objects and walls exist: (i) The motion of the immersed object is primarily influenced by a single wall on one side of the object. Any other walls or flow boundaries are too far from the immersed object to influence significantly its motion. In this case, the main effect of the wall is to decelerate particles' motion and drive the immersed object away from the wall, Figure 2-12(a). It applies to the situation where the characteristic dimension of immersed particle is much less than that of the flow channel, then particles' motion is dominated by their nearby walls, with the effects of the other walls negligible. (ii) When the immersed object is surrounded by the boundaries (walls) of the flow domain. Thus, the boundaries decelerate significantly the motion of the object, Figure 2-12(b). It happens if the characteristic dimension of immersed particle is of the order of the dimension of flow channel, such as small bubbles moving in capillaries, and the surrounding walls will constrain the motion of immersed particles [105].

First, we discuss the situation that the dimension of particles is much smaller than that of channel, and they are primarily influenced by a single wall. The direction of the particles' motion may be perpendicular or parallel to the walls. When the immersed sphere moves perpendicularly to a boundary, as shown in Figure 2-12(c), the effect of the boundary retards the motion of the particle, which is equivalent to the increase of the drag coefficient. Brenner [110] derived a first-order correction for the drag coefficient of a small sphere in creeping flow moving towards a solid wall.

$$f_d = \frac{16\mu v_t}{a} f \tag{2-27}$$

$$f = sinh\theta_w \sum_{n=1}^{\infty} \frac{n(n+1)}{(2n-1)(2n+3)} \times \left[\frac{2sinh[(2n+1)\theta_w + (2n+1)\sinh(2\theta_w]}{4sinh^2[(n+0.5)\theta_w] - (2n-1)^2 sinh^2(\theta_w)} - 1\right] \tag{2-28}$$

where $\theta_w = cosh^{-1}(2\, l_w/a)$ is a function of the ratio of distance from sphere centre to the wall to the particle diameter. l_w is the distance of sphere centre to boundary walls. It indicates that the hydrodynamic force on the particle increases significantly when the particle approaches the wall closely.

When the immersed sphere moves parallel to the boundary, Figure 2-12(d), a transverse lift force repels the particle away from the wall. Given the condition dimensionless distance $d^* \ll 1$, where $d^* = \rho_f\, l_w v_s/\mu$, the lateral migration velocity can be expressed as [111, 112]:

$$U_L = \frac{3}{64} Re_s v_s \left\{1 - \frac{11}{32} d^{*2} + \cdots \right\} \tag{2-29}$$

where v_s is the sedimentation velocity of the sphere in a quiescent fluid, and Re_s is a Reynolds number defined by the sedimentation velocity and particle diameter a, expressed as $Re_s = \rho_f a v_s / \mu$. Considering the implied condition of $d^* \ll 1$, so it can be further simplified as:

$$U_L = \frac{3}{64} Re_s v_s \tag{2-30}$$

It indicates that the migration velocity of sphere is constant when particle is in the vicinity of the wall. And this expression was experimentally validated by the data of Cherukat and McLaughlin [113] up to $Re_s = 3.0$.

In addition, when $d^* \gg 1$, the migration velocity then becomes [112]:

$$U_L = \frac{3}{16} Re_s v_s \left(d^{*-2} + 2.21901 d^{*-5/2} + \cdots \right) \tag{2-31}$$

It indicates that for large values of d^* (large distance between sphere and wall or large sedimentation velocity of sphere), the migration velocity decrease continuously and tends to zero as $d^* \to \infty$.

In addition to the lateral lift force that repel particle away from the wall, the effect of the boundary will also retard the sedimentation main motion of the particle, corresponding to an increased drag force. The drag force experienced by a sphere settling down in the neighbourhood of a plane wall ($\frac{a}{2l_w} \ll 1 \ll \frac{1}{Re_s}$) is [112]:

$$F_{drag} = 3\pi\mu a v_s \left(1 + \frac{3}{8} Re_s + \frac{9}{32} \frac{a}{l_w} + \cdots \right) \tag{2-32}$$

At a relative large distance ($\frac{a}{2l_w} \ll \frac{1}{Re_s} \ll 1$), the drag force is expressed as:

$$F_{drag} = 3\pi\mu v_s \left\{1 + \frac{3}{8} Re_s - 0.095 \frac{a}{l_w} \left(\frac{1}{Re_s}\right)^{3/2} + \cdots \right\} \tag{2-33}$$

In a bounded flow, when the characteristic dimension of the sphere is of the same order of magnitude as the size of the flow channel, the surrounding boundaries provide a physical constraint to the flow, and in general, the immersed objects move

close to the centreline of the channel, Figure 2-12(b). In order to prevent channel from being blocked, the blockage ratio δ (= a/D_C) should be less than 1, where D_C is diameter for a cylindrical channel. Besides, the boundaries decelerate significantly the motion of the object. A wall drag multiplier of rigid sphere moving in a cylindrical tube was derived and expressed as [105]:

$$K_{wall} = \frac{F_{drag}}{3\pi a\mu v_s} = [1 - 2.0144\delta + 2.0888\delta^3 - 6.948\delta^5 - 1.372\delta^6 + \cdots]^{-1} \quad (2\text{-}34)$$

In summary, the effects of walls on the motion of immersed spheres in a tube are to decelerate the motion of the sphere, and repel particles into the centreline of channel.

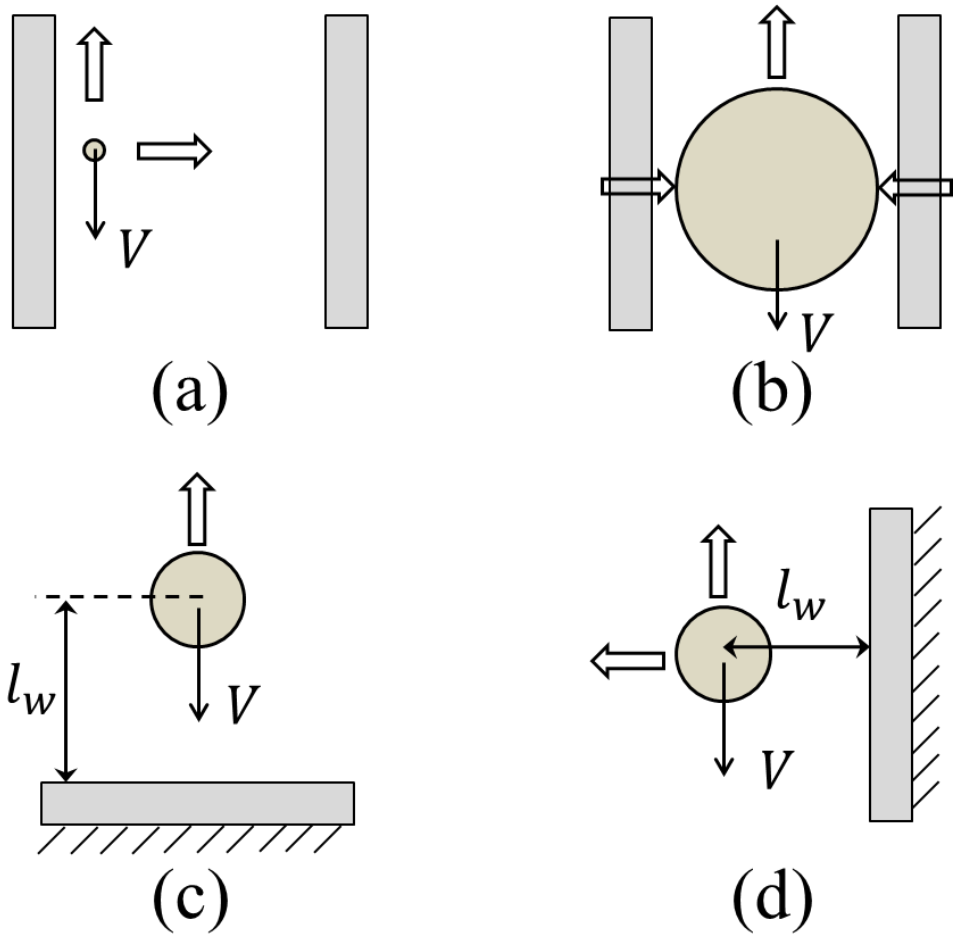

Figure 2–12 (a) Particle size is far less than the characteristic dimension of channel, and the motion of immersed particle is primarily influenced by a single wall. (b) Particle size is of the of the order of the dimension of channel, and boundaries retard

significantly the motion of the object. (c) Main flow direction is perpendicular to the boundary. (d) Main flow direction is parallel to the boundary.

2.3.2.3.5 Net inertial lift force

For a neutrally buoyant rigid sphere flowing in a straight wall-bounded Poiseuille flow, from our above discussion, besides a viscous drag force along the mainstream, there are four lateral forces acting on the sphere: Magnus force due to slip-rotation, Saffman force due to slip-shear, shear gradient lift force due to the curvature of undisturbed fluid velocity profile, and wall lift force due to the disturbance of flow filed around particles from wall. Among them, Magnus force and Saffman force are always very small and negligible. Shear gradient lift force, directing particles toward channel walls, and wall lift force, repulsing particles toward channel centreline, are commonly recognised as the dominant effects of the particles' lateral migration. The balance of shear gradient lift force and wall lift force creates several equilibrium positions halfway between the channel walls and centreline, and this theory can reasonably explain the observation of Segre and Silberberg reasonably [13, 14], Figure 2-13(a). It should be noted that such a breakdown is rather unconventional, because an unbounded parabolic velocity profile cannot be realized in practice, but it permits the separation of the effects due to the curvature of the undisturbed velocity profile and the wall-induced inertia [91].

Through the method of matched asymptotic expansions, Asmolov [91] derived an analytical expression of the net inertial lift force acting a small rigid sphere ($a/H \ll 1$) in a Poiseuille flow:

$$F_L = f_L \rho_f \gamma^2 a^4 \tag{2-35a}$$

It can be further simplified as:

$$F_L = f_L \rho_f U_f^2 a^4 / H^2 \tag{2-35b}$$

where U_f is the average flow velocity of fluid; H is the hydraulic diameter, which is the characteristic dimension of a channel. H *is* defined as $H = D_C$ for a circular channel (D_C is the diameter of circular cross-section) or $H = 2wh/(w + h)$ for a rectangular channel (w and h correspond to width and height of the rectangular cross-

section). f_L is the lift coefficient which is a function of the particle lateral position x and Reynolds number Re [91, 114], Figure 2-13(b). On the lateral position where $f_L = 0$, it corresponds to the inertial equilibrium positions. It should be noted that the channel centreline $x = 0$ is not a stable equilibrium position, since a little deflection from centreline will never return particles back. It also has been found that f_L decreases with increasing Re (or U_f), suggesting that inertial lift force scales less strongly than U_f^2 [5]. Recently, Zhou and Papautsky [115] derived a scaling for the lift coefficient based on their experimental results: $f_L \propto \frac{H^2}{a^2\sqrt{Re}}$. Although f_L varies with Reynolds number, at Re<100 that is typical for most microfluidic applications, the lift coefficient remains relatively constant, and can be approximated averagely as $f_L = 0.5$ [95].

For a finite-size particle ($0.05 \leq a/H \leq 0.2$), particle would cause a disturbance to the main channel flow. Recently Di Carlo et al. [94] calculated the inertial lift forces through finite element simulation, taking into account the finite-size effects of suspended particles. The net force was scaled near the channel centre and channel wall respectively. Near the channel centre, where the effects of wall lift force is very weak, the net lift force is scaled as $F_L \propto \rho_f U_f^2 a^4/H^2$. While near the channel wall, wall effects dominates that of shear gradient, and it is scaled as $F_L \propto \rho_f U_f^2 a^6/H^4$.

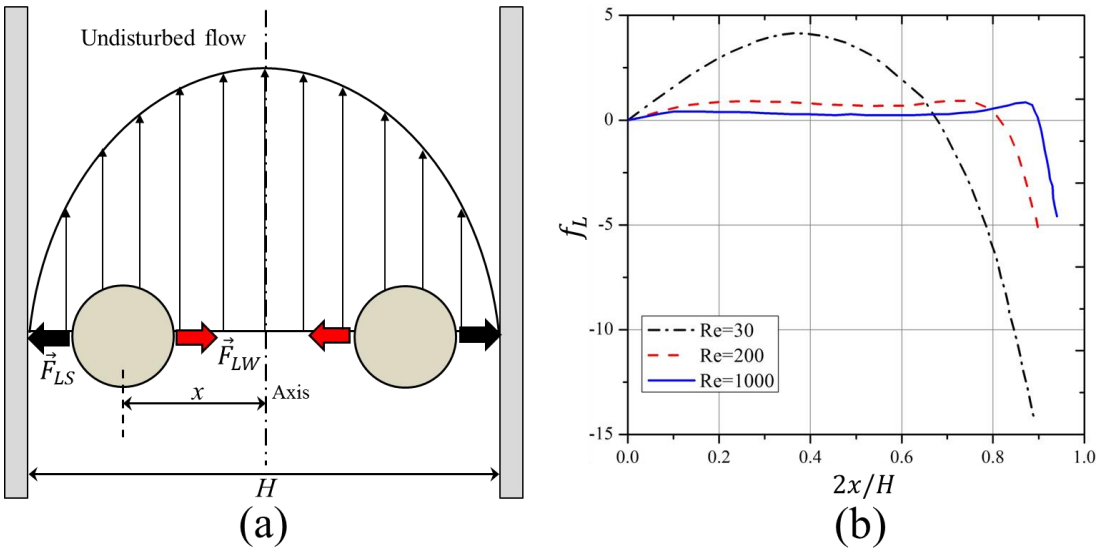

Figure 2–13 (a) Balance of shear gradient lift force and wall lift force results in the inertial equilibrium positions in a Poiseuille flow. (b) The net lift coefficient is the

function of particle lateral position *x* and Reynolds number Re. Reproduced from reference [116].

2.3.2.4 Deformability-induced lift force

Although solid rigid particles can be used as an effective and simple model in the study of hydrodynamic behaviour of particles in microchannel, the practical bio-particles such as cells and vesicles are not rigid but with deformability. And this deformability will induce an additional lift force on the particles. The deformability-induced lift force is perpendicular to the main undisturbed streamline, and it is believed to be the results of shape-change of particle and nonlinearities caused by the matching of velocities and stresses at the deformable particle interface [67]. Three dimensionless parameters can be used to characterize the relative deformation of a droplet: i) Weber number, $We = \frac{\rho_f U^2 a}{\sigma}$ (inertial stress *vs.* surface tension), where σ is surface tension; ii) Capillary number, $Ca = \frac{\mu U a}{\sigma h}$ (viscous stress *vs.* surface tension); and iii) Viscosity ratio, $\lambda_d = \mu_d/\mu$, here μ_d is the dynamic viscosity of fluid inside the droplet [67].

Chan and Leal [117, 118] derived an analytical expression for deformability-induced lift force , given the conditions that the drop or bubble is not too close to the walls:

$$F_{L,deformation} = \mu U a (\frac{a}{H})^2 \frac{d}{H} f(\lambda_d) \quad (2\text{-}36)$$

$$f(\lambda_d) = \frac{16\pi}{(\lambda_d+1)^3}\left[\frac{11\lambda_d+10}{140}(3\lambda_d^3 - \lambda_d + 8) + \frac{3}{14}\frac{19\lambda_d+16}{3\lambda_d+2}(2\lambda_d^2 - \lambda_d - 1)\right] \quad (2\text{-}37)$$

where d is the distance between drop and centre of channel. Furthermore, the condition of $\lambda_d < 1$ or $\lambda_d > 10$ was specified for the deformability-induced lift force directing towards the center of the channel [118].

The experimental measurements of the inertial lift force by Di Carlo et al. [94] extracted an expression for inertial lift force near the channel centre where $d/H < 0.1$. The negative sign indicates that this force, $F_{L,inertial}^{center}$, is directed towards the walls.

$$F_{L,inertial}^{center} = -10R_p\mu Ua\left(\frac{d}{H}\right) \quad (2\text{-}38)$$

When both drop deformation and inertial lift forces are small for $Ca < 0.01$ and $R_p(= R_e\frac{a^2}{H^2}) < 0.01$, Stan et al. [117] introduced an empirical formula for the net lift force on drop or bubble as:

$$F_{L,empirical} = C_L\mu Ua\left(\frac{a}{H}\right)^3\left(\frac{d}{H}\right) \quad (2\text{-}39)$$

The lift coefficient C_L must be determined from experimental measurements for each pair of continuous and dispersed phases. And C_L~31.25 can be used for the order-of-magnitude calculation [117].

Deformability-induced lift force can be used to separate and enrich malaria-infected red blood cells (*i*RBCs) from normal healthy RBCs (*h*RBCs) for the diagnosis of malaria. The parasite releases proteins that trigger the cross-linking of the spectrin network in the *i*RBC's phospholipid bilayer membrane, thus increases the rigidity of the *i*RBCs. Normal *h*RBCs are more deformable than *i*RBCs, migrating towards to the centre of the channel. Due to the massive hydrodynamic interactions and mechanical collisions between the RBCs in high haematocrit (Hct) blood, stiffer malaria *i*RBCs are displaced towards the sidewalls, and can be depleted and enriched by two-sided outlets [119].

In inertial microfluidics (R_p~1), Hur et al. [120] found that centre-directed deformability-induced lift force shifts inertial equilibrium positions a little closer to the channel centre than that of rigid particles, Figure 2-14. By the combination of size and deformability, circulating tumour cells (CTCs) with more deformability than the cells from the same organ, were separated and enriched from peripheral blood.

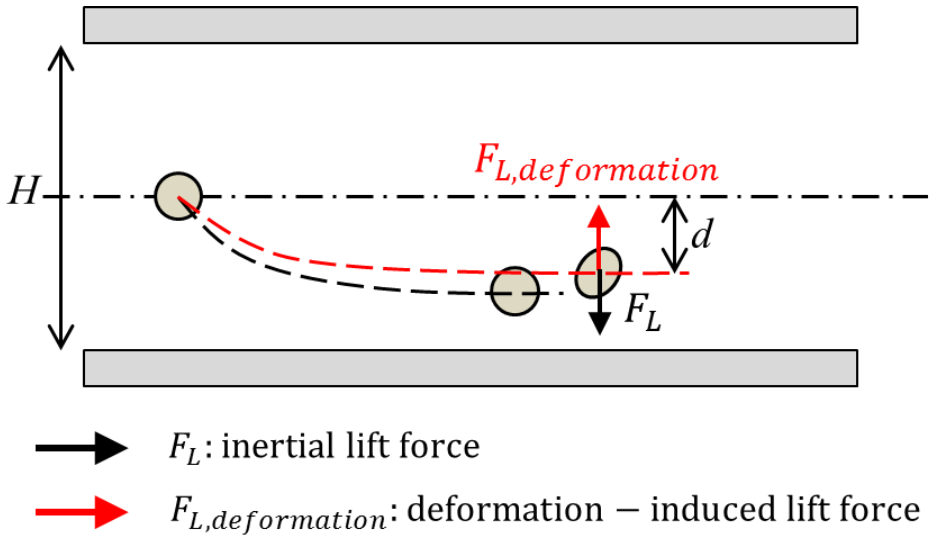

Figure 2–14 Deformability-induced lift force directs to the channel centre, and shifts inertial equilibrium positions closer to the channel center, compared with the rigid spherical particles.

Besides particle deformability, the shape of particles [96] and the properties of medium [121] also impact the inertial migration and equilibrium positions, which will not be detailed here. In the next section, the secondary flow within the cross-section of channel due to the channel curvature (or disturbance structure) will be discussed, and employment of effects of secondary flow on the inertial migration to assist and/or modify inertial focusing is a common practice in the design of inertial microfluidic device.

2.3.2.5 Secondary flow

It is well know that when fluid flows through a curved channel, a secondary flow arises due to the velocity mismatch in the downstream direction between fluid in the central and near-wall regions. The fluid elements near channel centreline have higher inertia and would tend to flow outward around a curve due to the centrifugal effect, creating a pressure gradient in the radial direction within the channel. In a fully-bounded channel, due to the centrifugal pressure gradient, relatively stagnant fluid near the walls re-circulates inward, finally forming two symmetric circulating vortices [5]. The parameters that influences the distribution and strength of the secondary flow in a curved channel includes Dean number *K*, Reynolds number Re and aspect ratio of the channel *AR* (=*h*/*w*). Dean number *K* is a function of Reynolds

number Re, the hydraulic diameter for the rectangular channel H and the radius of curvature R [122]:

$$K = (H/2R)^{1/2}Re \tag{2-40}$$

In a rectangular channel, hydraulic diameter is defined as:

$$H = 2wh/(w + h) \tag{2-41}$$

Following Squires and Quake [123], the secondary flow velocity scales as

$$U_D \sim K^2\mu/(\rho H) \tag{2-42}$$

Furthermore, the magnitude of secondary flow U_D can be approximated as [124, 125]:

$$U_D = 1.8\times10^{-4}\times K^{1.63} \tag{2-43}$$

In addition, it was found that the ratio of channel dimension to radius of curvature $\delta = H/2R$, Dean number K as well as the aspect ratio AR have important effects on the shape of the secondary flow field [122].

2.4 The recent progress of inertial microfluidics

According to the structure of the functional microchannel, the reported inertial microfluidic device can be mainly categorised as: (i) straight channel, (ii) spiral channel, (iii) straight channel with pillar arrays or expansion-contraction arrays, and (iv) serpentine channel. In the following sections, a detailed review on the current progress of inertial microfluidics will be presented, i.e. the phenomenon and mechanism of inertial migration in different structured micro-channels, and their applications.

2.4.1 Straight channels

It is well known that when particles are flowing in a straight channel with finite inertia, they experience two inertial lift forces: shear gradient lift force F_{LS} directing towards the channel walls and wall lift force F_{LW} pointing to channel centreline. The balance of these two inertial lift forces leads to several equilibrium positions within

the cross section. In a straight channel with circular cross-section, the randomly distributed particles migrate laterally to a narrow annulus at about 0.6 times of the channel radii form the axis [13, 116], Figure 2-15(a). However, in a straight channel with a rectangular cross-section which is the typical feature in the soft lithography, the situation becomes more complex. In a square straight channel (*AR*=height/width=1), particles normally focus to four equilibrium positions [126], facing the centre of each wall, Figure 2-15(b). Additionally, a further reduction to two equilibrium positions happens in a low aspect ratio (*AR*<0.5) channel, particles focus at the centre face about 0.2*H* away from the top and bottom walls [115, 127, 128], Figure 2-15(c). One explanation about this equilibrium positions' reduction was given by Zhou and Papautsky [115] by a two-stage migration model. Microparticles first migrate from the channel bulk toward equilibrium positions near walls under the influence of the shear gradient lift force and wall lift force. Then, particles migrate parallel to long walls into the centre of long walls under the influence of the rotation-induced lift force.

In straight channel, particles' lateral migration velocity (U_L) and the minimum channel length (L_{min}), as shown in figure 2-15(d), which is the minimum length that is required for particles to migrate to their inertial equilibrium positions, can be derived by balancing the net inertial lift force with stokes drag [114]:

$$F_{drag} = 3\pi\mu a U_L \tag{2-14b}$$

$$U_L = \frac{F_L}{3\pi\mu a} = \frac{\rho_f U_f^2 a^3}{6\pi\mu H^2} \tag{2-44}$$

$$L_{\min} \approx \frac{H}{2U_L} * U_f = \frac{3\pi\mu_f H^3}{\rho_f U_f a^3} \tag{2-45}$$

Two dimensionless Reynolds numbers can characterize the lateral migration of particles in straight channel, which are channel Reynolds number Re describing the ratio between inertial force and viscous force of fluid in a flow, and particle Reynolds number R_P additionally considering the ratio of particle size to channel size.

$$R_P = \mathrm{Re}\frac{a^2}{H^2} = \frac{\rho_f U_f a^2}{\mu H} \tag{2-46}$$

When R_P<<1, the viscous interaction of fluid and particles dominates the particles' movement in the channel. Under this condition, particles are subjected to the dominant viscous drag to follow fluid streamlines. However, increasing R_P to the order of 1, inertial lift forces become dominant that lateral migration of particles across the fluid streamlines becomes obvious [95].

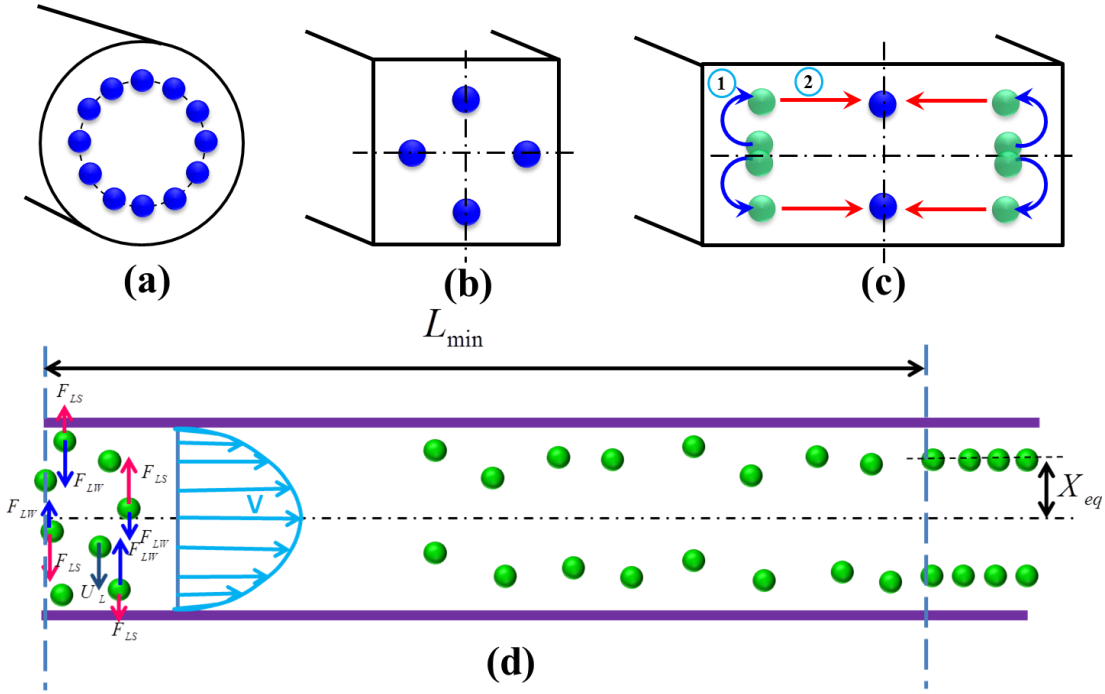

Figure 2–15 (a) Inertial equilibrium positions in a circular channel. (b) Inertial equilibrium positions in a rectangular channel with square cross-section. (c) Inertial equilibrium positions in a rectangular channel with low aspect ratio. And illustration of two-stage migration model proposed by Zhou and Papautsky [115]. (d) The lateral migration speed U_L and minimum channel length for particle focusing L_{min}.

Although straight channel is often employed as a basic model to investigate the fundamental mechanism of inertial migration due to its simplicity [92, 94, 115, 129-131], it has also shown the utility for a variety of applications, including focusing, filtration, enrichment and separation. Hur et al. [132] demonstrated the purification of adrenal cortical progenitor from digestions of murine adrenal glands utilizing hydrodynamic inertial lift forces in a straight micro-channel with high aspect ratio, Figure 2-16(a). The inertial focusing position depends on the cell size, where larger cells are closer to the channel center, and smaller cells are closer to the channel walls.

Differentially focused cells can be collected at designated outlets based on apparent-diameter. Primary murine cells processed through the device have been proven highly viable through in vitro culture for 10 days. Besides, cell deformability has been recognized as a unique label-free biomarker for cell phenotype with implications for assessment of cancer invasiveness. By a simple straight channel with *AR*=2, Hur et al. [120] employed deformability and cell size as distinguishing bio-markers to continuously classify and enrich target cancer cells in a high-throughput and label-free manner, Figure 2-16(b). This system takes advantages of the balance between deformability–induced lift force and inertial lift forces, where deformability-induced lift force shifts the original inertial equilibrium positions towards channel centre line. Cells with different deformability will occupy different lateral positions, enabling selective collection and enrichment. Another example to utilize deformability for cell classification is cell margination. It was defined from the phenomenon that white blood cells migrate toward the vessel walls in blood flows for their proper functioning near vascular endothelium. It depends on a number of conditions including haematocrit, flow rate, red blood cell aggregation and the deformability of both red and white cells [133]. The hydrodynamic interactions of blood cells with the vessel walls, as well as the collective behaviour between white blood cells (WBCs) and Red blood cells (RBCs), are responsible for the migration of the relatively rigid white blood cells toward vessel walls. Utilizing this mechanism, Hou et al. [134] developed a high-throughput microfluidic blood filtration technique for microbial removal from the whole blood, Figure 2-16(c). The filtration of *E.coli* and *S. cerevisiae* from whole blood has been demonstrated, with removal efficiency of ~80% and ~90% respectively. In addition, malaria-infected RBCs (*i*RBCS) with reduced deformability behave similarly to WBCs during margination, and they can also been differentiated and enriched from two side outlets. Ring stage and late trophozoite/schizont stage *i*RBCs have been tested, with recovery efficiency of ~75% for early stage *i*RBCs and >90% for late stage *i*RBCs [119].

Mach and Di Carlo [135] reported a massively parallelized microfluidic device that passively separates pathogenic bacteria from diluted blood, Figure 2-16(d). The device consists of 40 single straight micro-channels placed as a radial array. Each single channel consists of three different cross-sections, and uses a unique differential transit time by size-dependent inertial lift forces to obtain cell separation.

It has been demonstrated that >80% pathogenic bacteria can be removed after two passes of the single channel system. The parallel device can process 240 mL/h with an extreme throughput of 400 million cells per min. Later, Zhou et al. [136] utilized a more polished design of size and length for their cascaded straight channels, Figure 2-16(e). The separation concept is based on their theory of two-stage inertial migration which permits precise prediction of particle or cell position within the micro-channel. Randomly-distributed particles first flow through a high *AR* channel (segment I, w=27 μm, h=50 μm) where particles are focused at two sidewalls facing the centre of channel heights. Then the channel expands into a low *AR* channel (segment III, w=100 μm, h=50 μm), which modifies equilibrium positions to the centres of top and bottom walls. Since larger particles experiencing much stronger migration velocity, reach refocusing much faster than the smaller ones, while lift forces on smaller particles are too weak to alter the their lateral position, thus enabling a separation of particles by size. After this modification, a much higher separation efficiency (~ 99%) and purity (~ 90%) were achieved in their work.

Manual concentration, staining and washing procedures for cell suspension are routinely conducted by cytopathologists as a means of diagnosing malignancies and other diseases. However, current approaches for chemical treatments of cells and chemical reactions typically operate on slow time scales (~seconds to minutes), limiting the realm of fast molecular events. Inertial lateral migration has been subtly employed as a tool to mediate millisecond reaction time around particles and cells [137], as shown in Figure 2-16(f). The main transfer channel is designed with low aspect ratio, so particles will migrate to the centre of channel width as we discussed above. It consists of three inlets, with particles suspensions infused from two side inlets, and reagent pumped in from the central inlet. Lateral migration of particles from original medium to the middle stream area initiates the contact of particles/cells with chemical reagent, and duration of particles within middle stream mediates the reaction time. The proposed microfluidic system can perform several functions in the preparation of samples for cytopathology that (i) automates colorimetric staining on-chip, (ii) images cells in flow, and (iii) provides additional quantitative analyses of captured images to aid cytopathologists [97]. In addition, ordering particles along a specific stream within a simple straight microchannel could also be integrated with optical detector to form an on-chip flow cytometer system. Hur et al. [138] proposed

an extremely high-throughput on chip image flow cytometry, consisting of 256 high-aspect parallel straight channels and high-speed optical camera, promising interrogation rates up to 1 million cells per second, Figure 2-16(g).

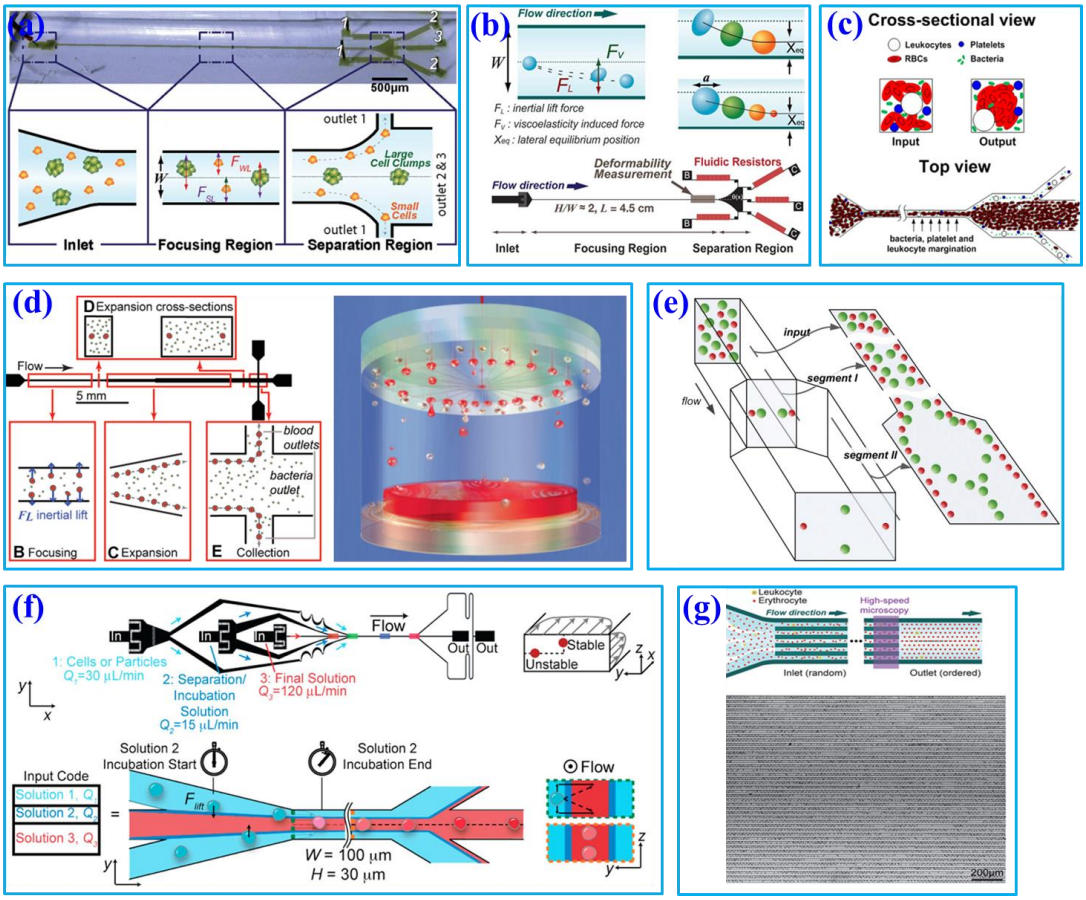

Figure 2–16 (a) Label free isolation of adrenal cortical progenitor cells by size-based differential inertial focusing in a straight channel [132]. (b) Classifying and separating cells and particles by deformability in inertial microfluidics. Besides inertial lift forces, deformable cells experiencing an extra deformability-induced lift force than rigid particles, shifting deformable cells towards channel centreline [120]. (c) Pathogen removal from blood using margination phenomenon in a straight channel. Deformable RBCs migrate axially to the channel centre, resulting in margination of other relative rigid cell types (bacteria, platelets and leukocytes) towards the channel walls, and subsequently removed from the side outlets [134]. (d) Separation of pathogenic bacteria from diluted blood in a series-connected straight channel which utilizes a unique differential transit time by size-dependent inertial lift forces to obtain cell separation [135]. (e) Complete separation of particles in a

cascaded channel with two straight segments with different aspect ratios (*AR*s). Randomly-distributed particles first flow through a high *AR* channel where particles are focused at two sidewalls facing the centre of channel heights. After all the particles are fully focused, the channel expands into a low *AR* channel, which modifies equilibrium positions to the centre of channel width. Since larger particles experiencing much stronger migration velocity, reach refocusing much faster than the smaller ones, thus enabling a separation of particles [136]. (f) Rapid inertial solution exchange in a straight channel for controlled interaction of reagents with cells and particles [137]. (g) Extremely high throughput microfluidic flow cytometry employing inertial ordering in 256 high *AR* parallel channels and high-speed optical interrogation method [138].

In general, straight channel has the advantages of simple structure, therefore the mechanism of inertial migration phenomenon in a straight channel is relatively clear and has already be fully studied and uncovered. This provides mature guidelines for efficient inertial microfluidic device design. However, since $F_L \propto H^{-2}$, the sizes of channel cross-section are normally restrained to provide enough lateral lift forces. Meanwhile, in order to achieve successful particle focusing, it would be better to satisfy $a/H > 0.07$ [95], limiting the dimension of microchannel. The small cross section leads to a high fluidic resistance, which needs more power to pump the sample into the microfluidic device. In addition, the channel is relatively long, which would add up the flow resistance and lead to a large device footprint.

2.4.2 Spiral channels

Particles flowing in a curved channel with finite inertial will experience both inertial lift forces and secondary flow drag. In most cases, the density of particle is very close to the density of fluid, so the effects of centrifugal force on the suspended particles around channel curvatures appear negligible. Compared with straight channel, the curved channel has following superior advantages in inertial microfluidics: (i) improvement of collection purity due to the adjustment of particles equilibrium positions; (ii) reduction of channel footprint for particles' lateral migration due to the assistance of secondary flow to accelerate lateral migration; and (iii) equilibrium separations of particles based on different equilibrium positions of particles with various sizes [5].

When the channel curvature is along a single direction, the curved channel is a spiral channel. And the direction of secondary flow within each cross-section is almost constant, even though there may be a little variation on its magnitude due to the change of channel curvature. By a first order approximation, one can make an assumption that the effects of inertial migration and secondary flow act in superposition on a particle in a spiral channel, Figure 2-17(a-c). A particle is held stationary at an inertial equilibrium position will experience a secondary flow drag whose magnitude is directly proportional to the local secondary flow velocity field [5]. This secondary flow drag (Dean drag) acts to entrain particles within the streamline of symmetrically rotating vortices, which is primarily an effects of mixing. In contrast, inertial lift forces tend to held particles at specific equilibrium positions within channel cross-section. Therefore, the ratio of magnitude between inertial lift forces and Dean drag $R_f = a^3R/H^3$ determines the final behaviour of the suspended particles. This dimensionless parameter is useful for the prediction of particle behaviour in curved channel, and at two limiting conditions where (i) $R_f \rightarrow 0$, Dean drag force dominates the behaviour of particles, particle streams will neglect inertial equilibrium positions, and remain entrained the secondary flow streamlines, and (ii) $R_f \rightarrow \infty$, inertial lift forces is dominant, particles will migrate to the inertial equilibrium positions independent of the secondary flow [5]. For most cases, in intermediate range of R_f , inertial equilibrium positions will be modified by the secondary flow, Figure 2-17(c), leading to very intriguing new focusing phenomenon, as well as extended applications. It has been noted that R_f is dependent on particle size, so that two different-sized particles may experience different behaviours in the same curved channel. Therefore, it would be possible to enable particle separation by size in spiral channel.

Meanwhile, Yoon et al. [139] proposed another possible explanation for particle separation in a curved channel. In their explanation, the separation is achieved by the effect of secondary flow velocity distribution on the cross-section, rather than the theory of the balance between secondary flow and inertial migration. Larger particles with diameter larger than $0.72h$ experiences a net secondary flow drag directing outward to the channel curvature, while smaller particle with diameter less than 0.27h experience a net secondary flow drag inward, Figure 2-17(d). Therefore, it

enables the particle separation by the different net directions of secondary flow on different-sized particles.

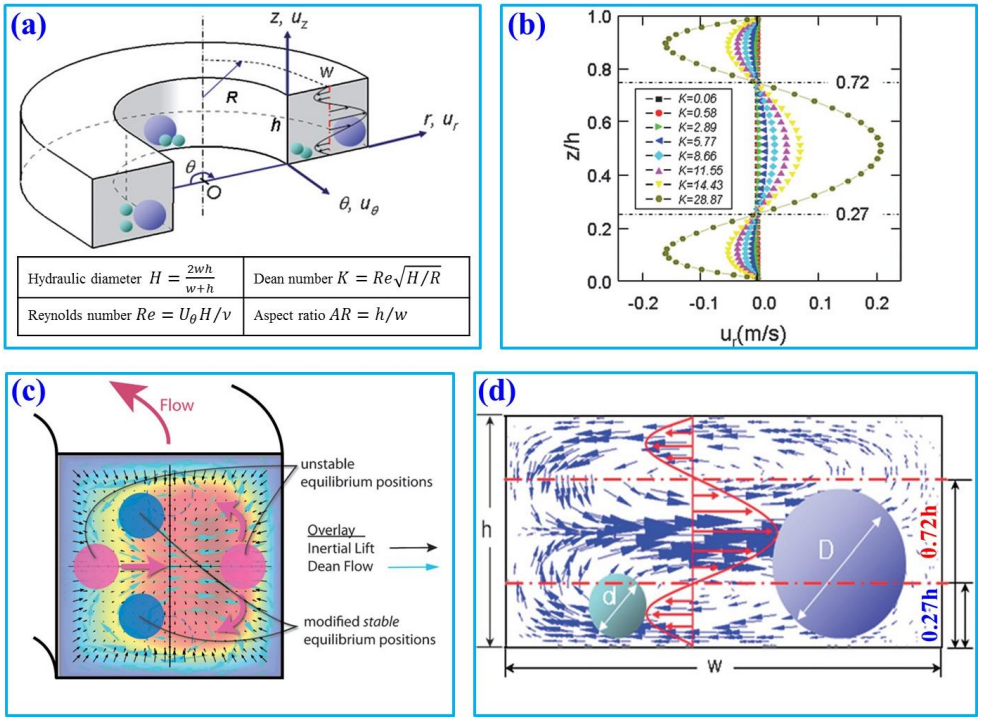

Figure 2–17 (a) Schematic illustration of inertial separation by particle size in a curved microchannel and its important design parameters [139]. (b) A typical distribution of velocity in a curved channel with Aspect ratio of 1, and θ=90º [139]. (c) Superposition of inertial lift force and Dean flow in curved channel modifies the number and position of the inertial focusing positions [5]. (d) Size-based separation along the direction of stokes drag exerted by the Dean flow. A large bead mainly experiences a net outward force due to main outward velocity around channel centre, while a small bead is dominated by the inward velocity distribution near top and bottom walls [139].

Spiral channels were investigated extensively for particle ordering and separation by Papautsky's group [140, 141], Go's group [139], Jiang's group [142, 143] and Han's group [144, 145]. Flow cytometer is a powerful single cell analysis tool for multi-parametric study. Bhagat et al. [124] proposed a sheath-less, on-chip flow cytometry system based on the principle of Dean coupled inertial microfluidics, Figure 2-18(a). The spiral channel design takes advantage of both Dean drag force and inertial lift forces, and a three-dimensional particle single stream focusing mode

without any assistance of external force field or sheath flow can be obtained. After assembly with a laser induced fluorescence detection setup, the microfluidic flow cytometry system could provide a high throughput of 2,100 particles per second. Besides, an integrated microfluidic system that combines cell-ordering in spiral channel with droplet microfluidic generator was reported by Kemna et al. [125]. Cells were focused in three dimensional along a single particle chain and ordered with a precise longitudinal spacing, which is critical for the downstream cell encapsulation in droplet, Figure 2-18(b). Single cell encapsulation was successfully demonstrated with single cell encapsulation efficiency about 80%. Such a system is very promising in the applications such as cell-based assays, drug screening and cell printing technologies.

Particle separation and sorting possess a wide range of industrial, biomedical and clinical applications such as wastewater purification, blood sample preparation and disease diagnosis. And passive separation and sorting of particles/cells is one of superior advantages for spiral microchannel, benefiting from the distinct size dependence characteristics of secondary flow and inertial lift forces, as discussed above. Bhagat et al. [140] demonstrated a complete separation of 7.32μm and 1.9 μm polystyrene particles at Dean number of 0.47 in a 5-loop spiral microchannel. Later on, Kuntaegowdanahalli et al. [141] from the same group extended the separation capability of spiral channel using Dean-coupled inertial migration. They have demonstrated continuous separation of triplet polystyrene beads (10, 15 and 20 μm in diameter) with an efficiency of 90% and a throughput of 1×10^6 cells/min in a similar spiral channel, Figure 2-18(c). Furthermore, this separation ability was employed to separate different-staged cells for cell cycle synchronization, which is essential for studying cellular properties, biological processes and elucidating genetic regulatory mechanisms and events involved in each phase prior to cell division. Lee et al. [146] developed a label-free, high-throughput inertial microfluidic fractionation platform with spiral structure, which was demonstrated by successfully fractionating asynchronous bone marrow-derived human mesenchymal stem cells (hMSCs) into enriched subpopulations of G0/G1 (>85%), S and G2/M phases, Figure 2-18(d). The proposed platform could provide significantly higher throughput (~15×10^6 cells per h) and cell viability (~95%) than the existing microfluidic systems, enabling diverse applications in the study and manipulation of cell proliferation.

Cancer, also known as a malignant tumour, is a group of diseases involving abnormal cell growth with the potential to invade or proliferate in other organs of the body. Metastases from primary tumours are the leading causes (~90%) of death for nonhematological cancers [147]. During the progression of metastasis, cancer cells escaped from solid tumours and enter the bloodstream, becoming circulating tumour cells (CTCs), which hold a great potential to serve as important biomarkers for early diagnosis of cancer metastases, as well as cancer prognosis and therapy monitoring. CTCs analyses are considered as a real-time "liquid biopsy", which is much less invasive than the current method for cancer diagnosis requiring invasive biopsy followed by molecular analysis. However, CTCs are extremely rare, comprising only a few out of one billion haematological cells in blood, making their isolation and characterization an extreme technological challenge. Hou et al. [148] employed a spiral channel to isolate CTCs from blood under the assistance of a sheath flow, and it achieved a recovery rate of more than 85%. This CTCs isolation platform is working in a label-free and clog-free continuous manner, significantly reducing the capturing costs and alternation of CTCs' morphology. In addition, a clinical validation with positive detection of CTCs from all the patients' blood samples was reported. Meanwhile, Sun et al. [142, 143] reported a passive double spiral microfluidic device, Figure 2-18(e), which can separate and enrich tumour cells (MCF-7 and Hela cells) from diluted whole blood continuously with a throughput of 3.33×10^{7} cell/min, an enrichment factor of 19 and a recovery rate of 88.5%. Compared with the single spiral microchannel, the double spiral device was claimed to provide better focusing behaviour of small blood cells and improved separation efficiency. To further enlarge the throughput of spiral channel, parallelization technology must be employed. Due to the nonlinear nature of spiral channel, it is hard to parallelize spiral channel within the horizontal plane. Then, a multiplexed microfluidic device stacked by three spiral channels along vertical direction for ultra-high throughput CTCs capturing and enrichment was reported by Warkiani et al. [149], as shown in Figure 2-18(f). The advantages of very fast processing speed (7.5 ml blood in less than 10 min) and the ability to collect more CTCs from larger blood volumes make it very promising for a range of potential genomic and transcriptomic applications.

At the same time, Guan et al. [17] introduced a novel spiral micro-channel with a trapezoidal cross-section and it showed a higher separation resolution than those with rectangular cross-section. In their study, they found that particle focusing in spiral channel with trapezoidal cross-section are sensitive to particle size and flow rate, and exhibits a sharp transition at a size-dependent critical flow rate. Wu et al. [145] applied this novel spiral channel for the separation of Leukocytes from blood sample. At the outlet, the larger white blood cells are focused near the inner walls, while smaller red blood cells are trapped at the core of dean vortex near the outer wall, Figure 2-18(g). And an enhanced separation resolution and efficiency (>80%) was demonstrated. Later, after a slightly adjustment of channel heights, isolation CTCs from cancer patients' blood samples was demonstrated using the similar slanted spiral micro-channel [144] by the same group, Figure 2-18(h). It has successfully isolated and recovered more than 80% of the tested cancer cell lines spiked in 7.5 ml blood within 8 min with high purity (400-680 WBCs ml^{-1}; ~4log depletion of WBCs). In the initial proof of clinical investigation, the trapezoid chip successfully isolated CTCs from 10 out of 10 (100%) patients with advanced stage metastatic breast and lung cancer (3–125 CTCs/ml), and it allowed extensive heterogeneity studies via immunostaining and DNA FISH analysis. Although the spiral micro-channel has a great potential for real clinical application, its throughput is still limited due to difficulties in parallelisation. Although stacking microchannel along the vertical direction may provide a route to for parallelization design, the problem of uneven input condition for each spiral channel may ruin the overall performance, especially for inertial microfluidics, whose functionality is very sensitive to the input flow speed. Therefore for parallelization design, a linear channel structure is more preferred.

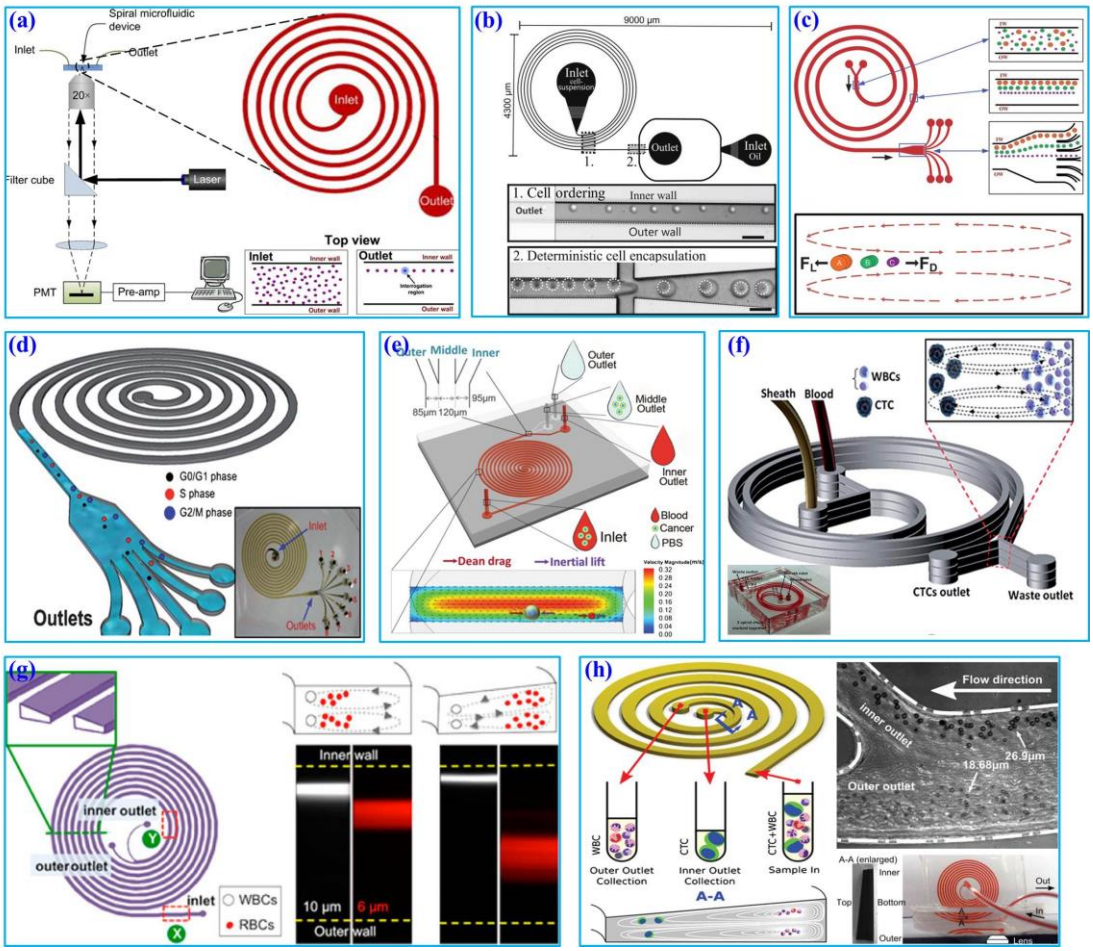

Figure 2–18 (a) Schematic of a microfluidic flow cytometry, in which spiral channel is applied as a particle focuser to provide high-throughput sheath-less 3-D focusing, followed by the downstream laser induced fluorescence setup for particle detection and counting [124]. (b) Microfluidic device consists of a spiral channel followed by an encapsulation part. The spiral channel promotes single cell stream ordering with a precise longitudinal spacing, and it is critical for downstream encapsulation of cells into the droplet [125]. (c) Continuous triplet-particle separation in a spiral channel by the Dean-coupled inertial migration [141]. (d) Schematic illustration of cell cycle synchronization in a spiral channel. Under the influence of inertial lift force and Dean drag force, asynchronous cell populations with different sizes will be differential ordering at the end of spiral channel for purification [146]. (e) Double spiral microchannel for tumour cell separation and enrichment [142]. (f) A multiplexed microfluidic device stacked by three spiral channels for ultra-high throughput CTCs capturing and enrichment [149, 150]. (g) Enhanced inertial separation of Leukocytes from red blood cells using spiral channel with trapezoid

cross-section. At the outlet, the larger white blood cells focus near the inner walls, while smaller red blood cells are trapped at the core of dean vortex near the outer wall [145]. (h) Ultra-fast, label-free enrichment of CTCs from blood samples by a spiral microfluidic device with trapezoid cross-section [144].

2.4.3 Straight channels with pillar arrays or expansion-contraction arrays

Besides curvature, the introduction of disturbance obstacles into straight channel will also induce convective secondary flow, which was first reported to enhance mixing effects in microchannel by continuously splitting and redirecting fluid streams [151]. Afterwards, by patterning a contraction-expansion array on single side of a straight channel, Lee et al. [152] successfully demonstrated three dimensional single stream particle focusing under a sheath flow. At the entrance of the contraction region, the centrifugal forces induce counter-rotating secondary flow, enveloping a sample flow with a sheath flow in three dimensions, Figure 2-19(a). Besides particle focusing, a series of particle separation in this kind of contraction-expansion array (CEA) channel were also reported by the same group, including polystyrene beads of 4 μm and 10 μm in diameter [128], blood plasma from red blood cells [153] and cancer cells from whole blood [154], Figure 2-19(b, c). Expansion-contraction array induces Dean-like secondary rotating flows, working together with inertial lift forces on the suspended particles. The balance of these effects on particles determines the net migration progress of particles, and is highly size-dependent, therefore enabling size-based particle separation. Large particles or cells (e.g. cancer cells) are influenced dominantly by the inertial lift forces, migrating towards contraction-expansion side, while small particles or cells (e.g. red blood cells and white blood cells) are dominated by Dean drag, shifting towards opposite side. Finally, it enables a size-based particle/cell separation and enrichment [154]. This device can handle highly concentrated bio-particle samples such as undiluted whole blood (1×10^9 counts/ml) due to the utilization of a sheath flow. However, the inclusion of a sheath flow will certainly contribute the complication of the whole system, diluting the sample and potentially causing contamination.

Besides the contraction-expansion array patterned on single side of a channel, it can also be patterned on two sides of the channel. Park et al. [155] investigated particle inertial focusing in a straight channel patterned with symmetrical expansion-

contraction array on both sides (multi-orifice microchannel), Figure 2-19(d). This device is working without the assistance of any sheath flow. The ordered particle distribution can be achieved at central or side regions according to a particle Reynolds number R_p. Generally, particles are focused at two side positions with R_p range of ~0.8 to 2.3 and at the centreline with the R_p range of 3.0 to 3.5. In their explanation, the mechanism of these focusing patterns is relying on the combination of inertial lift force and momentum-change-induced inertial force generated in the region of contraction-expansion region. The trajectory mismatching between particles and fluid element around the contraction-expansion region induces the lateral drift of the equilibrium position. The extent of this lateral drift is variable according to particle size and flow rate. It was found that at the Reynolds number range of 63-91, large polymer particle (~15 μm) were aligned along the centreline of outlet, whereas small particle (~7 μm) remained near both sidewalls. Therefore, size-based separation of particles in this kind of multi-orifice channel is achievable, and it was termed as Multiorifice Flow Fractionation (MOFF), Figure 2-19(e) [156]. The MOFF has several advantages such as continuous, label-free, sheath-less, and non-intrusive with minimal power consumption. However, it is limited by the relatively low recovery yield. Although the recovery yield may be increased by adjusting parameters such as the Reynolds number to enhance central focusing, poor purity inevitably followed. So it cannot keep both high recovery yield and high purity at the same time. Therefore, Sim et al. [157] presented a multi-stage multi-orifice flow fractionation (MS-MOFF), which is made by combining three multi-orifice segments, 3 inlets, 3 filters and 5 outlets, Figure 2-19(g). It could improve recovery and minimize loss of purity by collecting and re-separating non-selected particles from the first separation. The final recovery rate was successfully increased from 73.2% to 88.7% with a slight compromise on final purity (from 91.4% to 89.1% for 15 μm particles). Meanwhile, by a combination of multi-orifice flow fractionation (MOFF) and dielectrophoresis (DEP) techniques, Moon et al. [158] successfully separated human breast cancer cells (MCF-7) from spiked blood sample, Figure 2-19(f). The inertial separation by MOFF takes advantage of the high-throughput filtration of blood cells, and the serially connected DEP separator works as a precise post-processor to further enhance the efficiency and purity of the separation process.

It was claimed that 99.24% of RBCs and 94.23% of WBCs were removed, with a 162-fold increase in MCF-7 cells.

Diagnosis of malaria at the early stage of infection is challenging due to difficulty in detecting the low abundance of parasites from blood. Polymerase chain reaction (PCR) method can be especially useful for detecting low parasitemia levels, but efficiency is discounted by many factors, such as limited specificity of primers, presence of PCR inhibitors in blood serum and DNA contamination from nucleated blood cells. Recently, Majid et al. [159] present an improved detection method for malaria by the combination of inertial microfluidic processing and PCR detection, Figure 2-19(h). In their inertial microfluidic device with a symmetrical contraction-expansion channel, particles larger than 4 μm such as WBCs were focused along the channel walls and isolated via the peripheral outlets. The malaria parasites, on the other hand, were unfocused and distributed in all the three outlets. Therefore, enriched and purified blood sample would promote more reliable and specific PCR-based detection.

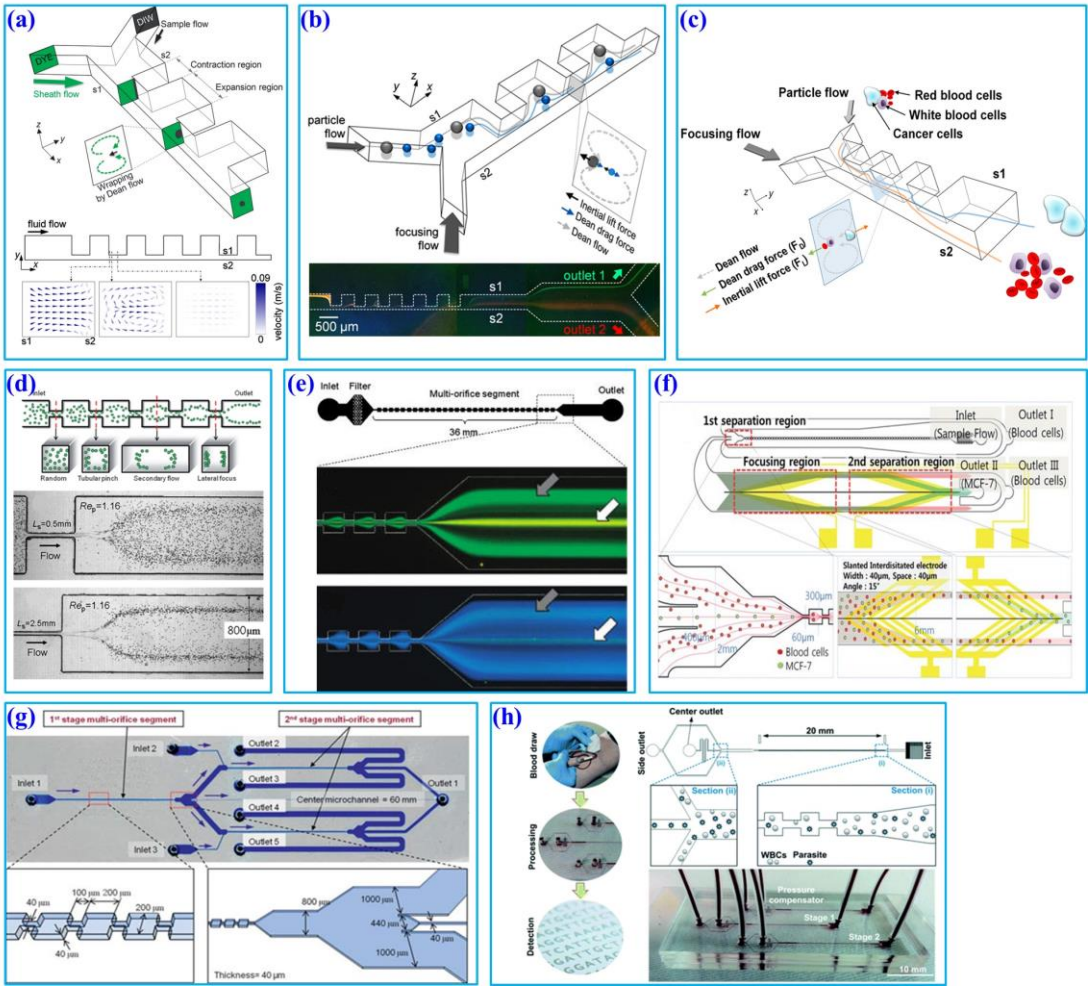

Figure 2–19 (a) Schematic of three dimensional hydrodynamic focusing in a contraction-expansion array (CEA) channel which is consisted of a straight channel with contraction-expansion arrays patterned on single side [152]. (b) Inertial separation of particles by size in a CEA channel under the assistance of a sheath flow [128]. (c) Label-free high throughput separation of cancer cells from whole blood in a CEA microchannel. Large cancer cells are influenced dominantly by the inertial lift forces, migrating towards s1, while small cells (red blood cells and white blood cells) are dominated by Dean drag, shifting towards s2 [154]. (d) Inertial focusing in a straight channel patterned with symmetrical expansion-contraction array on both sides (multi-orifice microchannel). The ordered particle distribution is achieved at central or side regions according to a particle Reynolds number [155]. (e) Continuous inertial separation in a multi-orifice microchannel according to the size-dependent lateral migration termed as Multiorifice Flow Fractionation [156]. (f) Continuous high-throughput separation of human breast cancer cells (MCF-7) from blood cells

by a combination of multi-orifice flow fractionation (MOFF) and dielectrophoresis (DEP). The inertial separation in MOFF takes advantage of the high-throughput filtration of blood cells, and the serially connected DEP separator further enhances the separation efficiency and purity [158]. (g) Schematic of Multi-stage Multiorifice Flow Fractionation (MS-MOFF) design [157]. (h) Modified detection of malaria by the integration of inertial microfluidic processing and PCR detection. Inertial enrichment and purification of malaria parasites from blood in a symmetrical expansion-contraction channel provides more reliable and specific PCR-based detection [159].

In addition to the secondary counter-rotating flow within the cross-section of main channel around the contraction-expansion region, a horizontal micro-vortex within the contraction-expansion chamber can also be generated due to the detachment of boundary layer under a high flow speed. Shelby et al. [160] was among the first to demonstrate a horizontal microvortex in a diamond shaped cavity under high flow speed in microfluidics. This microvortex can generate a maximum fluid rotational velocity as high as 12 m/s and a corresponding radial acceleration in the order of 10^6g. Such microvortex without any moving components are useful for the investigation of effects of high radial acceleration on biological and chemical process, as well as offering precise control and rotation of single cell [161], as shown in Figure 2-20(e). In their work, the single cell was actively trapped and positioned at the centre of the microvortex by an optical tweezer.

Later on, Di Carlo's group [162, 163] introduced the concept of "Centrifuge-on-a-chip" (or Centrifuge chip in short) to passively isolate target particles/cells from heterogeneous background by the effects of inertial migration and vortex trapping. Centrifuge chip was composed of a straight channel section and symmetric expansion-contraction array section, Figure 2-20(a, b). Rather than the optical tweezer, the selective trapping and positioning of micro-particles are based on purely fluid dynamic phenomenon: the cross-stream inertial migration of micro-particles in the cavity expanding area. The mechanism of trapping has been qualitatively explained by Mach et al. [163]. Briefly, the particles' selective trapping process can be divided into three steps: (I) inertial focusing in a straight channel, (II) lateral migration around the expanding area, and (III) circulation within microvortices, as

shown in Figure 2-20(a). (I) In the straight channel section, particles begin uniformly distributed across the channel cross-section when introduced into the micro-channel. Benefiting from inertial lift forces, they will migrate into two focusing streams around 0.2w from each sidewalls in a high aspect ratio microchannel (h/w>1) [94, 138]. (II) In the second step, when focused particles reach the suddenly expansion-contraction area, the adjacent micro-channel wall is out of its vicinity. Therefore, the wall lift force on the particles which is the result of hydrodynamic interaction between particles and walls disappears. The shear gradient lift force will solely act on the particles, leading particles to migrate towards the vortex. The lateral migration velocity U_L can be determined by the balance of the shear gradient lift force and stokes drag, and it is scaled as: $U_L \sim U_f^2 a^2/H$ [94]. It indicates that lateral migration velocity of particles is proportional to power of particle diameter. So that larger particles migrate much faster than the smaller ones, and possibly cross the streamline into the vortex, while smaller particles below a critical size can't enter the vortex. (III) After particles enter into the micro-vortex, the issue of maintaining particles in vortex becomes crucial. As the shear gradient still exists in the micro-vortex, the relevant shear gradient lift F_{Ls} should still act on the micro-particles, directing towards the vortex centre. However, this shear gradient lift force is rather difficult to be expressed explicitly as the shear rate and flow field is quite different from that the straight channel. There is an effective centrifuge force directing outwards due to the curve path of particles: $F_{Cent} = (\rho_p - \rho_f)\pi d^3 v_p^2/6r$, which is based on the assumption that the curve path of particles is a perfect circle, where v_p is the particle's tangential velocity, ρ_p is the particle density, r is the radius of the orbit. If $F_{Cent}/F_{LS} > 1$, particles are thrown out of the vortex; otherwise, if $F_{Cent}/F_{LS} \leq 1$, the particles remain trapped, and orbit within the vortex [163].

The functions of trapping, enrichment, labelling and solution exchange were proven in the Centrifuge chip [98, 163-166]. The most significant advantage of "Centrifuge-on-a-chip" is its ability to selectively trap particles from mainstream by size. It is believed as one of most size-sensitive separation methods [136]. The group of Di Carlo has conducted a series of investigation on its trapping sensitivity and efficiency through a variety of bio-samples, including cancer cells spiked in blood [163], pleural fluids [165] and blood sample [98] from cancer patients. One possible

drawback of this device is that it basically works in batch procedures, and specifically effective in trapping of rare cells (e.g. CTCs), due to limited capacity in expansion-contraction chambers. Later, Wang et al. [164] proposed a modified microvortex-aided device by adding a side outlet in each chamber to continuously siphon larger particles from chambers, facilitating high efficiency and high purity size-based particle separation in a continuous manner, Figure 2-20(c). However, it is still limited by the capability for bimodal separation with a single size cutoff and well-defined size difference. And it will become challenging when treating real-world samples that often include heterogeneous mixtures of multiple particle components. Then, Wang and Papautsky [167] developed a multi-modal inertial sorter that basically consisted of a long straight section and the series-connected separation units (expansion-contraction chamber with side outlets), Figure 2-20(d). They successfully demonstrated triple-sized particle separation with high resolution by sequencing two separation units and proper system parameters. Furthermore, due to the adjustment of the size cutoff in each stage, separation bandwidth or passband location could be modified in a wide range, promoting the flexibility and versatility of the system for multi-modal particle separation.

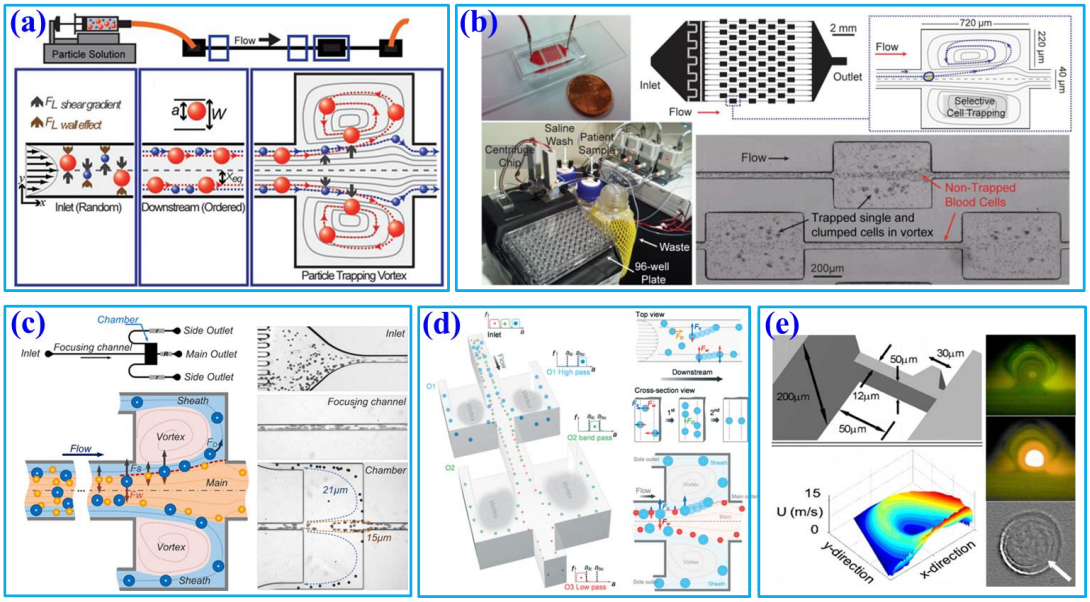

Figure 2–20 (a) “Centrifuge-on-a-chip” for the functions of selective trapping, enrichment, labelling and solution exchange [163]. Basically, there are three steps for the functionality of the “Centrifuge-on-a-chip”: (i) inertial focusing in the straight channel, (ii) lateral migration in the expanding area; and (iii) circulation within

horizontal micro-vortex. (b) Isolation and concentration of cancer cells and mesothelial cells from malignant pleural effusions by automated Centrifuge chip for improved molecular and cytomorphological diagnostics [165]. (c) Vortex-aided inertial microfluidic device for continuous sorting of particles by size. By utilizing the similar trapping mechanism of Centrifuge chip, larger particles are trapped in the horizontal vortices in the contraction-expansion chambers. A modified side outlet in each trapping chamber siphons them out continuously, meanwhile smaller particles exist through the main channel [164]. (d) Schematics of size-based Multi-modal microfluidic sorter. This microfluidic system can achieve continuous multimodal sorting (with multi cutoff sizes) of microparticles with high resolution and high tunability [167]. (e) Rotational control of single cells by microvortices in a diamond-shaped chamber [161].

Besides expansion-contraction chamber, a micro-pillar within a straight channel will also induce irreversible twisted flows at a finite inertia flow. Furthermore, the lateral position of the pillar can be used to tune the position of the net recirculating flows across the channel. Then, it may enable the precise control of the fluid transformation by programming the positions of sequenced cylindrical pillars, Figure 2-21(a). To explore the capabilities of this sequenced pillar microchannel, Amini et al. [168] have successfully demonstrated the sculpture of cross-sectional shape of a stream into complex geometries, moving and splitting a fluid stream, solution exchange and particle separation. By utilizing an in-house, freely available custom software (uFlow), Stoecklein et al. [169] identified eight fundamental fluid transformations (i.e. concave, convex, tilting, stretching, splitting, adding a vertex, shifting, and encapsulating another stream) using rationally sequenced pillars. And these basic functions were verified by the corresponding experimental validation. This demonstrated the possibility of shaping complex fluid deformation by the deterministic ordering of fundamental transformation units without significant design iteration. Later, Nunes et al. [99] utilized this microfluidic technique to fabricate polymeric microfibers with noncircular cross-sectional shapes through a user-friendly design software uFlow, Figure 2-21(b). The computer-aided design (CAD) tool uFlow has a stored library of pre-computed fluid deformations that are produced by individual pillars in the flow channel. And it is a useful tool for the design of pillar sequences, and to predict the shape of complex flow deformation. The cross-

sectional shapes of various fabricated microfibers agreed reasonably well with that predicted using the uFlow software.

Similar to the secondary flow induced by the contraction-expansion chamber or channel curvature, the locally induced secondary flows by sequenced pillars could also be used to modify the inertial migration progress. Chung et al. [170] demonstrated single-stream focusing of microparticles through controllable cross-stream migration aided by the locally tuned secondary flows created by the sequential micropillars, Figure 2-21(c). These pillars act to induce a localized pair of helical vortices that moves particles cloud to the final single focusing equilibrium position, therefore promoting rapid and long-term inertial focusing. Besides, programmable flow deformation in sequential micropillars can also be used to conduct solution transfer around particles or cells, Figure 2-21(d). The microfluidic device was applied for a functionalized bead bioassay, achieving high-yield and continuous separation of 98% of biotin-coated beads from 72.2% of extra FITC-biotin. Also, extraction of leukocytes from lysed blood with yield 89% was performed, further validating the functionality of the platform for the cellular sample preparation [171].

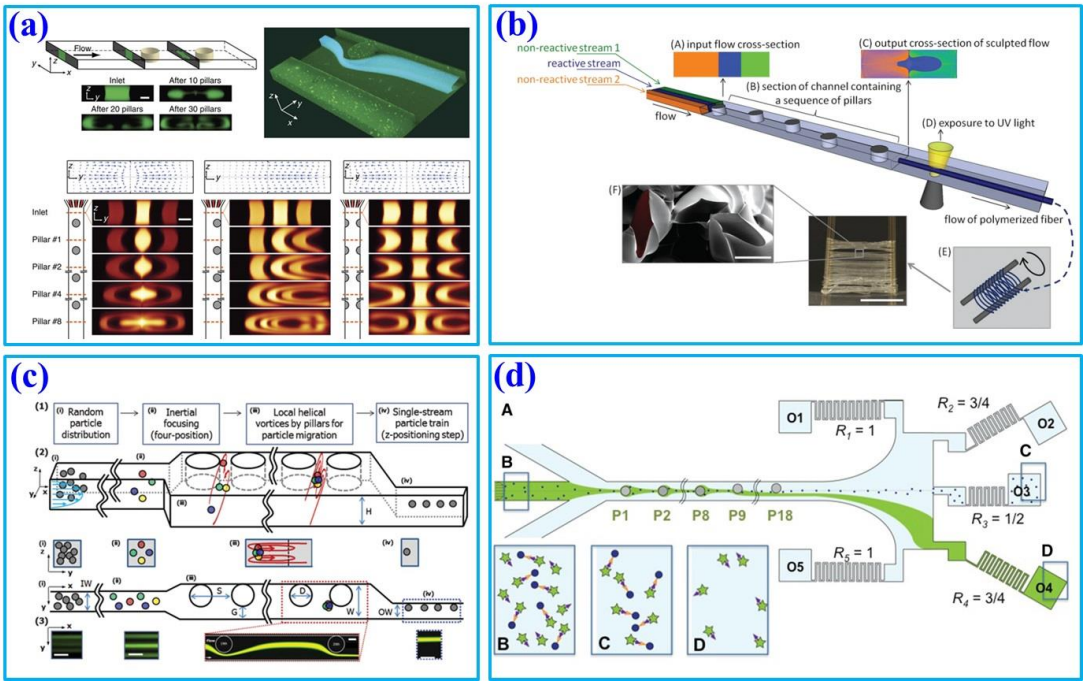

Figure 2–21 (a) Engineering desired inertial flow deformation by programing a sequence of cylindrical pillars within a straight microchannel [168]. (b) Schematic

illustration of synthesis of shaped polymeric microfibers using a programmable inertial microfluidic system [99]. (c) Single stream inertial focusing of microparticles in a straight channel with programmable micropillars. The sequential pillars induce local helical vortices to bring particles to a single focusing equilibrium positions [170]. (d) Exchange of solution around cells or particles by controllable cross-stream translation of fluid in micropillar sequenced microchannel [171].

2.4.4 Serpentine channels

In spiral channel, the curvature is along a single direction, therefore secondary flow can reach steady state after suitable channel length, and almost consistent within different cross-sections. Analysis of particle behaviour can be approximated by the static superposition of inertial lift force field with secondary flow field. This analysis method has been successfully employed in a lot of studies and applications. However, in a serpentine channel with alternating curvatures, it becomes more sophisticated. For example, with alternating curvatures, secondary flow may not approach steady state after each turns, the same with the movement of particles, and accumulation of this unsteady will cause uncertainty and unpredictable behaviour of particles. Analysis of particle behaviour by superposition methodology may cause large errors or even fault prediction.

Di Carlo et al. [95] is among the first to investigate the effects of alternating curvatures on the particle inertial migration. In their study, originally four equilibrium positions in a straight channel with square cross-section were reduced to two in a symmetric serpentine channel due to the symmetry of the system. And above a critical Dean number, focusing was perturbed. Furthermore, in an asymmetric serpentine channel, the number of equilibrium positions could be further reduced to one, focusing again became more complex as Dean number increased, Figure 2-22(a). From their understanding, the balance between inertial lift forces (F_L) and Dean drag force (F_D) determines the preferred location of focusing positions. Dean flow does not create particle focusing, but it acts in superposition with inertial lift forces to reduce the number of equilibrium positions created by the inertial lift forces. If $F_D >> F_L$, then no focusing will be observed, and if $F_D << F_L$, then focusing due to inertial lift forces alone will be observed. The ratio of inertial lift force to

Dean drag was scaled as: $F_L/F_D \sim \frac{2R}{H}(a/H)^3 R_e^n,\ (n < 0)$. This relation expresses that Dean flow will become irrelevant for the limit as *R* approaches infinite (i.e., straight channels), but also suggests a strong third-power dependence on the ratio of particle to channel dimensions. Even at the same Reynolds number, small particles may be still unfocused independent of channel length, because of dominant F_D, while larger particles may quickly become focused. Employment of this mechanism, an inertial filtration device using an asymmetrical serpentine channel was developed and tested [172], Figure 2-22(b). Within the expectation, large particles were well focused and small particles below a threshold remained unfocused and randomly distributed. Therefore, large particles were completely removed from the mixture, leaving behind small particles with a high purity (90%-100%). However, because small particles are still unfocused, plenty of them will enter the reservoirs meant for large particles, leading to undesirable purity of large particles' collection.

Inertial focusing in an asymmetric serpentine channel can produce well-defined particle focusing as well as highly regulated inter-particle spacing, which is very promising in a range of applications, e.g., the flow cytometry system [173], particle active sorting [174], and hydrodynamic stretching of single-cells [38]. Particle inertial focusing may replace the hydrodynamic focusing unit in the standard commercial flow cytometry, composing a compact microfluidic flow cytometry system [173], Figure 2-22(c). Besides, it could also be integrated with ultrafast optical capturing system for automated flow-through single-cell image analysis [175]. For particle sorting, Ozkumur et al. [174, 176] developed a hybrid microfluidic device which combined deterministic lateral displacement (DLD), inertial focusing and magnetophoresis (MP) to isolate rare circulating tumour cells (CTCs) in an antigen–dependent and independent way, Figure 2-22(d). In this device, after the sample of raw blood is introduced into the chip, the blood cells first encounter an array of circular pillars with a specific gap, where DLD size-based hydrodynamic force filtrate smaller red blood cells (RBCs) from white blood cells (WBCs) and CTCs with much larger size. Subsequently, the mixture of WBCs and CTCs flows into an asymmetric serpentine microchannel where they are rapidly focused along a single path by the inertial effects. At the end of the serpentine channel, a strong magnetic field is applied to deflect those cells that are magnetically

labelled. The CTCs can then be collected separately. Benefiting from the initial debulking of RBCs by DLD and its serpentine inertial focusing section, this device allows for a throughput as high as 10^7 cells per second. In addition, ordering particles stream along a specific path in a serpentine channel could be followed by a hydrodynamic stretching from two-sided sheath flows, to characterise the deformability of particles/cells in a single-cell level [39], Figure 2-22(e).

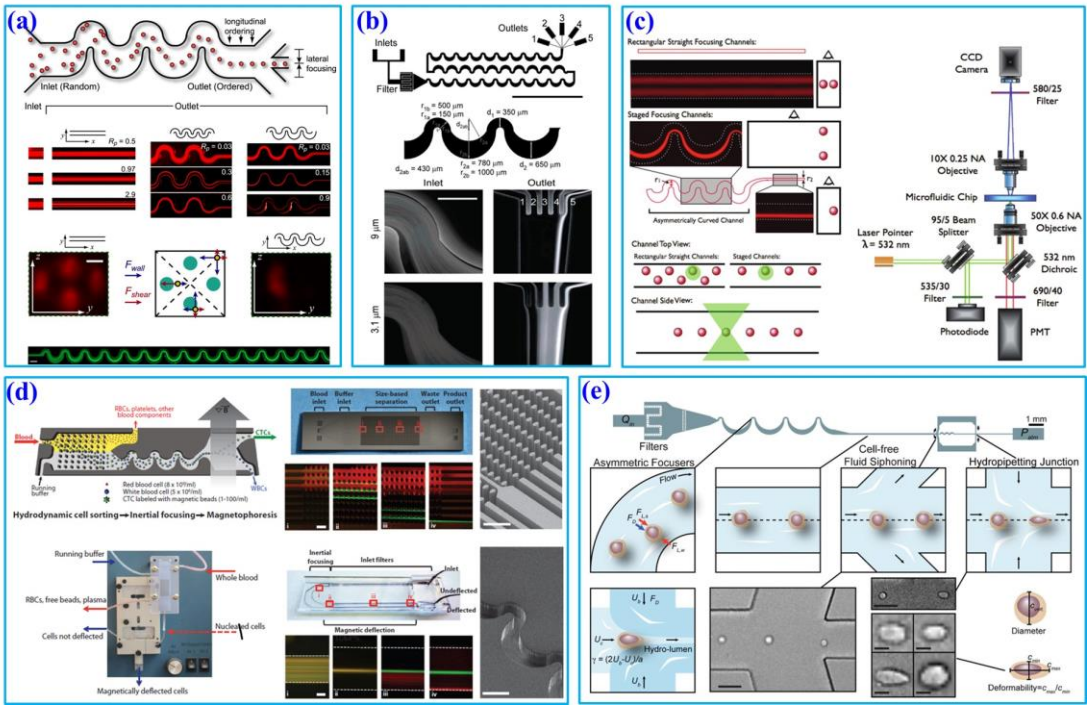

Figure 2–22 (a) Inertial focusing of particles in serpentine microchannel. In a straight channel with square cross-section, focusing of particles into four single streamlines is observed, with each of them facing the centre of each wall. For a symmetric serpentine channel, the symmetry of system reduces focusing to two streams. Above a critical Dean number, focusing is disturbed. In an asymmetric serpentine channel, focusing down to a single stream is observed, and more complex with Dean number increased [95]; (b) Equilibrium filtration by differential inertial focusing in a serpentine channel with 62 asymmetric turns, and 5 outlets. Above a critical size cut-off, particles are well focused as a single stream, while particles below this cut-off size remain unfocused [172]. (c) Schematic of microfluidic flow cytometry system. Combination of asymmetrically serpentine microchannel section with a high aspect ratio straight section provides three dimensional single stream focusing [173]. (d) A hybrid microfluidic device which integrates deterministic lateral displacement

(DLD), inertial focusing in asymmetrical serpentine channel and magnetophoresis (MP) to isolate rare circulating tumour cells (CTCs) in an antigen–dependent and independent way [174]. (e) Deformability cytometry to characterise mechanical morphology of single cells in large population. Inertial focusing of cells in a serpentine channel orders cells along a single stream is followed by the downstream hydrodynamic pinching [39].

2.5 Conclusion

In this chapter, we first briefly review the current manipulation technology for particles in microfluidics, and they can be categorized as passive techniques (mechnical filter, deterministic lateral displacement, hydrophoresis and inertial microfluidics) and active techniques (dielectrophoresis, magnetophoresis and acoustophoresis) according to the origin of dominant forces for the particles manipulation. Second, the physics of inertial migration including the basic fluid dynamics and fundamental dynamics of particle movement are discussed in detail.

Several lateral forces might act on particles in inertial microfluidic device. Viscous drag force, arising from the velocity difference between fluid element and particles, basically retains particles within streamlines of fluid. Lateral forces, such as Magnus force, Saffman force, shear gradient lift force and wall lift force are perpendicular to the main streamlines. They account for the intriguing phenomenon of particle lateral migration. In a wall-bounded Poiseuille flow, Magnus and Saffman force is very small compared with the shear gradient lift force and wall lift force. And the balance of centre-directed wall lift force and wall-directed shear gradient lift force can reasonably explain the experimental observation by Segre and Silberberg. Besides, the particles' property, e.g. deformability, may also influence the lateral migration. It was found that particle deformability can shift inertial focusing positions slightly closer to the channel center. Then, we review the recent progress of the inertial microfluidic technology according to the structure of functional microchannel, including straight, spiral, straight with expansion-contraction or pillar array, and serpentine. There has been intensive investigation on the first three types of inertial microfluidics. Serpentine channels with linear structure can be easily parallelized in a radial or array layout, to amplify the throughput of the system. It also has much shorter footprint than the straight channel, due to the assistance of

secondary flow in the inertial migration. Therefore, it is a very good candidate for ultra-high throughput particle ordering and separation. However, there are still some problems needed to be solved. There is very rare attention on the mechanism of inertial focusing pattern in serpentine channels. The alternation of curvature in serpentine channels brings unpredictable inertial migration phenomenon, which demands further fundamental study in order to provide more rigid inertial microfluidic design guidelines. It was thought that the alternating curvature in symmetric serpentine channel may counter each other, and fail to provide central inertial focusing. This may be not true, which can be seen in the following chapters. In addition, the current inertial separation technique in serpentine channel is actually based on the filtration concept: larger particles are focused well along specific paths, while smaller particles below a critical size still remain unfocused, which will inevitably reduce the purity of large particles collection. In order to develop a separation capability that can be comparable to that in spiral channel, more dedicated efforts are needed to modify the mechanism and design of current serpentine inertial microfluidic system.

3 INERTIAL FOCUSING IN SERPENTINE CHANNELS: SINGLE CENTRAL FOCUSING PATTERN

3.1 Introduction

Previous attention on the inertial focusing in sigmoidal channel was primarily paid on asymmetric serpentine channel, and it was argued that the central inertial focusing in the symmetric serpentine channel cannot be obtained due to the counteraction of secondary flows between the opposing curvatures [67, 95]. It has not been sufficiently examined and reasonably clarified. In this work, we have conducted a series of investigation on the inertial focusing in a symmetric serpentine channel through analytical analysis, numerical simulation and experiments, in order to fill the gap. Basically, three typical focusing patterns are observed in the proposed serpentine channel: i) single focusing streak along the channel centre, ii) two focusing streaks near two sidewalls, similar to the phenomenon in a straight channel, and iii) a transitional focusing pattern between above two distinct patterns. In this chapter, we mainly investigate the mechanism on the first focusing pattern, i.e. single central focusing pattern[1]. In this chapter, experimental examination of different inertial focusing patterns is first presented. Then, the focusing mechanism about the single central focusing pattern is proposed, with some design considerations discussed. A numerical modelling based on the proposed mechanism is conducted, and the numerical results are verified by the experiments. Meanwhile, the effects of the Reynolds number and particle size on the focusing performance are studied. The weightiness of particle centrifugal force on particle focusing are probed and carefully evaluated. Finally, the position and velocity of particles at the outlet are measured by a micro particle image velocimetry (micro-PIV) system, which further verifies the equilibrium positions of particles in the serpentine channels.

3.2 Materials and methods

3.2.1 Design and fabrication of the micro-channel

Figure 3-1 shows the structure of the serpentine channel used in our experiments. The channel consists of a 15.2 mm serpentine section with 15 periods. The depth of

[1] Results of this chapter are published in: [4] Zhang, J., Li, W., Li, M., Alici, G., and Nguyen, N.-T. (2013) Particle inertial focusing and its mechanism in a serpentine microchannel, *Microfluidics and nanofluidics 17*, 305-316.

the channel is uniform at 42 µm. The length and width of each U-turn are both 700 µm. The device was fabricated by standard photolithography and soft lithography techniques. The fabrication includes three main steps: rapid prototyping of a silicon master, Polydimethylsiloxane (PDMS) replica moulding, and sealing through plasma oxidation. Briefly, photoresist (SU-8 2025, MicroChem Corp., Newton, MA) was spun to a thickness of 42 µm on a silicon wafer, and then exposed to UV light through a designed mask using a mask aligner system (ABM, San Jose, CA). After that, the photoresist on the silicon wafer was developed in a SU-8 developer solution and rinsed by isopropylalcohol (IPA) to create a positive replica of channel geometry. PDMS mixture with a 10:1 ratio of base to agent (Dow Corning, Midland, MI) was poured over the silicon master, degassed to remove bubbles in a vacuum oven, and cured at 100°C for 45 mins. After cured, the PDMS slide was removed from the silicon master, and inlet and outlet holes were punched by a custom needle tip. Finally, PDMS slide was bonded with a clean glass slide after exposure to oxygen plasma (PDC-002, Harrick Plasma, Ossining, NY) for 3 mins. The detailed fabricating procedure can be found elsewhere [177].

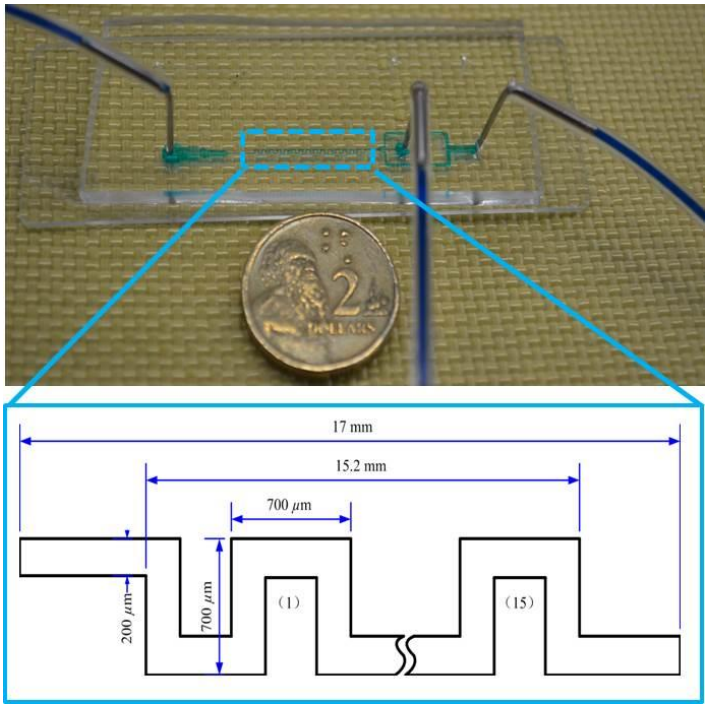

Figure 3–1 The fabricated microfluidic device and illustration of dimension of serpentine channel.

3.2.2 Particle suspension

Internally dyed fluorescent polystyrene particles were purchased from Thermo Fisher Scientific. Particles with a diameter a=8 μm (Product No. 36-3, CV18%), 9.9 μm (Product No. G1000, CV5%) and 13 μm (Product No. 36-4, CV16%) were suspended respectively in deionized (DI) water with 0.1% w/v Tween 20 (SIGMA-ALDRICH Product No. P9416), preventing the particles from aggregation. The weight ratio of particles in the suspension was 0.025%~ 0.1%.

3.2.3 Experimental setup and method

The microfluidic device was placed on an inverted microscope (CKX41, Olympus, Japan), illuminated by a mercury arc lamp. Particle suspension was pumped by a syringe pump (Legato 100, Kd Scientific). The fluorescence images were observed and captured by a CCD camera (Rolera Bolt, Q-imaging, Australia), and then post-processed and analysed using the software Q-Capture Pro 7 (Q-imaging, Australia). The exposure time for each frame was set at 100 ms. The streak width was determined by measuring the distance between points where the intensity profile crossed the 50% threshold. The streak position was taken as the middle of the 50% threshold intensity. Focusing was achieved when the streak width became less than 2 times the diameter of the particles [15]. The experimental setup was schematically shown in Figure 3-2. Besides, a micro-PIV (TSI, USA) system was also used to capture snapshots of fluorescent particles at the outlet, and to evaluate the focusing performance more specifically. The space and speed of the particles at the outlet were obtained by analysing the snapshot pairs.

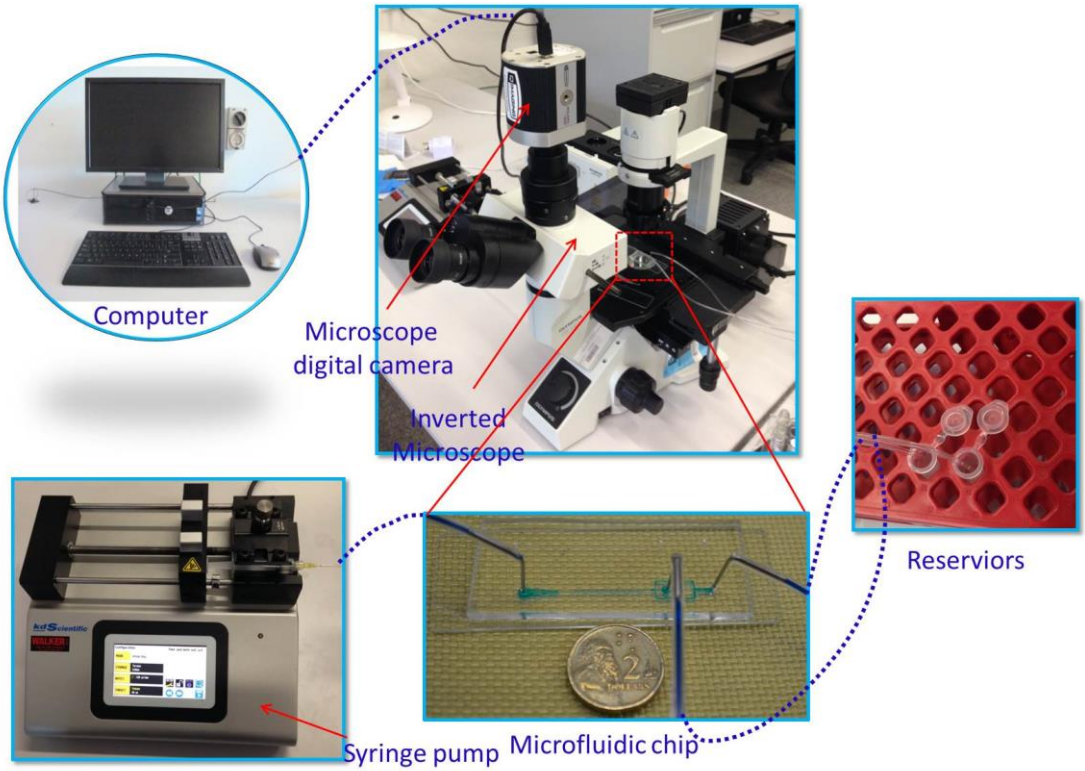

Figure 3–2 Experimental setup for inertial microfluidic device.

3.2.4 Numerical simulation

In order to understand and predict the focusing behaviour of the particles, numerical modelling was used to calculate the flow field and trajectory of the particles in the serpentine channel. A laminar steady incompressible flow model was used to calculate the flow field. A non-slip boundary condition was applied onto the surfaces of the channel, and then the calculated flow field was used to trace the particles with the mass model in COMSOL (Burlington, MA) to predict particle trajectory in the serpentine channel. Equations governing steady incompressible flow are given in equations (2-3) and (2-5).

The governing equation for particles' movement is:

$$m_p \ddot{\vec{X}} = \vec{F}_{drag} \tag{3-1}$$

$$F_{drag} = \frac{\pi}{4} a^2 \rho_f v_t^2 \left(1.84\,\mathrm{Re}'^{-0.31} + 0.293\,\mathrm{Re}'^{0.06}\right)^{3.45} \tag{3-2}$$

$$\mathrm{Re}' = v_t \rho_f a / \mu \tag{3-3}$$

$$v_t = v_f - v_p \tag{3-4}$$

Instead of stokes drag equation, here Khan and Richardson equation is used for calculation of viscous drag F_{drag}, as it has a wider agreement with experimental data compared with stokes drag [103].

3.3 Results and discussion

3.3.1 Particles inertial focusing in symmetric serpentine channels

Pumping 10 μm particles suspension into the proposed serpentine channel, and increasing the flow rate from 100 μl/min to 1000 μl/min gradually, three different particle focusing patterns were observed, Figure 3-3. If the flow condition was below a specific threshold A, particles were focused along the two sides of the channel (region I in Figure 3-3). The distances between the focused streaks and the side walls were both around 38 μm (19% channel width), which was close to the reported inertial equilibrium positions in a straight channel [115, 127, 128], so the observed two-sided focusing pattern was inferred as an inertial lift force dominated phenomenon. When flow condition exceeded level B (region III in Figure 3-3), a single focusing position along the channel centre was achieved. In this region, secondary flow (or Dean) drag was expected to be much stronger than inertial lift forces, and it dominated the migration of particles. It will be explained more in detail within this chapter. When the flow was in the region between A and B (region II in Figure 3-3), a transition phenomenon occurred. The inertial lift force and the secondary flow drag force were of the same order of magnitude, and competed against each other. Particles occupied the space between the two streaks and formed a single but wide streak band. The focused streaks approached the channel centre symmetrically as the flow rate increased, and finally formed a stable single streak, where secondary flow drag force began to dominate the movement of particles.

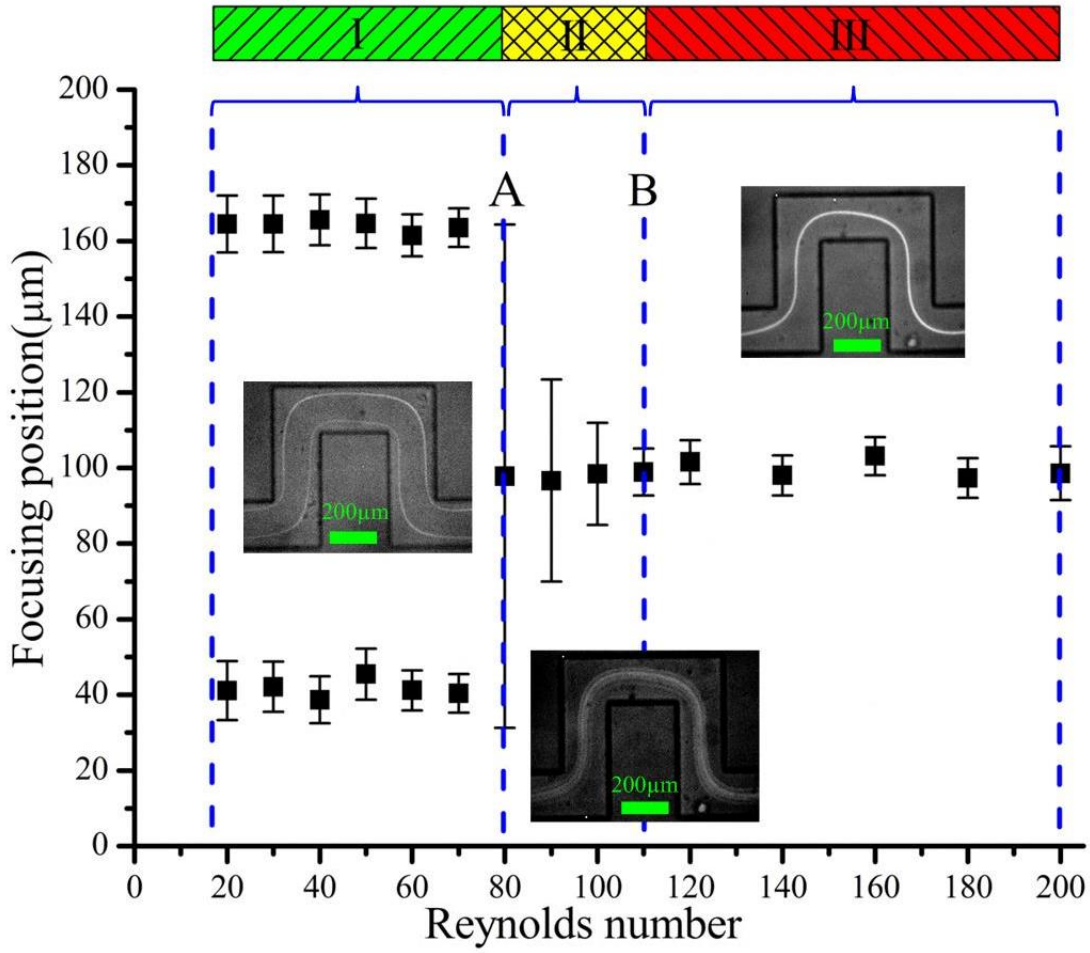

Figure 3–3 Three different particle focusing patterns in a serpentine channel with varying flow conditions, (I) Inertial lift force dominated region with two-sided focusing streaks, (II) transition region with a wide single central focusing band, and (III) Secondary flow dominated region with a single focusing streak at the channel centre. The error bars indicate the width of the focusing streak. Particle diameter is 10 µm.

3.3.2 Focusing mechanism and design considerations

3.3.2.1 Mechanism of single central focusing pattern

Figure 3-4(a) is a schematic view of particles focusing in a serpentine channel. Briefly speaking, particles are deflected into the channel centre after each period, due to the centrifugal force and secondary flow drag with alternating directions. And a final consequence is that particles are focused at the centre of channel after enough periods (top view). More detailed mechanism is discussed in the following.

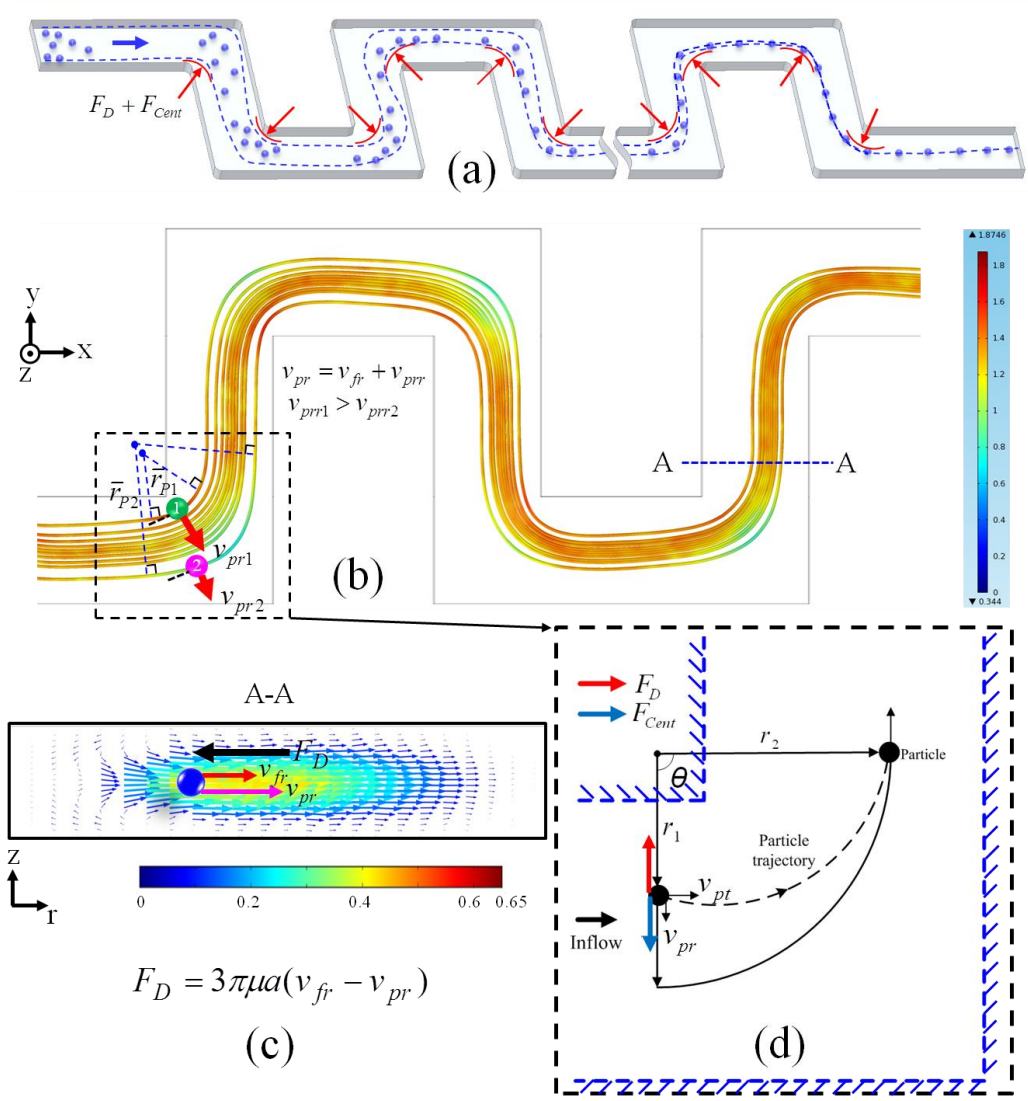

Figure 3–4 Focusing mechanism of particles in a serpentine channel. (a) Schematic view of particles focusing in a serpentine channel. (b) The trajectory and speed of particles in a serpentine channel. The coloured curves are the dynamic trajectory of micro-particles, and the colour legend is the speed of particles. Particle trajectory is obtained and speed by the numerical simulation. (c) The viscous drag F_D in the cross section of the channel. (d) Schematic illustration of centrifugal movement of single particle within one turn.

It is well known that when fluid is flowing in a channel with curvature (e.g. a serpentine channel), two counter-rotating vortices are generated due to the non-uniform inertia of fluid elements within the channel cross section [172]. Particles suspended in a fluid follow the streamlines due to viscous drag. The radial viscous drag F_D can be expressed by Stokes law as:

$$F_D = 3\pi\mu a(v_{fr} - v_{pr}) \tag{3-5}$$

where v_{fr} and v_{pr} are radial velocity of fluid and particles respectively, as shown in Figure 3-4(c).

Additionally, the inertia of particles at the turns causes a centrifugal force F_{Cent} [163, 178].

$$F_{Cent} = (\rho_p - \rho_f)\pi a^3 v_{pt}^2 / 6r \tag{3-6}$$

where ρ_p and v_{pt} are the density and tangential velocity of particles, respectively, and r is the radius of particle orbit.

When the viscous drag F_D acts as a centripetal force to balance the particle centrifugal force F_{Cent} within a turn, the trajectory of the particles will be a perfect circular curve. Unfortunately, the viscous drag F_D in a real situation cannot always balance the centrifugal force F_{Cent} because in the entrance of the turn ($v_{pr}\approx 0$), F_D directs from the inner corner to the outer corner, and the direction of F_{Cent} is determined by the sign of (ρ_p-ρ_f). In our experiments, particles are normally suspended in deionized (DI) water (unless otherwise specifically indicated), and $\rho_p > \rho_f$ (ρ_p=1.05 g/ml, ρ_f=1 g/ml). Therefore, F_D and F_{Cent} are pointing to the same direction, from the inner corner to the outer corner. Thus, the movement of particle within each turn is actually a centrifugal movement. The centrifugal movement of particles within one turn is illustrated schematically in Figure 3-4(d). Particles accelerate along the radial direction towards the outer corner until they finally exceed the fluid radial velocity. At this moment, the viscous drag F_D changes to the opposite direction to compete with the centrifugal force. The particles continue to accelerate until two forces reach the final balance. Reaching this point of balance may take some time, and the particles could possibly have arrived at a new tangential position. This time scale should be very small because particle acceleration is proportional to a^{-2} (10^{12} m/s^2 scale for micro-sized particle). For simplicity, the acceleration process of particles is neglected. The particle radial velocity v_{pr} can then be obtained by the balance of viscous drag F_D and centrifugal force F_{Cent}:

$$v_{pr} = v_{fr} + (\rho_p - \rho_f)a^2 v_{pt}^2 / 18r\mu \tag{3-7}$$

Two components contribute to the particle radial velocity: secondary flow v_{fr} and particle centrifugal force $(\rho_p-\rho_f)a^2v_{pt}^2/18r\mu$. Here, we define a new parameter: particle relative radial velocity v_{prr}, which is the relative velocity of particle and fluid elements along the radial direction. This is the only contribution made by the particle centrifugal force for particle focusing:

$$v_{prr} = v_{pr} - v_{fr} = (\rho_p - \rho_f)a^2 v_{pt}^2 / 18r\mu \tag{3-8}$$

Since the sign of v_{prr} is positive as discussed above, particles migrate across the streamlines from the inner corner to the outer corner with a relative migration velocity of v_{prr} at each turn. Furthermore, the speed of particles in the inner corner is much higher than the outer corner: $v_{pt1}>v_{pt2}$, and the radius of particle orbit in the inner corner is normally smaller than the outer corner: $r_{p1}<r_{p2}$, Figure 3-4(b). According to equation (3-8), the relative migration velocity v_{prr} is always faster at the inner corner than at the outer corner: $v_{prr1}>v_{prr2}$. Moreover, the inner and outer corners switch after each U-turn, with an alternate direction of relative migration velocity v_{prr}. The overall effect is that particles are deflected towards the centre of the channel after each period, and the final result will be a focused streak in the centre of the channel at the outlet. That means the centrifugal force of the particles alone can successfully focus the particles into the centre of the channel, if the density of particles is higher than that of fluid medium. It should be noted that the orbit of the particles in each corner is not a perfect circular curve, so r_{p1} and r_{p2} are actually the average radius of the particles' orbit within each curve section.

The efficiency of focusing can be evaluated by the ratio of the distance that particles move perpendicular to the streamline to the distance along the streamline, and this ratio is equivalent to the ratio of particle velocity perpendicular and parallel to the streamline [145]. For focusing efficiency, the larger is this ratio δ, the better.

$$\delta = \frac{L_r}{L_t} = \frac{v_{pr}}{v_{pt}} = \frac{v_{fr}}{v_{pt}} + \frac{(\rho_p - \rho_f)a^2 v_{pt}}{18r\mu} \tag{3-9}$$

The weightiness of the centrifugal force of the particles on particle focusing can be evaluated by the ratio of v_{prr} to v_{pr}. The larger is this ratio η_{cent}, the more significant is the centrifugal force on particle focusing.

$$\eta_{cent} = \frac{v_{prr}}{v_{pr}} = \frac{1}{18 v_{fr} r\mu / \left(\rho_p - \rho_f\right) a^2 v_{pt}^2 + 1} \tag{3-10}$$

Particles need to migrate transversely half of the channel width w to focus into the centre of the channel, so the minimum arc length of the channel (focusing length) L_{cmin} is:

$$L_{c\min} = \frac{w v_{pt}}{2\varepsilon\left(v_{fr} + \left(\rho_p - \rho_f\right) a^2 v_{pt}^2 / 18 r\mu\right)} \tag{3-11}$$

where ε is the correcting coefficient that takes into account the opposite effects of particle centrifugal force and secondary flow in the reversed turns where the inner and outer corners switch their positions. When particles are moving through the turn where the inner and outer corners switch, previous lateral (radial) displacement toward the centre of the channel (especially for particles in the previous inner corner) will be partially counteracted by the reversed centrifugal force and secondary flow in the new turn. Correction coefficient ε is between 0 and 1, and it should be a function of channel Reynolds number, particle size and channel dimension. When ε=1, it means that the opposite centrifugal force and secondary flow in the alternating turns have no negative effects on particle focusing. When ε=0, focusing effects of centrifugal force and secondary flow have been completely counteracted by their alternating counterparts, and no focusing can be achieved.

In a curved channel, the magnitude of secondary flow is quantified by the Dean number K [140].

$$K = \mathrm{Re}\sqrt{\frac{H}{2R}} \tag{2-40}$$

The velocity of secondary flow U_D can be calculated as [124, 125]:

$$U_D = 1.8\times10^{-4} \times K^{1.63} \tag{2-43}$$

Substituting equations (2-40) and (2-43) to equations (3-9) - (3-11) and assuming v_{fr}=U_D, v_{pt}=U_f and r=R, here U_f is the average fluid velocity, then:

$$\delta = 1.8\times10^{-4}U_f^{0.63}\left(\frac{\rho_f H}{\mu}\sqrt{\frac{H}{2R}}\right)^{1.63} + \frac{(\rho_p-\rho_f)a^2U_f}{18R\mu} \tag{3-12}$$

$$\eta_{cent} = \frac{v_{prr}}{v_{pr}} = \frac{1}{18.42\times10^{-4}\rho_f^{1.63}H^{2.445}R^{0.185}/\left(\rho_p-\rho_f\right)a^2U_f^{0.37}\mu^{0.63}+1} \tag{3-13}$$

$$L_{c\min} = \frac{w}{2\varepsilon\left(1.8\times10^{-4}\times U_f^{0.63}\times\left(\frac{\rho_f H}{\mu}\sqrt{\frac{H}{2R}}\right)^{1.63} + \left(\rho_p-\rho_f\right)a^2U_f/18R\mu\right)} \tag{3-14}$$

When the critical focusing length L_{cmin} was measured by experiments, the correction coefficient ε can be determined by:

$$\varepsilon = \frac{w}{2L_{c\min}\left(1.8\times10^{-4}U_f^{0.63}\left(\frac{\rho_f H}{\mu}\sqrt{\frac{H}{2R}}\right)^{1.63} + \left(\rho_p-\rho_f\right)a^2U_f/18R\mu\right)} \tag{3-15}$$

Based on above analytical analysis, one can determine the length of the serpentine channel to focus particles with certain size *a*, or the correction coefficient if the focusing length is given. It should be noted that the above analytical analysis only considers the effects of particle centrifugal force and secondary flow on the particle focusing process, and the effects of particle inertial migration phenomenon and mixing effects of secondary flow were neglected. In fact, inertial migration may play a significant role for particle focusing, which was even claimed as one of the dominant effects in a curved channel [95]. Inertial migration will become obvious when $a/H>0.07$, and even dominates particle behaviour when the particle Reynolds number R_p is on the order of 1 [95, 124, 140]. Also for the secondary flow, counter-rotating streamlines are prone to mix particles by entraining them within the rotating streamlines. Mixing effects must be inhibited to prevent particles from defocusing. In order to make our assumption valid, some design considerations for the channel structure need to be carefully addressed.

3.3.2.2 Design considerations: suppression of mixing effects of secondary flow and neglect of inertial lift force

Within the secondary flow, a counter-rotating vortex has the role of agitation and perturbation, which is beneficial for mixing [23, 24, 151] and heat transfer [179], but not desirable for particle focusing because it tends to defocus and pull particles along its circulating streamlines. In order to suppress the mixing effect, a micro-channel with a low aspect ratio (*AR*) was suggested [139], which was also verified by our numerical results, Figure 3-5(a). The fluid velocity along *z* (vertical) direction which is responsible for the mixing effect of secondary flow is almost proportional to the *AR* and the input velocity, Figure 3-5(b). For an extremely low aspect ratio channel, the fluid velocity along *z* (vertical) direction is too small to drag particles vertically, so outward and inward streams are impossible to circulate particles in the cross-section. Additionally, the ratio of particle to channel size was crucial for the exhibition of mixing effects. Yoon et al. [139] demonstrated that particles smaller than 27% of the channel height will obtain an inward velocity due to the mixing effects in a curved channel. However, due to the strong suppression on the circulating streamlines in an extremely low aspect ratio channel here, the ratio of particle diameter to channel height can actually be a little smaller than the theoretical value of 27%. In our experiments, we found that this ratio can be as small as 20%.

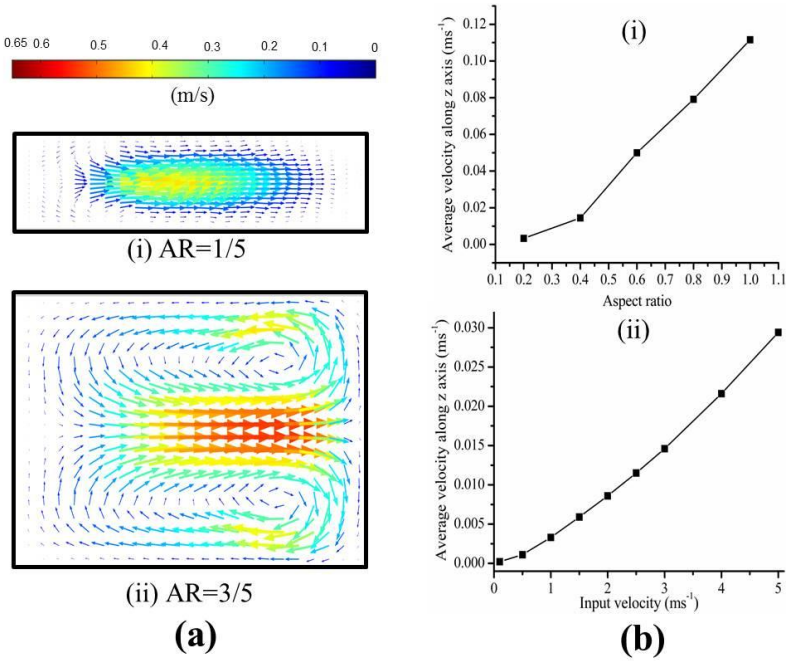

Figure 3–5 (a) The counter-rotating vortex in the cross section of serpentine channel with different aspect ratios (*ARs*), (i) *AR*=1/5 and (ii) *AR*=3/5. (b) The fluid velocity along *z* (vertical) direction is responsible for the mixing effect. Its average magnitude is plotted under (i) zigzag channel with different aspect ratios when input velocity is constant (1 m/s), and (ii) different input velocities when *AR* is set as 1/5. The average velocity along *z* axis is calculated as: $\oiint |v_z| dS/S$, where S is the area of channel cross section, and v_z is fluid velocity along *z* direction.

It is widely accepted that the inertial migration becomes apparent when $a/H>0.07$ and $R_p \sim 1$ [5, 95]. The number and position of the inertial equilibrium position depend mainly on the geometry of the channel. In a straight channel with *AR*=1 as shown in Figure 3-6(a), there are four equilibrium positions, facing the centre of each channel surface [5]. When *AR* is between 1/3 and 1/2, Figure 3-6(b), the equilibrium positions are reduced to two, due to the blunted velocity profile along the long face of the channel and corresponding reduction of shear gradient lift force [127]. However, by lowering the aspect ratio of the channel to 1/5, as the inertial lift force is very weak along the long face, it is hard to observe very distinct equilibrium positions, Figure 3-6(c). In our experiments the maximum ratio of particle diameter to channel width was 0.065, which is still less than 0.07. Therefore, inertial migration along the long face can be neglected, which is not expected to cause significant errors in the analysis of single central focusing pattern. The correction factor ε in equation (3-14) may also include the errors caused by the effects of inertial lift forces in the inertial migration. In the next section, numerical simulation without the consideration of inertial lift force was conducted. The numerical results were then verified by experimental ones, which further indicated that the above analysis and approximation were reasonable.

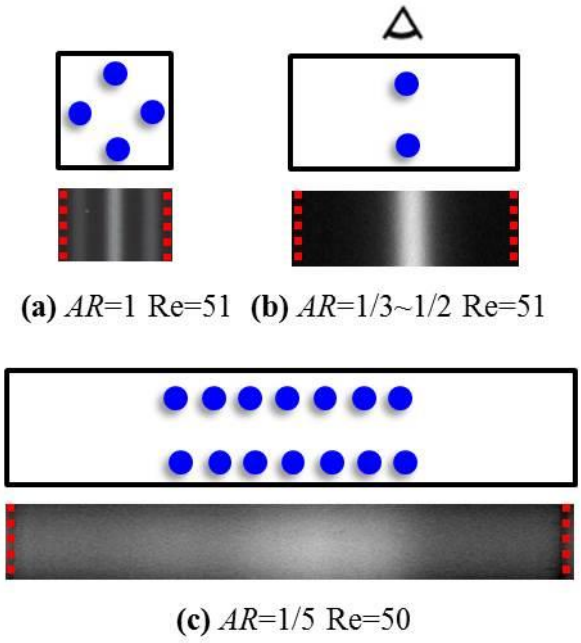

Figure 3–6 Particle equilibrium positions by inertial migration in a straight channel with different aspect ratios (*AR*s). (a) Four equilibrium positions when *AR*=1 [5]. (b) Two equilibrium positions when *AR*=1/3~1/2 [9]. (c) No distinct equilibrium positions along the long face when *AR*=1/5.

3.3.3 Validation of focusing concept and determination of correction coefficient ε

Figure 3-7(a~c) illustrated trajectory of particles in a serpentine microchannel obtained from numerical simulation, and its corresponding streak images from experiments. It can be seen that the simulation results agreed very well with the experimental ones. The randomly dispersed particles at the inlet shifted into the centre of the channel after each turn and the width of their streak decreased continuously, and finally they focused at the centre of channel at the outlet. It indicates that the proposed focusing mechanism which only takes account of particle inertia and secondary flow drag is reasonable. Although inertial lift force is still present in the actual situation, its effect is negligible compared with other two effects.

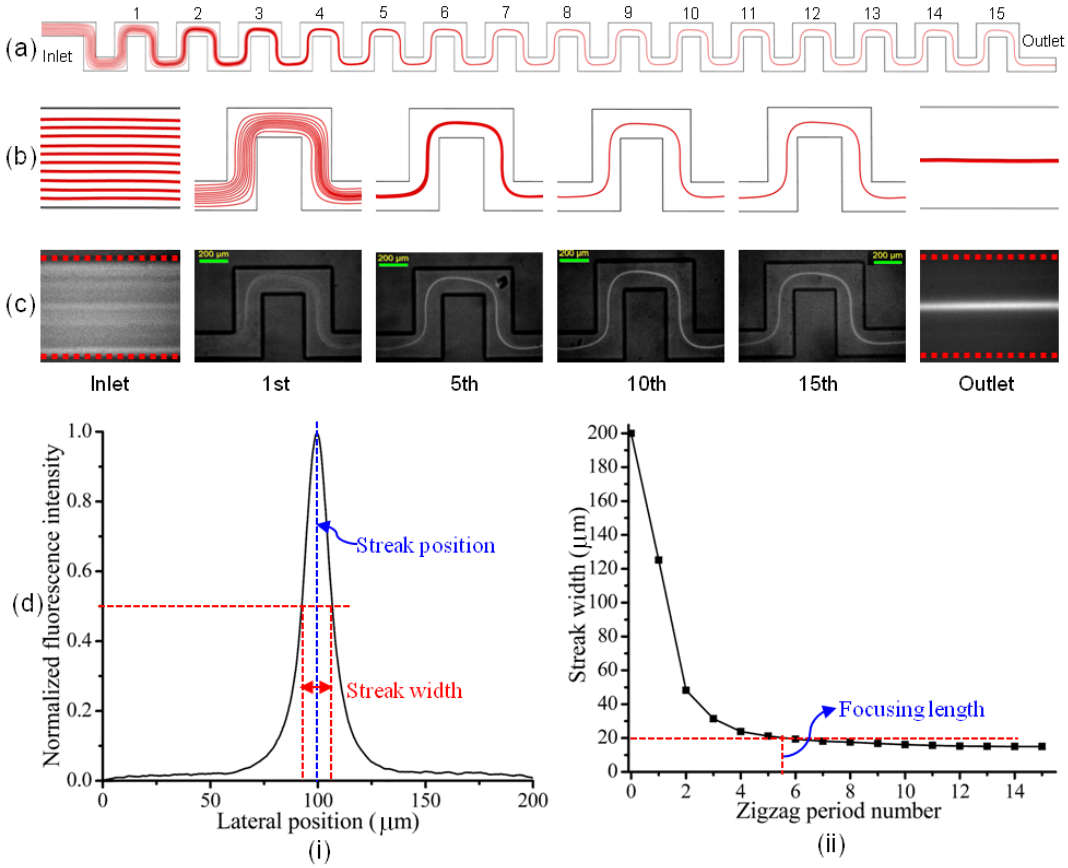

Figure 3–7 (a) The overview of particles focusing in a serpentine channel. (b) The numerical results of particles' trajectory at the inlet, typical zigzag periods and outlet of a serpentine channel. (c) The experimental streak images of fluorescent particles in the corresponding positions of the serpentine channel. (d) Particle streak width and position. (i) Determination of particle streak width and streak position from fluorescence intensity profile. (ii) Particle streak width under different numbers of zigzag turns. The input fluid average velocity is 1.1 m/s, corresponding to the Reynolds number of 110. Particle diameter is 9.9 μm.

The width of the focused particle streak under different numbers of zigzag periods was plotted in Figure 3-7(d). The width was determined by measuring the distance between two points where the intensity profile crossed the 50% threshold. The streak position was taken as the middle of the 50% threshold intensity, Figure 3-7d(i). The width of the particle streak decreased rapidly and particle focusing was achieved after the fifth zigzag period, Figure 3-7d(ii), with an arc length (focusing length) of about 11 mm when the channel Reynolds number was 110. In our experiments, best focusing happened when the channel Reynolds number was 160

and focusing length was only 3.75 mm. This focusing length is much shorter than the most of the focusing lengths reported in the literature, and it even reached the level of state-of-the-art asymmetric curving channels [95]. The mean and standard deviation of the lateral positions of particle streak were determined by fitting the counts to a Gaussian distribution, and the particle streak lateral position was 99.0±0.97 μm, perfectly within the centre of the channel. Furthermore, compared with the asymmetric curving channel reported previously, our serpentine channel is much simpler because the radii of a larger curvature and a smaller curvature are different in an asymmetric curving channel and must be determined respectively, whereas only one parameter needs to be selected in a symmetric serpentine channel here.

The correction coefficient ε in equations (3-11) and (3-14) was calculated under several typical Reynolds numbers in the experiments. When the Reynolds numbers 110, 120, 140, and 160, they correspond to a focusing length of about 10.8 mm, 6.75 mm, 4.75 mm, and 3.75 mm, respectively. According to equation (3-18), ε=0.258, 0.388, 0.504 and 0.578 respectively. The correction coefficient ε increases with an increasing channel Reynolds number because of the fast mainstream velocity of fluid at high Reynolds numbers, and there is less chance for opposite centrifugal force and secondary flow drag to deflect particles into two side walls in the alternating turns.

3.3.4 Effects of the Reynolds number

From equation (3-12), the focusing efficiency is proportional to the input fluid velocity (or Reynolds number). In the experimental validation, the width of the particle streak was measured at the outlet under various flow conditions, and the results were shown in Figure 3-8. The width of the streak decreases sharply with increasing Reynolds number, and after a critical value (defined as critical Reynolds number for particle focusing Re_C), complete focusing was achieved. The available working area on the Re-a space for particle focusing can be obtained. It is noted that this critical value was different for various particle sizes. This difference can be used to characterise the effects of particle size on focusing performance.

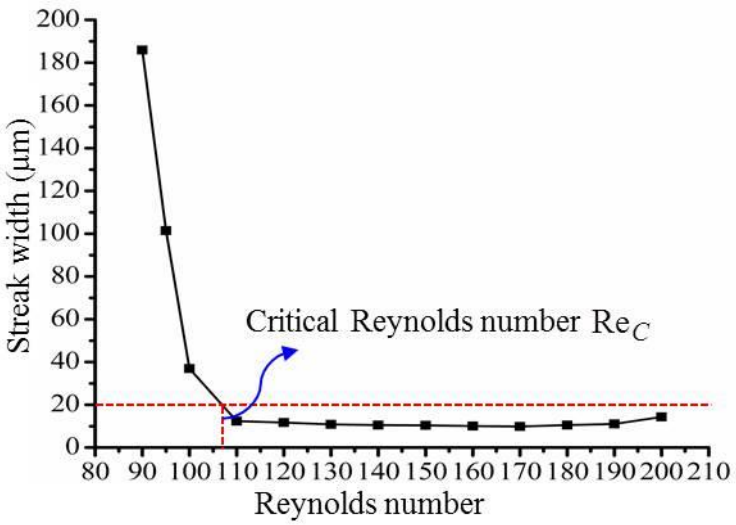

Figure 3–8 The particle streak width under different flow conditions (Reynolds number).

To evaluate particle focusing more specifically, a micro-PIV system was used to capture snapshot images of fluorescent particles at the end of the last zigzag period, and the results were compared with the images of particle streaks observed from the fluorescence microscope, Figure 3-9. Particles are distributed within the streak and migrate into the centre when the Reynolds number increases. This agrees well with the results from the streak images. However, when the channel Reynolds number exceeds the critical value for particle focusing, it is hard to evaluate the particle focusing more specifically by fluorescence streak image, such as particle space, particle speed, or the deflection of certain particles within the particle chain. A Micro-PIV system or high speed camera system (such as Photron SA-3, United Kingdom [125], and Phantom v7.3, Vision Research, Inc [180]) could be more effective to analyse particle focusing in a more detailed manner.

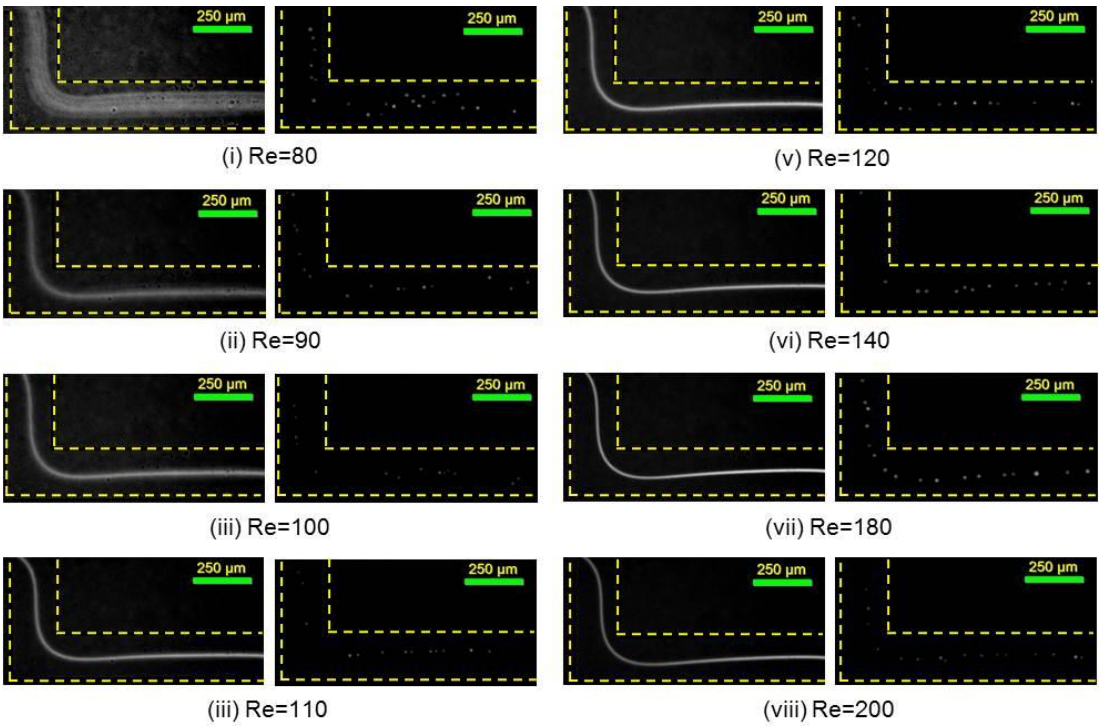

Figure 3–9 Particle streak images observed from fluorescence microscope (left) and particles snapshot image obtained from micro-PIV system (right) under different flow conditions.

3.3.5 Effects of particle size and particle inertia

Equations (3-11) and (3-14) indicate that particles with a larger diameter can achieve focusing within a shorter arc length (focusing length) when the input flow condition (Reynolds number Re) is constant, but determining the critical arc length for focusing under each flow condition is not easy. In practice, it is more important to know the available working area for particle focusing in a specific microfluidic device rather than the position where focusing occurs. Therefore, instead of a critical arc length for focusing, the critical Reynolds number Re_C (Figure 3-8) was used to evaluate the effects of particle size on focusing efficiency. Larger particles are expected to achieve focusing at a lower Reynolds number within the same arc length, which was verified by the experimental results in Figure 3-10. It also shows that larger particles can achieve focusing in a much wider available working area than smaller particles. The data is limited within the Reynolds number of 200, which corresponds to a flow rate of 1 ml/min (fluid average linear velocity 2 m/s). The reasons why the experiments stop at this flow rate are (i) sealing failure and liquid

leakage could happen when the flow rate is too large, and because the pressure within the microfluidic chip is too high, and (ii) the counter-rotating secondary flow is becoming strong enough to begin to mix and defocus particles.

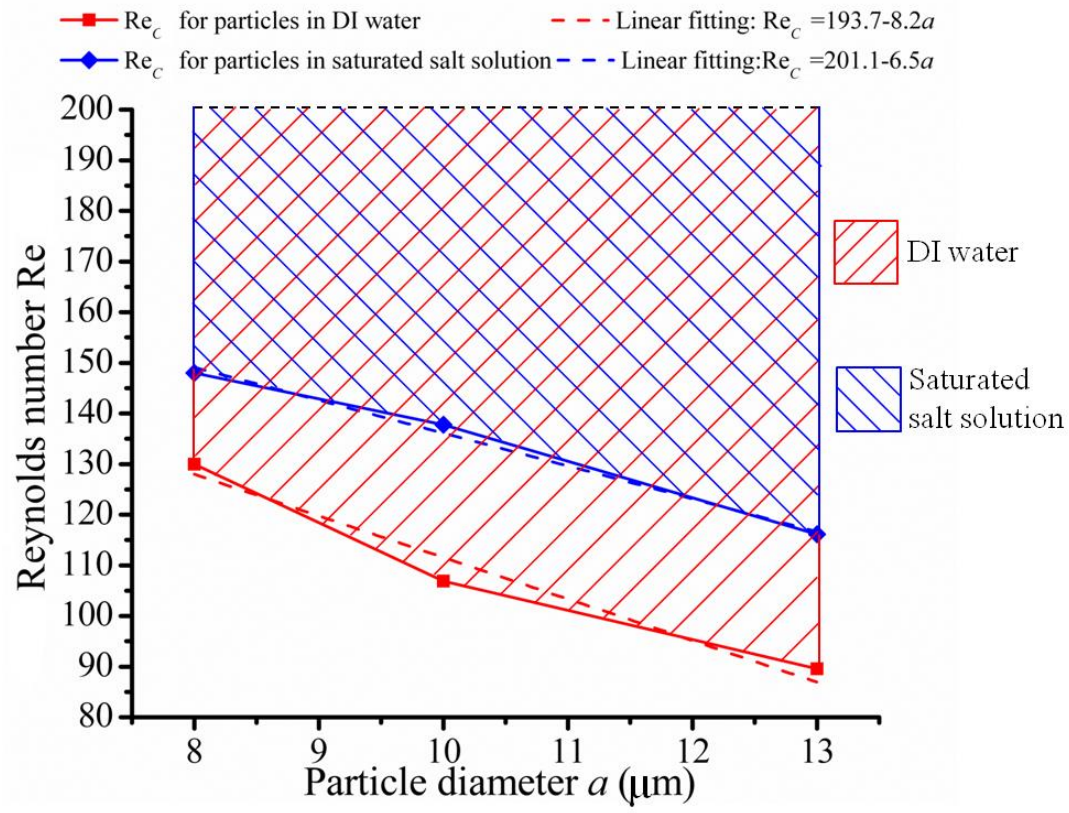

Figure 3–10 The effects of particle size and solution density on the critical Reynolds number for particle focusing.

In addition, 8 μm, 10 μm, and 13 μm particles were respectively prepared in a saturated salt solution (ρ=1.20 g/ml), and then used to study the effects of solution density on particle focusing. As known from equation (3-6), the centrifugal force of the particles will change to the opposite direction when particles are not as dense as the solution. If the centrifugal force of the particles is stronger than the secondary flow drag, particle focusing will disappear, but particle focusing still can be observed in our experiments. This observation indicates that secondary flow is much more important than particle centrifugal force in the particle focusing process. However, unlike the previous description that particle focusing is independent of solution density (particle centrifugal force) [95, 181], particle centrifugal force actually has a distinguishable impact on particle focusing, although it may be not a dominant effect.

The critical Reynolds number for these particles in a saturated salt water solution is much higher than its corresponding value in a solution of DI water, meaning that the opposing centrifugal force can actually hinder particle focusing and decreases its available working area.

More specifically, the contribution of particle centrifugal force on particle focusing can be evaluated by η_{cent}, as discussed above. For 10 μm polystyrene particles in DI water, when Re=110~200, η_{cent}=3.4% ~4.2%, but for particles with a higher density (such as silica or metal), the weight of particle centrifugal force will be much higher. Taking a silica (SiO_2) particle for example, ρ_{silica}=2.65 g/ml, with other parameters the same as the polystyrene particle suspension, the weight of particle centrifugal force on particle focusing can be as high as η_{cent}=53.7% ~59.1%. So the effect of solution density and particle centrifugal force needs to be evaluated carefully in the applications that the density difference between particle and medium is very obvious. In the application of cell manipulation, the density of cells is very close to that of its medium, so the influence of particle inertia is negligible to some extent. Therefore, that's why we defined this single central inertial focusing pattern as secondary flow dominated focusing pattern for simplicity.

3.3.6 Position and velocity of particles at the outlet

A micro-PIV system was used to evaluate particle focusing more specifically because particle position and particle velocity are additional important information that can be used to characterise the quality of particle focusing. The results were plotted in Figure 3-11. Particles were focused at the centre of the channel at the outlet, and the longitudinal position of the particles was not perfectly uniform, as expected in the real situations, with some particles deflecting from the particle chain. This may be due to the large deviation of particle size (CV16%). Also the particles were not uniform in the suspension in practice because their density was slightly more than the solution density (DI water), and they were gradually settling down in the container and the micro-channel. It was also found that particle space is generally independent of the flow conditions.

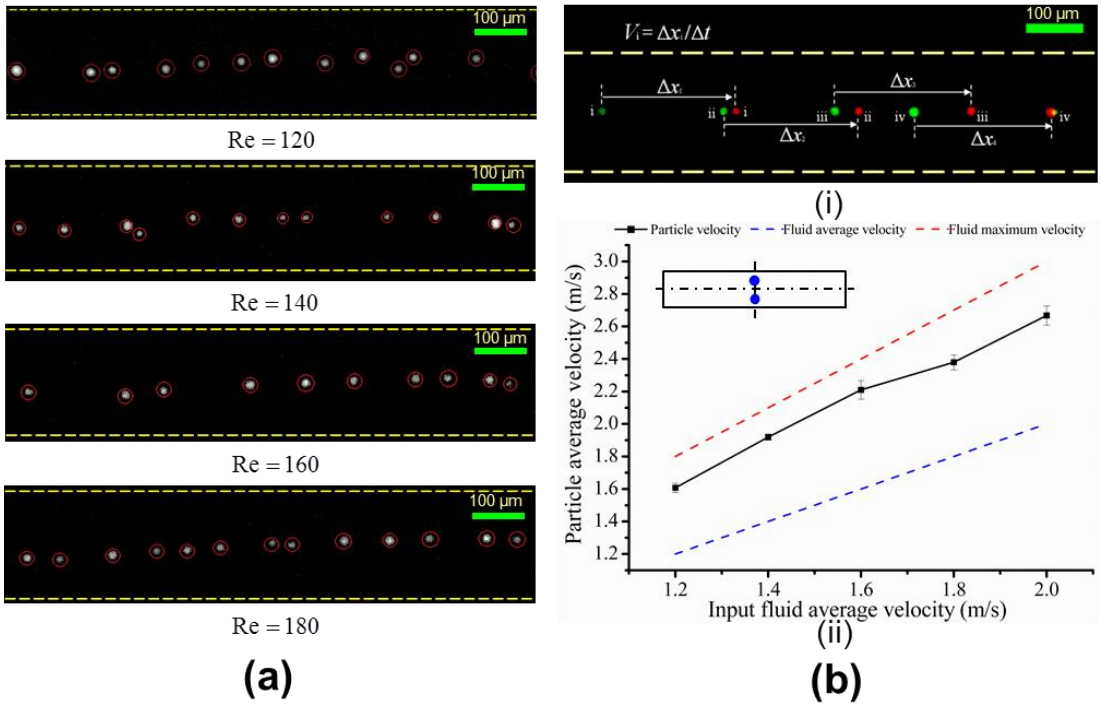

Figure 3–11 (a) Particle longitudinal space under different flow conditions. Particles are highlighted with red circle. (b) The particle velocity at the outlet. (i) Particle velocity is calculated as particle displacement divided by residence time Δt (100 μs). Particle positions at two moments are superposed with two different colours. Green symbol is particles at the initial moment, and red symbol is particle position after Δt. (ii) Particle average velocity with respect to input fluid velocity. Particle average velocity is calculated as: $\left(\sum_{i=1}^{n}\Delta x_i/\Delta t\right)\!/n$. Two blue dots are schematic position of particles within channel cross-section at the outlet. Fluid maximum velocity is calculated as U_m=1.5U_f [95].

Besides, the velocity of the particles was calculated as their displacement divided by their residence time, and its average value was plotted against the input fluid velocity, Figure 3-11(b). Particle velocity increased almost linearly with the average input fluid velocity. This value was greater than the average fluid velocity (blue dashed line), but less than the maximum velocity of the fluid (red dashed line). This is because the particles were focused at the centre of the channel along the long face where the fluid velocity was maximum, while along the short face (or height direction), due to strong shear-gradient induced lift force, the particles were actually focused half way between the axis of the channel and the top/bottom surface,

postulated as two blue dots in Figure 3-11b(ii), which agreed well with our prediction. Although our proposed serpentine channel can only focus particles in 2-D manner (a single focusing streak from top view), focusing particles in 3-D can easily be implemented after proper adjustment, such as (i) reducing channel height to less than 2 times of particle diameter so that only one particles can occupy short face or (ii) placing several grooves on the bottom of serpentine channel at the outlet to induce rotating flows to focus particles in 3D [127].

3.4 Conclusion

In this chapter, three distinct focusing patterns in a symmetric serpentine microchannel were first experimentally observed. And this chapter mainly investigated the mechanism of the single central focusing pattern: secondary flow dominated focusing pattern. Instead of previous mechanism utilizing the balance of secondary flow and inertial lift force, this chapter presented a new mechanism which only took into account secondary flow drag and particle centrifugal force to explain inertial focusing process. The focusing mechanism and design considerations were proposed, which provided useful guidelines for the design of curved channel for particle focusing. Numerical modelling based on the proposed focusing concept was conducted, and the results agreed quite well with experimental ones. An extremely low aspect ratio (1/5) channel was used to suppress the mixing effects of counter-rotating secondary flows, as well as keeping its positive effects for particles focusing in a serpentine channel. Effective particle focusing at the centre of a symmetric serpentine channel was available at a wide range of flow conditions. The effect of particle centrifugal force on the particle focusing was also evaluated. We found that particle centrifugal force could play a significant role on particle focusing in the applications where the density difference between particle and medium is significant. Focusing can be obtained within a very short length, with the significant advantage of lower fluidic resistance. In conclusion, this study not only extended our understanding about the mechanism of particle inertial focusing process in a curving channel, but also provided a simple focusing unit which can potentially be applied for particle filtration or in flow cytometry.

4 INERTIAL FOCUSING IN SERPENTINE CHANNELS: TWO-SIDED FOCUSING PATTERN AND ITS APPLICATION ON PLASMA EXTRACTION

4.1 Introduction

Plasma is a host of various analytes such as proteins, metabolites, circulating nucleic acids (CNAs), pathogens etc. The plasma needs to be cell-free for the effective detection of these analytes. The key process of plasma extraction is to eliminate the contamination from blood cells (erythrocytes, leukocytes and platelets) [182]. In human whole blood, blood plasma is a straw-coloured liquid component, which normally makes up about 55% of the whole blood volume. Although conventional methods including macroscale centrifugation and membrane filtration can provide efficient removal of blood cells, they are still facing some limitations. For example, centrifugation is generally labour-intensive, time consuming and even dangerous to some extent (containing high speed rotating components), and needs to be operated by well-trained staff. Membrane filtration suffers the problem of severe clogging due to the finite filtration capacity, and frequent rinse is lab-intensive and undesirable [183].

Inertial microfluidics is a promising technique due to its nature of high throughput, simple design and easy fabrication [5]. Inertial microfluidic device with serpentine channel is a promising candidates for plasma extraction, due to the linear structure (easy parallelization for amplify throughput), short footprint, and low resistance. In chapter 3, three different inertial focusing patterns were experimentally observed. The mechanism and characteristics of first focusing pattern: single focusing streak at the centre of a serpentine channel, were investigated [4]. In this chapter, the two-sided focusing pattern where two particle streaks form near the two sidewalls at a relatively low flow rate will be studied. Moreover, the application of this two-sided focusing pattern on the extraction of blood plasma will be demonstrated [2].

This chapter is organized as follows. First, the inertial focusing in straight channel with different aspect ratios was investigated; Then, serpentine channel with a

[2] Results of this chapter are published in: [184] Zhang, J., Yan, S., Li, W., Alici, G., and Nguyen, N.-T. (2014) High throughput extraction of plasma using a secondary flow-aided inertial microfluidic device, *RSC Advances 4*, 33149-33159.

low aspect ratio (*AR*=0.21) was selected to demonstrate the enhancement of secondary flow on the inertial focusing process, and mechanism of this enhancement was studied; Third, the effects of particle size on the performance of focusing and filtration were investigated. Subsequently, extraction of plasma in the serpentine channel was demonstrated with excellent plasma purity and high collection yield achieved. And the effects of cell concentration (haematocrit) on the inertial filtration were also studied. Finally, the parallelization technology for the serpentine channel was introduced and demonstrated, with some design considerations discussed.

4.2 Materials and methods

4.2.1 Design and fabrication

The serpentine channel used in our experiments consists of a 15.2 mm serpentine section with 15 zigzag periods. The depth of the channel is uniform at 42 μm. The length and width of each U-turn are both 700 μm. The width of micro-channel is 200 μm. A trifurcating outlet at the end of the channel is implemented at the end of serpentine channel. The two-sided symmetrical bifurcations are combined together as a single outlet to simplify collection. In order to investigate the effects of channel aspect ratio and dimension on the inertial focusing, straight micro-channels with different cross-sections of 50 μm×42 μm (width × depth), 100 μm×42 μm and 200 μm×42 μm were fabricated respectively. All devices were fabricated by standard photolithography and PDMS soft lithography techniques.

4.2.2 Particle and cell preparation

Internally dyed fluorescent polystyrene particles with diameters of 3 μm (Thermo Fisher Scientific, Product No. R0300, CV5%), 5 μm (Product No. G0500, CV5%) and 10 μm (Product No. G1000, CV5%) were suspended respectively in deionized (DI) water with 0.025% w/w. Tween 20 (SIGMA-ALDRICH Product No. P9416) with 0.1% w/v was added to prevent the particles from aggregation. These beads were used as a preliminary and simple model of blood cells, as they have similar dimensions and densities ($\rho_{\text{polystyrene beads}}$=1.05 g cm^{-3}, 1.04<$\rho_{\text{blood cells}}$<1.09g cm^{-3}), but they cannot reflect the ellipsoid geometry and deformability of red blood cells [172]. The human whole blood was taken from healthy adult male volunteers with a vacutainer tube (Vacuette) containing anticoagulant agent lithium heparin. The blood

sample was diluted with phosphate-buffered saline (PBS) by 1/5 ~ 1/20 before pumped into the microfluidic device.

4.3 Results and discussion

4.3.1 Inertial focusing in straight channels

Inertial migration becomes apparent when a/H>0.07 and R_p ~ 1 [95]. The number and position of the particle inertial equilibrium position depend mainly on the geometry of the channel and flow Reynolds number. In a straight channel with an aspect ratio (*AR*=height/width) ~1 as shown in Figure 4-1(a), there are four equilibrium positions, facing the centre of each channel surface. Increasing the channel width with the channel thickness constant, when *AR* is between 1/3 and 1/2, the equilibrium positions are reduced to two, due to the blunted velocity profile along the channel width and corresponding reduction in shear gradient lift force [127]. Two equilibrium positions are located at the centre of channel width, facing the top and bottom walls, Figure 4-1(b). In addition, when inertial focusing has been achieved completely, the inertial equilibrium positions (fluorescent streaks) are almost steady with varying Reynolds numbers in the tested area.

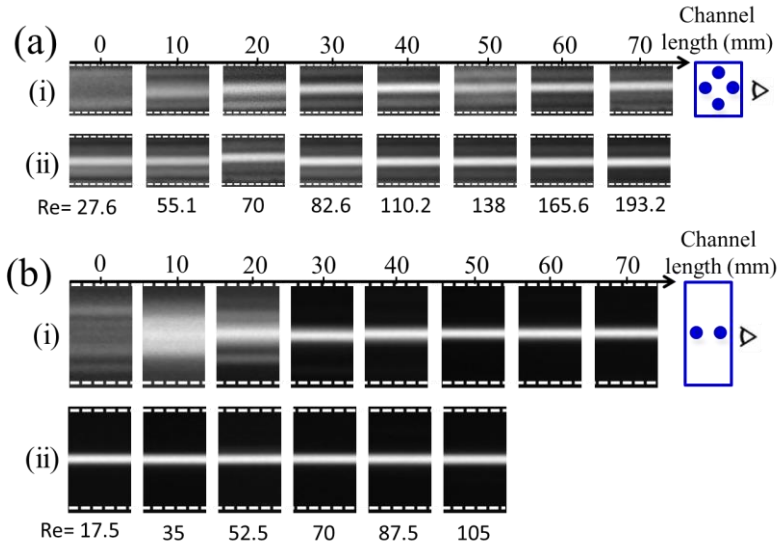

Figure 4–1 Inertial focusing phenomenon in a straight channel with cross sections of (width × height) of (a) 50 μm×42 μm, *AR*=0.84; (b) 100 μm×42 μm, *AR*=0.42.

However, when the *AR* is reduced to 1/5, as the inertial lift force is very weak along channel width, it is hard to observe distinct equilibrium positions, and a wide particle streak band is on the central area of channel, Figure 4-2.

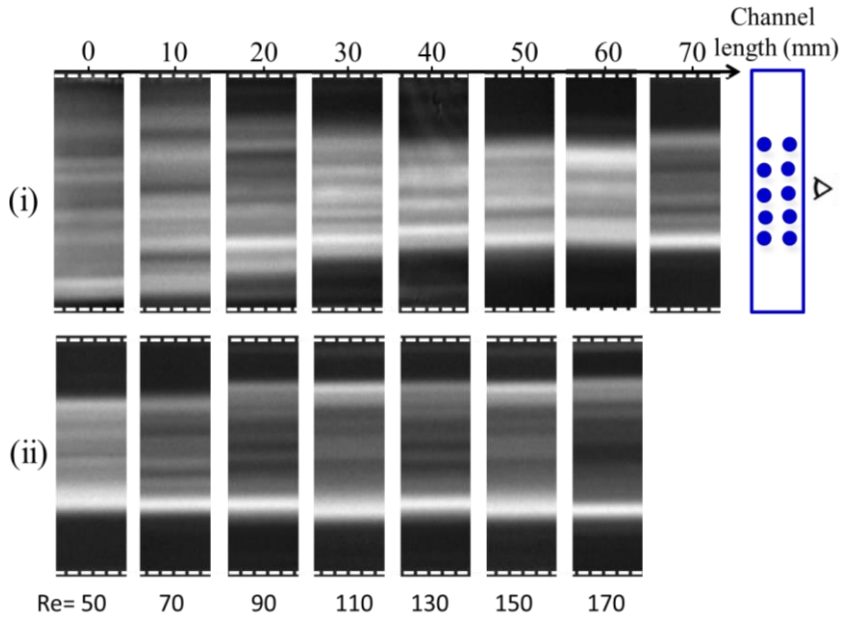

Figure 4–2 Inertial focusing phenomenon in a straight channel with cross sections of (width × height) of 200 μm×42 μm, *AR*=0.21.

According to equation (2-42), for the straight channel with a cross-section of 200 μm×42 μm, under an average flow velocity of 0.7 m/s (Re=70), the theoretical minimum channel length for 10-μm particles to migrate to their equilibrium positions is about 70 mm. However, it still cannot obtain decent focusing after 70 mm in the experiments. The main reason for this inconsistency is that the size ratio of particle to channel a/w=0.05 does not meet the minimum requirement of 0.07 [95]. This may also be explained by the shape of velocity profile along the channel width. With the decreasing aspect ratio, velocity distribution along the width becomes increasingly flat, Figure 4-3(a). In the channel with *AR*=0.21 (200 μm×42 μm), the fluid shear rate γ ($=du/dx$) is very small (~0) along a large central area ($-0.3w \le x \le 0.3w$). As the inertial lift force F_L is proportional to γ^2 [91], it is very small within this central area in this small *AR* channel, causing very slow even no inertial migration speed of particles along the width direction. Therefore, a lot of particles still occupy the channel central area even after 70 mm in the channel with *AR*=0.21, Figure 4-2. While along the depth direction, the velocity profile maintains as parabolic shape,

although the maximum magnitude of velocity shows a slightly decreasing trend with the aspect ratio, as shown in Figure 4-3(b). So it is expected that two equilibrium positions along depth direction due to the inertial lift forces still exist.

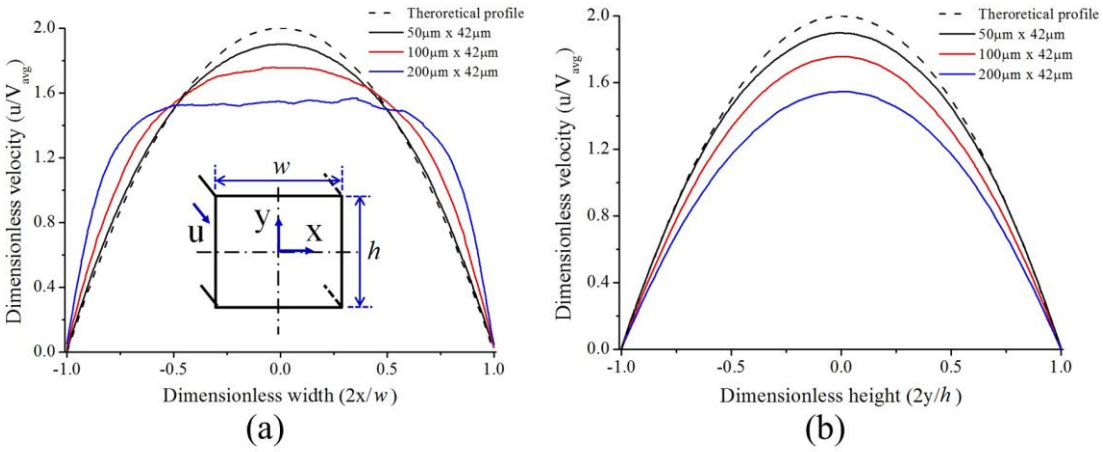

Figure 4–3 (a) Fluid velocity profiles along the channel width for straight channels with different cross-sections. Velocity distribution is evaluated along the central plane $y = 0$. (b) Velocity profiles along the channel depth for straight channels with different cross-sections. Velocity distribution is evaluated along the central plane $x = 0$. Velocity is normalized by input average velocity V_{avg}.

4.3.2 Secondary flow aided inertial focusing in serpentine channels

In order to demonstrate the enhancement of curvature on inertial focusing, the cross-section dimension of serpentine channel was set to 200 μm×42 μm, where even 10-μm particles cannot achieve adequate focusing in a straight channel with this cross-section as we demonstrated above, let alone smaller particles.

When the particles were pumped into the serpentine micro-channel, they randomly distributed at the inlet, represented by four different coloured particles in Figure 4-4(a), occupying four characteristic positions within micro-channel: two (purple and green dots) are near wall regions where the net inertial lift force is directing towards channel centre, and another two (red and blue dots) are near channel centre where inertial lift force is pointing to channel walls. Due to the large secondary flow drag and centrifugal force in the alternating turns, as well as the same effect of inertial lift force, Figure 4-4(b), the particles near channel sidewalls (purple and green dots) rapidly migrate to the final equilibrium positions. While for the

particles within the channel central area (red and blue dots), the direction of secondary flow drag varies along streamlines, in some positions it assists inertial lift force to accelerate particles to the equilibrium positions, in other positions it competes against inertial lift force to disturb particles from their equilibrium positions. Within the region of two sided inertial focusing pattern, although the secondary flow drag is larger than the inertial lift force within the central area where shear rate $\gamma \approx 0$, near the inertial equilibrium positions (near-wall regions), the inertial lift force can still dominate the secondary flow due to the large shear rate γ. The final effect is that the secondary flow is sweeping particles towards two sidewalls, facilitating migration of particles towards the inertial equilibrium positions. However, in the straight channel without the assistance of secondary flow, particles cannot reach the inertial equilibrium positions due to the very weak inertial lift force alone within the central area, Figure 4-2. This is the reason why the introduction of curvature can promote the particle inertial migration and focusing. It should be noted that the above analysis is based on the assumption that final equilibrium positions are the theoretical inertial equilibrium positions in a Poiseuille flow: 0.3 times diameter from channel centre. In the actual situation, the final trajectory of particles is a little different due to the rectangular cross-section and channel curvature, as shown in Figure 4-4(c). Figure 4-4(d) shows the fluorescent trajectory of 10 μm particles under different periods within a serpentine channel. Fluorescent light near channel sidewalls disappears promptly after about three periods, while fluorescent light within channel central area weakens gradually and vanishes after more than ten periods. This indicates that the particles near two-sided walls migrate much faster to the equilibrium positions than their counterparts near the channel centre, which again validates above analysis.

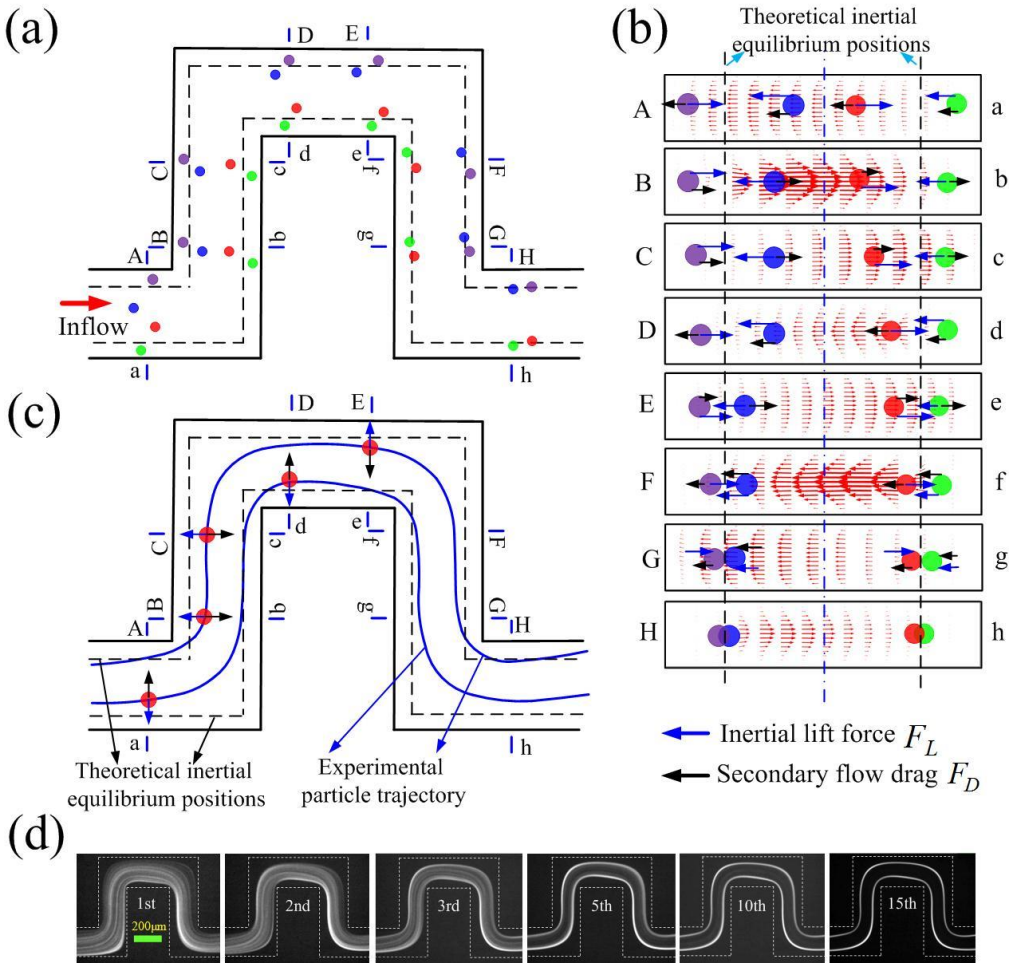

Figure 4–4 (a) Schematic illustration of particle inertial focusing process in a serpentine channel. (b) Dynamic analysis of particles within eight typical cross-sections under the influence of secondary flow. (c) The theoretical inertial equilibrium positions and the experimental particle trajectory. (d) The fluorescent images of particle trajectory in different zigzag periods of a serpentine channel.

4.3.3 Effects of particle size

The cellular components of blood range in size from 7 to 15 μm for spherical leukocytes (WBCs), to 6-8 μm × 2 μm for discoid RBCs, while platelets are between 2 and 4 μm in diameter. The concentration of blood cells are ~5×10^9 RBCs/ml, (2-5)×10^8 platelets/ml, and (5-10)×10^6 WBCs/ml [185]. Since the RBCs account for 98% of blood cells, the filtration of blood cells normally focuses on the RBCs. RBCs are not perfectly spherical but discoid, their characteristic size is hard to determine. It was reported that they behaved similarly as ~ 4 μm spherical particles [153]. For more effective filtration of blood cells from plasma, it would better take the whole

size range of blood cells in to account. So the effects of size on the inertial focusing in the serpentine channel need to be evaluated.

Before the filtration of human whole blood, inertial focusing of particles with three typical sizes, i.e. 3 μm, 5 μm and 10 μm in diameter, in a serpentine was investigated. The fluorescent images and their corresponding fluorescent profiles within different positions were plotted in Figure 4-5 to 4-7. It was found that inertial focusing of 10 μm particles was efficiently obtained after 10^{th} period, with an effective length of 10 mm, Figure 4-5. Even stretching the serpentine to a straight line, the effective length is only 20 mm. This is far less than the 70 mm straight channel, in which 10 μm particles still cannot achieve successful focusing. There were three particle-free areas at the outlet, located at 0~37.25 μm, 58.25~140.85 μm and 162.35~200 μm respectively, occupying ~78.75% channel width.

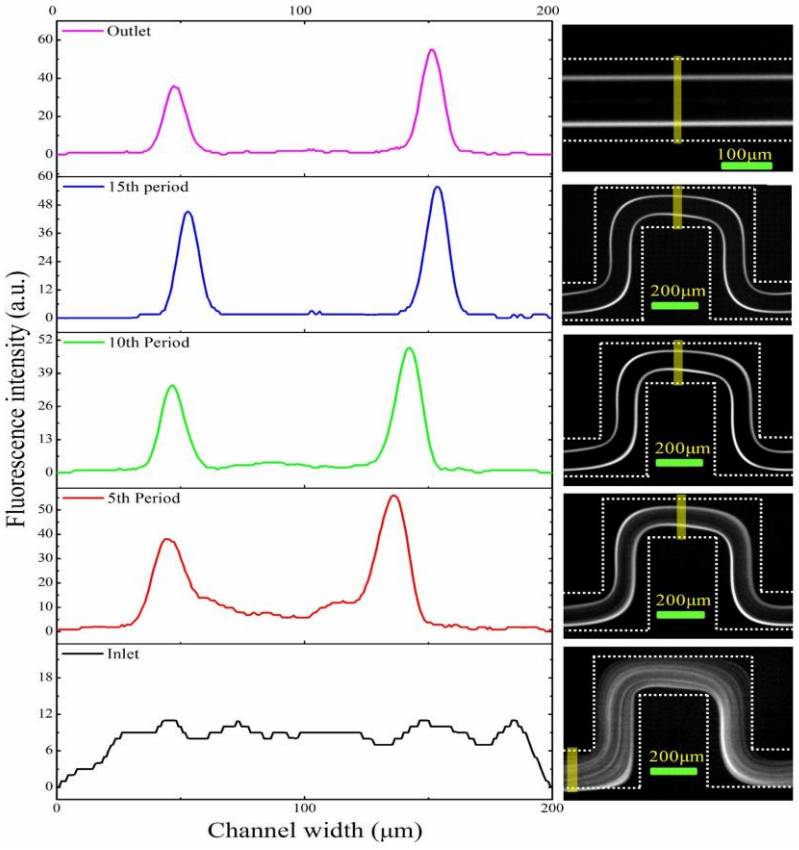

Figure 4–5 Two-sided inertial focusing pattern in a serpentine channel for polystyrene beads with 10 μm in diameter. (Left) Fluorescent intensity profile and (Right) their corresponding fluorescent images at different zigzag periods.

While for smaller particles, these particle-free areas were decreased to 66.25% for 5 μm beads (Figure 4-6) and 33.2% for 3 μm beads (Figure 4-7). One reason why smaller particles cannot focus as tight as their larger counterparts is that the inertial lift force and secondary flow drag are both proportional to the particle size. In addition, for the same weight ratio of particle suspension, the concentration of smaller particles is much higher than that of larger ones. And the interaction of particles in high concentration could deteriorate inertial focusing quality.

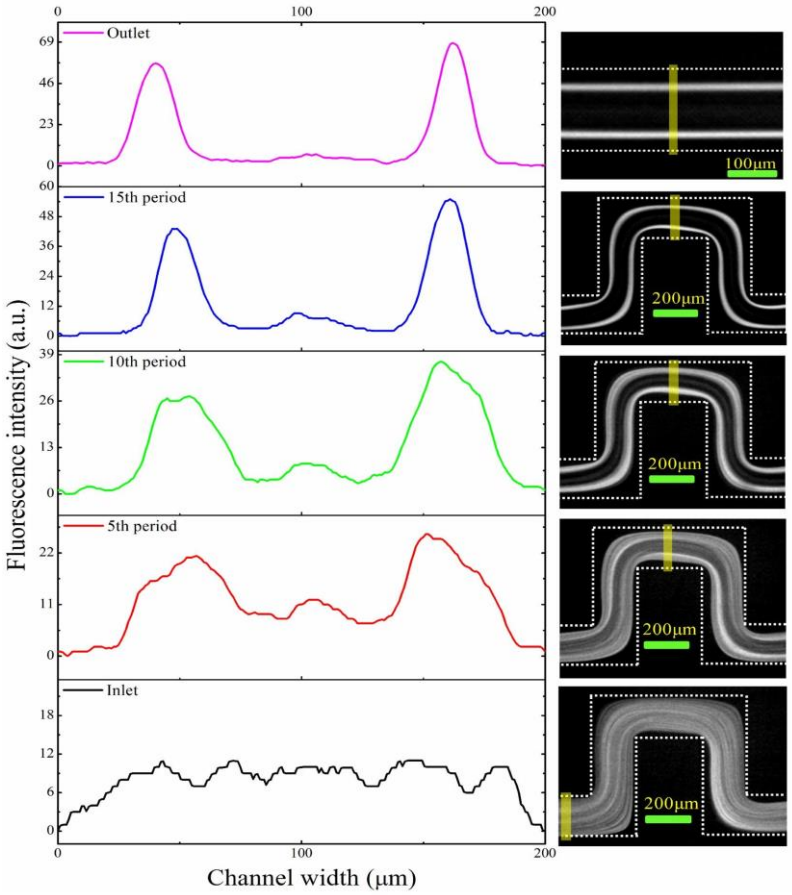

Figure 4–6 Two-sided inertial focusing pattern in a serpentine channel for polystyrene beads with 5 μm in diameter. (Left) Fluorescent intensity profile and (Right) their corresponding fluorescent images at different zigzag periods.

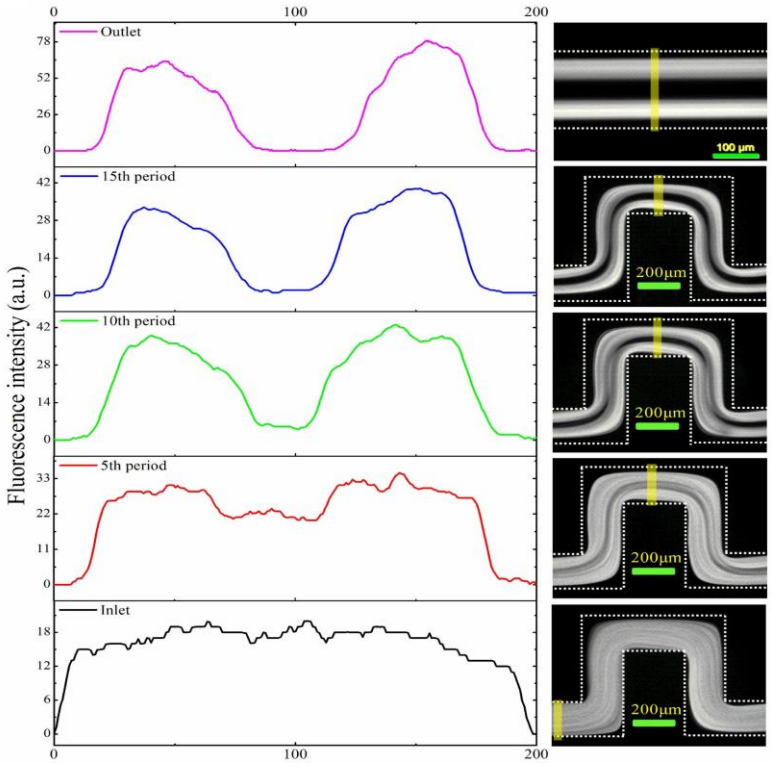

Figure 4–7 Two-sided inertial focusing pattern in a serpentine channel for polystyrene beads with 3 μm in diameter. (Left) Fluorescent intensity profile and (Right) their corresponding fluorescent images at different zigzag periods.

The evaluation of inertial focusing performance of different-sized particles in the serpentine channel confirmed that there were three basic particle free regions at the channel outlet, which can be utilized for extracting plasma, Figure 4-8(a). Here, the central particle free region was selected since it occupies much more plasma volumetric flow rate than the other two regions, Figure 4-8(b), therefore a trifurcation outlet system was implemented at the end of serpentine channel. Three kinds of polystyrene beads were pumped through the device. The concentrations of particles before and after filtration were plotted in Figure 4-8(c). An average filtration efficiency of more than 99% was obtained after a single process, which is higher than most of previous passive devices [153, 186-188].

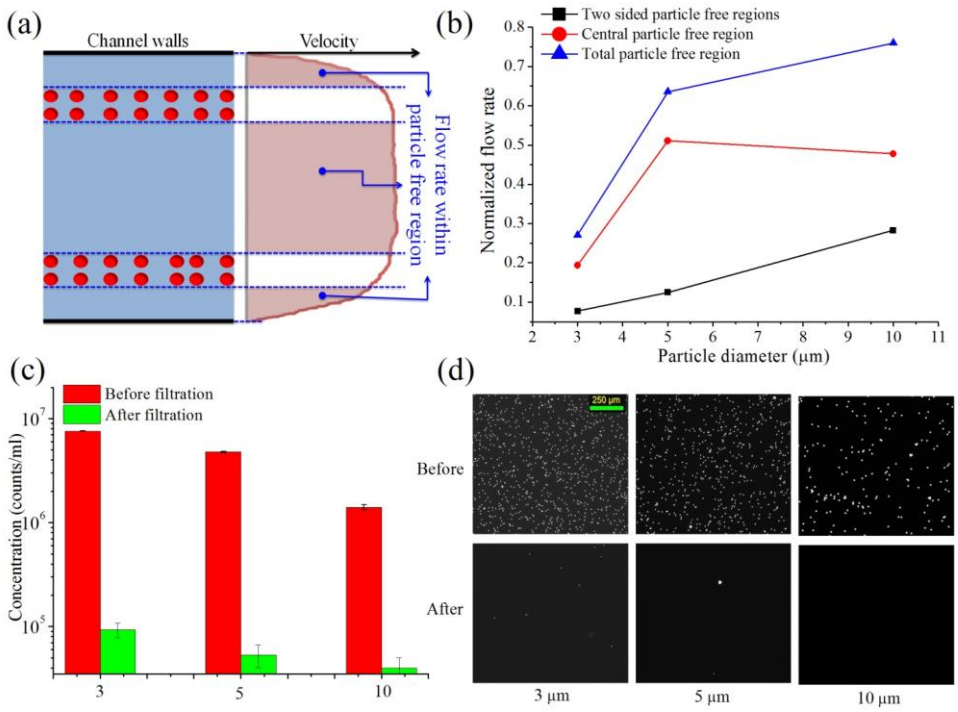

Figure 4–8 (a) Three particle-free regions at the channel outlet, and their corresponding volumetric flow rates. (b) The normalized fluid flow rate within particle free regions for different-sized particles. (c) The concentrations of 3 μm, 5 μm and 10 μm polystyrene beads suspension before and after a single filtration process, and (d) their corresponding fluorescent images in the hemocytometer.

4.3.4 Extraction of blood plasma

The blood sample was taken from a healthy adult male volunteer, and it was stored in a vacutainer tube (Vacuette) containing anticoagulant agent lithium heparin. The blood sample was diluted by 20 times with phosphate-buffered saline (PBS) before pumped into the microfluidic device with a flow rate of 350 μl/min. The blood plasma was extracted from the central branch of bifurcation, as schematically illustrated in Figure 4-9(a). From the bright-field image of blood cells inertial focusing at the outlet, Figure 4-9(b), there were two blood cell focusing streaks (two-sided black streaks). This was within our expectation according to the primary tests with polystyrene beads. After two consecutive filtrations were conducted by the same device, the blood cell concentrations before and after filtration were plotted in Figure 4-9(c). More than 99.75% blood cells were removed after the first process, with a further improvement of rejection ratio > 99.95% achieved by the second

process. The average depletion capacity of ~10^2 blood cells was provided in each process. Additionally, the plasma collection yield was as high as 46%. The images of the working device, two collections and original blood sample demonstrated the excellent filtration capacity of our device, Figure 4-9(d).

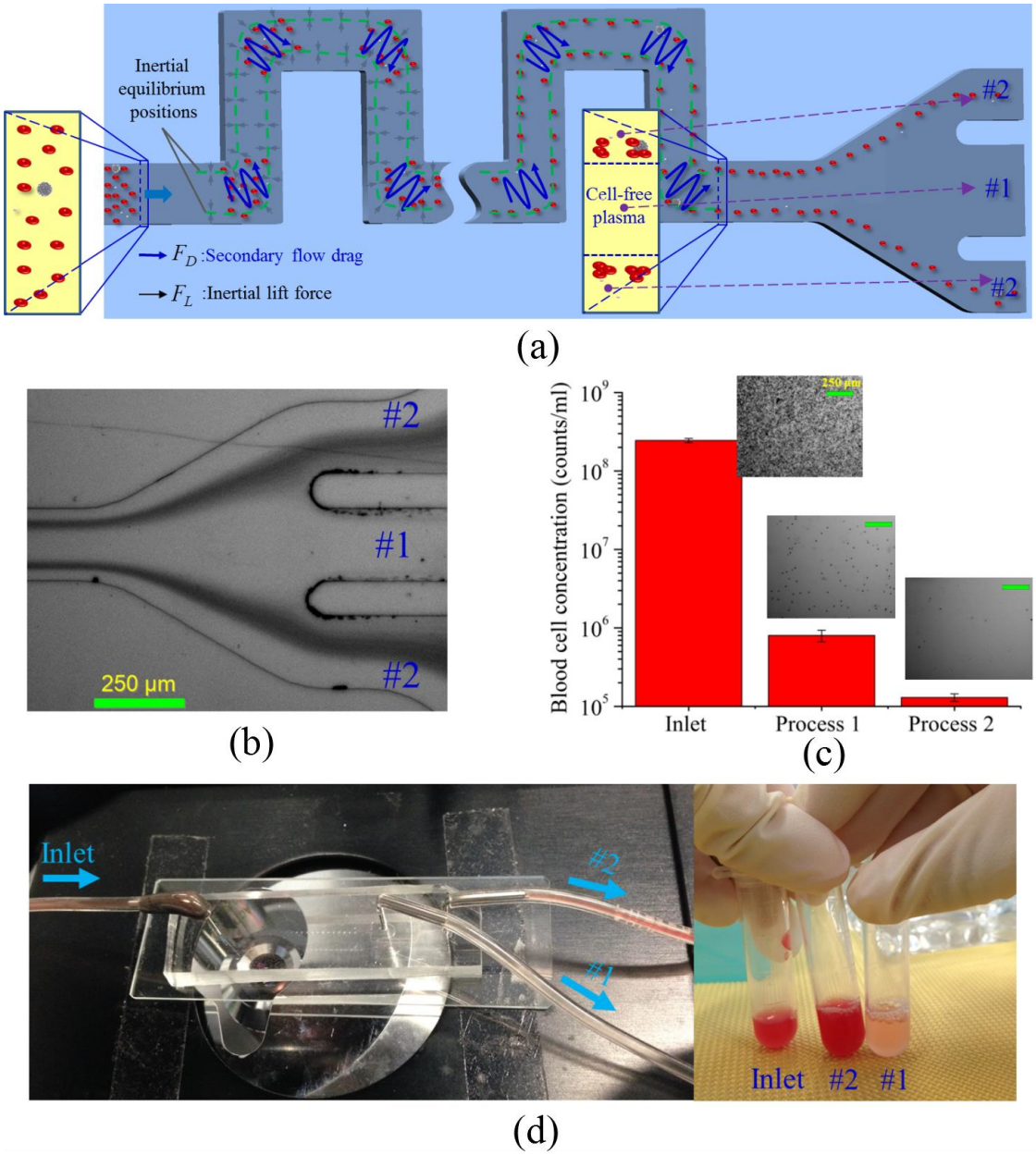

Figure 4–9 (a) Schematic illustration of the extraction of plasma in the symmetric serpentine channel; (b) Bright field image of filtration of blood cells at the outlet; (c) Concentration of blood cells after each process, inserted with bright field images of blood sample before and after each filtration. In the second process, the input blood sample is the blood plasma obtained from the first process. Error bars represent the standard deviation of three measurements in hemocytometer. (d) (Left) Working

image of the microfluidic device, one can clearly observe that the tubes of outlet #1 is clear, indicating barely red blood cells passing through, while tubes of inlet and outlet #2 are in red colour, filled with massive red blood cells; (Right) Optical images of input blood sample and two collections from each outlets.

One may also concern the effects of shear stress on the blood cells, since blood cells could be lysed by strong shear stress [154]. In the micro-channel with low aspect ratio (h= 42 μm, w=200 μm), the velocity profile in a straight channel along lateral direction (*x*) is blunted, so the shear rate is very small within the central region of channel width. Therefore, the shear stress on the blood cells is actually very small. Moreover, in the proposed inertial microfluidic device, the average linear velocity of fluid is 0.7 m/s when the flow rate of serpentine channel is 350 $\mu lmin^{-1}$. Thus, the duration of blood cells within the serpentine channel with 15 mm long is 21.4 ms, which means that the effect of shear stress is too short to impact blood cells significantly. Furthermore, the obtained blood plasma was further purified by the membrane filtration (Millipore, Cat NO. HNWP02500, Hydrophilic nylon membrane filters, Pore size~450nm), and its haemoglobin content was measured by a Roche Sysmex XE-2100 Hematology-Analyzer in Southern IML Pathology, a medical testing laboratory in Wollongong, NSW, Australia. We found that the haemoglobin which indicates the content of lysed red blood cells is the same as that obtained from the standard centrifugation, which demonstrates that there is no significant red blood cell lysis during the inertial filtration process. Therefore, the effects of shear stress on blood cells lysis are negligible in blood cells separation and filtration in the proposed inertial microfluidic device.

4.3.5 Effects of haematocrit (Hct)

Besides, the effect of haematocrit (Hct) on the inertial focusing in serpentine channel was investigated. Haematocrit, also known as erythrocyte volume fraction (EVF), is the volume percentage (%) of red blood cells in blood. It is normally about 45% for men and 40% for women. The whole blood sample was diluted by 1/5, 1/10, and 1/20 with PBS respectively. And the corresponding Hct are 9.0%, 4.5% and 2.25%, respectively. Pumping these samples into the device, bright field images at the end of serpentine channel and bifurcation were shown in Figure 4-10(a). And the bright field intensity profile along the channel width was plotted in Figure 4-10(b).

Increasing Hct, the width of cells focusing streaks expands, and the area of cell-free region reduces. When Hct ≥9.0%, cells almost occupy the whole channel width, which is impossible to collect cell-free plasma under this situation. This is due to the serious cell-cell interaction in blood sample with such high concentration (~1×10^9 cells/ml), which deteriorates cell focusing performance. This is actually one main limitation of inertial microfluidics.

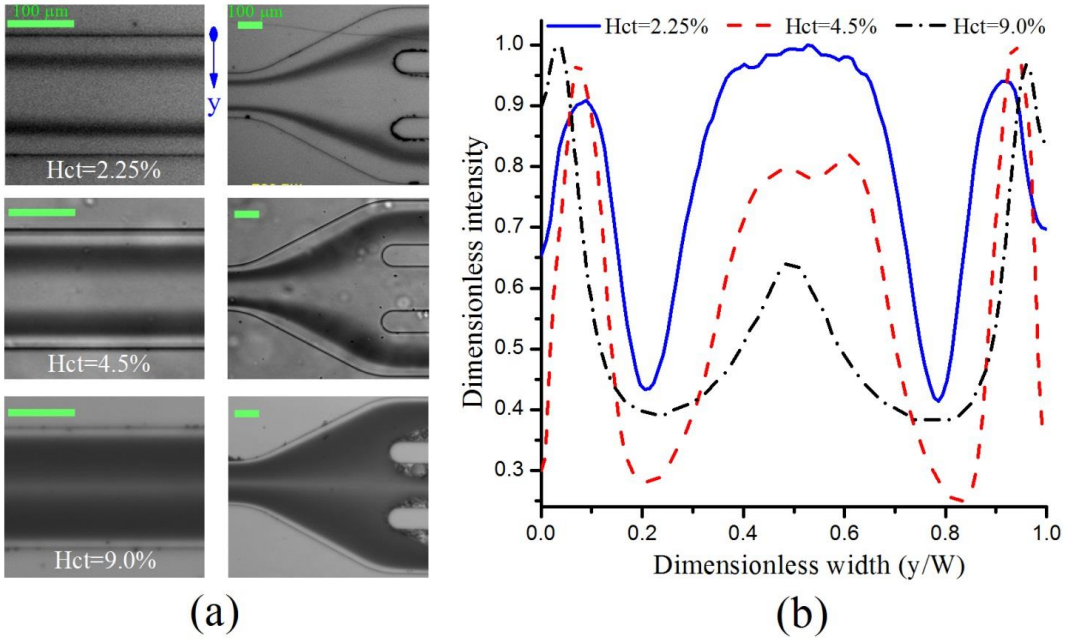

Figure 4–10 Effects of blood haematocrit (Hct) on two sided inertial focusing. (a) The bright field images of blood cells focusing at the end of serpentine channel (left) and bifurcation outlet (right). (b) The bright field intensity profile at the end of serpentine channel along the channel width. It should be noted that in bright field images, the higher the intensity, the less cells occupy, allowing more illuminating light to be captured by camera.

4.3.6 Parallelization technique

In inertial microfluidics, particle-particle interaction always requires to be reduced by the dilution of blood sample, in order to prevent the deterioration of inertial focusing and separation performance. The dilution actually reduces the net throughput of device, although the volumetric flow rate of inertial microfluidic device is very high. In order to improve the throughput to the scale of conventional device, i.e. macroscale centrifugation with a throughput of ~ml/min, a parallelization technology

is needed. Parallelization design can be along the vertical direction or planar direction. On vertical direction, device is stacked by many layers to amplify the throughput of the whole device by the number of layers [189], however it faces challenges of hard implementation of uniform input condition for each layers, which is critical for inertial microfluidic device. On planar direction, the whole throughput is determined by the number of parallel channels, and the channel with linear geometry is always preferred, i.e. straight, expansion-contraction or serpentine. Here, we designed and fabricated a device with eight parallel serpentine channels along the planar direction, Figure 4-11(a, b). A symmetric design for the inlet and outlet sections is implemented to ensure that the input and outlet conditions for all the serpentine channels are uniform, so that their flow fields and stream splitting at bifurcations are the same. Base on the Hagen-Poiseuille's law, the network of microfluidic channel can be described by electric circuit analogy [102], as shown in Figure 4-11(c). The flow rate in each branch of bifurcation is expressed as:

$$Q_4 = \left(P_{in} - Q_0 R_0 - \frac{Q_0}{2} R_1 - \frac{Q_0}{4} R_2 - \frac{Q_0}{8} R_3 - P_0 \right) \Big/ \left(R_4 + 16R_{12} + 8R_{11} + 4R_9 + 2R_7 \right) \tag{4-1}$$

$$Q_5 = \left(P_{in} - Q_0 R_0 - \frac{Q_0}{2} R_1 - \frac{Q_0}{4} R_2 - \frac{Q_0}{8} R_3 - P_0 \right) \Big/ \left(R_5 + 8R_{10} + 4R_8 + 2R_6 \right) \tag{4-2}$$

$$\frac{Q_5}{Q_4} = \frac{R_4 + 16R_{12} + 8R_{11} + 4R_9 + 2R_7}{R_5 + 8R_{10} + 4R_8 + 2R_6} = \frac{\frac{R_4}{R_5} + 16\frac{R_{12}}{R_5} + 8\frac{R_{11}}{R_5} + 4\frac{R_9}{R_5} + 2\frac{R_7}{R_5}}{1 + 8\frac{R_{10}}{R_5} + 4\frac{R_8}{R_5} + 2\frac{R_6}{R_5}} \tag{4-3}$$

When $R_{6\text{-}12} << R_{4,5}$, then

$$\frac{Q_5}{Q_4} \approx \frac{R_4}{R_5} \tag{4-4}$$

The hydraulic resistance $R_H = C_{geometry}\, \mu L/A^2$, where $C_{geometry}$ is the geometric coefficient, L is the channel length and A is the area of channel cross-section [102].

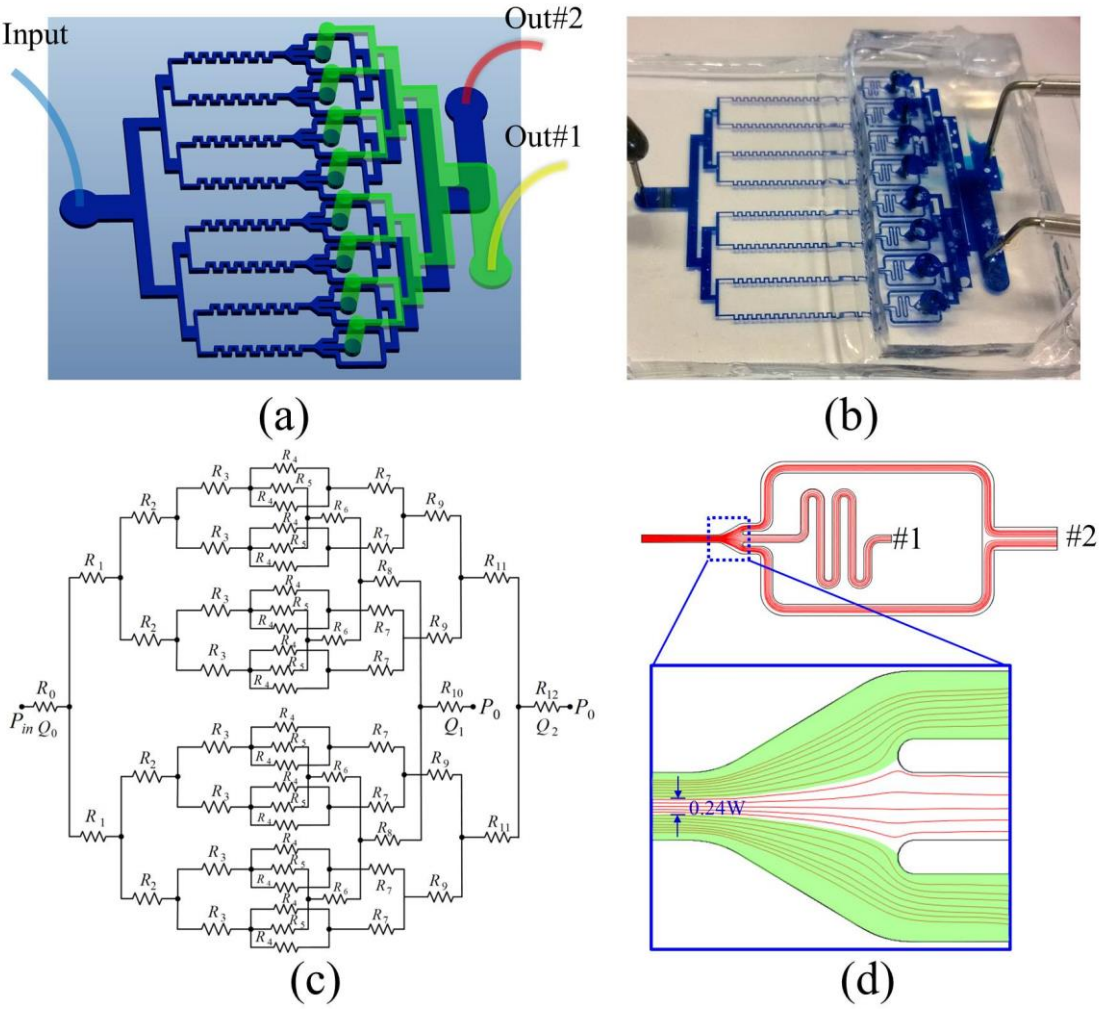

Figure 4–11 (a) Schematic structure of the parallelized microfluidic device with eight serpentine channels; (b) The picture of fabricated parallelized inertial microfluidic device. The blue food dye was injected into the device for better visualization of micro-channel structure; (c) Fluidic circuit of the parallelized microfluidic device; (d) Simulated flow field within one trifurcation outlet unit.

In order to make the assumption $R_{6\text{-}12} << R_{4,5}$ valid, the following design considerations were adopted: (i) The connecting channel sections corresponding to $R_{6\text{-}12}$ should have a large width and short length as much as possible, to reduce the corresponding hydraulic resistances; (ii) In order to obtain a relatively large resistance for $R_{4,5}$, the micro-channels representing $R_{4,5}$ should be much narrower with longer length. The micro-channel section corresponding to R_5 was even designed with serpentine structure to further increase its resistance. After that, computational costs (time and space) can be reduced significantly, and only one

bifurcation outlet unit is needed for the simulation of flow field, to optimize the splitting of streamlines, as shown in Figure 4-11(d). The whole device was tested with diluted whole blood at a flow rate of 2.8 ml min^{-1}, with a high throughput of ~7×10^{8} cells min^{-1}. The parallel device can work very well under such a high flow rate. In Figure 4-12, the uniform two-sided focusing of blood cells and streamline bifurcation at each parallel serpentine channel demonstrate the feasibility of this design scheme.

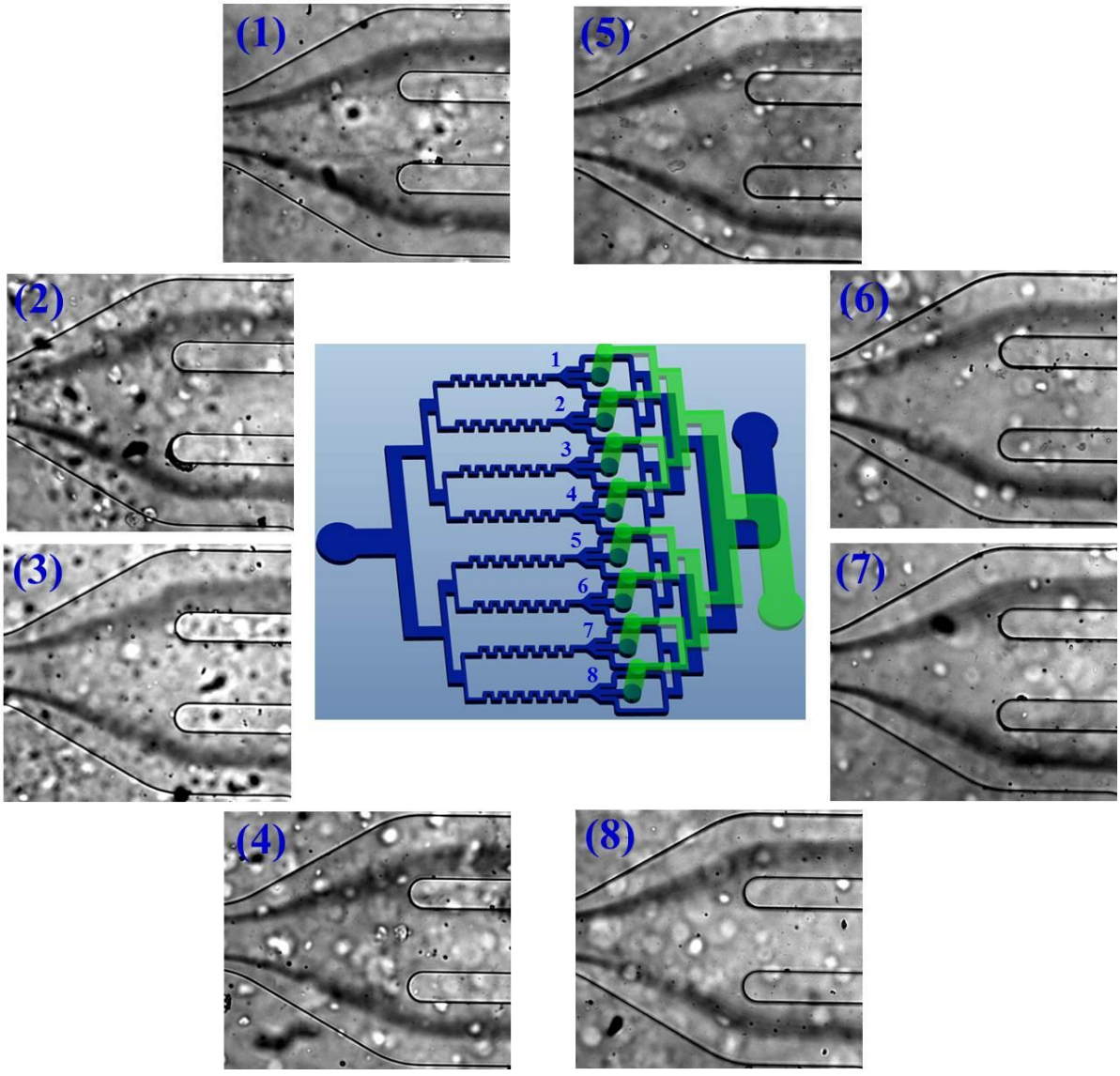

Figure 4–12 Bright field images at each outlet bifurcation in the parallel device. The uniform streamline splitting and blood cells filtration at each outlet validate our parallelization design considerations.

4.4 Conclusion

In this chapter, we reported a continuous, passive high-throughput filtration device, employing secondary flow aided inertial migration of particles in a serpentine channel. The mechanism of inertial focusing enhancement by the introduction of alternating curvature was analysed. The two-sided inertial focusing pattern is dominated by the inertial lift force near the channel sidewalls, and alternating secondary flow drag acts to assist the inertial migration process of particles, especially for the particles within the channel central area where inertial lift force is very small due to the blunt velocity profile. The effects of particle size and haematocrit on the inertial focusing performance were investigated experimentally. Diluted whole blood was processed by the proposed device, with about 99.95% blood cells removed. The collection yield of plasma was as high as 46%. We also explored the parallelization design of the serpentine channel for processing a large volume of samples. Some parallelization design rules for parallel serpentine channels were proposed and discussed. These rules are also applicable to other types of microchannel with linear structure. The fabricated device with eight parallel serpentine channels can process massive blood sample with volumetric flow rate of 2.8 ml/min and ultra-high throughput of ~7×10^8 cells/min. Due to its nature of simple design, easy fabrication, continuous manner and high throughput, the proposed device can not only become a good alternative for conventional device working standalone, but also potentially be integrated with other components in the same device to form a sample-to-answer system.

5 INERTIAL PARTICLE SEPARATION BY DIFFERENTIAL EQUILIBRIUM POSITIONS: EMPLOYING OVERLAP BETWEEN SINGLE CENTRAL FOCUSING PATTERN AND TWO-SIDED FCOUSING PATTERN

5.1 Introduction

Particle separation has a wide range of industrial, biomedical and clinical applications such as wastewater purification, blood sample preparation and disease diagnosis [190]. Conventional macro-scale techniques such as physical filter and differential centrifugation can be used for this purpose. However, centrifugation is bulky, expensive, labour intensive and even dangerous because it contains components moving at high speed [172, 191]. Centrifugation is also limited by the heterogeneity of sample source. Furthermore, exposure to a high acceleration will likely alter the immunophenotype [192] and viability [193] of cells. Physical filters are prone to clogging, and frequent cleaning is labour intensive. Thus, a simple, low cost, more efficient and less offensive technique is desired. The recently emerged microfluidic technology is endeavoured to satisfy these demands.

Inertial microfluidic technology employing inertial migration [13] and inertial effects of fluid (secondary flow) [5] and particles (centrifugal force) [95] under a high flow speed can provide excellent separation efficiency and purity with a massive throughput. Inertial microfluidics is also label-free, which eliminates the need for potentially cell-damaging immuno-labelling procedures, and promises a cost-effective cell separation method for downstream biological assays [132]. Generally, there are six criteria to evaluate inertial microfluidic separation/sorting device. (i) Footprint. A small device footprint not only reduces the fabrication cost, but also improves the portability. (ii) Throughput. High throughput is essential in processing a large volume of sample, which is actually the main advantage of inertial microfluidics. (iii) Parallelizability. An effective method to amplify the throughput is to pattern parallel channels in the same device. Basically, a microchannel with linear structure (e.g. straight or serpentine) is prone to be parallelized. (iv) Performance. High separation purity and efficiency (or recovery ratio) are important for the downstream application, including enumeration, molecular assay and drug screening, etc. (v) Resolution. The minimum particle property (size, deformability and shape) difference required to achieve effective particle separation. (vi) Complexity. Sheath

flow and complicated microchannel structure (e.g. double layer microchannel) are not in favour of fabrication costs and portability. Although great progress in the inertial microfluidics has been achieved recently [98, 115, 136, 144], so far there is still lack of techniques with an integrative ability to satisfy all the required criteria simultaneously. For example, spiral channel with nonlinear structure is not beneficial for parallelization design, although it can enable very excellent separation. The linear structure of straight channel is good for parallelization, however, complete focusing and separation of particles in a straight channel normally requires long enough channel length and restricted dimension of channel cross-section, which inevitably cause large device footprint and high flow resistance.

In terms of small footprint and easy parallelization, a serpentine channel with linear structure is an optimal choice. A serpentine channel not only is easy to parallelize, but also can achieve focusing and separation within a much shorter length due to the assistance of secondary flow [95, 180]. Unfortunately, little effort has been paid to separate particles by a serpentine channel in inertial microfluidics. To date, only one inertial filtration device that consists of an asymmetrical serpentine channel was reported [172]. In that filtration system, large particles were well focused and small particles below a threshold remained unfocused and randomly distributed. Therefore, large particles were completely removed from the mixture, leaving behind small particles with a high purity (90%-100%). However, because small particles are still unfocused, plenty of them will enter the reservoirs meant for large particles, leading to unsatisfactory purity (~20%) of large particles collection. Also the recovery efficiency of small particles was low (~56%). More efforts are still needed to separate binary particles mixture with high purity as well as high efficiency.

In order to provide a continuous separation technique with high-throughput, good parallelizability, small footprint and high separation performance, we developed an innovative inertial microfluidic device with serpentine channel to continuously separate particles based on the size-dependent differential equilibrium positions. This device is based on the observed three different focusing patterns in a symmetrical serpentine channel that has been reported in the preceding chapters. A single focusing streak can be achieved at the centre of the channel where Dean (or secondary flow) drag force dominates particles' migration in a serpentine channel at

a relative high flow rate. As inertial lift force and Dean drag force scale differently with the particle size, particles below a certain threshold could be dominated by the inertial lift force, and are focused along two sides of the channel. Therefore, a complete separation may be achieved with a proper outlet system [3].

In this chapter, we first examined the focusing patterns of different-sized particles under varying flow conditions. The results were placed into a Reynolds number - particle size operation space map. After that, the available working area for particle separation could be easily determined from this map. Then, we tested the separation capacity of two pairs of polystyrene particle mixtures (3 μm/10 μm, and 5 μm/13 μm particles). Finally, the separation ability of this device on biological cells through a series of cell mixtures was examined, including erythroleukemia cells with 5 μm polystyrene particles, erythroleukemia cells with blood cells, and different blood cells.

5.2 Materials and methods

5.2.1 Device fabrication

Based on our previous study of particle inertial focusing [4], we implemented a trifurcating outlet at the end of the channel, so that three different particle streaks could be collected in the corresponding branches. The two-sided symmetrical bifurcations were combined to a single outlet to simplify handling. The device with a single serpentine channel has a footprint of 36 mm × 5 mm. The device was fabricated by standard photolithography and soft lithography techniques.

5.2.2 Cell culture

Murine erythroleukemia (MEL) cells were maintained in a complete culture medium (RPMI-1640 medium containing 10% fetal calf serum and 2 mM L-glutamine) at 37°C and 95% air/5% CO_2 as previously described [194]. In order to visualize the trajectory of MEL cells in the microfluidic device, MEL cells were labelled using PKH26 red fluorescent cell linker kit (Sigma-Aldrich, Product No. P9691) according to the manufacturer's instructions as follows. Cell clusters were removed using a 70

[3] Results of this chapter are published in: [183] Zhang, J., Yan, S., Sluyter, R., Li, W., Alici, G., and Nguyen, N.-T. (2014) Inertial particle separation by differential equilibrium positions in a symmetrical serpentine micro-channel, *Scientific reports 4*, Art No. 4527.

μm cell strainer (Becton Dickinson, Product No. 352350) and the single cell suspension was washed twice with serum-free RPMI-1640 medium (400×g for 5 min at 22°C). Cells (2×10^7 cells/ml) were then re-suspended in 1 ml of Diluent C (Product No. G8278) and rapidly mixed with 1 ml of Diluent C containing 2×10^{-6} M PKH26 ethanolic dye solution (Product No. P9691). Immediately following mixing, 2 ml of fetal calf serum was added, and the mixture was incubated for 1 min. The cells were then washed three times in 10 ml of complete medium (400×g for 5 min at 22°C) and finally suspended in the complete medium at ~4.4×10^6 cells/ml.

5.2.3 Particle and cell mixture preparation

To conduct the separation of polystyrene beads mixtures, two pairs of beads mixture (3 μm/10 μm beads mixture, and 5 μm/13 μm beads mixture) were prepared in DI water with 0.1% w/v tween. Their concentrations were listed in Figures 5-5(b) and 5-6(b). For testing mixture of MEL cells and 5 μm polystyrene beads in the proposed device, 5 μm polystyrene beads and PKH26-labelled MEL cells were mixed by a ratio of ~ 1:1, and suspended in phosphate-buffered saline (PBS) with a MEL cell concentration of ~2.46×10^6 counts/ml. The whole blood was donated from a healthy male. The MEL cells were spiked into the whole blood sample, with a ratio of ~1:100 for the separation of MEL cells from the whole blood. The mixture was diluted by PBS to the concentration of the whole cells ~7.5×10^7 counts/ml.

5.2.4 Experimental setup and method

The microfluidic device was placed on an inverted microscope (CKX41, Olympus), illuminated by a mercury arc lamp. Particle suspension was pumped by a syringe pump (Legato 100, KD Scientific). The fluorescent images were observed and captured by a CCD camera (Rolera Bolt, Q-imaging), and then post-processed and analyzed using the software Q-Capture Pro 7 (Q-imaging). The exposure time for each frame was kept constant at 100 ms. Concentrations of particles and cells were measured by a hemocytometry. The purity of particle suspensions collected from different outlets was calculated from three measurements by hemocytometry. An LSR II flow cytometer (BD Biosciences) was also used to further verify the separation purity from two collections. The flow cytometer data were analyzed using FlowJo software (Tree Star).

5.3 Results and discussion

5.3.1 Differential equilibrium positions of different-sized particles

In order to determine the working conditions for complete particle separation, particles with a series of sizes were tested in the serpentine channel. Fluorescent streak images of different-sized particles at the outlet were plotted in Figure 5-1(a). It showed that smaller particles had a wider region I, and particles were occupying two sides of the channel. A more intriguing phenomenon was that small particles (≤5 μm) become unfocused rather than focused into the centre of the channel even at a large Reynolds number (Re=160~200), which was different from their large counterparts (≥8 μm). Two effects are responsible for this phenomenon. First, mixing effects of Dean vortex is more effective on small particles. Small particles are prone to being retained by the counter-rotating streamlines of a Dean vortex, so that focusing at the centre of the channel is hard to be obtained. Yoon et al. [139] demonstrated that particles smaller than 27% of the channel height posed an inward velocity due to the mixing effects in a curved channel. In Chapter three, we found that this ratio could be as small as 20% in a low-aspect-ratio serpentine channel, due to the suppression on mixing streamlines [4]. The channel height is 42 μm, so that particles smaller than 8 μm are prone to being affected by the mixing effects of Dean flow. Therefore, the theory of Dean drag force and particle centrifugal force induced central focusing may be not suitable for these small particles. Second, even at our high testing flow condition, Dean drag force maybe still cannot overcome inertial lift force, so that this defocusing status could remain longer downstream.

The focusing pattern of different-sized particles was placed into three standard regions, and plotted in the channel Reynolds number versus particles size operation map, Figure 5-1(b), which indicates the available working area for the separation of particles with specific sizes. The operation map showed a distinct overlap between region I of 3 μm and 5 μm particles and region III of 10 μm and 13 μm particles. The transition threshold A for 3 μm (A3=130) and 5 μm (A5=120) particles was obviously higher than the transition threshold B for 10 μm (B10=107) and 13 μm (B13=90) particles. So it is possible to completely separate particles based on their size-dependent differential equilibrium positions in the serpentine channel, a fact that will be demonstrated in the following sections.

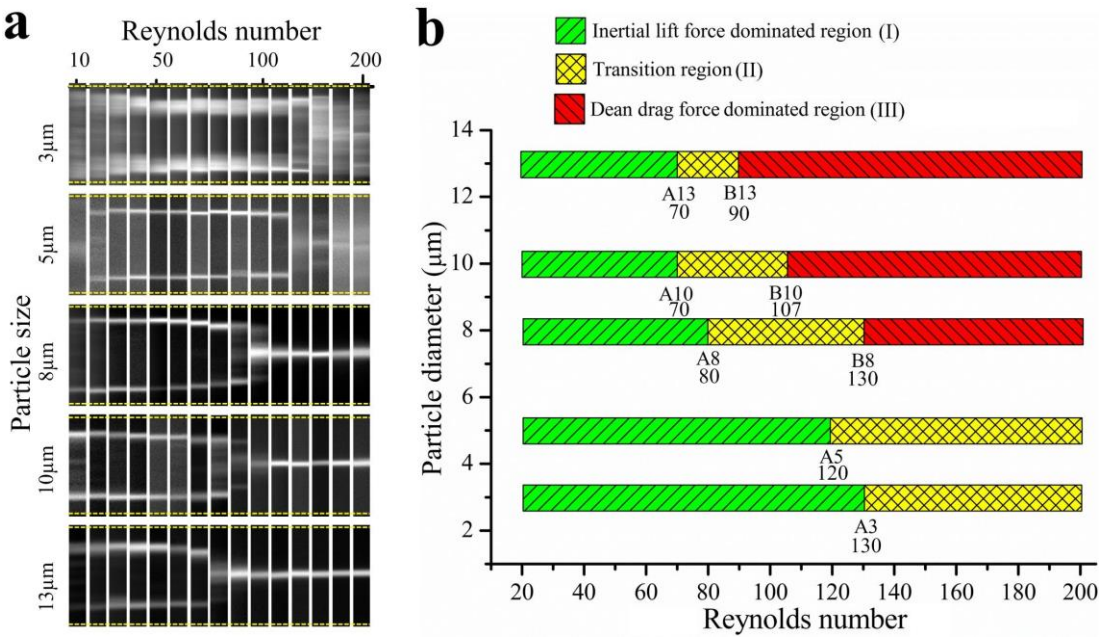

Figure 5–1 (a) Experimental observation of outlet fluorescent streak images for different-sized particles under various flow conditions; (b) Translation of particle focusing pattern into three standard regions in the Reynolds number – particles diameter space.

The quantitative particle streak position and width under various flow conditions were shown in Figure 5-2. The streak position is not only useful for the determination of the available flow condition, but also important for designing a proper outlet system for particle separation.

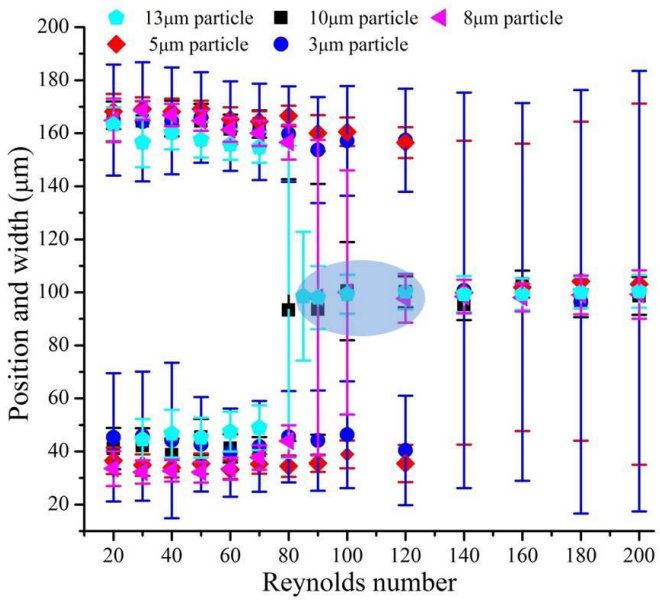

Figure 5–2 Quantitative illustration of focusing positions and widths for different-sized particles under various flow conditions. Error bars indicate the streak width, which was determined by standard FWHM (full width at half maximum). The streak position was taken as the middle of the half maximum intensity.

The circular shadow illustrates the available region for complete separation of 3~5 μm and 8~13 μm particles. After that, the outlet system need to be designed by the analysis of fluidic circuit. The relative resistance of three outlets determines the trifurcation of streamlines, and therefore the collection of focused particles. From Figure 5-3, we can see that when increasing the flow resistance of outlet #1 (can be easily achieved by adding additional serpentine sections), more streamlines will enter outlet #2. Due to very promising focusing performance of large particles (10/13 μm) at the outlet (particles are almost focused along a single line), so even in design (III) where a central band with only ~0.22w (44 μm) width for the collection of large particles is good enough. However, focusing performance of small particles is not very good: small particles cannot focus into a tight single position, but a much wider band area, which is evaluated by the FWHM (full width at half maximum). In design (I), part of small particles will enter into collection #1 in this situation, which consequently contaminates the purity of large particles. In designs (II) and (III), this contamination was prevented, because sided focusing particle streaks were included within the side streamlines completely (green area). This led to a much better separation purity of large particles. In the following separation, design (II) is selected for the collection of differentially-focused particles.

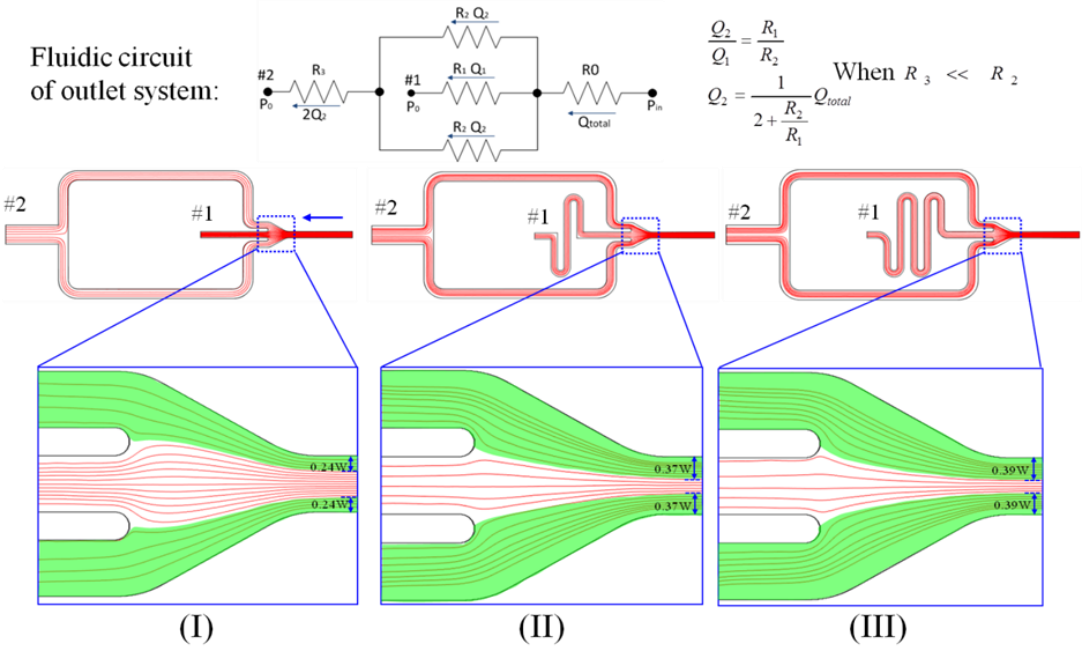

Figure 5–3 The optimization of fluid streamline bifurcation at the outlet.

5.3.2 Separation of polystyrene particles

A mixture of fluorescent particles with diameters of 3 μm and 10 μm were tested in the designed device to demonstrate the concept of complete separation. Figure 5-4(a) is a schematic illustration of microchannel structure used for particle separation in the present work. Pillar arrays acting as a filter upstream of the serpentine channel was used to prevent clogging by large debris.

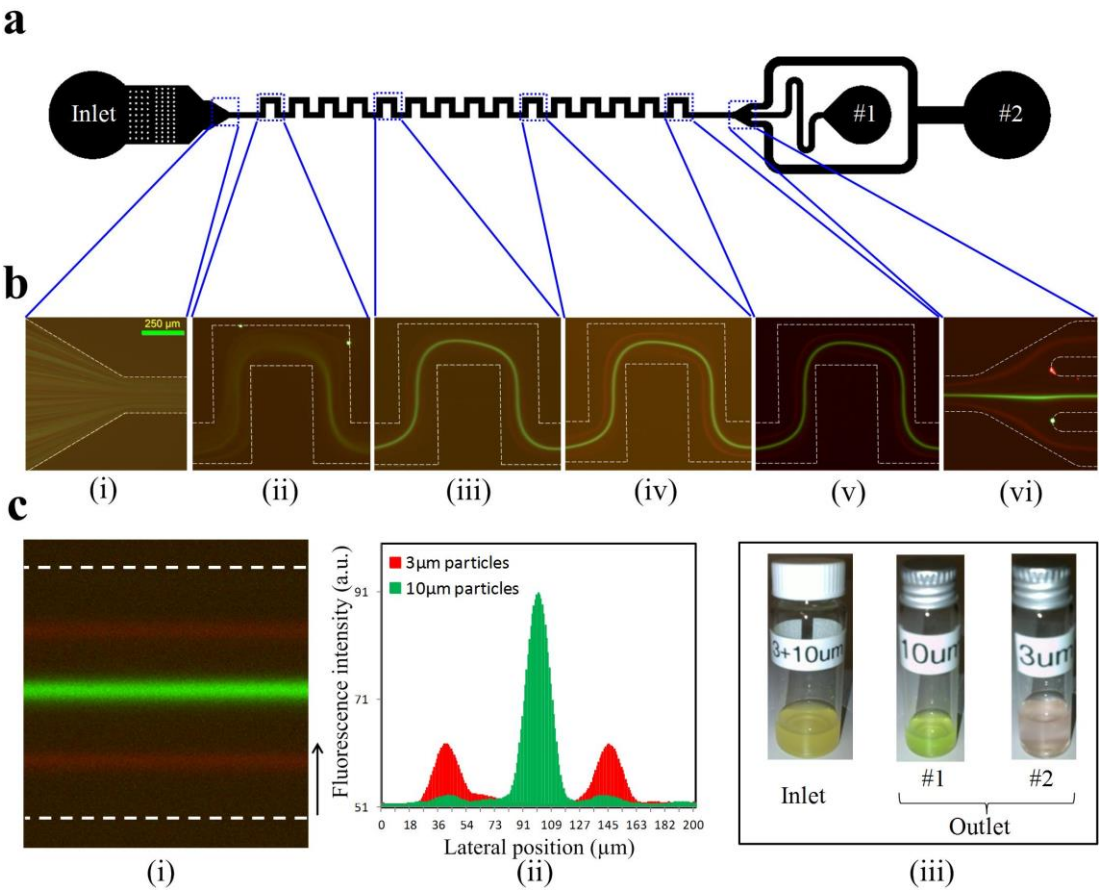

Figure 5–4 (a) Schematic illustration of the micro-channel structure used for particle separation in this work. A filter upstream of the serpentine channel prevents the channel from being blocked by large debris. A trifurcation outlet system with two symmetrical side branches merged together as a single outlet #2 was used. (b) Superimposed fluorescent images illustrating the distribution and position of the 10 μm (pseudo-coloured green) and 3 μm (pseudo-coloured red) particles in different periods of serpentine channel. (c) (i) Fluorescent images of the particle mixture at the outlet of the serpentine channel, and (ii) its cross sectional fluorescence intensity profile presents differential equilibrium positions for binary particles. (iii) Pictures of particles suspension before and after processing indicate an effective particle separation in the serpentine channel.

The fluorescent images of particles at different periods in the serpentine channel are shown in Figure 5-4(b). Particles were randomly distributed at the channel inlet, Figure 5-4b(i). After passing through several serpentine periods, large particles migrated into the channel centre dominated by the Dean drag force, while small

particles occupied two sides of the channel due to the dominant inertial lift force, Figure 5-4b(ii~v). At the end, a three-branch outlet system was used to collect particles from different lateral positions, Figure 5-4b(vi). Figure 5-4c(i) shows the distribution and position of 10 μm and 3 μm particles before the trifurcation. The fluorescence intensity profile clearly demonstrates distinct lateral positions of 10 μm and 3 μm particles, Figure 5-4c(ii), facilitating particle separation by size. Figure 5-4c(iii) shows particle suspensions before and after the treatment by the proposed microfluidic device, clearly indicates an effective separation of the particles mixture.

The particles mixture was tested in the microfluidic device with different throughputs to quantitatively evaluate the separation performance. Particle concentration, particle purity (collected target particle number/ collected total number [136]) and separation efficiency (collected target particle number/input target particle number [64, 190]) were measured and shown in Figures 5-5(b-d), respectively. The sample collected from outlet #2 had a very high purity (~99%) of small 3 μm particles, due to excellent focusing of larger 10 μm particles at the channel centre. However, for collection from outlet #1, purity of large 10 μm particles was not as high as expected. The maximum purity was around 88.7 %, although this value was much greater than the input purity of 24.2%. The main reason was that small 3 μm particles still could not experience enough inertial lift force in the migration process even with the assistance of Dean drag force. There was no distinct single lateral equilibrium position for them, but a wide band area. The wide band reduced the separation distance between large and small particles along the lateral direction, and increased the possibility of small particles entering outlet #1, finally deteriorated the purity of the collected large 10 μm particles. In addition, the separation efficiencies for both large particles and small particles are more than 90% (97.5% for 10 μm particles and 92.8% for 3 μm particles), which implies that most input particles can be effectively separated and recovered at their corresponding collectors.

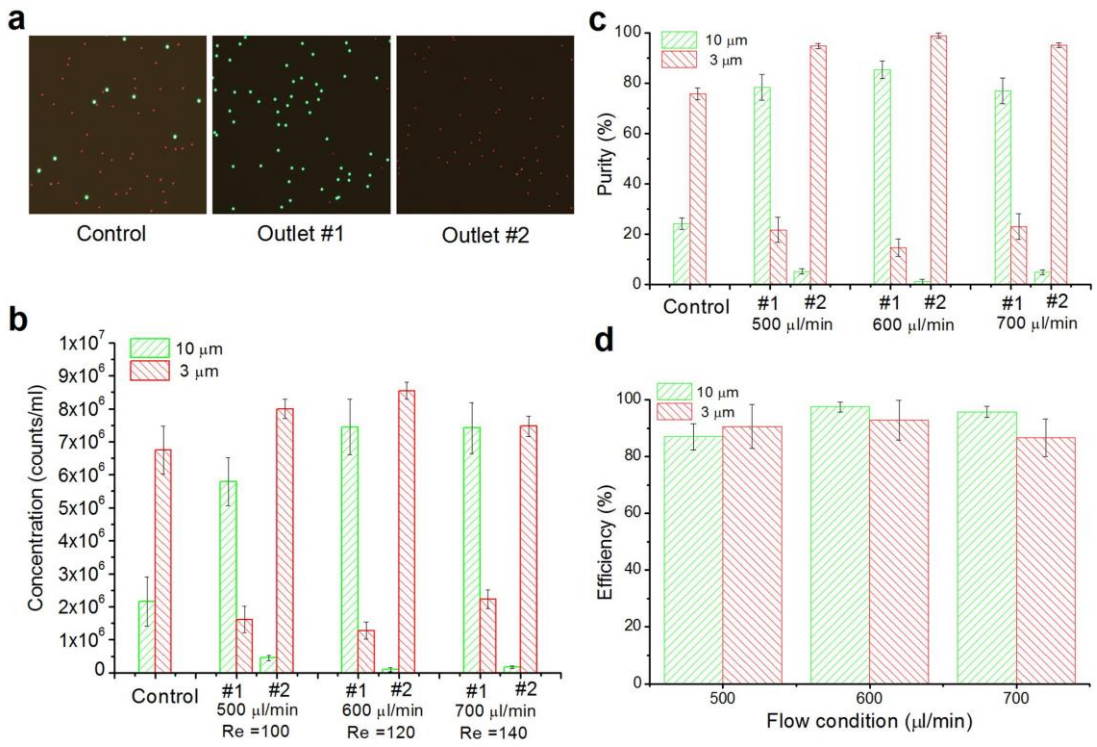

Figure 5–5 Separation of 3 μm and 10 μm particles in the serpentine channel. (a) Fluorescent images of collections from control and two outlets. The control is particle mixture collected before passing through the serpentine channel. Pseudo-coloured green and red dots represent 10 μm and 3 μm particles respectively. (b) Particle concentrations from control and two outlets under different processing flow conditions (flow rate or Reynolds number). (c) The purity of particles from two collectors at various flow conditions. (d) The separation efficiency for 3 μm and 10 μm particles under different flow conditions. Error bars represent the standard deviation of three measurements by hemocytometry.

We also tested the separation of a mixture of 5 μm and 13 μm particles, as shown in Figure 5-6. Since 5 μm particles had a larger size and experienced a much larger inertial lift force (F_L) and Dean drag force (F_D) as well as a faster lateral migration speed than 3 μm particles, two narrow focusing streaks along the channel could be observed in Figure 5-1. As expected, at the optimal flow rate (600 μl/min), the purity of large 13 μm particles collected at outlet #1 could be as high as 91.6%. Small 5 μm particles collected at outlet #2 also achieved a high separation purity of more than 99.2%, Figure 5-6(c). The fluorescent images of particles from the control and outlets in the hemocytometer showed the excellent separation performance of

our device. It should be noted that the purity of collected particles sample was taken from a single process, so it is expected that complete separation with purity of more than 99% could be obtained by a cascading process.

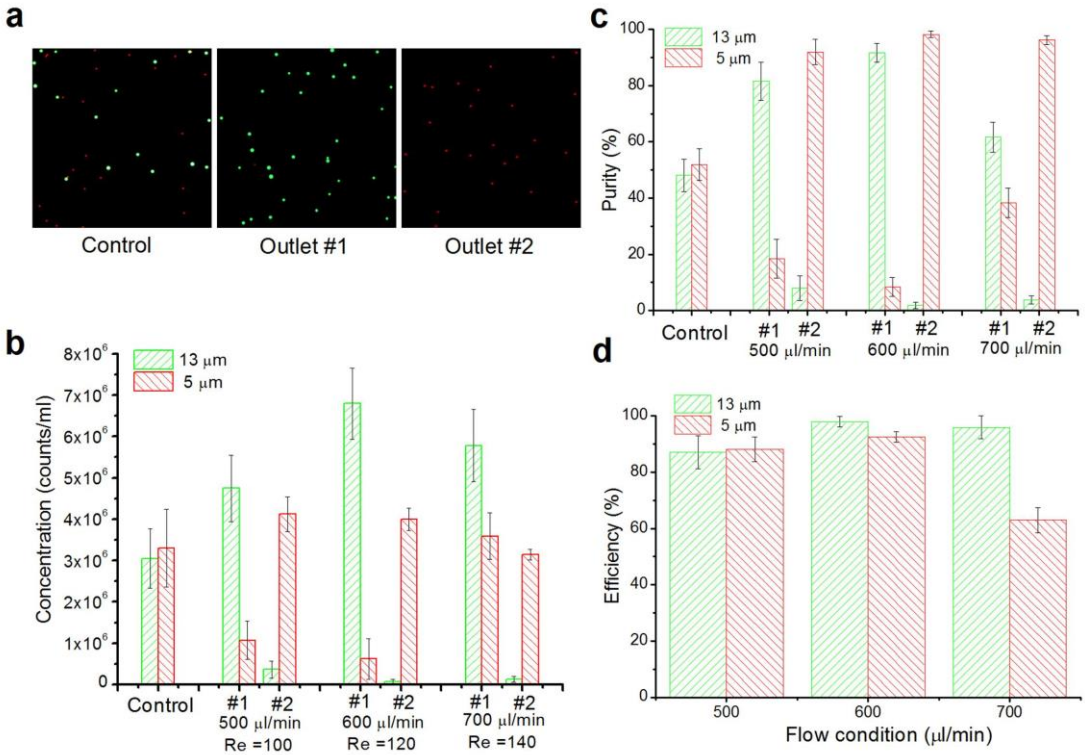

Figure 5–6 Separation of 5 μm and 13 μm particles in the serpentine channel. (a) Fluorescent images of collections from control and two outlets. Pseudo-colored green and red dots represent 13 μm and 5 μm particles respectively. (b) Particle concentrations from control and two outlets under three different processing flow conditions. (c) The purity of particles from two collectors at various flow conditions. (d) The separation efficiency for 5 μm and 13 μm particles under different flow conditions. Error bars represent the standard deviation of three measurements by hemocytometry.

5.3.3 Separation of biological particles

5.3.3.1 Murine erythroleukemia (MEL) cells and 5 μm polystyrene beads

MEL cells, as a commonly used model of red blood cell biology [195, 196], are used to investigate molecular events involved in the oncogenesis of erythroleukemias [197]. Microscopic measurements of 70 randomly selected MEL cells revealed that

live MEL cells have a mean diameter of ~12.6 µm with a standard deviation of ~2 µm. In order to test the separation capacity of our device on biological cells, MEL cells were mixed with 5 µm polystyrene particles at a ratio of ~1:1 in PBS solution. The mixture was then pumped into the microfluidic device under the optimal flow rate of 600 µl/min. Beads and MEL cells concentration and purity from input mixture and two collections from outlets were plotted in Figures 5-7(a, b). The flow cytometry system (BD), which characterizes the bio-physical properties of cells through laser beam detection in one-by-one manner, was employed to evaluate the separation purity in our work. The flow cytometric data were plotted as forward scatter FSC to side scatter SSC, as shown in Figure 5-7(c), as well as FSC to cell counts in Figure 5-7(d). Excellent separation purity can be concluded from the flow cytometric data, and it further supports the high separation performance of our device.

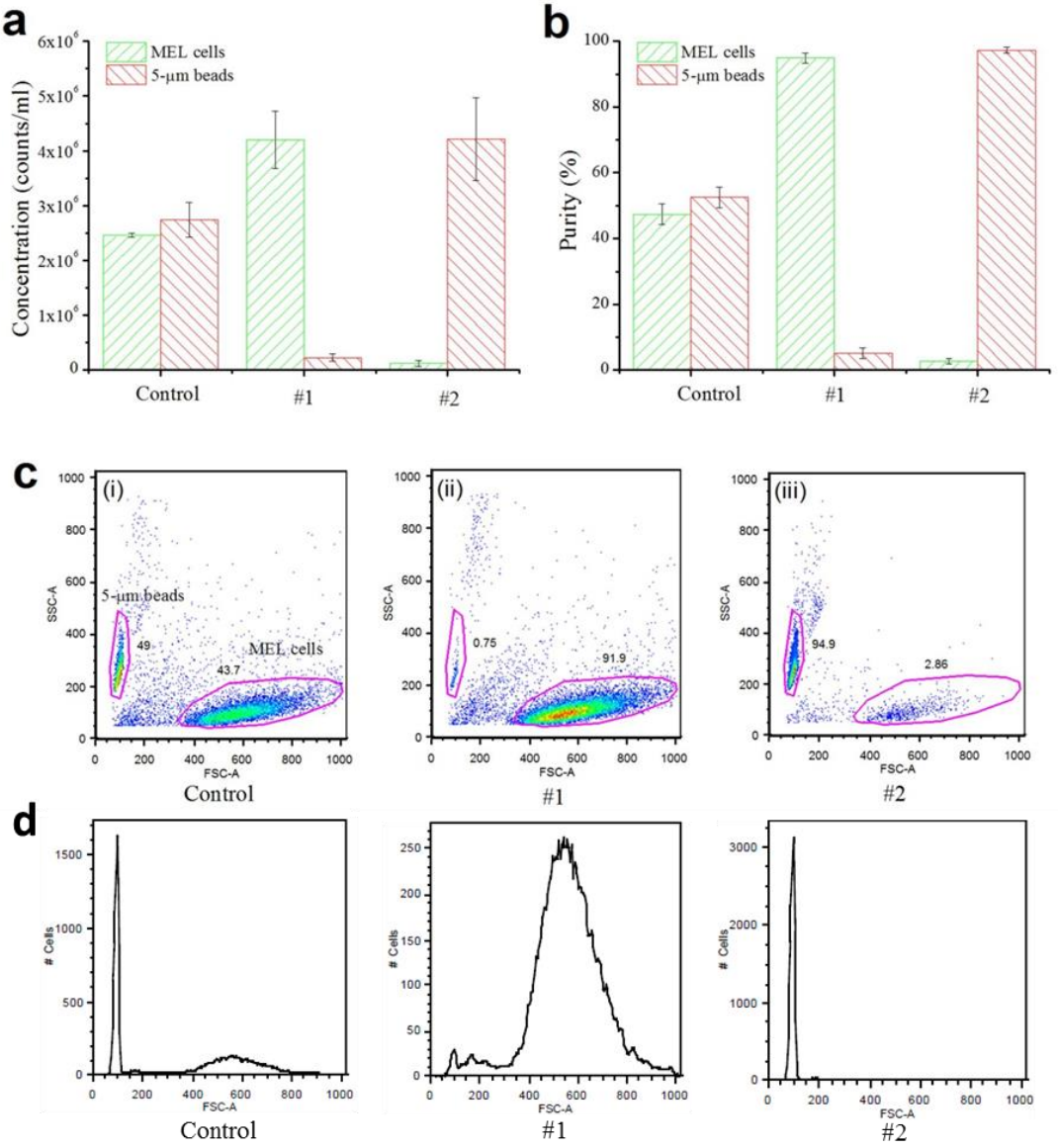

Figure 5–7 (a) Concentrations of 5 μm polystyrene beads and MEL cells from control and two outlets under the flow condition of Re=120. (b) Purity of 5 μm polystyrene beads and MEL cells before and after a single process by the proposed microfluidic device. (c) FSA-SSC data of flow cytometric data indicate relative percent of (i) input mixture of 5 μm polystyrene beads and MEL cells, (ii) collection from outlet #1, and (iii) collection from outlet #2. The number near the gated group represents the percentage of group number on the total particle events. (d) FSA-cell counts data reveals the cell/particle size distribution from each collection. The FSA data is proportional to the particle size.

The bright field and fluorescent images of each collection were shown in Figure 5-8. Within our expectations, sample collected from outlet #2 resulted in a very high

purity (~98%) of 5 μm particles. Also, a high purity of ~94.9% was also achieved for MEL cells obtained from outlet #1.

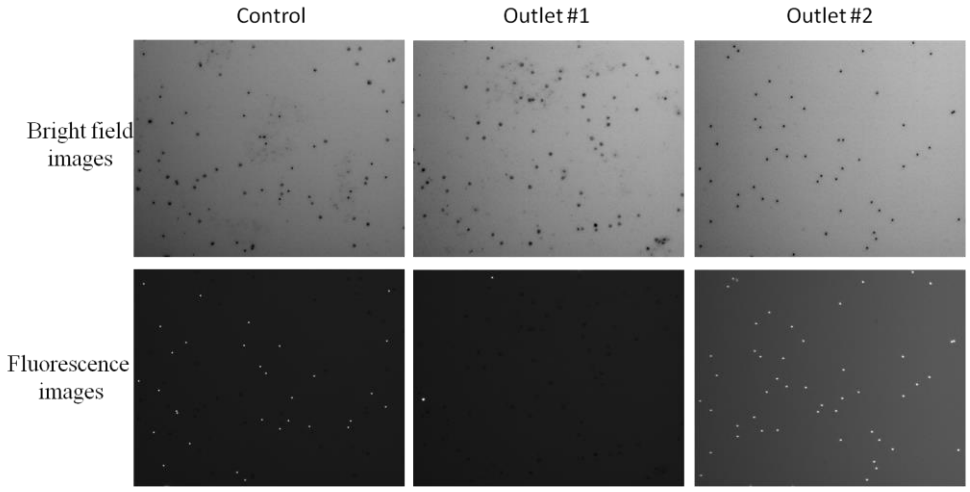

Figure 5–8 The bright field and fluorescence images from control and two collections. In bright field image, both of MEL cells and 5 μm polystyrene beads can be observed. While in fluorescent images, only 5 μm fluorescent polystyrene beads can be observed. The number of MEL cells can be easily obtained by subtracting number of 5 μm polystyrene beads from the total number of MEL cells and 5 μm polystyrene beads.

5.3.3.2 Erythroleukemia (MEL) cells and Blood cells

Additionally, MEL cells were spiked into the human blood sample as a model of circulating tumours cells. The ratio of MEL cells to human blood cells was set as 1:100, and the concentration of the whole cells was around 5×10^7 counts/ml. The results of separation of MEL cells from human blood cells in a single process were plotted in Figure 5-9. The purity of MEL cells can be improved from 1.25% to 45.4%, indicating an effective purification and enrichment of MEL cells.

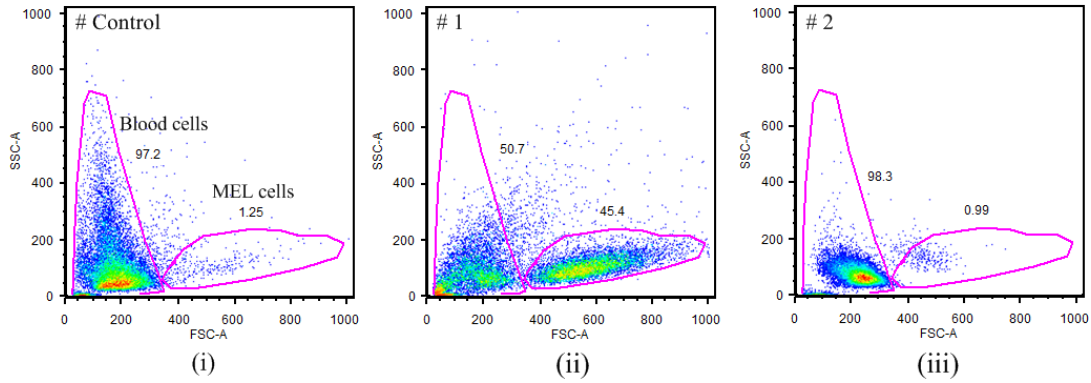

Figure 5–9 Separation of MEL cells from the whole blood cells. (i) FSC-SSC results of cells mixture; (ii) FSC-SSC results of collection #1 indicate purified MEL cells; (iii) FSC-SSC results of collection #2.

5.3.3.3 White blood cells from the whole blood

The interaction of particles in the microchannel influences the performance of inertial focusing and separation in inertial microfluidics, and dilution of whole blood sample to a lower concentration is a common practice to reduce their interference. We used the proposed device to process the whole blood diluted by ×1/20 PBS. With two processes, the white blood cells are increased from 0.26% to 40.4%, Figure 5-10, with an enrichment ratio of 155.4. The average enrichment ratio for one process is around 12.5. It can enrich the white blood cells once just ~1/1000 of red blood cells number to the amount of the same order.

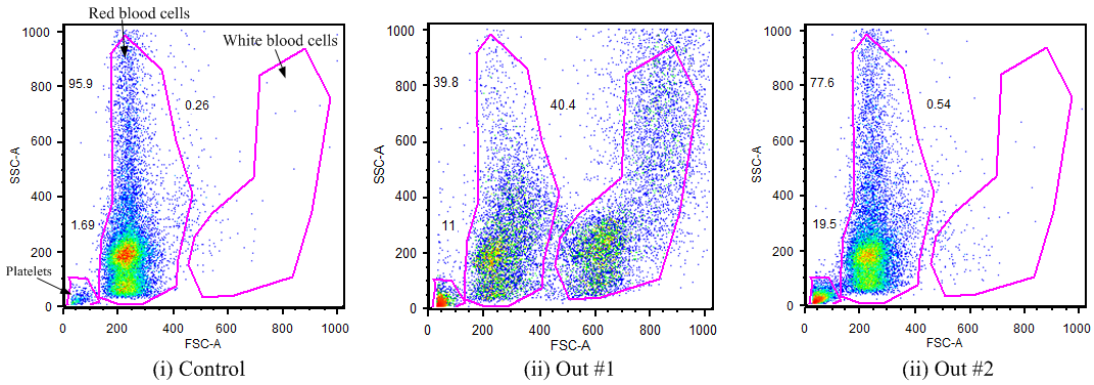

Figure 5–10 Separation of white blood cells from the whole blood. (i) FSC-SSC results of input whole blood cells, it is very hard to observe the existence of white blood cells from massive red blood cells; (ii) FSC-SSC results of collection #1, the

percentage of white blood cells is increased to about 40.4%; (iii) FSC-SSC results of collection #2.

Particle separation in the device reported here relies on the overlap area between inertial lift force dominated region (region I) and Dean drag force dominated region (region III) for different-sized particles, Figure 5-1. Normally, small particles have a wider region I, and large particles have a wider region III. The overlap between these areas is the working space available for particle separation. The cut-off size of particles in this work was around 8 µm, equivalent to 20% of the channel height. Demonstrated size difference for particle separation were 7 µm (for 3 µm and 10 µm particles mixture) and 8 µm (for 5 µm and 13 µm particles mixture) respectively. Although we demonstrated that the complete separation happened at the overlap of region I and region III. In the actual situation, an efficient separation can still be achieved between region I and region II. In the region II, particles are focused to a band at the channel centre, which have not reached complete focusing. If the lateral distance between this focusing band of large particles and two-sided focusing streaks of small particles is large enough, particle separation can still be achieved with carefully tailored trifurcating outlets. For example, under the condition of a channel Reynolds number of Re=120, Figure 5-1(a), particles with a diameter of 8 µm are focused at the central area of channel with a width of 37 µm. Under the same flow condition, 5 µm particles are focused at the two sides of the channel symmetrically, 58 µm away from channel centre, with each streak width of about 15 µm. So the minimum lateral distance between 8 µm and 5 µm particle streaks is about 32 µm, which is still sufficient for particle separation using the right outlet geometry. Therefore, the actual size difference for complete particle separation could be much smaller, even less than 3 µm.

In our work, due to the assistance from secondary flow, inertial focusing can be achieved within much shorter channel length in a serpentine channel than that in a straight channel [136], therefore leading to a smaller device footprint. In addition, the separation performance (purity and efficiency) is improved greatly than the reported asymmetric serpentine channel [172], and even comparable to the most outstanding spiral inertial microfluidic devices [128, 136, 154]. After a detailed comparison of existing inertial microfluidic techniques to our work, as shown in Table 1, we can

conclude that the proposed device holds an integrative advantage over existing ones, including excellent separation purity and efficiency, good parallelizability, small footprint and high separation resolution, although it is not significantly superior on specific single criteria.

5.4 Conclusion

In this chapter, we investigated the complete separation of particles by size-dependent differential equilibrium positions in a symmetric serpentine channel. We first examined the focusing patterns of different-sized particles under varying flow conditions, and plotted these focusing patterns into a Reynolds number - particle size map. From this map, the available working area for particle separation can be easily determined. Finally, the separation ability is evaluated by a series of particle mixtures, including erythroleukemia cells with 5 μm polystyrene particles, erythroleukemia cells with blood cells, and different blood cells. Excellent separation purity and efficiency was demonstrated. In conclusion, the proposed inertial microfluidic device is expected to be a good alternative for the conventional separation devices. And it promises a cost-effective, label-free and robust method for the cell preparation and clinical diagnosis.

Table 1 Comparison of existing inertial microfluidic techniques for binary-particle separation

Channel Type	Throughput	Purity	Efficiency	Channel dimension	Device footprint	Particle size/cell type	Size difference (Resolution)	Need sheath flow?	Parallelizability	Reference
Straight	Re=40 (100 μlmin-1)	20 μm particle 90.8% 9.94 μm 99.6%	20 μm particle 99.3% 9.94 μm 94.5%	27 μm×50 μm (width×height) upstream 100 μm×50 μm downstream	Straight micro-channel section >36mm	9.9 μm, 20 μm polystyrene beads	~10 μm	No	Good	[136]
	40 parallel channels with 240 ml/h, 4×10^8 cells/min	NA	88% red blood cells (RBCs) E Coli: NA	20 μm×60 μm upstream 160 μm×60 μm down stream	7cm×7cm	RBCs~8 μm Eschericha coli ~1 μm	~7 μm	No	Good	[135]
Expansion-contraction array	111 beads/s	10 μm particle 100% 4 μm particle 99%	NA	CEA 350 μm ×38 μm Contraction region 50 μm ×300 μm	Micro-channel length >9 mm	4 μm, 10 μm polystyrene beads	6 μm	Yes	Good	[128]
	$1.1x10^8$ cells/min Re=8	Blood cell reject ratio 88.9%	Cancer cells: 99.1% Blood cells: NA	CEA 350 μm ×63 μm Contraction region 50 μm ×1200 μm (width×length)	Micro-channel length >11.4 mm	MCF-7 , blood cells	NA	Yes	Good	[154]
Spiral	3 ml/hr	NA	Cancer cell lines >85% Blood cells: NA	Spiral channel 500 μm×160 μm	Total micro-channel length ~10cm	MCF-7, Hela, MDA-MB-231	NA	Yes	Hard	[148]
	7.5 ml blood within 8 mins	NA	>80% Blood cells:NA	Width 100 μm Inner/outer height 80 μm/130 μm	NA	T24, MVF-7, MDA-MB-231	NA	No	Hard	[144]
Double spiral	3.33×10^7 cells/min	NA	99.66%: 5 μm particles 92.75%: 15 μm particles 88.5% tumor recovery	300 μm in width and 50 μm in height The radius of the outermost curvature is 9 mm	NA	5 μm, 15 μm polystyrene beads MCF-7 and Hela cells spiked in whole blood	10 μm	No	Hard	[142]
Asymmetric serpentine	0.9 ml/min R_p=1.53	9 μm particle: 16.3% one tier, 25.3% Two tier processes 3.1 μm particle: ~99.9% after two tiers	3.1 μm: ~56% after two tiers; 9 μm: NA	Height: 50 μm Width: 100~650 μm	Channel length ~6.9cm	3.1 μm and 9 μm polystyrene beads	~6 μm	No	Good	[172]

Symmetric serpentine in this work	600 μl/min Re=120 4.8ml/min for 8 parallel serpentine channels	3 μm:~99% 10 μm:~88.7% 5 μm:~99.2% 13 μm:~~91.6% 5 μm:~98% MEL cells:~94.9%	Large particles:>97% Small particles:>92%	200μm×42μm	Whole device: 36 mm×5mm (length ×width); Serpentine channel with a length of ~15mm	3,5, 10 and 13-μm polystyrene beads and MEL cells Human blood cells and MEL cells	~7 μm demonstrated; ≤ 3μm in principle	No	Good	This work

6 REAL-TIME CONTROL OF INERTIAL FOCUSING IN MICROFLUIDICS USING DIELECTROPHORESIS (DEP)

6.1 Introduction

In microfluidics, there are active techniques [7-9] and passive techniques [5, 10, 11] according to the source of manipulative force. An active technique generally allows for a more precise control of target particles, while being very flexible for a wide range of biological particles and tuneable in real-time. However, the flow speed is always limited because particles must be exposed to the outer force field for sufficient duration to achieve effective functionality, which reduces their throughput. In contrast, a passive microfluidic device is always very robust and has a high throughput. However, the fixed geometry and design of passive devices limit their manipulative capability, making them only effective for a specific range of particle properties. Ideally then, a combination of high-throughput passive techniques with precisely tuneable active ones would result in a more powerful and versatile platform.

Attempts to combine active and passive techniques in one microfluidic device have been reported in the past [158, 174, 176, 198]. In most of these reported works, the active and passive techniques are actually connected in series, where there is no coupling of physics. To broaden the scope and capability of microfluidic technology further, in this chapter, we explored the possibility of combining DEP and inertial focusing in a fully-coupled manner, and proposed a new scheme which is called DEP-inertial microfluidics [4]. A vertical DEP force was used to levitate particle equilibrium positions vertically to the centre of the channel. Due to the no-slip boundary, the fluid velocity at the centre of the channel is at its maximum, which imposes a much stronger secondary flow (Dean) drag onto the particles. This means the inertial focusing pattern and position of the particles along the horizontal plane can even be tuned. The mechanism of this tuneable DEP-inertial microfluidic device was discussed, and the effects of the DEP force on each inertial focusing pattern were investigated.

[4] Results of this chapter are published in: [199] Zhang, J., Yan, S., Alici, G., Nguyen, N.-T., Di Carlo, D., and Li, W. (2014) Real-time control of inertial focusing in microfluidics using dielectrophoresis (DEP), *RSC Advances 4*, 62076-62085.

6.2 Materials and Methods

6.2.1 Design and fabrication of the DEP-inertial hybrid device

The serpentine channel used in our experiments consisted of 15 symmetric zigzag periods. The width of the micro-channel was 200 μm. The length and width of each U-turn were both 700 μm. The height of the channel was uniformly 40 μm. The polydimethylsiloxane (PDMS) slab embedded with the micro-channel was fabricated by standard photolithography and soft replica techniques [177]. On the glass slide, a 50-nm Ti/150-nm Pt electrode layer was patterned using the standard lift-off process [47]. The spacing and width of the interdigitated electrodes (IDEs) were both 20 μm. The IDEs were 13.5 mm long, which left one zigzag period of micro-channel uncovered by IDEs to allow for the clear observation of particle trajectory. The PDMS slab and glass slide were bonded with the help of oxygen plasma after being carefully aligned. Figure 6-1 shows a schematic illustration and photo of the proposed DEP-inertial microfluidic device.

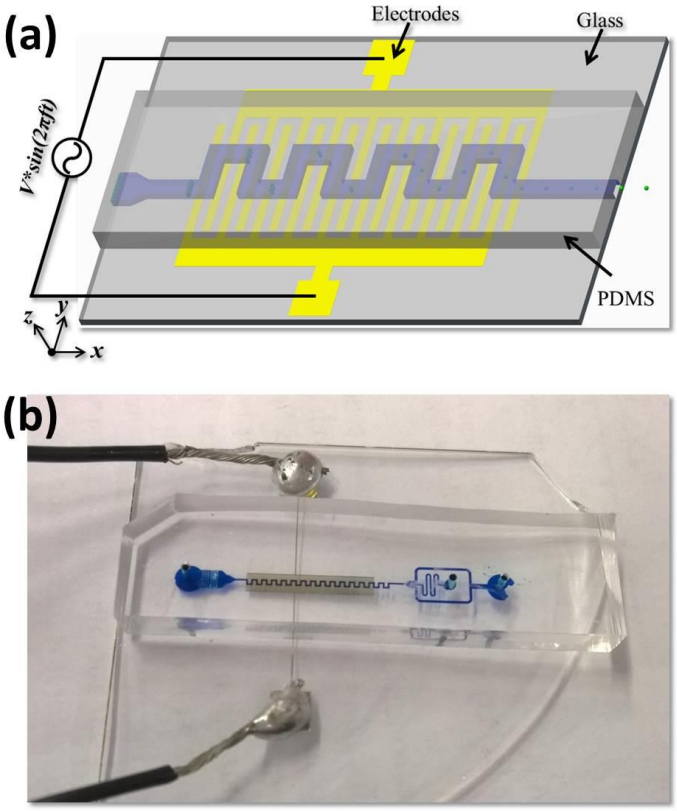

Figure 6–1 (a) Schematic of DEP-inertial microfluidic device; and (b) the photo of DEP-inertial microfluidic device. The serpentine micro-channel is embedded in the

PDMS slab, and the slab is bonded with a clean glass slide where interdigitated electrodes (IDEs) are patterned. The particle suspension is delivered into the micro-channel by a syringe pump. An alternating current (AC) signal is imported into the IDEs, activating DEP force to levitate particles along the vertical *z* direction.

6.2.2 Particle preparation

Internally dyed fluorescent polystyrene particles (10 μm in diameter, Thermo Fisher Scientific) were suspended in deionized (DI) water with 0.025% *w*/*w*. Tween 20 (SIGMA-ALDRICH Product No. P9416) with 0.1% *w*/*v* was added to prevent the particles from aggregating. Bulk conductivity and permittivity of the polystyrene beads are 2.4×10^{-4} S/m and $2.6\varepsilon_o$, respectively. The conductivity and permittivity of DI water are 1.5×10^{-4} S/m and $78\varepsilon_o$, respectively [200].

6.2.3 Experimental setup and methods

The sinusoidal signal with a frequency of 1 MHz was generated by a waveform generator (33250A, Agilent, USA) and amplified by an RF power amplifier (TIA-1000-1R8-2, Mini-Circuits, USA). The applied frequency in all experiments was set to 1 MHz. Copper wires with one end soldered onto the IDEs pads were connected to the power amplifier to activate the electrodes.

6.3 Mechanism

6.3.1 Inertial migration

As mentioned in Chapter 2, the net inertial lift force F_L is expressed by equation (2-35b) when the particle size is small compared with the channel size [5, 91]. The situation of F_L=0 corresponds to the dynamic stable and unstable equilibrium positions. The introduction of channel curvature in the downstream direction introduces additional inertial forces from the fluid (secondary flow drag) and the particles (centrifugal force), which will modify and assist the inertial focusing progress [95]. Normally the particle centrifugal force is negligible unless the particle has quite different density compared with the fluid. Subsequently, the focusing pattern (e.g. position and number of dynamic equilibrium positions) is always determined by the competition between secondary flow drag and inertial lift force. When secondary flow is too weak to alter inertial focusing, the focusing pattern is

still determined by the inertial lift force, and particles are normally ordered on the two sides of a channel [184]. If the secondary flow is strong enough, it can modify particles as a single stream in a curved channel from top view [4, 95, 183].

6.3.2 The n-DEP force in interdigitated electrodes (IDEs)

Dielectrophoretic (DEP) forces occur on particles/cells when a non-uniform electrical field interacts with field-induced electrical polarisation. A particle immersed in an alternating electrical field is subject to a time-averaged DEP force determined by the frequency-dependent polarisability of the particle relative to the medium, given by [201]:

$$F_{DEP} = 2\pi\varepsilon_m r_p^3 \,\mathrm{Re}[K(\omega)]\nabla\left|E_{rms}\right|^2 \tag{6-1}$$

where ε_m is the permittivity of the medium, r_p represents the particle radius, $|E_{rms}|$ is the root-mean-squared value of the applied electrical field, and $K(\omega)$ refers to the Clausius–Mossotti (CM) factor. Re indicates the real part of the factor, and $K(\omega)$ depends on the relative permittivity of the particle and the suspending medium, as well as the frequency of the external electric field.

$$K(\omega) = \left(\varepsilon_p^* - \varepsilon_m^*\right) \Big/ \left(\varepsilon_p^* + 2\varepsilon_m^*\right) \tag{6-2}$$

where $\varepsilon^* = \varepsilon - i\sigma/\omega$ is the complex permittivity, σ is the electrical conductivity, and ω is the frequency of the electric field. The subscripts p and m denote the particle and suspending medium, respectively.

When the dielectric constant of a particle is larger than the medium, $\mathrm{Re}[K(\omega)]>0$, the DEP is positive, and particles move towards the location with the highest electric field gradient. But when the dielectric constant of a particle is smaller than the medium, $\mathrm{Re}[K(\omega)]<0$, the DEP force is negative and particles move to locations with the lowest electric field gradient.

In the present work, an IDEs array was patterned onto the bottom of the micro-channel to generate a negative DEP (n-DEP) on the particles and push them upwards, Figure 6-2(a). Since the DEP force in the horizontal direction is relatively small and negligible, we focused on the vertical DEP force (F_{DEPz}) and its counteraction with

the inertial lift force along the vertical plane. Without a specific notice, the DEP force in the whole manuscript indicates the DEP force component in the vertical (z) direction. Near the surfaces of the electrodes ($z \leq 10$ μm), the magnitude of DEP force oscillates along the longitudinal (x) direction. The peak points are on the edges of the electrodes, while the trough points are at the centre of the electrodes and their gaps. Moreover, the closer the particle to the electrode covered surface, the higher is the magnitude of the oscillation, Figure 6-2(b). Meanwhile, when particles move away from the surface of the electrodes, the magnitude of the DEP force decreases sharply as well as the magnitude of oscillation, Figure 6-2(b and c). However, the DEP force remains almost constant in the longitudinal direction, within the region far from the surface of the electrodes ($z \geq 10$ μm). When fluid flows rapidly through this microchannel patterned with IDEs, e.g. Re~100 (or U~1 m/s), the particles suspended in the medium will follow the main streamline at a very high speed. The net effect on particles of the fluctuating DEP force depends on its average magnitude.

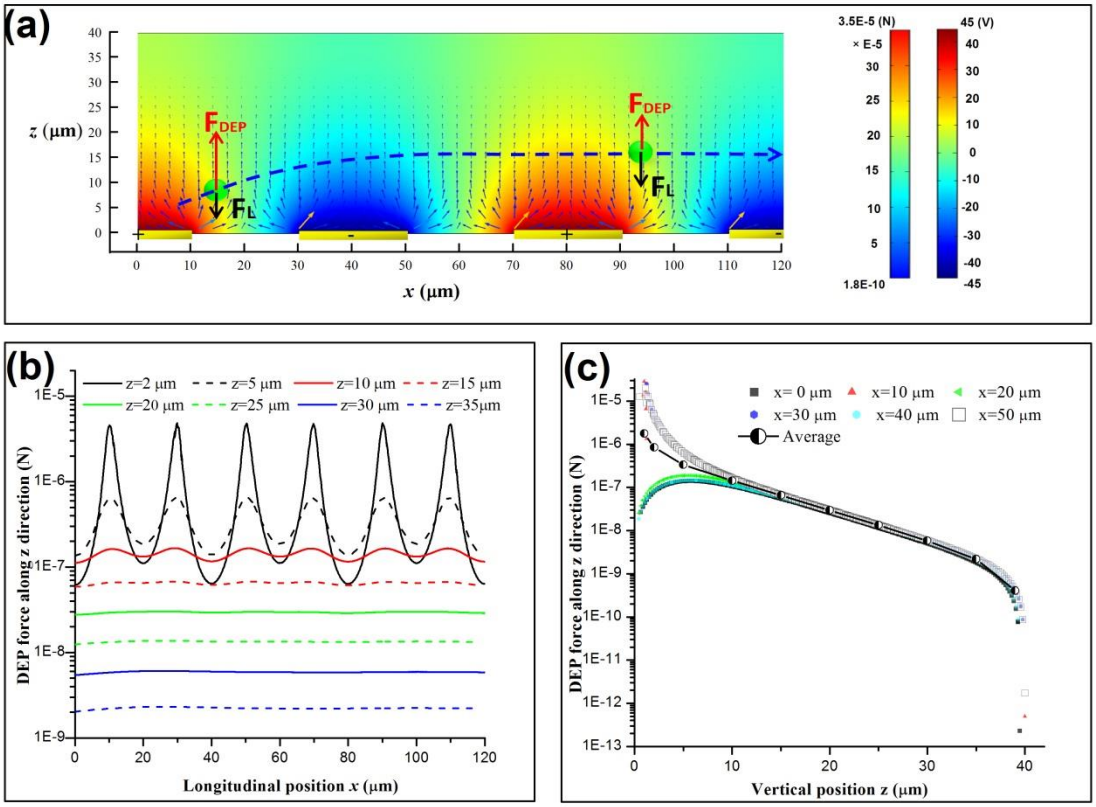

Figure 6–2 (a) The electrical field and n-DEP force distribution within a longitudinal section. The arrow vectors represent the magnitude and direction of n-DEP force. The magnitude of n-DEP force along *z* direction is implied by the vectors' colour, and corresponds to the left colour bar. Colour map surface shows the electric field distribution, and corresponds to the right colour bar. (b) Longitudinal distribution of n-DEP force along *z* direction (F_{DEPz}). (c) Vertical distribution of n-DEP force along *z* direction (F_{DEPz}). COMSOL Multi-physics 4.3 was used to calculate the electric field, and the DEP force was calculated using equation (6-1). Particle diameter is 10 μm, and Re[$K(\omega)$] for polystyrene beads in DI water at electric frequency of 1MHz is approximated as -0.5.

6.3.3 Coupling of n-DEP force and inertial lift force along vertical direction

If particles are close to the walls of the channel in the vertical direction *z*, a wall lift force F_{LW}, generated by the wall-induced disturbance on the flow field around the particles, pushes them towards the centre of the channel. The parabolic nature of the fluid velocity profile directs the shear gradient induced lift force F_{LS} towards the channel wall, acting against the F_{LW}. The net inertial force F_L, the dashed curve in Figure 6-3(a), exhibits two dynamic stable equilibrium positions located about 0.2 times the height of the channel away from the walls. In addition, these equilibrium positions move closer to channel walls with increasing Reynolds number [202].

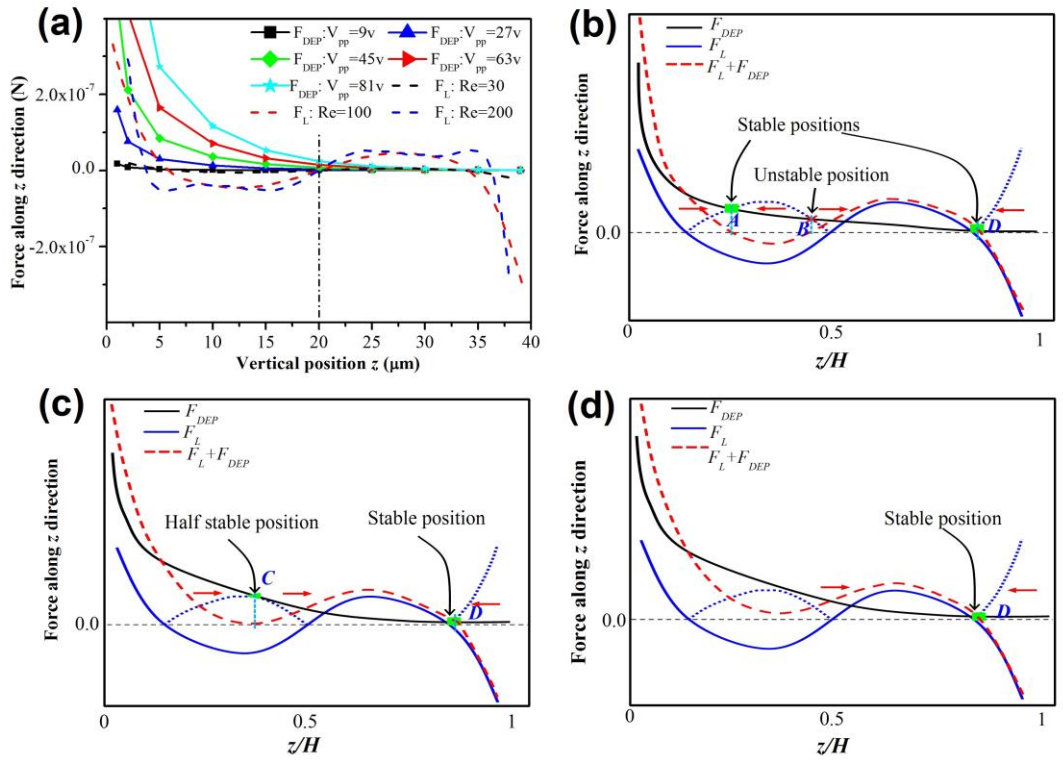

Figure 6–3 (a) The distribution of dielectrophoresis (DEP) force F_{DEP} and inertial lift force F_L along the height of the channel z. The inertial lift force is obtained from the analytical solution from Matas et al. [116, 202] and n-DEP force is obtained from the simulation results by COMSOL Multi-physics. Particle diameter is 10 μm. (b) At relative low applied voltages, two stable equilibrium positions (A and D) along z exist, which are modifications of the original inertial equilibrium positions. The direction of the net force (red arrows) on both sides of stable positions will always point to themselves because they can overcome any small disturbance. However, point B is in an unstable position because the net force along both sides is directed outwards, and a little disturbance will induce the particles to move away from point B. The blue dashed curve is the mirror image of the F_L negative part on a positive coordinate. (c) At a critical voltage (V_{cpp}), the F_{DEP} curve is tangential with the F_L negative mirroring curve at point C, which is in a half stable (saddle) position. If particles were shifted downward ($z < z_C$), the net force will attract particles back to position C, but when the particles were shifted upward ($z > z_C$), the net force is directed upwards and particles will never return. (d) When the applied voltage is higher than the critical voltage V_{cpp}, there is only one vertical equilibrium position D on the upper half of the channel.

The n-DEP force is always upwards (positive z direction), shown as solid curves in Figure 6-3(a), which is consistent with the direction of F_L near the bottom of the channel. The particles in this region ($z<0.2H$) experience a large upward net force and migrate rapidly away from the surface of the channel. If the particles reach the region where F_L is negative, three different situations occur: (i) At low voltage, the DEP force curve intersects with the negative F_L mirroring curve (blue dashed line) at points A and B on the bottom half of the channel, as well as at point D which is very close to the original inertial equilibrium position F_L=0 on the top half, Figure 6-3(b). Between A and B ($z_A<z<z_B$), the net force of F_L and F_{DEP} is negative and is directed downwards. However, outside the A-B section ($z<z_A$ or $z>z_B$), the net force is positive. Therefore, point A is a stable equilibrium position because the net force is directed at point A on both sides, which can overcome any small disturbance and draw particles back to point A. Meanwhile, point B is an unstable position because the net force on each side is directed outwards, so even a little disturbance can easily induce particles to move away. (ii) At a critical voltage V_{cpp}, the F_{DEP} curve is tangent with the F_L mirroring curve at a point C, Figure 6-3(c). This is a half stable position because the net force always points to the positive z direction no matter it's below or above point C. If particles were shifted below ($z < z_C$), the net force will attract particles back to position C. If particles were shifted above ($z > z_C$), the net force is directed upwards and the particles will never return. So very few particles are stable at point C. (iii) When the applied voltage is larger than V_{cpp}, there is only one node D on the top half of the channel, Figure 6-3(d), and it is common to the other two situations. This point is very close to the original inertial equilibrium positions because the DEP force decreases exponentially with increasing z and is negligible on the top half of the channel with almost no effect on the inertial equilibrium position.

We can conclude from this discussion that particles will gradually be levitated as the applied voltages (DEP force) are increased. Finally, all the particles will be focused into the equilibrium position D on the top half channel if the DEP force at point C can overcome the inertial lift force. A schematic illustration of particle migration progress in the channel cross-section under increasing voltage is shown in Figure 6-4. It should be noted that the force of gravity [$F_G= (4/3)\pi r_p^3(\rho_p-\rho_f)g$] was omitted in this analysis because the density of particles (ρ_p=1050 kg·m^{-3}) was very close to its suspension medium (ρ_f=1000 kg·m^{-3}).

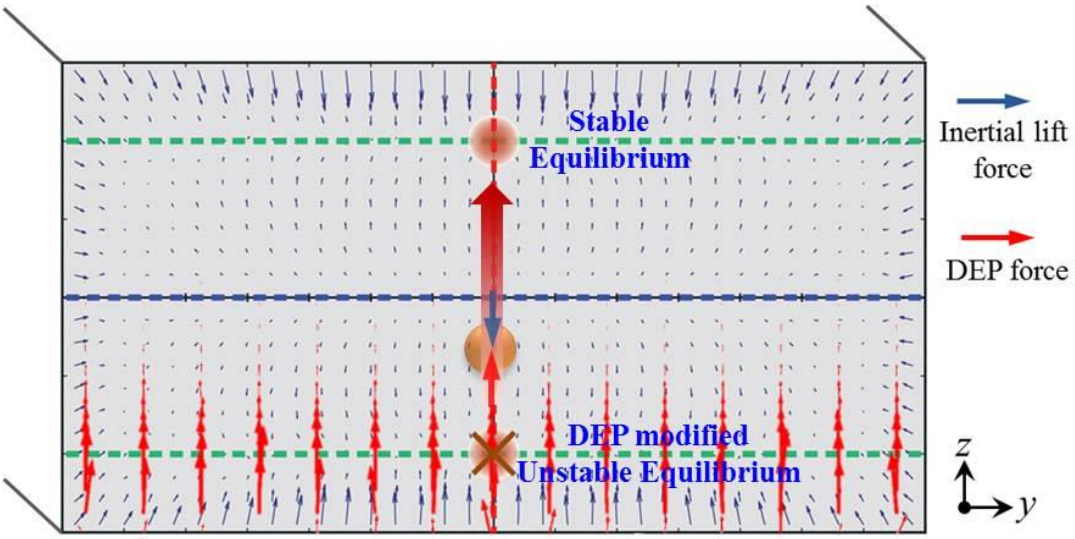

Figure 6–4 A schematic illustration of particle migration progress in the channel cross-section under increasing voltage within a cross section of DEP-inertial microfluidic device. DEP force competes with inertial lift force along *z* direction, thus alters the final vertical position of particles. As a result, the inertial focusing process and pattern can be tuned in three dimensions.

Because of the no-slip boundary condition, the fluid velocity is zero at the walls of the channel and at its maximum velocity in the centre of the channel. The secondary flow drag [$F_D=3\pi\mu a(v_{fr}-v_{pr})$] is enhanced if the particles are levitated towards the vertical centre of the channel by DEP force. Then, the particle trajectory along the horizontal plane will be modified. Here, v_{fr} and v_{pr} are the radial velocity of fluid and particles respectively [4]. Finally, by using DEP force to control the vertical position of particles, their inertial focusing pattern in 3D can be modified and adjusted.

In order to test the above hypothesis, we developed a numerical model of the serpentine micro-channel, and released micro-particles from different heights at the inlet using particle tracking module in COMSOL Multiphysics. The results showed that particles released near the channel vertical centre can migrate and focus much faster to the channel lateral centre than those released near channel walls, Figure 6-5, which agreed with our hypothesis. It should be noted that in this simulation, inertial lift force were not taken into account, since there is not an explicit equation to

express it, furthermore it is not easy to implement it in a curved channel with alternating curvatures in the numerical simulation.

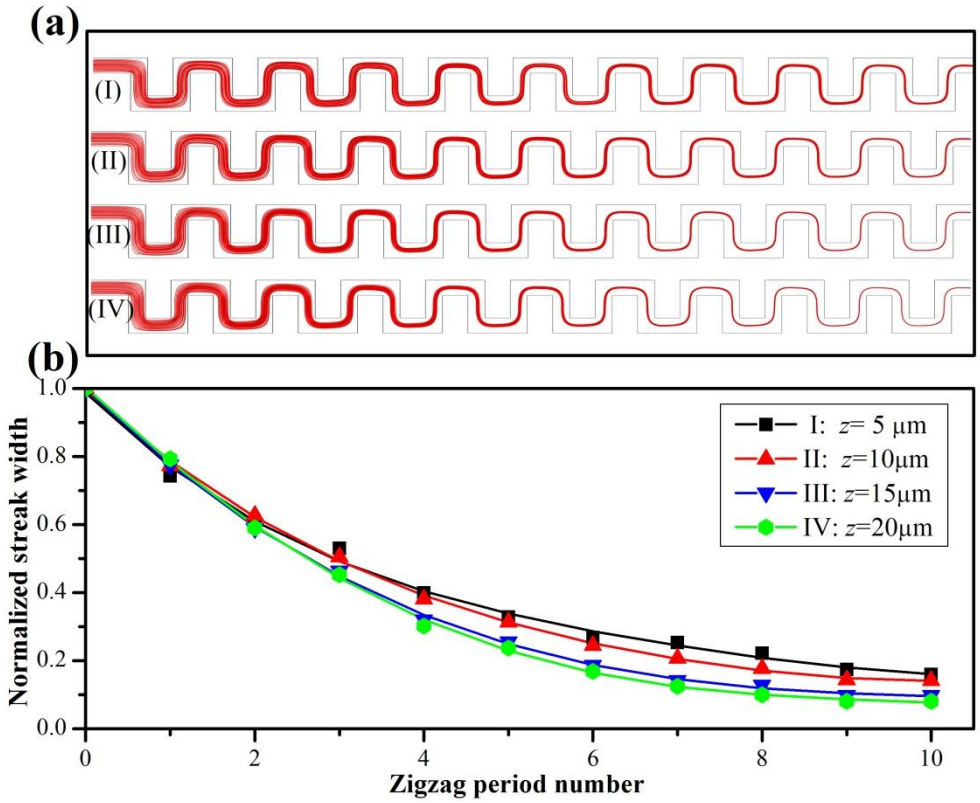

Figure 6–5 (a) Simulated particles' trajectories released from different heights. (b) Normalized particle streak widths after traveling through different channel lengths. The particles released near the channel vertical centre focus into the channel lateral centre much faster than that released near channel walls, because fluid velocity is at maximum at the channel centre, and its corresponding secondary flow drag and centrifugal force is much stronger than that near channel walls.

In the following sections, the pure inertial focusing pattern and its equilibrium positions in a serpentine channel were first presented, without applying the DEP force field. Under different Re, three basic focusing patterns emerged. Next, a vertical DEP force generated by IDEs was applied onto these three inertial focusing patterns respectively, to explore its effects on inertial focusing patterns. Finally, a V_{pp}~Re map was summarised to illustrate the dominance of force under different working conditions.

6.4 Results and Discussions

6.4.1 Inertial focusing patterns in serpentine channels under varying Re

In a previous work, we discussed the mechanism of inertial focusing in a serpentine channel [4], and showed how particles with different sizes were separated according to their differential lateral positions [183]. In order to observe the side-view, a PDMS device was fabricated from three PDMS slabs using the method reported by Reference [17], Figure 6-6(c). The PDMS device could be placed vertically onto the microscope stage, giving a clear, side view of the serpentine channel, Figure 6-6(b). The top view and side view enable the dynamic equilibrium positions of the particles to be determined easily.

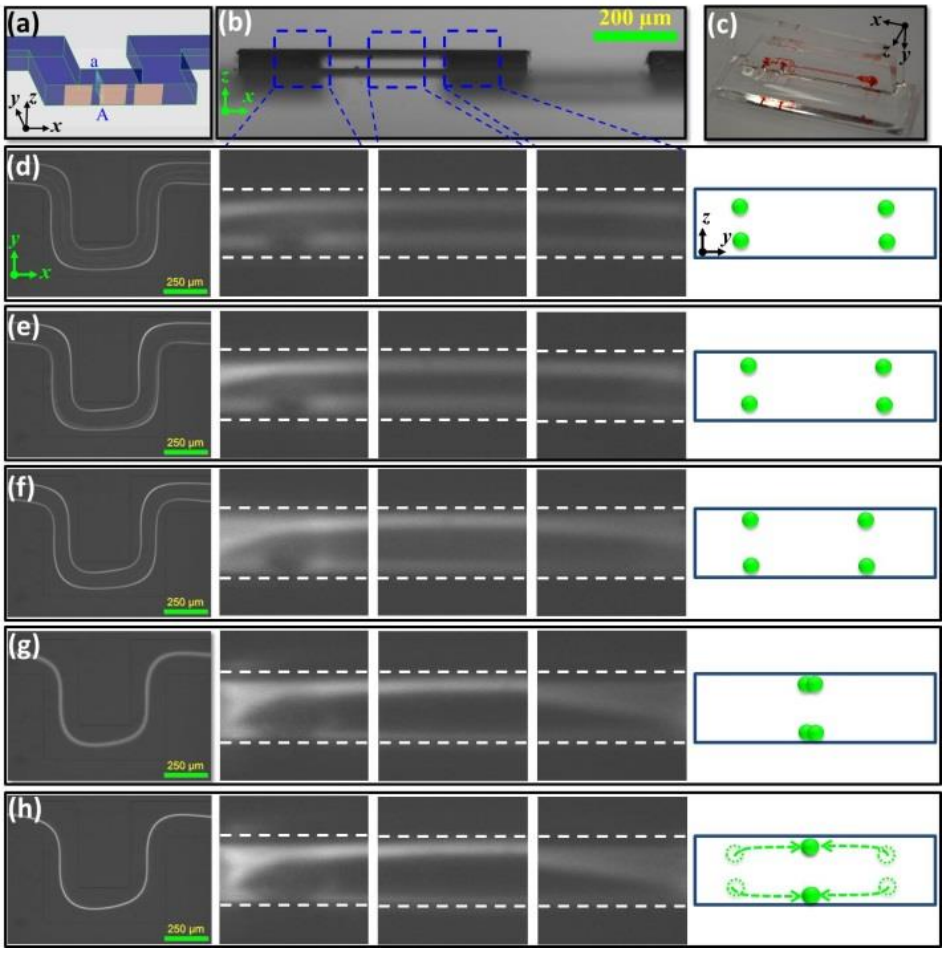

Figure 6–6 (a) Schematic 3D structure of one period in the serpentine channel and (b) its side view optical image; (c) The fabricated PDMS device was used to observe the serpentine channel from both top-down and side-side view in the experiments. (d-h) Inertial particle focusing patterns under varying flow conditions: (d) Re=41.7; (e)

Re=62.5; (f) Re=83.3; (g) Re=104.2; (h) Re=125. (Left) Top views of fluorescent particles trajectory at the last zigzag period of serpentine; (Middle) Sided views of fluorescent particles at the last zigzag period; and (Right) The dynamic equilibrium positions of particles at cross-section A-a.

From the top view [Left in Figure 6-6(d~h)], focusing streaks could be seen on the two sides of the channel at a relatively low Re, Figure 6-6(d~f), but as the Re increased, these two-sided focusing streaks migrated towards the centre of the channel, moved closer and closer together and then merged into a single wide streak, Figure 6-6(g). This was because the secondary flow drag increased much faster than the inertial lift force within the horizontal plane as Re increased. They gradually dominated the two-side-directed inertial lift forces and finally pinched the particles into the centre of channel, where the net drag forces are weaker and partly cancelled. As Re continued to increase, the focusing streak became tighter until its width could reach the single diameter of a particle. The side view, Middle in Figure 6-6(d~h), shows two focusing streaks near the top and bottom walls, which migrated toward the top and bottom walls as Re increased, in agreement with previous reports [91, 95, 202]. The dynamic equilibrium positions within the cross section "A-a" were deduced and were illustrated schematically (green dots) in the right of Figure 6-6(d~h). In summary, as Re increased, the dynamic equilibrium positions in a serpentine channel shifted towards the centre of channel in the lateral direction (y), as well as moving closer to the walls of channel in the vertical direction (z).

6.4.2 Influence of n-DEP on two-sided inertial focusing pattern: modification of focusing pattern by levitation of particles

At a relatively low Re (41.7 to 83.3), the focusing streaks at the bottom half of the channel (blue dots) were symmetric with those on the top half (green dots) along the vertical centreline, which is observed as two streaks from a top view, Figure 6-7(a). However, when a DEP force was applied to deflect the particles upwards, this symmetry was broken. The bottom two focusing streaks detached from the original overlapping streaks, Figure 6-7(b, c). A very intriguing phenomenon occurred when the two focusing streaks at the bottom migrated towards the lateral centreline of the channel as the voltage increased, and then merged to become a single streak. This means that not only by controlling the flow conditions, Re, but also by adjusting the

DEP force, inertial focusing position and pattern can be modified. The underlying mechanism for this phenomenon is that with an increased DEP force, the particles levitated upwards where the secondary flow velocity were much stronger, and the symmetrically oscillating secondary flow drag exerted a much stronger centre-directed pinch effect to focus the particles towards the centre of the channel. After reaching a certain height, the two-sided focusing streaks could even be combined as a single streak at the lateral centre of channel.

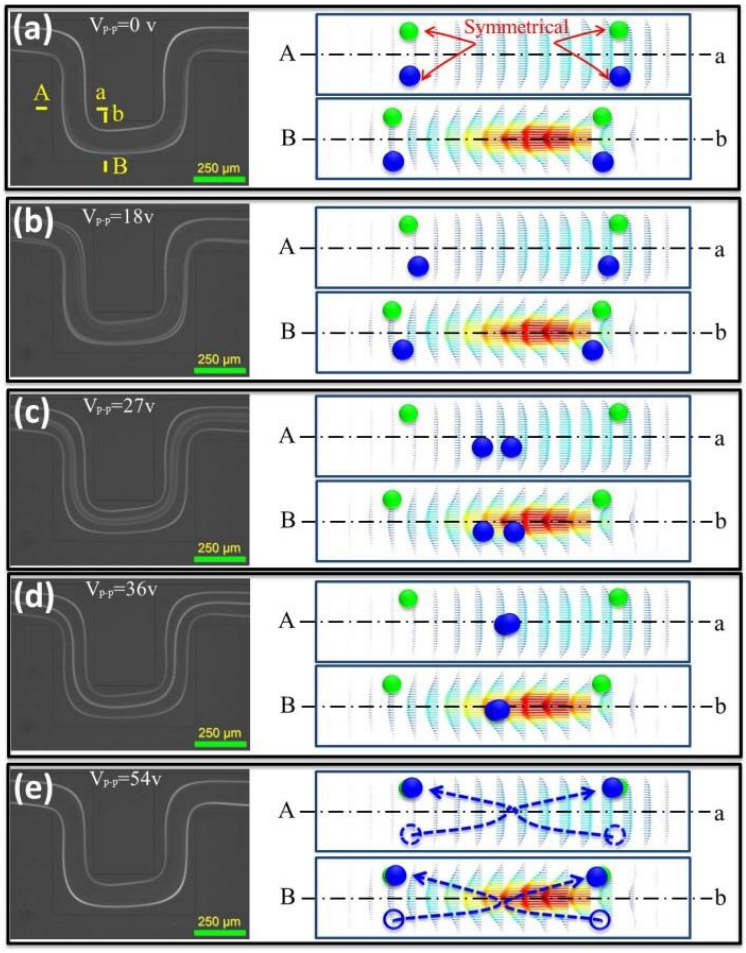

Figure 6–7 Migration of particle focusing patterns under different AC voltages of (a) V_{p-p}=0 v, (b) V_{p-p}=18 v, (c) V_{p-p}=27 v, (d) V_{p-p}=36 v and (e) V_{p-p}=54 v. (Left) trajectory of fluorescent particles from Top view, and (Right) their corresponding postulated dynamic equilibrium positions within two typical cross-sections "A-a" and "B-b". Flow condition is Re=62.5.

When the applied voltage was higher than a corresponding critical voltage V_{cpp}, the single focused streak collapsed because there was no stable position in the bottom

half of the channel and all the particles escaped into the top two equilibrium positions, where the DEP force was too small to have an effect. The overall trajectory of the equilibrium positions with increasing DEP force is shown as a dashed line in Figure 6-7(e).

6.4.3 Influence of n-DEP on inertial single-stream focusing pattern: sheath-less three-dimensional focusing

At a high Re (>110), without the existence of a DEP force, the centre-directed pinch effect from secondary flow was already strong enough to focus particles along the channel centre as a single focusing streak in the horizontal plane. In the vertical direction, particles were focused symmetrically along the top and bottom walls due to the inertial lift force, Figure 6-8(a). Due to the symmetry, only one focusing streak could be observed from the top view in this case. However, when a DEP force was applied in the vertical direction, the previously unobserved focusing streak from the bottom half of the channel appeared, Figures 6-8(b, c). The particles continued to behave as a single focusing streak, and their lateral position became more prone to follow the secondary flow streamline due to the larger secondary flow drag. The electrical voltage was gradually increased until it exceeded the critical value V_{cpp}, at which point the upward DEP force became strong enough to overcome the downward inertial lift force. Finally, all particles within bottom half transitioned to the equilibrium position D at the top of the channel, forming a truly single focusing streak in three dimensions, Figure 6-9(d). Such high-throughput sheath-less three-dimensional particles focusing promises wide potential applications, such as on-chip flow cytometry [173, 203, 204], deformability cytometry [38, 39, 205], and imaging cytometry [175].

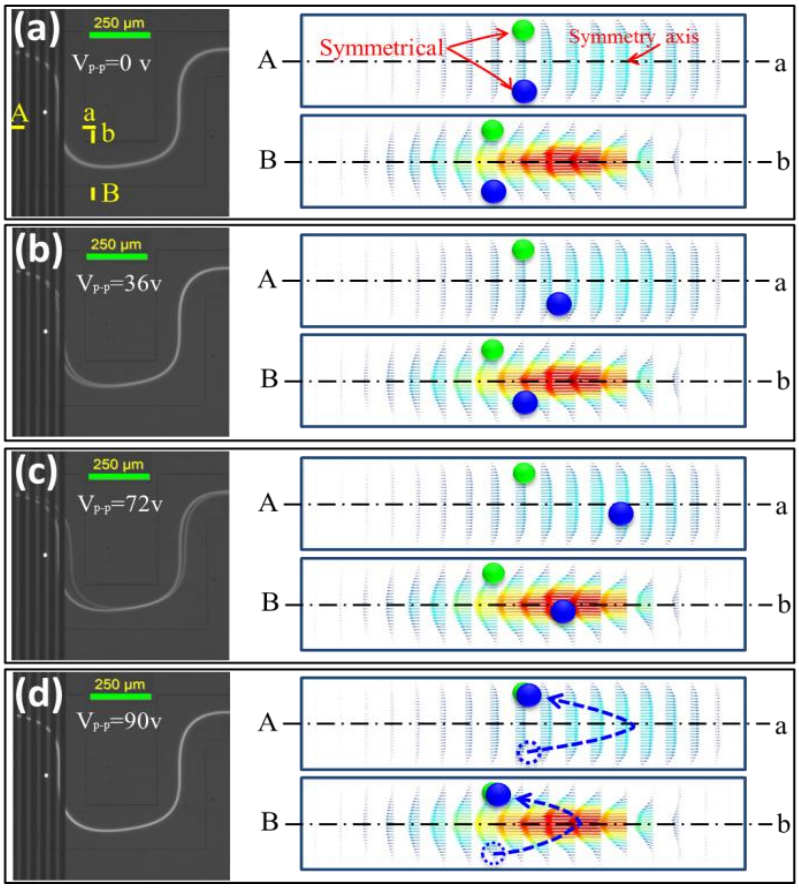

Figure 6–8 Migration of particle single central focusing patterns under different AC voltages of (a) V_{p-p}=0 v, (b) V_{p-p}=36 v, (c) V_{p-p}=72 v and (d) V_{p-p}=90 v. (Left) trajectory of fluorescent particles from top view, and (Right) their corresponding postulated dynamic equilibrium positions within two typical cross-sections "A-a" and "B-b". Flow condition is Re=114.6.

6.4.4 Influence of n-DEP on inertial transitional focusing patterns: pinching of widely distributed particles into a tight focusing streak

Without DEP, when Reynolds number Re was between 90 and 110, two-sided focusing streaks were combined as a single wide focusing streak in this flow region, which was considered as a transition between a two-sided focusing pattern and a single central focusing pattern. The particles in this pattern were distributed within a wide band near the centre of the channel, Figure 6-9(a). After a vertical DEP force was introduced, and within our expectations, the widely distributed particles at the bottom half of the channel migrated together if they were levitated upwards. However, it was unexpected that particles on the top half were also pinched closer in

these experiments, Figure 6-9(c-e). The DEP force on the particles at the top half of the channel should be very small, since it decreases exponentially with the distance *z*, as discussed previously, Figure 6-2(c). From our understanding, the centre-directed inertial effect (secondary flow drag) and the two-side-directed inertial lift force were in a delicate balance within this transitional region, so a tiny DEP force could probably break this balance, and inadvertently promoted the central focusing. A single focusing streak in 3D could also be achieved when the electric voltage surpassed the corresponding critical voltage V_{cpp}. Using the DEP force to transform the transitional focusing pattern into a single central focusing pattern actually improved the inertial focusing performance and expanded the available working region of the original single central focusing. The results could be beneficial for complete separation of particles according to their differential lateral equilibrium positions in the serpentine channel, because a narrower focusing streak facilitates easier collection, and higher collection purity and efficiency.

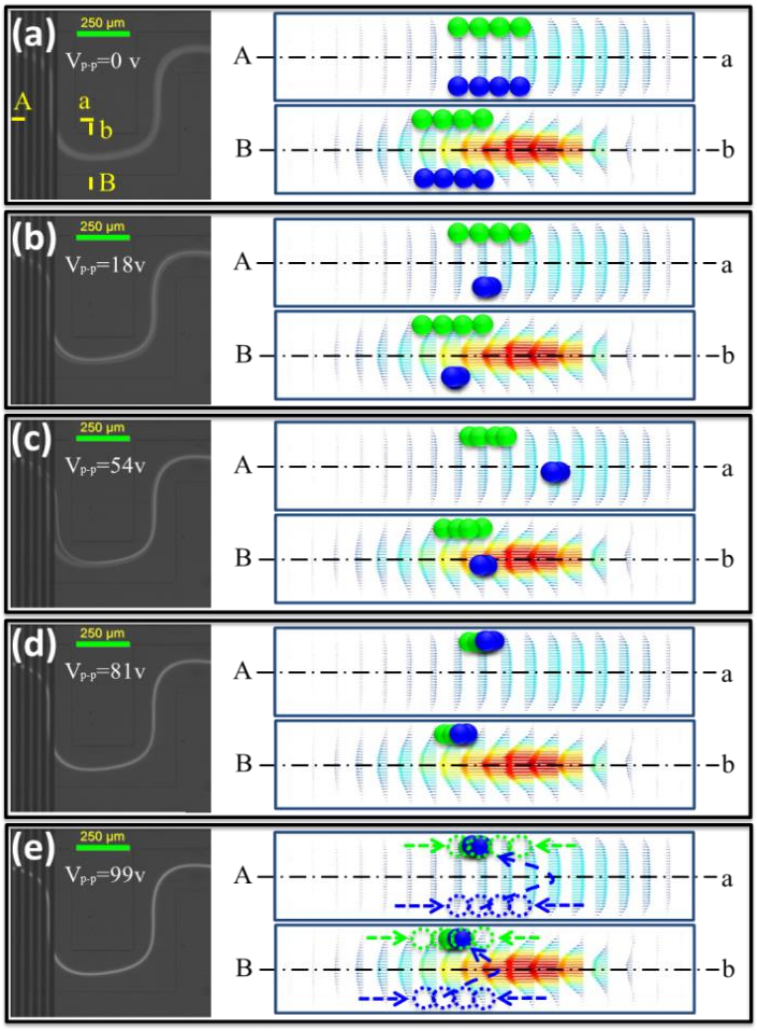

Figure 6–9 Migration of particle transitional focusing patterns under different AC voltages of (a) $V_{p\text{-}p}$=0 v, (b) $V_{p\text{-}p}$=18 v, (c) $V_{p\text{-}p}$=54 v, (d) $V_{p\text{-}p}$=81 v and (e) $V_{p\text{-}p}$=99 v. (Left) trajectory of fluorescent particles from top view, and (Right) their corresponding postulated dynamic equilibrium positions within two typical cross-sections "A-a" and "B-b". Flow condition is Re=99.

6.4.5 V_{pp}-Re operation map

The critical voltage V_{cpp} is a very important parameter for determining the vertical position of the particles because if the applied voltage is larger than V_{cpp}, the particles will be pushed over to the top half of the channel where inertial lift becomes more dominant, otherwise they will remain within the bottom half where their exact position depends on the balance of vertical inertial lift force and DEP force. A dimensionless factor δ was defined to scale with the ratio between DEP force and inertial lift force at tangent point C (see Figure 6-3):

$$\delta = \left| \frac{F_{DEP}}{F_L} \right|_C = \left| \frac{\pi H^2 \varepsilon_m \,\mathrm{Re}[K(\omega)] \nabla |E_{rms}|^2}{4 |f_L(Re, z)| a \rho_f U_f^2} \right|_C \tag{6-3}$$

From the definition, V_{cpp} is the applied voltage when δ =1, but if δ >1 all the particles will be pushed up to top half of the channel, and when δ <1, particles below the top half will remain in this region. It is difficult to determine the exact position of the tangent point C because the lift coefficient curve varies with channel Reynolds number Re. Therefore, it is not practical to derive an explicit analytical expression to calculate V_{cpp}. However, from an experimental perspective, we could roughly determine the V_{cpp} region. In the experiments, fewer particles travelled along the bottom half of the channel with increasing DEP force, as inferred by the decreased fluorescence intensity. More particles moved into equilibrium positions D in the top half of the channel leading to an increase in fluorescence intensity, as shown in Figure 6-10.

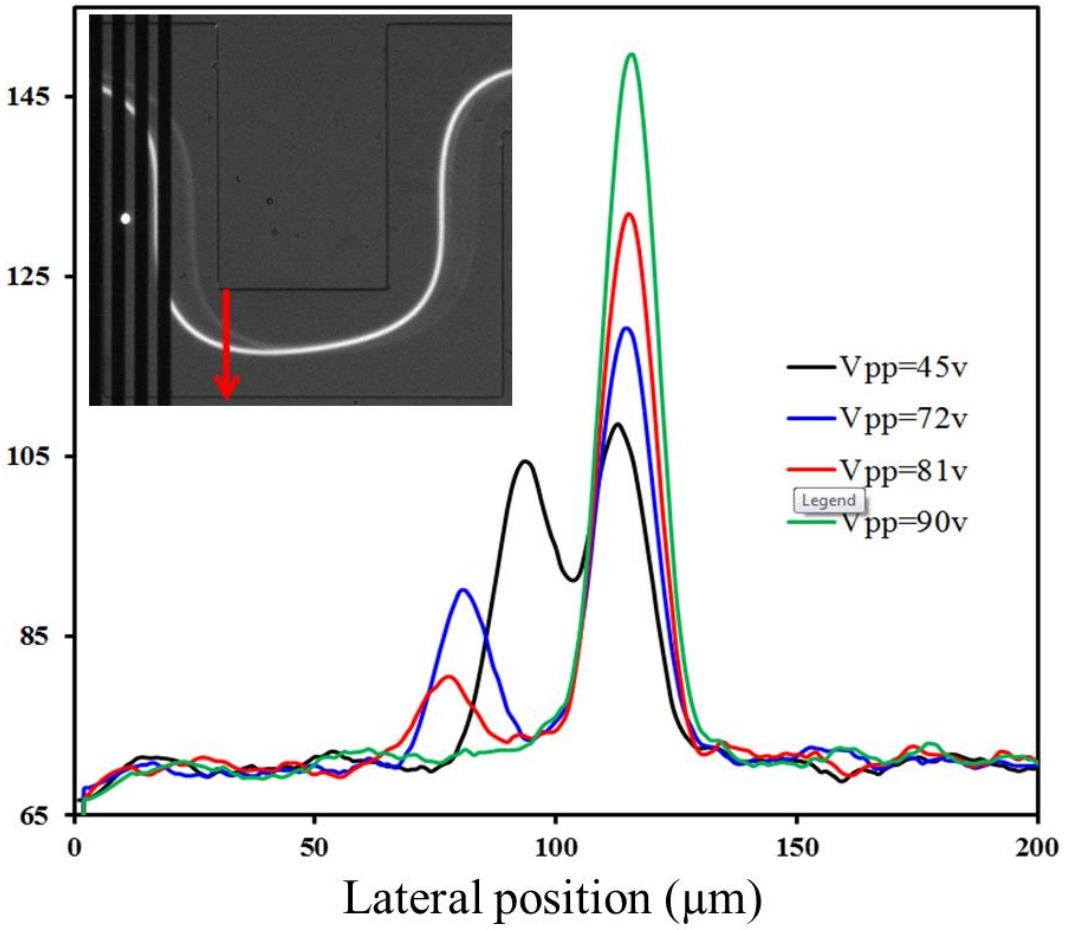

Figure 6–10 Distribution of lateral fluorescence intensity with various applied voltages.

Point C is a half stable position [Figure 6-3(c)], and the last position where a few particles remained at the bottom half of the channel. Therefore, the range of V_{cpp} can be estimated between the maximum voltage where the bottom particles still existed and the minimum voltage where all the bottom particles disappeared shown as a dashed line with error bars in Figure 6-11. From the V_{pp}-Re map, the critical voltage V_{cpp} was roughly proportional to Re because the order of applied voltage in DEP force was the same as Re ($\propto U_f$) in the inertial lift force [Equation (6-4)]. Of course, the dependency of the lift coefficient f_L(Re, z) on Re would bring a little nonlinear nature into the V_{cpp}-Re relationship. Above the V_{cpp}-Re curve, the DEP force was strong enough to push all particles onto the top half of the channel. Below this curve, the particles were levitated but still remain within the bottom half.

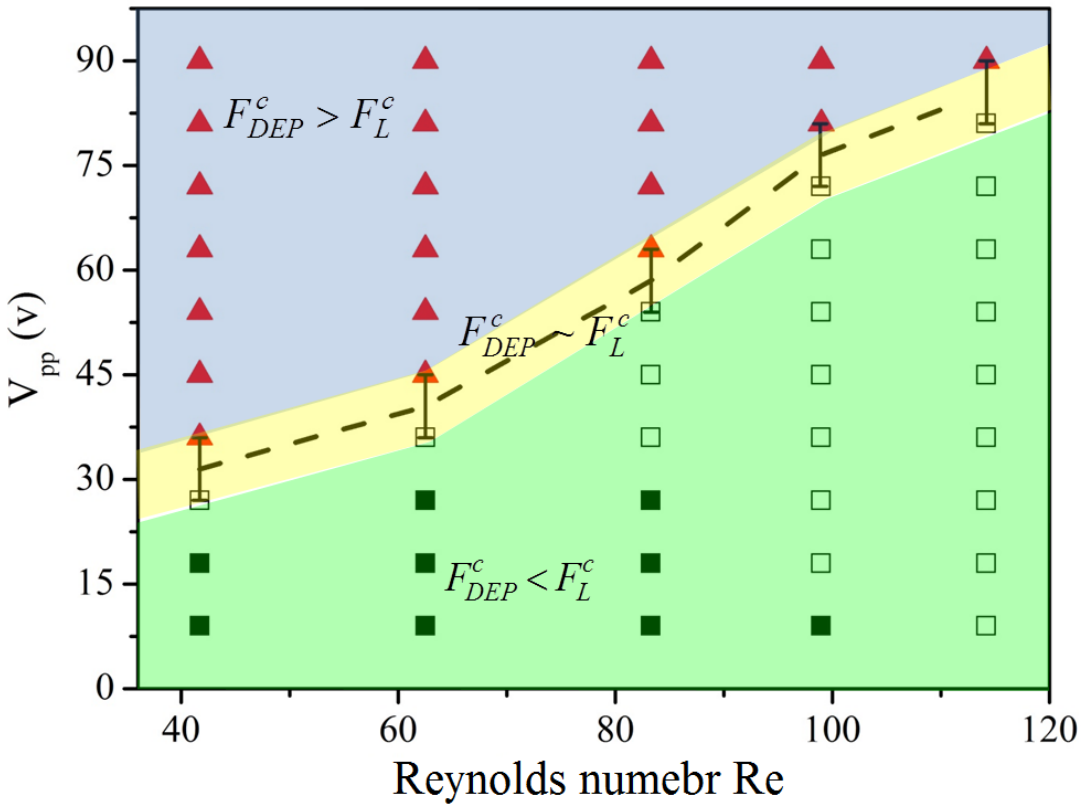

Figure 6–11 V_{pp}-Re map illustrates the working range of DEP-inertial microfluidic device. The red triangles are experimental data where particles are pushed onto the top half of the channel. The applied voltages are larger than the critical voltage. The empty rectangles are experimental data where particles under bottom half part of channel are focused into a single central focusing streak under the effects of DEP force. The solid rectangles are the experimental data where DEP force is not sufficient to alter particle inertial focusing pattern in bottom half part of channel.

6.5 Conclusions

This work, for the first time, proposed an innovative DEP-inertial microfluidic device that fully couples the DEP force and inertial lift force in a serpentine microchannel. A DEP force component was used to adjust the particle equilibrium positions in the vertical direction. Due to the much stronger secondary flow drag imposed on particles when they were near the vertical centre of the channel, focusing patterns and positions of particles along horizontal plane could be adjusted by their vertical position. The mechanism of this DEP-inertial microfluidic device was investigated numerically and experimentally. The advantages of DEP-inertial microfluidic device includes real-time controllability, three dimensional single

stream focusing and enhanced focusing quality, as well as the ability to manipulate particles in microfluidic platform.

7 CONCLUSIONS AND FUTURE WORK

7.1 Conclusions

The main objectives of this research are to investigate the inertial focusing phenomenon in the symmetric serpentine micro-channels and to exploit it for continuous-flow high-throughput particle and cell separations in microfluidic devices. Three different focusing patterns were observed: (i) single focusing streak at the channel centre, which is dominated by secondary flow; (ii) two focusing streaks at two sidewalls, dominated by inertial lift force; (iii) Transition patterns between the above focusing patterns where secondary flow and inertial lift play comparable roles. Moreover, the mechanism of these three focusing patterns was investigated using a combined experimental and numerical method, and the applications of these focusing patterns were demonstrated.

7.1.1 The mechanism of single central focusing pattern

In chapter 3, sufficient single focusing pattern was achieved in a symmetric serpentine channel, which revised the previous argument that single focusing streak cannot be obtained due to the complete counteraction of symmetric secondary flow during the alternating curvatures [67, 95]. For the Dean flow, its mixing effect by the counter-rotating streamlines was widely acknowledged and extensively applied to enhance fluid mixing and heat transfer. In the current work we also found that Dean vortex can actually apply a dominant positive focusing effect on particles under specific situation, rather than counteract completely in the symmetric serpentine channel. In a microchannel with low-aspect ratio, where the mixing effects of Dean vortex could be suppressed largely, particles can be pinched and aligned into the channel centre by the pure alternating effects of secondary flow (Dean vortex). This mechanism was proven by numerical simulation and experimental validation. This finding has advanced our understanding on the roles of Dean vortex on the particle focusing in the curved channel.

7.1.2 The mechanism of two-sided focusing pattern and its application on plasma extraction

When the flow is relatively slow ($20 \leq Re \leq 70$), the particle focusing is dominated by the inertial lift force. Rather than hindering the inertial migration, the Dean vortex

was found to assist and enhance the inertial focusing. The mechanism how the Dean vortex promotes the inertial focusing process was discussed. This two-sided inertial focusing pattern is very effective to act as a filtration device. Its application on blood plasma extraction was demonstrated, with more than 99.95% blood cells removed as well as high recovery yield of 46% obtained. The parallelization design rules for serpentine channel were proposed, and verified by design, fabrication and tests of microfluidic device with eight parallel serpentine channels. And this parallelized device can provide ultra-high flow rate of 2.8 ml/min.

7.1.3 High throughput separation of particles by differential equilibrium positions in serpentine channels

In addition, complete separation of particles by differential lateral equilibrium positions in a serpentine channel was demonstrated. The complete separation was based on the size-dependent distinct focusing patterns in serpentine channels: single central focusing for large particles dominated by the Dean flow and two-sided focusing pattern for small particles dominated by the inertial lift forces. This separation scheme is a great advance compared with the previous reported asymmetric serpentine channel [172], where particle separation was based on the filtration concept and cannot provide high purity and high recovery for both particles. The excellent separation ability of the proposed serpentine channel was demonstrated by the classification of a series of particle mixtures, including mixture of polystyrene beads, mixture of MEL cells and blood cells, and blood cells mixture.

7.1.4 Manipulation of particles by a hybrid DEP-inertial microfluidic device

Finally, based on the above investigation on the inertial focusing in the symmetric serpentine channel, we, for the first time, proposed an innovative hybrid device which coupled DEP force and inertial lift forces. The vertical DEP force was employed to modify the inertial focusing positions in three dimensional, and its effects on three different focusing patterns were investigated. This hybrid device has great potential for multi-criteria particle manipulation and classification.

In summary, we hope that our study not only can extend the fundamental understanding on inertial focusing process in symmetric serpentine channel, but also

can provide versatile and effective particle separation and filtration platform, with great potential for biological sample treatment and clinical diagnosis.

7.2 Future work

7.2.1 Separation of multiple particles by cascaded connected serpentine channels

In the current work, we demonstrated the separation of binary particles with high purity and efficiency in the proposed symmetric serpentine channel. However, it will become challenging when treating real-world samples that often includes heterogeneous mixtures of multiple particle components. The future work is to develop cascaded connected serpentine channels for separation of particle mixtures with multiple sizes. In the current work, we found the cut off size was about 20% channel height, and it is possible to modify the height of serpentine channel to adjust the particle cutoff size. It will require a multi-layer photolithography technology to deposit serpentine channels with multi heights in the same silicon master. In addition, the flow condition in each serpentine channel needs to be maintained at the optimal flow condition, which can be accomplished by an extra sheath flow, to adjust the flow rate. One practical application of cascaded connected serpentine channels is to separate the whole blood into three different components: platelets, red blood cells and white blood cells. So that it can replace the traditional density gradient centrifugation, which is rather bulky, and time consuming, requiring well-trained operators.

7.2.2 Separation and enrichment of circulating tumor cells (CTCs) by the serpentine channels

In this thesis, we have demonstrated the excellent separation of particles by size. The Murine erythroleukemia (MEL) cells, acting as a model of circulating tumor cells (CTCS), were spiked in the whole blood for separation test. The purity of MEL cells can be improved from 1.25% to 45.4%, and it demonstrated an effective purification and enrichment of MEL cells. A second separation process is expected to provide more purified (>90%) MEL cells suspension. However, the MEL cells are not the real CTCs, and even for CTCs, different types possibly have different biophysical properties, and they maybe behave differently in the serpentine channel. Therefore, more cancer cell lines e.g., Breast cancer cells (MCF-7), human prostate cancer cells

(PC3), Hela cells etc. and even clinical blood sample from cancer patients need to be tested, to verify the separation ability and efficiency of the proposed device. And from this study, we hope to push this technology a little step closer towards the practical application in clinics.

7.2.3 Exploring the application of the hybrid DEP-inertial microfluidic device

The proposed hybrid DEP-inertial microfluidic device possesses several potential applications. For example, the DEP force could be used as a force probe to investigate the mechanism of particle inertial focusing process. Meanwhile, utilisation of different focusing patterns of particles by varying the DEP forces in real-time could possibly act as an online active sorter. In addition, this hybrid device could be used to separate or isolate particles/cells by multi-criteria. The levitation of particles by n-DEP force can shift the two-sided focusing streaks toward channel centre and finally combines them as a single central focusing streak. As we know, biological cells exhibit varying induced boundary polarisations dependent on applied electric frequency and their physiological states [206], after choosing a proper frequency and suspending medium, cells/particles can be separated by the differences in their dielectric properties, such as separation of viable and non-viable cells [70, 207], blood cells and cancer cells [158, 208], and CD34+ cells from peripheral-stem-cell harvests [209] etc.

For the DEP-inertial microfluidic device, a separation scheme could be imagined here. All the particles could be first squeezed down to the bottom half of the channel by a sheath flow after entering the microchannel. Then, applying and adjusting a proper AC signal on the IDEs, the target particles experiencing a negative DEP could be levitated upwards and focused at the channel centre, while particles with different dielectric properties experiencing a weaker or even no DEP force, could still occupy the two-sided equilibrium positions. In this way, target particles could be isolated according to their dielectric properties, as well as particle size in our previous report [183]. Therefore, modification of inertial focusing patterns by DEP force implies a more versatile capacity to differentiate and separate particles/cells by dielectric properties as well as particle size in a high-throughput tuneable manner.

REFERENCES

[1] Whitesides, G. M. (2006) The origins and the future of microfluidics, *Nature 442*, 368-373.

[2] Sackmann, E. K., Fulton, A. L., and Beebe, D. J. (2014) The present and future role of microfluidics in biomedical research, *Nature 507*, 181-189.

[3] Bhagat, A. A. S., Bow, H., Hou, H. W., Tan, S. J., Han, J., and Lim, C. T. (2010) Microfluidics for cell separation, *Medical & Biological Engineering & Computing 48*, 999-1014.

[4] Zhang, J., Li, W., Li, M., Alici, G., and Nguyen, N.-T. (2013) Particle inertial focusing and its mechanism in a serpentine microchannel, *Microfluidics and nanofluidics 17*, 305-316.

[5] Di Carlo, D. (2009) Inertial microfluidics, *Lab on a Chip 9*, 3038-3046.

[6] Mach, A. J., Adeyiga, O. B., and Di Carlo, D. (2013) Microfluidic sample preparation for diagnostic cytopathology, *Lab on a Chip 13*, 1011-1026.

[7] Çetin, B. and Li, D. (2011) Dielectrophoresis in microfluidics technology, *Electrophoresis 32*, 2410-2427.

[8] Forbes, T. P. and Forry, S. P. (2012) Microfluidic magnetophoretic separations of immunomagnetically labeled rare mammalian cells, *Lab on a Chip 12*, 1471-1479.

[9] Wang, Z. and Zhe, J. (2011) Recent advances in particle and droplet manipulation for lab-on-a-chip devices based on surface acoustic waves, *Lab on a Chip 11*, 1280-1285.

[10] Yamada, M., Nakashima, M., and Seki, M. (2004) Pinched flow fractionation: continuous size separation of particles utilizing a laminar flow profile in a pinched microchannel, *Analytical Chemistry 76*, 5465-5471.

[11] Huang, L. R., Cox, E. C., Austin, R. H., and Sturm, J. C. (2004) Continuous particle separation through deterministic lateral displacement, *Science 304*, 987-990.

[12] Cristofanilli, M., Budd, G. T., Ellis, M. J., Stopeck, A., Matera, J., Miller, M. C., *et al.* (2004) Circulating tumor cells, disease progression, and survival in metastatic breast cancer, *New England Journal of Medicine 351*, 781-791.

[13] Segre, G. (1961) Radial particle displacements in Poiseuille flow of suspensions, *Nature 189*, 209-210.

[14] Segre, G. and Silberberg, A. (1962) Behaviour of macroscopic rigid spheres in Poiseuille flow Part 2. Experimental results and interpretation, *Journal of Fluid Mechanics 14*, 136-157.

[15] Martel, J. M. and Toner, M. (2012) Inertial focusing dynamics in spiral microchannels, *Physics of Fluids 24*, 032001.

[16] Xiang, N., Chen, K., Sun, D., Wang, S., Yi, H., and Ni, Z. (2013) Quantitative characterization of the focusing process and dynamic behavior of differently sized microparticles in a spiral microchannel, *Microfluidics and nanofluidics 14*, 89-99.

[17] Guan, G., Wu, L., Bhagat, A. A., Li, Z., Chen, P. C., Chao, S., *et al.* (2013) Spiral microchannel with rectangular and trapezoidal cross-sections for size based particle separation, *Scientific reports 3*, Art No. 1475.

[18] Martel, J. M. and Toner, M. (2014) Inertial Focusing in Microfluidics, *Annual Review of Biomedical Engineering 16*, 371-396.

[19] Oh, K. W. and Ahn, C. H. (2006) A review of microvalves, *Journal of Micromechanics and Microengineering 16*, R13-R39.

[20] Unger, M. A., Chou, H. P., Thorsen, T., Scherer, A., and Quake, S. R. (2000) Monolithic microfabricated valves and pumps by multilayer soft lithography, *Science 288,* 113-116.
[21] Iverson, B. D. and Garimella, S. V. (2008) Recent advances in microscale pumping technologies: a review and evaluation, *Microfluidics and nanofluidics 5,* 145-174.
[22] Ha, S. M., Cho, W., and Ahn, Y. (2009) Disposable thermo-pneumatic micropump for bio lab-on-a-chip application, *Microelectronic Engineering 86,* 1337-1339.
[23] Stroock, A. D., Dertinger, S. K. W., Ajdari, A., Mezić, I., Stone, H. A., and Whitesides, G. M. (2002) Chaotic mixer for microchannels, *Science 295,* 647-651.
[24] Sudarsan, A. P. and Ugaz, V. M. (2006) Multivortex micromixing, *Proceedings of the National Academy of Sciences 103,* 7228-7233.
[25] Nguyen, N. T. and Wu, Z. (2005) Micromixers—a review, *Journal of Micromechanics and Microengineering 15,* R1-R16.
[26] Wei, H., Chueh, B., Wu, H., Hall, E. W., Li, C., Schirhagl, R., *et al.* (2011) Particle sorting using a porous membrane in a microfluidic device, *Lab on a Chip 11,* 238-245.
[27] Takagi, J., Yamada, M., Yasuda, M., and Seki, M. (2005) Continuous particle separation in a microchannel having asymmetrically arranged multiple branches, *Lab on a Chip 5,* 778-784.
[28] Choi, S., Karp, J. M., and Karnik, R. (2012) Cell sorting by deterministic cell rolling, *Lab on a Chip 12,* 1427-1430.
[29] Nagrath, S., Sequist, L. V., Maheswaran, S., Bell, D. W., Irimia, D., Ulkus, L., *et al.* (2007) Isolation of rare circulating tumour cells in cancer patients by microchip technology, *Nature 450,* 1235-1239.
[30] Pamme, N. and Wilhelm, C. (2006) Continuous sorting of magnetic cells via on-chip free-flow magnetophoresis, *Lab on a Chip 6,* 974-980.
[31] Liu, C., Lagae, L., Wirix-Speetjens, R., and Borghs, G. (2007) On-chip separation of magnetic particles with different magnetophoretic mobilities, *Journal of Applied Physics 101,* 024913.
[32] Pamme, N. and Manz, A. (2004) On-chip free-flow magnetophoresis: continuous flow separation of magnetic particles and agglomerates, *Analytical Chemistry 76,* 7250-7256.
[33] Kose, A. R., Fischer, B., Mao, L., and Koser, H. (2009) Label-free cellular manipulation and sorting via biocompatible ferrofluids, *Proceedings of the National Academy of Sciences 106,* 21478-21483.
[34] Zhu, T., Marrero, F., and Mao, L. (2010) Continuous separation of non-magnetic particles inside ferrofluids, *Microfluidics and nanofluidics 9,* 1003-1009.
[35] Xuan, X., Zhu, J., and Church, C. (2010) Particle focusing in microfluidic devices, *Microfluidics and nanofluidics 9,* 1-16.
[36] Choi, S. and Park, J. K. (2008) Sheathless hydrophoretic particle focusing in a microchannel with exponentially increasing obstacle arrays, *Analytical Chemistry 80,* 3035-3039.
[37] Shi, J., Mao, X., Ahmed, D., and Huang, T. J. (2008) Focusing microparticles in a microfluidic channel with standing surface acoustic waves (SSAW), *Lab on a Chip 8,* 221-223.

[38] Gossett, D. R., Henry, T., Lee, S. A., Ying, Y., Lindgren, A. G., Yang, O. O., *et al.* (2012) Hydrodynamic stretching of single cells for large population mechanical phenotyping, *Proceedings of the National Academy of Sciences 109*, 7630-7635.

[39] Dudani, J. S., Gossett, D. R., Henry, T., and Di Carlo, D. (2013) Pinched-flow hydrodynamic stretching of single-cells, *Lab on a Chip 13*, 3728-3734.

[40] Grier, D. G. (2003) A revolution in optical manipulation, *Nature 424*, 810-816.

[41] Lieu, V. H., House, T. A., and Schwartz, D. T. (2012) Hydrodynamic tweezers: Impact of design geometry on flow and microparticle trapping, *Analytical Chemistry 84*, 1963-1968.

[42] Holmes, D. and Morgan, H. (2010) Single cell impedance cytometry for identification and counting of CD4 T-cells in human blood using impedance labels, *Analytical Chemistry 82*, 1455-1461.

[43] Holmes, D., Pettigrew, D., Reccius, C. H., Gwyer, J. D., Van Berkel, C., Holloway, J., *et al.* (2009) Leukocyte analysis and differentiation using high speed microfluidic single cell impedance cytometry, *Lab on a Chip 9*, 2881-2889.

[44] Chen, J., Zheng, Y., Tan, Q., Shojaei-Baghini, E., Zhang, Y. L., Li, J., *et al.* (2011) Classification of cell types using a microfluidic device for mechanical and electrical measurement on single cells, *Lab on a Chip 11*, 3174-3181.

[45] Dharmasiri, U., Njoroge, S. K., Witek, M. A., Adebiyi, M. G., Kamande, J. W., Hupert, M. L., *et al.* (2011) High-throughput selection, enumeration, electrokinetic manipulation, and molecular profiling of low-abundance circulating tumor cells using a microfluidic system, *Analytical Chemistry 86*, 2301-2309.

[46] Song, Y. X., Yang, J. D., Shi, X. F., Jiang, H., Wu, Y. B., Peng, R., *et al.* (2012) DC dielectrophoresis separation of marine algae and particles in a microfluidic chip, *SCIENCE CHINA Chemistry 55*, 524-530.

[47] Li, M., Li, S., Wu, J., Wen, W., Li, W., and Alici, G. (2012) A simple and cost-effective method for fabrication of integrated electronic-microfluidic devices using a laser-patterned PDMS layer, *Microfluidics and nanofluidics 12*, 751-760

[48] Pethig, R. (2010) Review Article—Dielectrophoresis: Status of the theory, technology, and applications, *Biomicrofluidics 4*, 022811.

[49] Shafiee, H., Caldwell, J. L., Sano, M. B., and Davalos, R. V. (2009) Contactless dielectrophoresis: a new technique for cell manipulation, *Biomedical microdevices 11*, 997-1006.

[50] Gao, Y., Jian, Y., Zhang, L., and Huang, J. (2007) Magnetophoresis of nonmagnetic particles in ferrofluids, *The Journal of Physical Chemistry C 111*, 10785-10791.

[51] Pamme, N., Eijkel, J. C. T., and Manz, A. (2006) On-chip free-flow magnetophoresis: Separation and detection of mixtures of magnetic particles in continuous flow, *Journal of Magnetism and Magnetic Materials 307*, 237-244.

[52] Petersson, F., Åberg, L., Swärd-Nilsson, A.-M., and Laurell, T. (2007) Free flow acoustophoresis: microfluidic-based mode of particle and cell separation, *Analytical Chemistry 79*, 5117-5123.

[53] Shi, J., Huang, H., Stratton, Z., Huang, Y., and Huang, T. J. (2009) Continuous particle separation in a microfluidic channel via standing surface acoustic waves (SSAW), *Lab on a Chip 9*, 3354-3359.
[54] Shi, J., Ahmed, D., Mao, X., Lin, S.-C. S., Lawit, A., and Huang, T. J. (2009) Acoustic tweezers: patterning cells and microparticles using standing surface acoustic waves (SSAW), *Lab on a Chip 9*, 2890-2895.
[55] Son, J. H., Lee, S. H., Hong, S., Park, S.-m., Lee, J., Dickey, A. M., *et al.* (2014) Hemolysis-free blood plasma separation, *Lab on a Chip 14*, 2287-2292.
[56] Liu, C., Mauk, M., Gross, R., Bushman, F. D., Edelstein, P. H., Collman, R. G., *et al.* (2013) Membrane-based, sedimentation-assisted plasma separator for point-of-care applications, *Analytical Chemistry 85*, 10463-10470.
[57] Aran, K., Fok, A., Sasso, L. A., Kamdar, N., Guan, Y., Sun, Q., *et al.* (2011) Microfiltration platform for continuous blood plasma protein extraction from whole blood during cardiac surgery, *Lab on a Chip 11*, 2858-2868.
[58] Stott, S. L., Hsu, C. H., Tsukrov, D. I., Yu, M., Miyamoto, D. T., Waltman, B. A., *et al.* (2010) Isolation of circulating tumor cells using a microvortex-generating herringbone-chip, *Proceedings of the National Academy of Sciences 107*, 18392-18397.
[59] Xu, Y., Phillips, J. A., Yan, J., Li, Q., Fan, Z. H., and Tan, W. (2009) Aptamer-based microfluidic device for enrichment, sorting, and detection of multiple cancer cells, *Analytical Chemistry 81*, 7436-7442.
[60] Phillips, J. A., Xu, Y., Xia, Z., Fan, Z. H., and Tan, W. (2008) Enrichment of cancer cells using aptamers immobilized on a microfluidic channel, *Analytical Chemistry 81*, 1033-1039.
[61] Henslee, E. A., Sano, M. B., Rojas, A. D., Schmelz, E. M., and Davalos, R. V. (2011) Selective concentration of human cancer cells using contactless dielectrophoresis, *Electrophoresis 32*, 2523-2529.
[62] Choi, S., Song, S., Choi, C., and Park, J. K. (2008) Hydrophoretic sorting of micrometer and submicrometer particles using anisotropic microfluidic obstacles, *Analytical Chemistry 81*, 50-55.
[63] Choi, S. and Park, J. K. (2007) Hydrophoresis: A New-Phoretic Method for High-Resolution Particle Separation, *Actuators and Microsystems Conference*, Lyon 1769-1772.
[64] Loutherback, K., D'Silva, J., Liu, L., Wu, A., Austin, R. H., and Sturm, J. C. (2012) Deterministic separation of cancer cells from blood at 10 mL/min, *AIP advances 2*, 042107.
[65] Holm, S. H., Beech, J. P., Barrett, M. P., and Tegenfeldt, J. O. (2011) Separation of parasites from human blood using deterministic lateral displacement, *Lab on a Chip 11*, 1326-1332.
[66] Inglis, D. W., Davis, J. A., Austin, R. H., and Sturm, J. C. (2006) Critical particle size for fractionation by deterministic lateral displacement, *Lab on a Chip 6*, 655-658.
[67] Amini, H., Lee, W., and Di Carlo, D. (2014) Inertial microfluidic physics, *Lab on a Chip 14*, 2739-2761.
[68] Srivastava, S. K., Gencoglu, A., and Minerick, A. R. (2011) DC insulator dielectrophoretic applications in microdevice technology: a review, *Analytical and Bioanalytical Chemistry 399*, 301-321.

[69] Regtmeier, J., Eichhorn, R., Viefhues, M., Bogunovic, L., and Anselmetti, D. (2011) Electrodeless dielectrophoresis for bioanalysis: Theory, devices and applications, *Electrophoresis 32,* 2253-2273.

[70] Shafiee, H., Sano, M. B., Henslee, E. A., Caldwell, J. L., and Davalos, R. V. (2010) Selective isolation of live/dead cells using contactless dielectrophoresis (cDEP), *Lab on a Chip 10,* 438-445.

[71] Khoshmanesh, K., Nahavandi, S., Baratchi, S., Mitchell, A., and Kalantar-zadeh, K. (2011) Dielectrophoretic platforms for bio-microfluidic systems, *Biosensors and Bioelectronics 26,* 1800-1814.

[72] Srivastava, S. K., Baylon-Cardiel, J. L., Lapizco-Encinas, B. H., and Minerick, A. R. (2011) A continuous DC-insulator dielectrophoretic sorter of microparticles, *Journal of Chromatography A 1218,* 1780-1789.

[73] Salmanzadeh, A., Kittur, H., Sano, M. B., Roberts, P. C., Schmelz, E. M., and Davalos, R. V. (2012) Dielectrophoretic differentiation of mouse ovarian surface epithelial cells, macrophages, and fibroblasts using contactless dielectrophoresis, *Biomicrofluidics 6,* 024104.

[74] Shen, F., Hwang, H., Hahn, Y. K., and Park, J. K. (2012) Label-Free Cell Separation Using a Tunable Magnetophoretic Repulsion Force, *Analytical Chemistry 84,* 3075-3081.

[75] Liu, C., Stakenborg, T., Peeters, S., and Lagae, L. (2009) Cell manipulation with magnetic particles toward microfluidic cytometry, *Journal of Applied Physics 105,* 102014.

[76] Winkleman, A., Perez-Castillejos, R., Gudiksen, K. L., Phillips, S. T., Prentiss, M., and Whitesides, G. M. (2007) Density-based diamagnetic separation: devices for detecting binding events and for collecting unlabeled diamagnetic particles in paramagnetic solutions, *Analytical Chemistry 79,* 6542-6550.

[77] Zhu, T., Cheng, R., Lee, S., Rajaraman, E., Eiteman, M., Querec, T., *et al.* (2012) Continuous-flow ferrohydrodynamic sorting of particles and cells in microfluidic devices, *Microfluidics and nanofluidics 13,* 645-654.

[78] Gossett, D. R., Weaver, W. M., Mach, A. J., Hur, S. C., Tse, H. T. K., Lee, W., *et al.* (2010) Label-free cell separation and sorting in microfluidic systems, *Analytical and Bioanalytical Chemistry 397,* 3249-3267.

[79] Loutherback, K., Chou, K. S., Newman, J., Puchalla, J., Austin, R. H., and Sturm, J. C. (2010) Improved performance of deterministic lateral displacement arrays with triangular posts, *Microfluidics and nanofluidics 9,* 1143-1149.

[80] Davis, J. A., Inglis, D. W., Morton, K. J., Lawrence, D. A., Huang, L. R., Chou, S. Y., *et al.* (2006) Deterministic hydrodynamics: taking blood apart, *Proceedings of the National Academy of Sciences 103,* 14779-14784.

[81] Green, J. V., Radisic, M., and Murthy, S. K. (2009) Deterministic lateral displacement as a means to enrich large cells for tissue engineering, *Analytical Chemistry 81,* 9178-9182.

[82] Liu, Z., Huang, F., Du, J., Shu, W., Feng, H., Xu, X., *et al.* (2013) Rapid isolation of cancer cells using microfluidic deterministic lateral displacement structure, *Biomicrofluidics 7,* 011801.

[83] Inglis, D. W., Herman, N., and Vesey, G. (2010) Highly accurate deterministic lateral displacement device and its application to purification of fungal spores, *Biomicrofluidics 4,* 024109.

[84] Choi, S. and Park, J. K. (2007) Continuous hydrophoretic separation and sizing of microparticles using slanted obstacles in a microchannel, *Lab on a Chip 7*, 890-897.
[85] Choi, S., Song, S., Choi, C., and Park, J. K. (2009) Microfluidic self-sorting of mammalian cells to achieve cell cycle synchrony by hydrophoresis, *Analytical Chemistry 81*, 1964-1968.
[86] Cherukat, P. and Mclaughlin, J. B. (1994) The inertial lift on a rigid sphere in a linear shear flow field near a flat wall, *Journal of Fluid Mechanics 263*, 1-18.
[87] Saffman, P. G. (1965) The lift on a small sphere in a slow shear flow, *Journal of Fluid Mechanics 22*, 385-400.
[88] Drew, D. A. (1978) The force on a small sphere in slow viscous flow, *Journal of Fluid Mechanics 88*, 393-400.
[89] McLaughlin, J. B. (1993) The lift on a small sphere in wall-bounded linear shear flows, *Journal of Fluid Mechanics 246*, 249-265.
[90] JOSEPH, D. D. and OCANDO, D. (2002) Slip velocity and lift, *Journal of Fluid Mechanics 454*, 263-286.
[91] ASMOLOV, E. S. (1999) The inertial lift on a spherical particle in a plane Poiseuille flow at large channel Reynolds number, *Journal of Fluid Mechanics 381*, 63-87.
[92] Chun, B. and Ladd, A. (2006) Inertial migration of neutrally buoyant particles in a square duct: An investigation of multiple equilibrium positions, *Physics of Fluids 18*, 031704.
[93] Tanaka, T., Ishikawa, T., Numayama-Tsuruta, K., Imai, Y., Ueno, H., Yoshimoto, T., *et al.* (2012) Inertial migration of cancer cells in blood flow in microchannels, *Biomedical microdevices 14*, 25-33.
[94] Di Carlo, D., Edd, J. F., Humphry, K. J., Stone, H. A., and Toner, M. (2009) Particle segregation and dynamics in confined flows, *Physical Review Letters 102*, 94503.
[95] Di Carlo, D., Irimia, D., Tompkins, R. G., and Toner, M. (2007) Continuous inertial focusing, ordering, and separation of particles in microchannels, *Proceedings of the National Academy of Sciences 104*, 18892–18897.
[96] Hur, S. C., Choi, S.-E., Kwon, S., and Di Carlo, D. (2011) Inertial focusing of non-spherical microparticles, *Applied Physics Letters 99*, 044101.
[97] Tan, A. P., Dudani, J. S., Arshi, A., Lee, R. J., Henry, T., Gossett, D. R., *et al.* (2014) Continuous-flow cytomorphological staining and analysis, *Lab on a Chip 14*, 522-531.
[98] Sollier, E., Go, D. E., Che, J., Gossett, D. R., O'Byrne, S., Weaver, W. M., *et al.* (2014) Size-selective collection of circulating tumor cells using Vortex technology, *Lab on a Chip 14*, 63-77.
[99] Nunes, J. K., Wu, C. Y., Amini, H., Owsley, K., Di Carlo, D., and Stone, H. A. (2014) Fabricating Shaped Microfibers with Inertial Microfluidics, *Advanced Materials 26*, 3712-3717.
[100] Karniadakis, G., Beskok, A., and Aluru, N. (2006) Microflows and nanoflows: fundamentals and simulation, *Springer Science & Business Media*.
[101] Bretherton, F. P. (1962) The motion of rigid particles in a shear flow at low Reynolds number, *Journal of Fluid Mechanics 14*, 284-304.

[102] Oh, K. W., Lee, K., Ahn, B., and Furlani, E. P. (2012) Design of pressure-driven microfluidic networks using electric circuit analogy, *Lab on a Chip 12,* 515-545.
[103] Richardson, J. F., Coulson, J. M., Harker, J., and Backhurst, J. (2002) Chemical Engineering: Particle technology and separation processes, *Butterworth-Heinemann*.
[104] Mazo, R. M. (2002) Brownian motion: fluctuations, dynamics, and applications, *Clarendon press Oxford*.
[105] Michaelides, E. (2006) Particles, bubbles & drops: their motion, heat and mass transfer, *World Scientific*, Singapore.
[106] Rubinow, S. and Keller, J. B. (1961) The transverse force on a spinning sphere moving in a viscous fluid, *Journal of Fluid Mechanics 11*, 447-459.
[107] Matas, J., Morris, J., and Guazzelli, E. (2004) Lateral forces on a sphere, *Oil & Gas Science and Technology 59,* 59-70.
[108] Kim, Y. W. and Yoo, J. Y. (2009) Axisymmetric flow focusing of particles in a single microchannel, *Lab on a Chip 9,* 1043-1045.
[109] Feng, J., Hu, H. H., and Joseph, D. D. (1994) Direct simulation of initial value problems for the motion of solid bodies in a Newtonian fluid. Part 2. Couette and Poiseuille flows, *Journal of Fluid Mechanics 277,* 271-301.
[110] Brenner, H. (1961) The slow motion of a sphere through a viscous fluid towards a plane surface, *Chemical Engineering Science 16,* 242-251.
[111] Cox, R. and Hsu, S. (1977) The lateral migration of solid particles in a laminar flow near a plane, *International Journal of Multiphase Flow 3,* 201-222.
[112] Vasseur, P. and Cox, R. G. (1977) The lateral migration of spherical particles sedimenting in a stagnant bounded fluid, *Journal of Fluid Mechanics 80,* 561-591.
[113] Cherukat, P. and McLaughlin, J. (1990) Wall-induced lift on a sphere, *International Journal of Multiphase Flow 16,* 899-907.
[114] Bhagat, A. A. S., Kuntaegowdanahalli, S. S., and Papautsky, I. (2009) Inertial microfluidics for continuous particle filtration and extraction, *Microfluidics and nanofluidics 7,* 217-226.
[115] Zhou, J. and Papautsky, I. (2013) Fundamentals of inertial focusing in microchannels, *Lab on a Chip 13,* 1121-1132.
[116] Matas, J.-P., Morris, J. F., and Guazzelli, É. (2004) Inertial migration of rigid spherical particles in Poiseuille flow, *Journal of Fluid Mechanics 515,* 171-195.
[117] Stan, C. A., Ellerbee, A. K., Guglielmini, L., Stone, H. A., and Whitesides, G. M. (2013) The magnitude of lift forces acting on drops and bubbles in liquids flowing inside microchannels, *Lab on a Chip 13,* 365-376.
[118] Chan, P.-H. and Leal, L. (1979) The motion of a deformable drop in a second-order fluid, *Journal of Fluid Mechanics 92,* 131-170.
[119] Hou, H. W., Bhagat, A. A. S., Chong, A. G. L., Mao, P., Tan, K. S. W., Han, J., *et al.* (2010) Deformability based cell margination—a simple microfluidic design for malaria-infected erythrocyte separation, *Lab on a Chip 10,* 2605-2613.
[120] Hur, S. C., Henderson-MacLennan, N. K., McCabe, E. R., and Di Carlo, D. (2011) Deformability-based cell classification and enrichment using inertial microfluidics, *Lab on a Chip 11,* 912-920.

[121] Lim, E. J., Ober, T. J., Edd, J. F., Desai, S. P., Neal, D., Bong, K. W., *et al.* (2014) Inertio-elastic focusing of bioparticles in microchannels at high throughput, *Nature Communications 5*, Art No. 4120.
[122] Berger, S., Talbot, L., and Yao, L. (1983) Flow in curved pipes, *Annual review of fluid mechanics 15*, 461-512.
[123] Squires, T. M. and Quake, S. R. (2005) Microfluidics: Fluid physics at the nanoliter scale, *Reviews of modern physics 77*, 977.
[124] Bhagat, A. A. S., Kuntaegowdanahalli, S. S., Kaval, N., Seliskar, C. J., and Papautsky, I. (2010) Inertial microfluidics for sheath-less high-throughput flow cytometry, *Biomedical microdevices 12*, 187-195.
[125] Kemna, E. W., Schoeman, R. M., Wolbers, F., Vermes, I., Weitz, D. A., and van den Berg, A. (2012) High-yield cell ordering and deterministic cell-in-droplet encapsulation using Dean flow in a curved microchannel, *Lab on a Chip 12*, 2881-2887.
[126] Choi, Y.-S., Seo, K.-W., and Lee, S.-J. (2011) Lateral and cross-lateral focusing of spherical particles in a square microchannel, *Lab on a Chip 11*, 460-465.
[127] Chung, A. J., Gossett, D. R., and Di Carlo, D. (2013) Three Dimensional, Sheathless, and High ‐ Throughput Microparticle Inertial Focusing Through Geometry ‐ Induced Secondary Flows, *Small 9*, 685-690.
[128] Lee, M. G., Choi, S., and Park, J. K. (2011) Inertial separation in a contraction–expansion array microchannel, *Journal of Chromatography A 1218*, 4138-4143.
[129] Amini, H., Sollier, E., Weaver, W. M., and Di Carlo, D. (2012) Intrinsic particle-induced lateral transport in microchannels, *Proceedings of the National Academy of Sciences 109*, 11593-11598.
[130] Lee, W., Amini, H., Stone, H. A., and Di Carlo, D. (2010) Dynamic self-assembly and control of microfluidic particle crystals, *Proceedings of the National Academy of Sciences 107*, 22413-22418.
[131] Liu, C., Hu, G., Jiang, X., and Sun, J. (2015) Inertial focusing of spherical particles in rectangular microchannels over a wide range of Reynolds numbers, *Lab on a Chip 15*, 1168-1177.
[132] Hur, S. C., Brinckerhoff, T. Z., Walthers, C. M., Dunn, J. C., and Di Carlo, D. (2012) Label-free enrichment of adrenal cortical progenitor cells using inertial microfluidics, *PLoS One 7*, e46550.
[133] Fedosov, D. A. and Gompper, G. (2014) White blood cell margination in microcirculation, *Soft Matter 10*, 2961-2970.
[134] Hou, H. W., Gan, H. Y., Bhagat, A. A. S., Li, L. D., Lim, C. T., and Han, J. (2012) A microfluidics approach towards high-throughput pathogen removal from blood using margination, *Biomicrofluidics 6*, 024115.
[135] Mach, A. J. and Di Carlo, D. (2010) Continuous scalable blood filtration device using inertial microfluidics, *Biotechnology and Bioengineering 107*, 302-311.
[136] Zhou, J., Giridhar, P. V., Kasper, S., and Papautsky, I. (2013) Modulation of aspect ratio for complete separation in an inertial microfluidic channel, *Lab on a Chip 13*, 1919-1929.
[137] Dudani, J. S., Go, D. E., Gossett, D. R., Tan, A. P., and Di Carlo, D. (2014) Mediating Millisecond Reaction Time around Particles and Cells, *Analytical Chemistry 86*, 1502-1510.

[138] Hur, S. C., Tse, H. T. K., and Di Carlo, D. (2010) Sheathless inertial cell ordering for extreme throughput flow cytometry, *Lab on a Chip 10*, 274-280.
[139] Yoon, D. H., Ha, J. B., Bahk, Y. K., Arakawa, T., Shoji, S., and Go, J. S. (2008) Size-selective separation of micro beads by utilizing secondary flow in a curved rectangular microchannel, *Lab on a Chip 9*, 87-90.
[140] Bhagat, A. A. S., Kuntaegowdanahalli, S. S., and Papautsky, I. (2008) Continuous particle separation in spiral microchannels using dean flows and differential migration, *Lab on a Chip 8*, 1906-1914.
[141] Kuntaegowdanahalli, S. S., Bhagat, A. A. S., Kumar, G., and Papautsky, I. (2009) Inertial microfluidics for continuous particle separation in spiral microchannels, *Lab on a Chip 9*, 2973-2980.
[142] Sun, J., Li, M., Liu, C., Zhang, Y., Liu, D., Liu, W., *et al.* (2012) Double spiral microchannel for label-free tumor cell separation and enrichment, *Lab on a Chip 12*, 3952-3960.
[143] Sun, J., Liu, C., Li, M., Wang, J., Xianyu, Y., Hu, G., *et al.* (2013) Size-based hydrodynamic rare tumor cell separation in curved microfluidic channels, *Biomicrofluidics 7*, 011802.
[144] Warkiani, M. E., Guan, G., Luan, K. B., Lee, W. C., Bhagat, A. A. S., Chaudhuri, P. K., *et al.* (2014) Slanted spiral microfluidics for the ultra-fast, label-free isolation of circulating tumor cells, *Lab on a Chip 14*, 128-137.
[145] Wu, L., Guan, G., Hou, H. W., Bhagat, A. A. S., and Han, J. (2012) Separation of Leukocytes from Blood Using Spiral Channel with Trapezoid Cross-Section, *Analytical Chemistry 84*, 9324-9331.
[146] Lee, W. C., Bhagat, A. A. S., Huang, S., Van Vliet, K. J., Han, J., and Lim, C. T. (2011) High-throughput cell cycle synchronization using inertial forces in spiral microchannels, *Lab on a Chip 11*, 1359-1367.
[147] Sheng, W., Chen, T., Kamath, R., Xiong, X., Tan, W., and Fan, Z. H. (2012) Aptamer-enabled efficient isolation of cancer cells from whole blood using a microfluidic device, *Analytical Chemistry 84*, 4199-4206.
[148] Hou, H. W., Warkiani, M. E., Khoo, B. L., Li, Z. R., Soo, R. A., Tan, D. S.-W., *et al.* (2013) Isolation and retrieval of circulating tumor cells using centrifugal forces, *Scientific reports 3*, Art No. 1259.
[149] Warkiani, M. E., Khoo, B. L., Tan, D. S.-W., Bhagat, A. A. S., Lim, W.-T., Yap, Y. S., *et al.* (2014) An ultra-high-throughput spiral microfluidic biochip for the enrichment of circulating tumor cells, *Analyst 139*, 3245-3255.
[150] Khoo, B. L., Warkiani, M. E., Tan, D. S.-W., Bhagat, A. A. S., Irwin, D., Lau, D. P., *et al.* (2014) Clinical validation of an ultra high-throughput spiral microfluidics for the detection and enrichment of viable circulating tumor cells, *PLoS One 9*, e99409.
[151] Lee, M. G., Choi, S., and Park, J. K. (2009) Rapid laminating mixer using a contraction-expansion array microchannel, *Applied Physics Letters 95*, 051902.
[152] Lee, M. G., Choi, S., and Park, J. K. (2009) Three-dimensional hydrodynamic focusing with a single sheath flow in a single-layer microfluidic device, *Lab on a Chip 9*, 3155-3160.
[153] Lee, M. G., Choi, S., Kim, H. J., Lim, H. K., Kim, J. H., Huh, N., *et al.* (2011) Inertial blood plasma separation in a contraction–expansion array microchannel, *Applied Physics Letters 98*, 253702.

[154] Lee, M. G., Shin, J. H., Bae, C. Y., Choi, S., and Park, J.-K. (2013) Label-free cancer cell separation from human whole blood using inertial microfluidics at low shear stress, *Analytical Chemistry 85,* 6213-6218.
[155] Park, J. S., Song, S. H., and Jung, H. I. (2009) Continuous focusing of microparticles using inertial lift force and vorticity via multi-orifice microfluidic channels, *Lab on a Chip 9,* 939-948.
[156] Park, J.-S. and Jung, H.-I. (2009) Multiorifice flow fractionation: Continuous size-based separation of microspheres using a series of contraction/expansion microchannels, *Analytical Chemistry 81,* 8280-8288.
[157] Sim, T. S., Kwon, K., Park, J. C., Lee, J.-G., and Jung, H.-I. (2011) Multistage-multiorifice flow fractionation (MS-MOFF): continuous size-based separation of microspheres using multiple series of contraction/expansion microchannels, *Lab on a Chip 11,* 93-99.
[158] Moon, H. S., Kwon, K., Kim, S. I., Han, H., Sohn, J., Lee, S., *et al.* (2011) Continuous separation of breast cancer cells from blood samples using multi-orifice flow fractionation (MOFF) and dielectrophoresis (DEP), *Lab on a Chip 11,* 1118-1125.
[159] Warkiani, M. E., Tay, A. K. P., Khoo, B. L., Xiaofeng, X., Han, J., and Lim, C. T. (2015) Malaria detection using inertial microfluidics, *Lab on a Chip 15,* 1101-1109.
[160] Shelby, J. P., Lim, D. S., Kuo, J. S., and Chiu, D. T. (2003) Microfluidic systems: high radial acceleration in microvortices, *Nature 425,* 38-38.
[161] Chiu, D. T. (2007) Cellular manipulations in microvortices, *Analytical and Bioanalytical Chemistry 387,* 17-20.
[162] Hur, S. C., Mach, A. J., and Di Carlo, D. (2011) High-throughput size-based rare cell enrichment using microscale vortices, *Biomicrofluidics 5,* 022206.
[163] Mach, A. J., Kim, J. H., Arshi, A., Hur, S. C., and Di Carlo, D. (2011) Automated cellular sample preparation using a Centrifuge-on-a-Chip, *Lab on a Chip 11,* 2827-2834.
[164] Wang, X., Zhou, J., and Papautsky, I. (2013) Vortex-aided inertial microfluidic device for continuous particle separation with high size-selectivity, efficiency, and purity, *Biomicrofluidics 7,* 044119.
[165] Che, J., Mach, A. J., Go, D. E., Talati, I., Ying, Y., Rao, J., *et al.* (2013) Microfluidic purification and concentration of malignant pleural effusions for improved molecular and cytomorphological diagnostics, *PLoS One 8,* e78194.
[166] Zhou, J., Kasper, S., and Papautsky, I. (2013) Enhanced size-dependent trapping of particles using microvortices, *Microfluidics and nanofluidics 15,* 611-623.
[167] Wang, X. and Papautsky, I. (2015) Size-based microfluidic multimodal microparticle sorter, *Lab on a Chip 15,* 1350-1359.
[168] Amini, H., Sollier, E., Masaeli, M., Xie, Y., Ganapathysubramanian, B., Stone, H. A., *et al.* (2013) Engineering fluid flow using sequenced microstructures, *Nature Communications 4,* 1826.
[169] Stoecklein, D., Wu, C.-Y., Owsley, K., Xie, Y., Di Carlo, D., and Ganapathysubramanian, B. (2014) Micropillar sequence designs for fundamental inertial flow transformations, *Lab on a Chip 14,* 4197-4204.
[170] Chung, A. J., Pulido, D., Oka, J. C., Amini, H., Masaeli, M., and Di Carlo, D. (2013) Microstructure-induced helical vortices allow single-stream and long-term inertial focusing, *Lab on a Chip 13,* 2942-2949.

[171] Sollier, E., Amini, H., Go, D., Sandoz, P., Owsley, K., and Di Carlo, D. (2015) Inertial microfluidic programming of microparticle-laden flows for solution transfer around cells and particles, *Microfluidics and nanofluidics* 1-13.
[172] Di Carlo, D., Jon, F., Irimia, D., Tompkins, R. G., and Toner, M. (2008) Equilibrium separation and filtration of particles using differential inertial focusing, *Analytical Chemistry 80,* 2204-2211.
[173] Oakey, J., Applegate Jr, R. W., Arellano, E., Carlo, D. D., Graves, S. W., and Toner, M. (2010) Particle focusing in staged inertial microfluidic devices for flow cytometry, *Analytical Chemistry 82,* 3862-3867.
[174] Ozkumur, E., Shah, A. M., Ciciliano, J. C., Emmink, B. L., Miyamoto, D. T., Brachtel, E., *et al.* (2013) Inertial focusing for tumor antigen–dependent and–independent sorting of rare circulating tumor cells, *Science Translational Medicine 5,* 179ra147.
[175] Goda, K., Ayazi, A., Gossett, D. R., Sadasivam, J., Lonappan, C. K., Sollier, E., *et al.* (2012) High-throughput single-microparticle imaging flow analyzer, *Proceedings of the National Academy of Sciences 109,* 11630-11635.
[176] Karabacak, N. M., Spuhler, P. S., Fachin, F., Lim, E. J., Pai, V., Ozkumur, E., *et al.* (2014) Microfluidic, marker-free isolation of circulating tumor cells from blood samples, *Nature Protocols 9,* 694-710.
[177] Duffy, D. C., McDonald, J. C., Schueller, O. J. A., and Whitesides, G. M. (1998) Rapid prototyping of microfluidic systems in poly (dimethylsiloxane), *Analytical Chemistry 70,* 4974-4984.
[178] Lim, D. S. W., Shelby, J. P., Kuo, J. S., and Chiu, D. T. (2003) Dynamic formation of ring-shaped patterns of colloidal particles in microfluidic systems, *Applied Physics Letters 83,* 1145-1147.
[179] Zheng, Z., Fletcher, D. F., and Haynes, B. S. (2013) Laminar heat transfer simulations for periodic zigzag semicircular channels: chaotic advection and geometric effects, *International Journal of Heat and Mass Transfer 62,* 391-401.
[180] Gossett, D. R. and Carlo, D. D. (2009) Particle focusing mechanisms in curving confined flows, *Analytical Chemistry 81,* 8459-8465.
[181] Russom, A., Gupta, A. K., Nagrath, S., Di Carlo, D., Edd, J. F., and Toner, M. (2009) Differential inertial focusing of particles in curved low-aspect-ratio microchannels, *New journal of physics 11,* 075025.
[182] Kersaudy-Kerhoas, M. and Sollier, E. (2013) Micro-scale blood plasma separation: from acoustophoresis to egg-beaters, *Lab on a Chip 13,* 3323-3346.
[183] Zhang, J., Yan, S., Sluyter, R., Li, W., Alici, G., and Nguyen, N.-T. (2014) Inertial particle separation by differential equilibrium positions in a symmetrical serpentine micro-channel, *Scientific reports 4,* Art No. 4527.
[184] Zhang, J., Yan, S., Li, W., Alici, G., and Nguyen, N.-T. (2014) High throughput extraction of plasma using a secondary flow-aided inertial microfluidic device, *RSC Advances 4,* 33149-33159.
[185] Toner, M. and Irimia, D. (2005) Blood-on-a-chip, *Annual Review of Biomedical Engineering 7,* 77-103.
[186] Lee, M. G., Shin, J. H., Choi, S., and Park, J.-K. (2014) Enhanced blood plasma separation by modulation of inertial lift force, *Sensors and Actuators B: Chemical 190,* 311-317.

[187] Rodríguez-Villarreal, A. I., Arundell, M., Carmona, M., and Samitier, J. (2010) High flow rate microfluidic device for blood plasma separation using a range of temperatures, *Lab on a Chip 10,* 211-219.
[188] Kersaudy-Kerhoas, M., Dhariwal, R., Desmulliez, M. P., and Jouvet, L. (2010) Hydrodynamic blood plasma separation in microfluidic channels, *Microfluidics and nanofluidics 8,* 105-114.
[189] Choi, S., Ku, T., Song, S., Choi, C., and Park, J.-K. (2011) Hydrophoretic high-throughput selection of platelets in physiological shear-stress range, *Lab on a Chip 11,* 413-418.
[190] Jin, C., McFaul, S. M., Duffy, S. P., Deng, X., Tavassoli, P., Black, P. C., *et al.* (2014) Technologies for label-free separation of circulating tumor cells: from historical foundations to recent developments, *Lab on a Chip 14,* 32-44.
[191] Bhagat, A. A. S., Hou, H. W., Li, L. D., Lim, C. T., and Han, J. (2011) Pinched flow coupled shear-modulated inertial microfluidics for high-throughput rare blood cell separation, *Lab on a Chip 11,* 1870-1878.
[192] Fukuda, S. and Schmid-Schönbein, G. W. (2002) Centrifugation attenuates the fluid shear response of circulating leukocytes, *Journal of Leukocyte Biology 72,* 133-139.
[193] Xie, Y., Zheng, D., Li, Q., Chen, Y., Lei, H., and Pu, L. L. (2010) The effect of centrifugation on viability of fat grafts: an evaluation with the glucose transport test, *Journal of Plastic, Reconstructive and Aesthetic Surgery 63,* 482-487.
[194] Constantinescu, P., Wang, B., Kovacevic, K., Jalilian, I., Bosman, G. J., Wiley, J. S., *et al.* (2010) P2X7 receptor activation induces cell death and microparticle release in murine erythroleukemia cells, *Biochimica et Biophysica Acta (BBA)-Biomembranes 1798,* 1797-1804.
[195] Wang, B. and Sluyter, R. (2013) P2X7 receptor activation induces reactive oxygen species formation in erythroid cells, *Purinergic Signalling 9,* 101-112.
[196] Friend, C., Scher, W., Holland, J., and Sato, T. (1971) Hemoglobin synthesis in murine virus-induced leukemic cells in vitro: stimulation of erythroid differentiation by dimethyl sulfoxide, *Proceedings of the National Academy of Sciences 68,* 378-382.
[197] Tsiftsoglou, A. S., Pappas, I. S., and Vizirianakis, I. S. (2003) Mechanisms involved in the induced differentiation of leukemia cells, *Pharmacology & Therapeutics 100,* 257-290.
[198] Yan, S., Zhang, J., Li, M., Alici, G., Du, H., Sluyter, R., *et al.* (2014) On-chip high-throughput manipulation of particles in a dielectrophoresis-active hydrophoretic focuser, *Scientific reports 4,* Art No. 5060.
[199] Zhang, J., Yan, S., Alici, G., Nguyen, N.-T., Di Carlo, D., and Li, W. (2014) Real-time control of inertial focusing in microfluidics using dielectrophoresis (DEP), *RSC Advances 4,* 62076-62085.
[200] Baek, S. H., Chang, W.-J., Baek, J.-Y., Yoon, D. S., Bashir, R., and Lee, S. W. (2009) Dielectrophoretic technique for measurement of chemical and biological interactions, *Analytical Chemistry 81,* 7737-7742.
[201] Collins, D. J., Alan, T., and Neild, A. (2014) Particle separation using virtual deterministic lateral displacement (vDLD), *Lab on a Chip 14,* 1595-1603.
[202] Matas, J.-P., Morris, J. F., and Guazzelli, É. (2009) Lateral force on a rigid sphere in large-inertia laminar pipe flow, *Journal of Fluid Mechanics 621,* 59-67.

[203] Cheung, K. C., Di Berardino, M., Schade‐Kampmann, G., Hebeisen, M., Pierzchalski, A., Bocsi, J., *et al.* (2010) Microfluidic impedance‐based flow cytometry, *Cytometry Part A 77*, 648-666.
[204] Spencer, D. C., Elliott, G., and Morgan, H. (2014) A sheath-less combined optical and impedance micro-cytometer, *Lab on a Chip 14*, 3064-3073.
[205] Henry, T., Gossett, D. R., Moon, Y. S., Masaeli, M., Sohsman, M., Ying, Y., *et al.* (2013) Quantitative diagnosis of malignant pleural effusions by single-cell mechanophenotyping, *Science Translational Medicine 5*, 212ra163.
[206] Li, H. and Bashir, R. (2002) Dielectrophoretic separation and manipulation of live and heat-treated cells of *Listeria* on microfabricated devices with interdigitated electrodes, *Sensors and Actuators B: Chemical 86*, 215-221.
[207] Lapizco-Encinas, B. H., Simmons, B. A., Cummings, E. B., and Fintschenko, Y. (2004) Dielectrophoretic concentration and separation of live and dead bacteria in an array of insulators, *Analytical Chemistry 76*, 1571-1579.
[208] Alazzam, A., Stiharu, I., Bhat, R., and Meguerditchian, A. N. (2011) Interdigitated comb‐like electrodes for continuous separation of malignant cells from blood using dielectrophoresis, *Electrophoresis 32*, 1327-1336.
[209] Stephens, M., Talary, M., Pethig, R., Burnett, A., and Mills, K. (1996) The dielectrophoresis enrichment of CD34+ cells from peripheral blood stem cell harvests, *Bone Marrow Transplantation 18*, 777-782.